STRAIN AND INTERFACE-INDUCED CHARGE, ORBITAL AND SPIN ORDERINGS IN TRANSITION-METAL OXIDE PEROVSKITES

DAVID PESQUERA HERRERO

Memoria presentada para la obtención de la titulación de Doctor

Supervisor: Prof. Josep Fontcuberta i Griñó
Institut de Ciència de Materials de Barcelona

Tutor: Prof. Javier Rodíguez Viejo

Programa de Doctorado en Ciencia de Materiales - Departamento de Física
Facultad de Ciencias
Universidad Autónoma de Barcelona
2014

ICMAB CSIC

UAB
Universitat Autònoma de Barcelona

Prof. Josep Fontcuberta i Griñó, Profesor de Investigación del Consejo Superior de Investigaciones Científicas, y el **Prof. Javier Rodríguez Viejo**, Catedrático de la Universidad Autónoma de Barcelona,

CERTIFICAN:

Que David Pesquera Herrero, licenciado en Ciencias Físicas por la Universidad Complutense de Madrid ha llevado a cabo esta tesis doctoral bajo su dirección, portando por título "*Strain and interface induced electronic states in transition metal oxides*", la cual queda recogida en esta memoria para optar al grado de Doctor en el programa de Ciencia de Materiales.

Y para que así conste, firman el presente certificado:

Prof. Josep Fontcuberta i Griñó

Prof. Javier Rodriguez Viejo

Bellaterra, 21 de julio de 2014

To *the Girl from the North country*.

Imagination will often carry us
to worlds that never were.
But without it we go nowhere.

— Carl Sagan

ABSTRACT

Transition metal oxides display a rich variety of physical and chemical properties making them potential candidates for many different technological applications. At the origin of this richness lies a complex puzzle of electron, phonon, charge and spin interactions that still requires for larger observation and testing in order to put all the pieces together. A keystone that can provide many answers to this puzzle is the important role of the transition metal *d* electrons contributing to the valence or conduction bands. These electrons interact with each other, and with electrons in the neighbour oxygens, transporting the charge or ordering their magnetic moments in many ways, with a large sensitivity to structural characteristics or to external parameters like temperature, pressure, electromagnetic fields, ...

It is thus of high interest for the understanding of the physics governing the properties of transition metal oxides to directly access the electronic structure, and explore its response as a function of these intrinsic or extrinsic parameters. The possibility to perform such fundamental experiments has been enabled in the recent decades, thanks to the development of synchrotron accelerator laboratories that have provided a powerful boost to x-ray techniques, which allow to use photon-electron interactions as direct probe of electronic configurations of the different elements independently. Moreover, tunable photon polarizations have been used in the recent years to reveal the fine characteristics of the electronic structure and explore the anisotropy of electron clouds or spin arrangements.

In this thesis we have taken advantage of these techniques, and other more standard ones, to monitor the electron and spin orderings in different transition metal oxide compounds, allowing us to address the following topics:

1. **Influence of strain in the electron distribution of transition metal oxide films**: When growing nanometric films of these materials on single crystal substrates, bulk properties can be widely modified, due to the breaking of symmetry around the transition metal ions as induced by the strain imposed by the coherent growth of the films, adapting to the substrate lattice constraints. We study how strain in thin films can induce charge localization, and how depending on the sign of the strain, distinct electronic configurations can be stabilized, favouring different orbital states that can couple to the spin ordering as we will show in materials presenting magnetic order. Structural distortions as induced by strain can also affect the band structure due to modified bondings between transition metal and oxygen ions. As we demonstrate in this thesis, important covalency effects need to be taken into account and correlate well with the measured macroscopic properties.

2. **Effect of symmetry breaking at surfaces of transition metal oxides**: Although strain effects are important and can dominate the response of thin films, a large symmetry breaking is inevitably found at interfaces. Boundaries can impose a completely different atomic surrounding to transition metals, that will strongly affect to the electronic structure. A large effort in this thesis has been dedicated to disentangle the interface effects and separate them from strain induced effects. Special attention has been directed to the free surface of these oxides, where the large rupture of symmetry -at surface/vaccuum or surface/atmosphere interfaces-

is expected to promote profound alterations on the local electronic structure and induce a large charge localization.

3. **Interfacial reconstructions in transition metal oxide heterostructures**: When growing heterostructures of transition metal oxides, the configuration at interfaces can also suffer from rearrangements leading to charge deviations or orbital and spin reconstructions. We explore these phenomena at interfaces between dissimilar oxides showing how the orbital hierarchy can be tuned at interfaces by proper selection of layer components or crystallographic orientations.

Our study has been focused to different trending systems (mixed-valence manganites, nickelates and $LaAlO_3/SrTiO_3$ heterostructures) where the information of the strain and interface induced configurations can provide new insight into the observed effects in these materials. Nevertheless, the methodology used in this work and the conclusions derived from our results can be of relevance for the understanding of interface-related phenomena in other transition metal oxides.

RESUMEN

Los óxidos de metales de transición muestran una gran variedad de propiedades físicas y químicas que los hacen candidatos potenciales para diversas aplicaciones tecnológicas. El origen de esta diversidad yace en un complejo puzzle de interacciones que aún requiere de una mayor observación y experimentación que permita juntar todas las piezas. Una pieza angular en este puzzle viene dada por los electrones *d* de los metales de transición que forman las bandas de conduccion o de valencia. Estos electrones interactúan entre ellos, y con los electrones de los oxígenos vecinos, transportando carga o ordenando sus momentos magnéticos en diversas maneras, siendo muy susceptibles a las características estructurales o a parámetros externos como temperatura, presión, campos electromagnéticos, etc.

Es por tanto de gran interes para el entendimiento de la física que gobiernas las propiedades de los óxidos de metales de transición examinar su estructura electrónica y explorar su respuesta en función parámetros intrínsecos del material o de parámetros extrínsecos inducidos sobre él. La posibilidad de realizar dichos experimentos ha sido posible en las últimas décadas, gracias al desarrollo de laboratorios de luz sincrotrón, que han ayudado a perfeccionar las técnicas de rayos-X, que permiten emplear las interacciones fotón-electrón para investigar la configuración electrónica de diferentes elementos independientemente. Además, la polarización de la luz ha podido ser usada como herramienta en los últimos años para revelar la estructura fina de las configuraciones electrónicas y explorar la anisotropía de la distribucion electrónica y del ordenamiento magnético.

En la presente tesis hemos sacado provecho de estas técnicas, y de otras más estándar, para monitorizar el ordenamiento electronico y de espines en diferentes compuestos de óxidos de metales de transición:

1. **Influencia de la tensión en la distribución electrónica de capas finas de óxidos de metales de transición:** Al crecer capas nanométricas de estos materiales en sustratos cristalinos, las propiedades del material masivo pueden verse profundamente modificadas, debido a la ruptura de simetría inducida en torno a los iones de metales de transición por la tensión impuesta por el crecimiento coherente de las capas, que adaptan su red cristalina a la del sustrato. Estudiamos en esta tesis cómo la tensión en capas finas puede inducir localización de carga, y cómo dependiendo del signo de la tensión, distintas configuraciones electronicas pueden estabilizarse, favoreciendo diferentes estados orbitales que pueden influir en el ordenamiento de los espines, como demostraremos en materiales que presentan orden magnético. Las distorsiones estructurales inducidas por la tensión pueden también modificar la estructura de bandas debido a las alteraciones producidas en los enlaces entre los iones de metales de transición y los oxígenos. Como demostramos en esta tesis, efectos de covalencia han de ser tenidos en cuenta ya que se correlacionan visiblemente con las propiedades macroscópicas.

2. **Efecto de la ruptura de simetría en la superficie de óxidos de metales de transición:** A pesar de que los efectos debidos a la tensión son importantes y pueden dominar la respuesta de las capas finas, en las intercaras puede existir una considerable ruptura de simetría al imponerse un entorno atómico totalmente distinto, que alterará notablemente la estructura electrónica de los metales de transición. En esta tesis se ha dedicado un amplio esfuerzo para desentrañar los efectos de intercara y separarlos de los efectos debidos a la tensión. Se ha dedicado una atención especial a la superficie libre de estos óxidos, donde la importante ruptura de simetría -en la superficie en contacto con el vacío o la atmósfera- puede producir profundas alteraciones en la estructura electrónica local e inducir importantes efectos de localización de carga.

3. **Reconstrucciones en las intercaras de heteroestructuras de óxidos de metales de transición:** Al crecer heteroestructuras de óxidos de metales de transición, la configuración en las intercaras puede también sufrir reestructuraciones dando lugar a desviaciones de carga o a reconstrucciones orbitales o magnéticas. Aquí exploramos estos fenómenos en las intercaras entre distintos óxidos mostrando cómo la jerarquía orbital pude ser modificada en las intercaras mediante la apropiada selección de materiales y de orientaciones cristalográficas.

Nuestro estudio se ha focalizado en diferentes sistemas de gran interés en la actualidad (manganitas de valencia mixta, niquelatos y heteroestructuras $LaAlO_3/SrTiO_3$) en los que el conocimiento adquirido sobre las configuraciones inducidas por efectos de tensión y de intercaras puede proveer un mayor entendimiento de las propiedades observadas en estos materiales. No obstante, la metodología empleada en este trabajo y las conclusiones derivadas de nuestros resultados pueden ser de amplia relevancia para el entendimiento de los fenómenos de intercara de otros sistemas de óxidos de metales de transición.

ACKNOWLEDGMENTS

Firstly, I would like to express a deep gratitude to my supervisor, Pep, for all the knowledge and expertise that he has provided to my work in this thesis and to myself, helping me to develope as a scientist and as a person. In this gratitude I should also include Gervasi: without his support and his participation in the long discussions at Pep's office this work would have been impossible.

I would like to thank to our main collaborators abroad. Marek and Ewa, for receiving me so kindly in my stage at his lab in Warsaw. A special recognition goes to Alessandro, who helped me to understand and analyze the tons of data from our synchrotron experiments and pushed me to have a critical view in the data adquisition and treatment by thousands of mails interchanged even at intempestive hours. Thanks to the ladies from Elettra, Federica and Elena, for their hard job performing endless measurements, and to Eric also for his tireless support in our beamtimes fighting against the Bora wind, and to the people at BOREAS (Pierlu, Manu, Javi) for making possible our ideas in their beamline.

I recognize the support of the technicians of AFM, XRD, clean room, etc. from ICMAB. A special mention to Bernie who was always very helpful in the SQUID and PPMS measurements, and to Vassil for his patience and expertise.

I would like to acknowledge to all the people in magnetic materials group, the "old school" members (Xavi, Franco, Ignasi, Romais, Micha, Ondrej...), and the young members (Blai, Mateusz,...) and, specially, to those who were always there: Roque, that showed me the wonders of MOKE and the best mojitos in Barcelona - besides many other things; Diego, always available for a coffee and for discussing about experiments and ideas, and Nico, that put so much effort in producing the best samples for me. And to Floren, for his wide knowledge in the films growth that enabled this work.

With all my heart I thank the big family of ICMAB. To my confidant "little sister" for all the shared moments in the day by day life, in the good times and in the bad times. To the girls from the third floor, always inducing a smile in every meeting at the corridors or at the coffee machines and to the people staying at "la Comuna" that received me with open arms when I first came to Barcelona: Dr. Rouco, Dra. Marteta, Dr. Carretero, Mr. Maciá, and so many more... The lunch group with Prof. Roquetas and his endless ideas, Pablazza, that helped so much in the personal and in the professional life, the big Marc, the supercomputer guy that provided so much fun and laughs, and Miss Greta for the moments and discussions shared in the last stands of our thesis. Thanks to Willy, Melchi, Sarita, Nina, Yarbi and all those who supported me and made me enjoy my days in Barcelona making me think of this time as "those wonderful thesis years", and to Victor, Gogu and all the ones that sent me their support from Madrid.

And last but not least, special recognition deserves my family, who made everything possible for me to arrive at this point, and Катя, за делать дни светлее.

Financial support for this thesis has been provided by FPI-CSIC-MICINN (Formacion de Profesorado Investigador-Consejo Superior de Investigaciones Cienticas) grant with reference BES-2009-020418. Support from Spanish Government (Projects MAT2008-06761-C03, MAT2011-29269-CO_3 and NANOSELECT CSD2007-00041) and Generalitat de Catalunya (2009 SGR 00376) are also acknowledged.

CONTENTS

NOMENCLATURE

2DEG	2-dimensional electron gas
BTO	$BaTiO_3$
DE	Double exchange
DOS	Density of states
DSO	$DyScO_3$
FTJ	Ferroelectric Tunnel Junction
GSO	$GdScO_3$
JT	Jahn-Teller
KE	Kinetic energy
LAO	$LaAlO_3$
LCMO5	$La_{1/2}Ca_{1/2}MnO_3$
LGO	$LaGaO_3$
LNO	$LaNiO_3$
LSAT	$(LaAlO_3)_{0.3} - (Sr_2AlTaO_6)_{0.7}$
LSMO5	$La_{1/2}Sr_{1/2}MnO_3$
LSMO	$La_{2/3}Sr_{1/3}MnO_3$
m_o	Orbital magnetic moment
ML	Monolayer
M_S	Saturation magnetization
m_s	Spin magnetic moment
n_e	Number of electrons
NGO	$NdGaO_3$
n_h	Number of holes
NMR	Nuclear magnetic resonance
NSO	$NdScO_3$
PEY	Partial electron yield
PLD	Pulsed laser deposition

PS Phase separation

QW Quantum well

RBS Rutherford backscattering spectroscopy

RHEED Reflection high energy electron diffraction

RSM Reciprocal Space Map

SQUID Superconducting quantum interference device

SRO $SrRuO_3$

STO $SrTiO_3$

SZO $SrZrO_3$

T_C Curie temperature

TEY Total electron yield

TMO Transition metal oxide

uc unit cell

XAS X-ray absorption spectroscopy

XLD X-ray linear dichroism

XMCD X-ray magnetic circular dichroism

XMLD X-ray magnetic linear dichroism

XNLD X-ray natural linear dichroism

YAO $YAlO_3$

Part I

INTRODUCTION

1 INTRODUCTION

1.1 INTRODUCTORY CONCEPTS

1.1.1 *Electronic states and orbital physics in transition metal oxides*

Transition metal oxide (TMO) perovskites are highly versatile materials. They can be superconductors with high transition temperatures, they can decrease their resistivity by several orders of magnitude upon the application of a magnetic field, or they can show coexistance of diverse magnetic phases and even ferroelectricity, among other countless fascinating properties. The possibility to present different properties that can be tuned with temperature, pressure, magnetic field, or other external stimulus is a result of the complexity of their microscopic interactions. Unveiling the origin of such interactions is thus a stimulant challenge for physicists and provides a great potentiality for technological applications.

In a general description, perovskite oxides are compounds with ABO_3 composition where an alkaline earth or rare earth is positioned in the A-site at the corner of the lattice, as shown in the fig.1.1(a), while B- sites, at the center of the lattice are occupied by transition metal elements, surrounded by 6 oxygen ions forming a regular octahedron. This coordination profoundly affects the electronic structure of transition metal (TM) ions, having a nd configuration. As d orbitals are strongly anisotropic, the electronic cloud in each orbital is very directional and can point either towards the oxygen ions or away from them. Naturally, electrons prefer to orient their clouds away from the oxygens to reduce the electrostatic repulsion and these orbitals (named t_{2g}) get their energy reduced with respect to the orbitals pointing towards the oxygens (e_g) (fig.1.1(b)). This *crystal field* induced breaking of the degenerancy is inherent to the cubic environment of the TM. Further lowering of this symmetry, e.g., by volume-preserving tetragonal distortion, produce an additional removal of degenerancy in which the orbitals oriented along the directions with shortened $B-O$ distances will increase their energy (fig.1.1(c)).

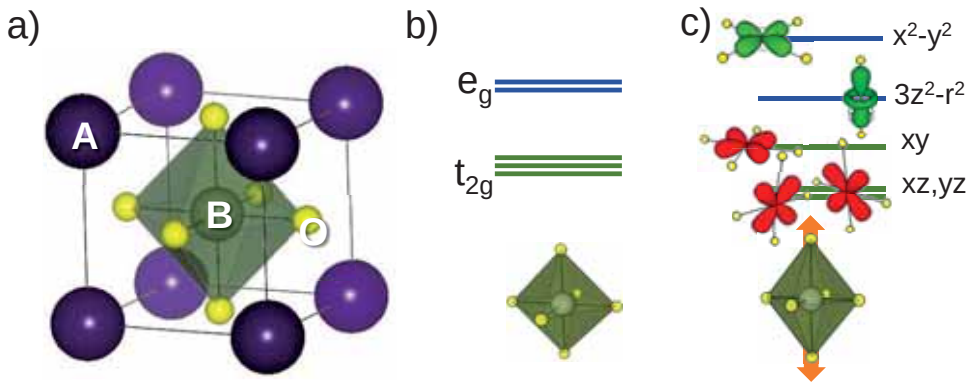

Figure 1.1: a) Perovskite structure of ABO_3 compounds. b) Splitting of d levels in octahedral crystal field (cubic symmetry). c) Splitting in tetragonal symmetry; schematic drawings indicating the shape and orientation respect neighbouring oxygens of corresponding orbitals for each level are pictured

This coupling between the oxygen displacements and the crystal field splitting of the TM is known as Jahn-Teller coupling, and reveals the strong correlation effects in these perovskites due to electron-electron and electron-lattice interactions.

In TMOs the electronic and magnetic structure is dictated by these d electrons that constitute the valence/conduction bands. Correlation effects due to electron-electron interactions can promote insulating behaviour in materials that, according to one electron picture, should be metallic given the presence of partially occupied bands; however, the large repulsive Coulomb energies between d electrons can promote **charge** localization, impeding the electron jump among TM sites. On top of that, in some TMOs, the overlapping between oxygen p and TM d orbitals leads to largely hybridized bands in which the hybridization strength of d bands with that of oxygen ligands determines the effective bandwidth, thus certifying the semi-covalent character of atomic bonds in these compounds. On the other hand, **orbital** ordering, as induced by symmetry constraints imposed by the **lattice**, can influence the charge transfer process (different orbitals will hybridize differently), promoting larger electron delocalization in certain directions or difficulting the electron jump in others. This induced anisotropy can strongly affect the interatomic **spin**-spin interactions leading to different types of magnetic order coupled to the orbital order[1].

It is therefore the interplay between these charge, orbital, lattice and spin degrees of freedom what provides the richness of physics phenomena to TMOs.

1.1.2 *Strain tuning of electronic structure*

One way to explore and manipulate the electronic interactions in TMOs is to play with the lattice degree of freedom imposing different symmetry constraints that will influence in the charge, orbital and spin orders. This can be done by strain engineering.

The good structural stability of TMO perovskites permits the fabrication of heterostructures in the form of thin films, or multilayers, deposited in single crystal substrates. Physical vapour deposition techniques (pulsed laser ablation, sputtering, molecular beam epitaxy) allow to obtain, under the appropiate conditions, a crystalline textured growth with a proper stoichiometric transfer between the target material and the substrate. An epitaxial growth (that is, with single domain orientation) can be achieved in thin films of materials having a lattice parameter (a_{film}) with a low mismatch with that of the substrate (a_{subs}). If the lattice mismatch is high, or if the film thickness is large enough, the film lattice will relax towards its bulk structure, creating extended defects. Other possible relaxation mechanisms include cation segregation or creation of oxygen vacancies, that will reduce the elastic energy needed by the film lattice to adapt to that of the substrate.

As many TMO materials show good structural compatibility with commercially available single crystal oxide substrates, epitaxial films with high quality can be obtained of a wide range of interesting materials. In this manner, structural distortions promoted by the substrate lattice can profoundly alter the TM symmetry in the B site, which will be mainly affected by the modification of $B-O$ distances and $O-B-O$ angles promoted by octahedra tetragonal distortions and rotations, respectively. This way, by proper substrate selection, strain induced in the films can be tuned from in-plane compressive ($a_{subs} < a_{film}$) to in-plane tensile ($a_{subs} > a_{film}$), enabling the tuning of TM electronic structure. In fig.1.2, the lattice parameters (approximated by a pseudo-cubic unit cell) of several typical TMOs used as substrates or target materials are shown.

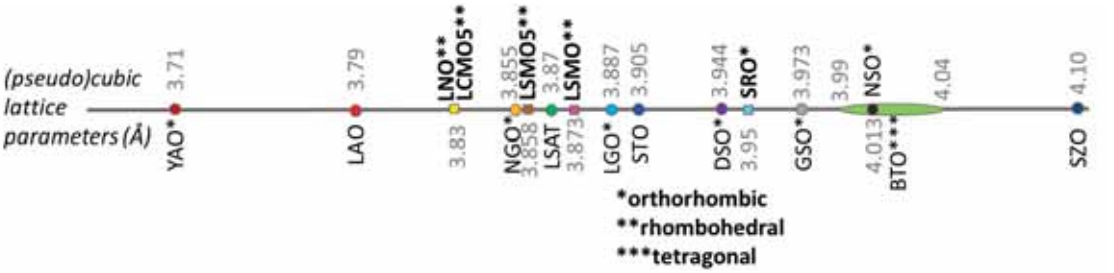

Figure 1.2: Pseudocubic lattice parameters of different oxides in their bulk structures.

1.1.3 *New physics and new materials at interfaces*

Strain provides a way to impose symmetry constraints in thin films, extending for several tens or even hundreds of nanometers. However, boundary conditions cannot be avoided and the presence of interfaces imposes additional symmetry constraints. At interfaces, the local crystalline environment of the TM is dissimilar to that of the bulk material. This symmetry breaking thus promotes a different crystal field that can induce local reconstructions of the orbital, charge and spin configurations, leading to new modified properties at interfaces.

Relevant phenomena occuring at the interface between two dissimilar TMOs include charge transfer, the same way it occurs in semiconductor structures. However, in TMOs, electron or hole doping can have striking effects on the material behaviour, as is can induce a phase change, completely altering the properties at the interface. This permits for example to obtain large magnetolectric coupling at interfaces between a doping sensitive magnetic TMO and a ferroelectric. Furthermore, electronic reconstruction at interfaces can lead to the occurrence of unexpected 2-dimensional high mobility phases between insulating systems, or even superconductivity.

All these phenomena at interfaces are ultimately associated to the state of the d electrons in the transition metals at interfaces and their relative occupancies. Therefore, determining the d orbitals configuration is of primary importance to unveil the origins of interfacial phenomena in TMO heterostructures.

1.2 OUTLOOK

In this thesis we will explore the origins and effects of electron redistribution, as induced extendedly by epitaxial strain in TMO thin films, or locally due to the presence of structural defects and interfaces. Among the different studied interfaces, special attention will be given to the free surface, which is the most dramatic one and provides an ideal scenario to study the symmetry breaking effects in the electronic configuration.

Mixed valence manganites ($(R_{1-x}A_x)(Mn^{3+}_{1-x}Mn^{4+}_x)O_3$, R= rare-earth, A=alkali) are archetypical systems to explore charge and orbital dependent phenomena. In manganites, the transport mechanism is mediated by electron hopping between $Mn^{3+}$and Mn^{4+} sites and the magnetic moments are coupled by double exchange mechanisms between the cations. The carge mobility can be tuned by stoichiometric variations (changing hole doping x), but also charge localization can be promoted by strain (that can reduce the hopping in certain directions) or by the occurrence of structural defects. In thin films, an important source of charge trapping is found at interfaces, where the magnetotransport mechanism can be completely suppressed. In **chapter** 3, we shall study the origin and extension of this charge trapping phenomena in manganite films with a

doping $x = 1/3$, optimal for stabilizing a ferromagnetic metallic phase. Using Nuclear Magnetic Resonance spectroscopy we design experiments to monitor the evolution of the charge localization and magnetic anisotropy sensed by Mn nuclei, as a function of samples thickness or induced defects in the films, providing new insights into the phase separation phenomena in manganites.

In **chapter 4** we inspect the microscopic origins of charge localization in optimally doped manganites. By means of x-ray absorption measurements we get access to the electron occupancy of the different d states in the conduction band. The orbital polarization, given by the occupancy difference of the e_g states, is known to depend on the strain imposed in the films. However, in ultrathin films, this Jahn-Teller related effect on the orbital occupancy seems to be violated. By extensive examination on the films thickness, orientation and layer termination dependence of the anisotropy of the absorption signal we identify the contribution of free surfaces to the orbital polarization.

The rupture of symmetry at the free surfaces must necessarily be modified when capping the manganite films with layers of other structurally equivalent TMOs. In **chapter 5** we study the induced charge modifications at the interfaces between optimally doped magnanites and oxide capping layers. More specifically, charge transfer and orbital reconstructions are explored at the manganite interfacial layers in contact with several capping materials, as well as their influence on the magnetic interactions. The results put some light into the factors regulating the electron distribution at oxide interfaces.

The strain tunability of orbital order can have a profound impact on the properties of manganite thin films having a composition in the verge of two magnetic phases. This is proved in **chapter 6**, where low temperature polarized x-ray absorption is used to reveal the magnetic order of half-doped manganites ($x = 1/2$) thin films. The results show a strong correlation between magnetic and orbital orders, and explain the strain regulation of the coexistance between ferromagnetic and antiferromagnetic phases in manganite compounds with this doping. Furthermore, by substituting the doping cation, the effect of different bandwidth on the effectivity of the strain regulation is examined.

The knowledge acquired in the prototypical manganite system is tested in another system with similar electronic configuration in **chapter 7**. We study here for $LaNiO_3$ epitaxial thin films the role of the strain and surface contributions to the orbital polarization, enabling a explanation for the apparent assymetric orbital response to strain reported for this system. Moreover, we explore the relevant covalency effects due to hybridization of nickel and oxygen states and the relevance of strain and surface induced distortions in the $Ni - O$ distances and bonding angles affecting the orbital overlapping and, consequently, the conduction properties in the films.

Finally, in **chapter 8** we study the observed orbital reconstruction of the $Ti - 3d$ states at the interface between two insulating TMOs ($SrTiO_3$ and $LaAlO_3$). At these interfaces, a highly mobile electron gas is observed, and proposed to be responsible for the orbital reconstruction. The promoted orbital symmetry in the lowest energy states can also influence in the interactions giving rise to magnetism and superconductivity in these interfaces. We show here, how, by proper selection of crystallographic samples orientation, this orbital symmetry can be modified.

Chapter iii is dedicated to compeil the results obtained in the thesis, analyzed in a wider perspective and proposing ideas for future works in transition metal oxides.

2

SOFT X-RAYS ABSORPTION TECHNIQUES APPLIED TO TRANSITION METALS

The development of x-ray sources have enabled the advance in the investigation of matter. Nowadays, synchrotron radiation sources allow for the use of powerful techniques to study the inner structure of matter at the nanoscale. Synchrotron radiation provides a photons flux 10^9 times larger than typical x-ray tubes allowing for a larger data adquisition in reduced time and with higher quality. Other features enabled by synchrotron radiation sources are the posibility to tune the x-rays energy allowing for element selective measurements, or the high focalization of x-ray beam that permits having micrometer focal spot sizes. Furthermore, the energy resolution have been profoundly improved with the use of insertion devices like wigglers and undulators, which also enable to precisely adjust the polarization of x-rays in the soft x-ray regime (photon energies lower than $5keV$), which is the region of interest to study the core to valence band transitions in many common elements, specially in the transition metals.

In this chapter we will review the basics of X-ray absorption related techniques applied to the study of electronic structure of transition metals. For a deeper understanding on the soft X-ray absorption techniques, recommended lectures can be found in refs. [2, 3, 4, 5].

2.1 X-RAY ABSORPTION

Since the first observation of an absorption edge by Maurice de Broglie in 1913 [6], there has been a profound development in the x-ray spectroscopic techniques, which nowadays allow to have an insight into the electronic structure and the local atomic environment of materials.

One of the main spectroscopic techniques is x-ray absorption spectroscopy (XAS), where the absorption coefficient is measured as a function of the energy of the incident photons. This absorption process is produced through the excitation of a core electron to an empty state in the valence shell, followed by a de-excitation process in which photons, Auger and secondary electrons are emitted (see fig.2.1). The absorption is resonant and produces a clear peak in the spectra, at the energy corresponding to the energy difference between excited and core states. In addition, an step jump is observed at the same energy due to core electrons excited into the continuum, producing a non-resonant absorption process, that contributes to the background intensity of the spectra. Thus, the absorption intensity depends on how many available states are for the excited electrons: the larger number of empty final states, the more photons are absorbed.

There are different methods to measure the absorption coefficient. The most direct method is to measure the intensity of the transmitted photons though the sample, however, due to the strong absorption in the soft x-ray regime, this technique is rarely used. Most common are the detection methods based on the measurement of the intensity of emitted photons in the de-excitation process (fluorescence yield mode, FY) or the detection of emitted electrons (total electon yield, TEY). The probability of emission of both photons and electrons is proportional to the absorption probability (excluding phenomena like saturation effects [7]). The main difference between both detection modes is the

characteristic probing depth in each case: while FY mode probing depth is limited by fluorescence photons escape depth, which is in the order of $50 - 100nm$, in TEY mode, where the signal is dominated by the secondary electrons (inelastically scattered electron cascade originating from the primary Auger electrons), the sampling depth is in the order of $2 - 5nm$, thus TEY mode provides a more surface sensitive measurement of the absorption coefficient, while FY signal has larger contribution from the bulk of the sample. FY has the advantage to be aplicable to insulating materials [8], however, in general FY measurements are largely affected by self-absorption effects [**?**].

In this thesis we have mainly used TEY mode for the XAS measurements of our samples, measuring the sample drain current by means of a picoammeter inserted between the surface of the sample and ground. The detected current is a direct measurement of the total emitted electrons by the sample in the absorption process. An alternative mode is the partial electron yield (PEY) in which the emitted electrons are detected by a channeltron electron detector, placed behind a mesh where a variable retarding voltage is applied. In this manner, only the electrons with kinetic energy larger than the retarding voltage are detected [9]. As the electron mean free path depends on their kinetic energy, by varying the retarding voltage, one can modify the probing depth of the detected signal.

The transition probability in the absorption process (which will be proportional to the absorption coefficient) can be described by the Fermi's golden rule,

$$\Gamma_{i\to f} \propto \left| \langle f | \, A_0 \vec{\varepsilon} e^{-i(\vec{k}\vec{r}-\omega t)} \, | i \rangle \right|^2 \rho(E_f) \tag{2.1}$$

where $|i\rangle$ and $|f\rangle$ are the initial and final states, A_0, $\vec{\varepsilon}$, $\vec{k}$ and ω are the wave amplitude, polarization, wave vector and frequency of the incident electromagnetic field, and $\rho(E_f)$ describes the density of the final states.

Large intensities are achieved with dipole allowed transitions. For most of the transition metals, the most suitable dipolar transition available is $2p \to 3d$, that is, an excitation of a $2p$ core electron to a $3d$ available state in the valence shell. The energy necessary to produce this excitation will depend on the element studied (the more protons in the nucleus, the larger binding energy of the core electrons to the ion), so that the absorption edge will appear at different energies depending on the atom explored. The absorption edge due to this $2p \to 3d$ transitions is traditionally known as L edge. In fig.2.2(a) some examples of L edge absorption spectra are shown for different transition metal atoms. It is firstly noticed that two peaks appear in the absorption spectra: the origin of this two edges lies in the spin-orbit coupling of the core $2p$ levels, which are

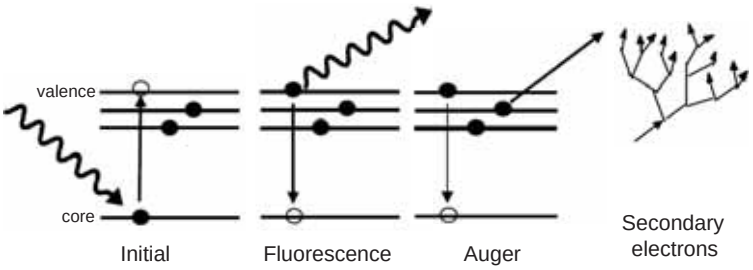

Figure 2.1: X-ray absorption process by core to valence transition, and subsequent decay channels: x-ray fluorescence emission and Auger electron emission. Auger primary electrons originate a cascade of inelastically scattered secondary electrons

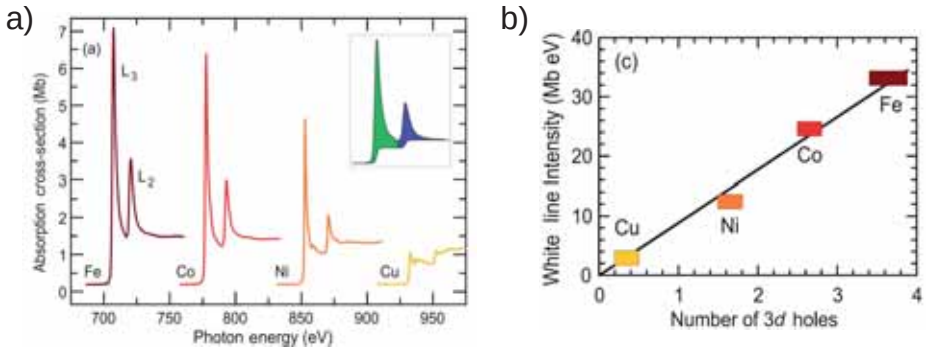

Figure 2.2: a) L-edge x-ray absorption spectra for $3d$ transition metals Fe, Co, Ni and Cu; inset: integrated area under XAS (after proper background substraction); b) Integrated area as a function of calculated number of holes for each transition metal. Figure extracted from[2]

splitted in $2p_j$ ($j = |l+s|, |l-s| = \frac{3}{2}, \frac{1}{2}$) levels, giving rise to the two observed edges, named L_3 (for transitions from $2p_{3/2}$) and L_2(for transitions from $2p_{1/2}$). In transition metals, $2p$ core levels do not overlap between neighbouring atoms and therefore their density of states (DOS) can be treated as a delta function, so that the XAS intensity, which is a convolution of the initial and final states, will reflect only the DOS of the unoccupied valence shell. As there are two times more electrons in the $2p_{3/2}$ level, L_3 edge will have 2 times larger intensity than L_2 edge, but the reflected DOS for both edges will be equivalent.

The second important observation that one can get from the spectra shown in 2.2(a) is that the absorption cross-section (the normalized intensity of the spectra) varies for different elements. This is an evidence of the fact that XAS depends on the DOS of the unoccupied valence states, that is, the XAS resonance intensity is proportional to the total number of available final states. The area under the XAS spectra (after substraction of non-resonant absorption) is directly proportional to the total number of valence holes h in the electronic ground state (fig.2.2(b)):

$$I_{av} = C \cdot h \tag{2.2}$$

where C is a proportionality constant, and the subscript av indicates that the intensity needs to be averaged over all sample directions to account for element symmetry, as will be explained later on.

Although the main characteristics of XAS have been explained under a one-electron scheme, electron correlations should be taken into account to describe the different features in the absorption spectra of transition metals. In TMOs, ligand orbitals are provided by oxygen atoms, whose p orbitals can hybridize with transition metal d orbitals. The hybridization strength, which is parametrized by Δ (the energy necessary for one $O-2p$ electron to jump to the transition metal d shell), depends on the orbitals considered and will be affected by the crystal field or local symmetry of the transition metal. Furthermore, the splitting between the different states within one configuration will depend on the electron-electron repulsion, parametrized by U (Coulomb repulsion energy between electrons in $3d$ shell - U_{dd}, or between $2p$ and $3d$ electrons - U_{pd}). Taking into account these interactions, the possible final $2p^5 3d^{n+1}$ states can split in energy, giving rise to a large number of transitions that produce the so called multiplet structures in

the XAS spectra, providing information on the local electronic structure of the ground states.

2.2 POLARIZATION DEPENDENCE. PROBING ORBITAL AND MAGNETIC ORDERS

For dipoled allowed transitions, the intensity for the final state depends on the symmetry of the inital ground state. This symmetry can be explored with the absorption dependence on the incident light polarization, which will interact with either the spin configuration (case of circularly polarized light) or with the charge distribution (case of linearly polarized light) of the core and valence shells.

X-ray circular dichroism

By using photons with a defined helicity, the absorption process can be made spin-dependent. If the incident x-rays are circularly polarized, and the valence states exhibit a Stoner splitting, the measured absorption signal is shown to be dependent on the relative orientation of the photon angular momentum and the sample magnetization. The difference absorption between parallel and antiparallel orientations of the sample magnetization and the incident photon momentum -that gives the x-ray circular dichroism (XMCD) signal- is shown to be proportional to the magnetic moment $\vec{m}$ of the sample.

The atomic process giving rise to the XMCD signal can be divided into two steps: first, the circularly polarized incident photon transfers its angular momentum $\vec{L}_{ph}$ to the excited photoelectron through spin-orbit coupling. In the most typical case of an L edge, the p core electrons are spin-orbit splitted into $l+s$ and $l-s$ levels. Therefore, the spin polarization will be opposite at the two edges and more spin down (spin up) electrons will be excited with positive (negative) helicity x-rays. In the second step, the exchange split valence band acts as a detector for the spin of the excited photoelectrons. For the case presented in fig.2.3(a) , the positive (negative) helicity x-rays mainly cause the absorption to the states in the minority (majority) band. Due to the opposite polarization of L_3 and L_2 edges, the XMCD signal will have opposite sign at each edge, but same magnitude, proportional to the imbalance of the majority and minority bands. However, apart from an spin imbalance in the valence band, it can also occur that the valence band posseses an orbital magnetic moment. In that case, there exists an imbalance in the states with quantum numbers $+m_l$ and $-m_l$ and this will cause that the XMCD signal at the L_3 and L_2 edges will not be identical.

As a consequence, the spin and orbital magnetic moments (m_s and m_o) can be determined from the analysis of the XMCD spectra. The sum rules derived for the $L_{3,2}$ edges [10, 11] link the dichroism integrated intensities to the atomic values of m_s and m_o:

$$m_s = \mu_B(2\Delta L_2 - \Delta L_3)/C \tag{2.3}$$

$$m_o = -2\mu_B(\Delta L_3 + \Delta L_2)/3C \tag{2.4}$$

where C is the proportionality constant defined in eq.2.2. Thus, knowing the number of holes h and the averaged XAS intensity I_{av}, XMCD signal provides the spin and orbital magnetic moments per atom, by integrating over the L_2 (ΔL_2) and L_3 (ΔL_3) edges in the XMCD signal. These sum rules have to be applied with caution, as in some cases, the overlapping between L_3 and L_2 edges can cause an important error in the determination of m_s [12]. Also, an additional term in eq.2.3 may be considered,

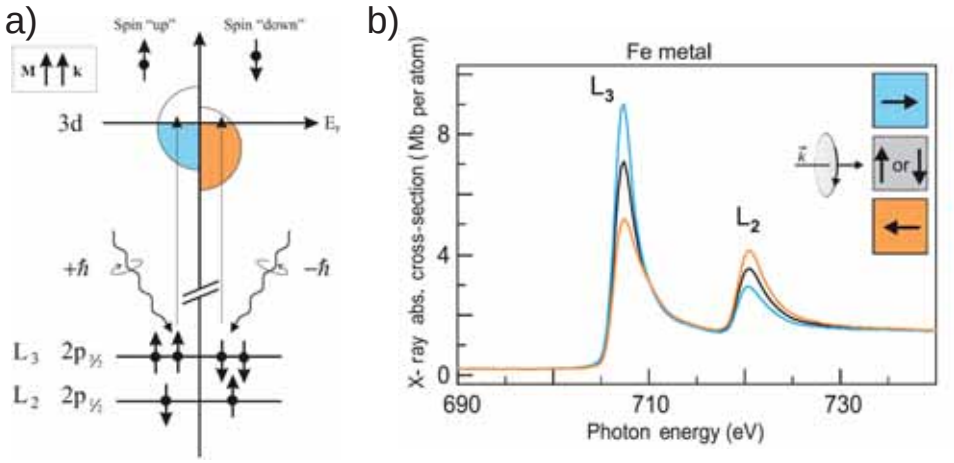

Figure 2.3: a)Scheme for helicity dependent transitions at the $L_{3,2}$ edges of a $3d$ transition metal with spin polarization in the valence band. b) Resulting XAS spectra for circularly polarized x-rays with angular momentum parallel (blue), antiparallel (orange) and perpendicular (black) to sample magnetization. Figures adapted from [3, 2]

accounting for the asphericity of the spin magnetization [13], and saturation effects can drive for a wrong determination of magnetic moments [7].

The XMCD signal will be optimal for the case of photon angular momentum parallel to magnetic moment, and scales as $\cos\theta$ (θ being the angle between $\vec{L}_{ph}$ and $\vec{m}$). Being odd in the magnetization, XMCD is therefore not sensitive to antiferromagnetic order, which in turn will be sensed by linear dichroism measurements, as shown below.

X-ray linear dichroism

X-ray absorption with linearly polarized light is sensitive to the charge distribution around the atoms causing the absorption. In the case of a non-spherical charge distribution, atoms can produce a different absorption for different orientations of the linear polarization respect to the sample. The resulting linear dichroism can be originated by anisotropic charge distribution due to anisotropic atomic bondings, leading to a "natural" linear dichroism (XNLD), or due to a magnetically induced deformation of the charge distribution, leading to a "magnetic" linear dichroism (XMLD).

The XNLD can be explained by the "search light effect" of the linearly polarized light: the transition intensity is proportional to the projection of the number of holes in the direction of the electric field vector $\vec{E}$. By measuring along three orthogonal directions, one can get the averaged number of holes in the final state, as it was stated in eq.2.2.

XNLD in transtition metals is usually originated due to a difference in orbital occupation at the d levels. By measuring the difference in the XAS at L-edge transitions ($2p \rightarrow 3d$) with linearly polarized light parallel to the different orientations of the d orbitals, we can access to the preferred d orbitals occupancy. A clear example is shown in fig.2.4, where the $Cu - L_{3,2}$ XAS edges have been measured in a cuprate system with Cu:$3d^9$ configuration, for two orthogonal orientations of the electric vector of the incident x-rays. The crystal field in the system lifts the degenerancy of the $3d$ levels, localizing the only hole in the $3d(x^2 - y^2)$ orbitals. Therefore, when the incident light is polarized in the z direction (perpendicular to the $(x^2 - y^2)$ orbitals orientation), no reso-

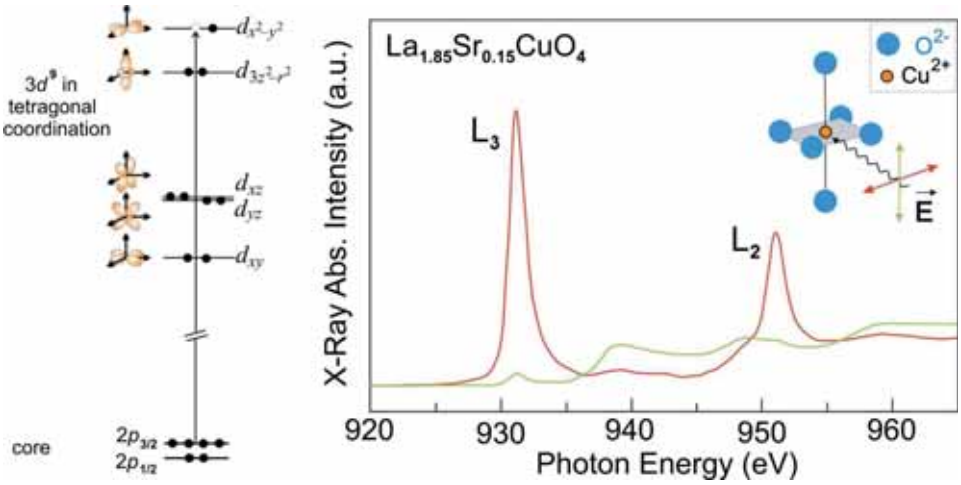

Figure 2.4: X-ray $L_{3,2}$ edge absorption spectra for $3d^9$ Cu in $La_{1.85}Sr_{0.15}CuO_4$ perovskite, taken with linear polarization parallel to ab plane (red) and parallel to c axis (green) as drawn in the inset of right figure. Left scheme shows the $2p \rightarrow 3d$ transitions, considering single hole in $e_g(x^2 - y^2)$ states. Figure adapted from [14]

nant absorption is observed, while a large absorption occurs when the light is polarized in the x direction (parallel to the orientation of $(x^2 - y^2)$).

The transition probability is governed by the integrals $\langle p_i \, |q| \, d_i \rangle$, where the subscript i denotes the different orbitals and q is the wave vector with linear polarization (x, y or z). In a $2p \rightarrow 3d$ transition, the only integrals related to e_g states which are non-zero are $\langle p_x \, |x| \, d_{x^2} \rangle$, $\left\langle p_y \, |y| \, d_{y^2} \right\rangle$ and $\langle p_z \, |z| \, d_{3z^2-r^2} \rangle$, for the three polarization directions. Here $d_{x^2} = -\sqrt{\frac{1}{4}} d_{3z^2-r^2} + \sqrt{\frac{3}{4}} d_{x^2-y^2}$, and thus with x polarized light both $3z^2 - r^2$ and $x^2 - y^2$ orbitals are excited, in a proportion 1 to 3.

From the evaluation of the transition integrals for all possible transitions and light polarizations, sum-rules for $2p \rightarrow 3d$ transitions relating the integral intensity of XAS measured with polarization i (I_i) with the number of holes h in the d-orbitals can be derived [5]. For a system with tetragonal symmetry O_h:

$$\begin{aligned} I_x = I_y &= \tfrac{1}{h}(\tfrac{1}{2}h_{xy} + \tfrac{1}{2}h_{xz} + \tfrac{1}{6}h_{z^2} + \tfrac{1}{2}h_{x^2-y^2}) \\ I_z &= \tfrac{1}{h}(\tfrac{1}{2}h_{xz} + \tfrac{1}{2}h_{yz} + \tfrac{2}{3}h_{z^2}) \end{aligned} \tag{2.5}$$

, and in the case of filled t_{2g} band, we can write $h_{xy} = h_{xz} = h_{yz} = 0$, thus obtaining:

$$\begin{aligned} 2I_x &= \tfrac{1}{h}(\tfrac{1}{3}h_{z^2} + h_{x^2-y^2}) \\ I_z &= \tfrac{1}{h}(\tfrac{2}{3}h_{z^2}) \end{aligned} \tag{2.6}$$

, reflecting the mixed contribution of $x^2 - y^2$ and $3z^2 - r^2$ orbitals to the XAS measured with in-plane polarization. After some calculation, we can obtain the expression for the holes ratio in the e_g orbitals:

$$X = \frac{h_{3z^2-r^2}}{h_{x^2-y^2}} = \frac{3I_z}{4I_x - I_z} \tag{2.7}$$

, which is applicable for systems with a single hole in the $3d - e_g$ orbitals, allowing for a quantitative analysis of the XNLD spectra from the XAS integrated intensities for linear polarization parallel to $(x^2 - y^2)$ (I_x) and parallel to $(3z^2 - r^2)$ (I_z)[15, 16].

So far, we have seen how a linear dichroism is originated by the difference in the population of d levels. However, in the case of completely empty d orbitals, a XLD signal can also be detected if a energy splitting exists in the d states. For e_g states, an energy splitting between $(x^2 - y^2)$ and $(3z^2 - r^2)$ levels will be manifested by a shift in the energy position of the L_3 and L_2 absorption edges explored with the different x-ray polarizations, resulting in a XLD signal with derivative-like shape, as it is the case for Ti^{4+}, explored in chapter 8.

Experimentally it is rather difficult to achieve a measurement geometry such that $\vec{E}$ is parallel to c-axis ($\vec{E} \parallel (3z^2 - r^2)$ in a system like in fig.2.4). Usually, a grazing incidence geometry allows to have a large projection of $\vec{E}$ parallel to the c-axis. In that case, a geometric correction to the XAS is applied, accounting for the light incidence angle θ (angle between surface sample and incidence light vector):

$$I_{\parallel}^{corr} = (1/\cos^2(\theta))(I_{\parallel} - I_{\perp}\sin^2(\theta)) \tag{2.8}$$

where $I_{\parallel}^{corr}$ is the corrected intensity for the XAS obtained with $\vec{E}$ closely parallel to the c-axis. For the typical case of $\theta = 30$ deg, eq. 2.8 yields [17]:

$$I_{\parallel}^{corr} = \frac{4}{3}(I_{\parallel} - \frac{1}{4}I_{\perp}) \tag{2.9}$$

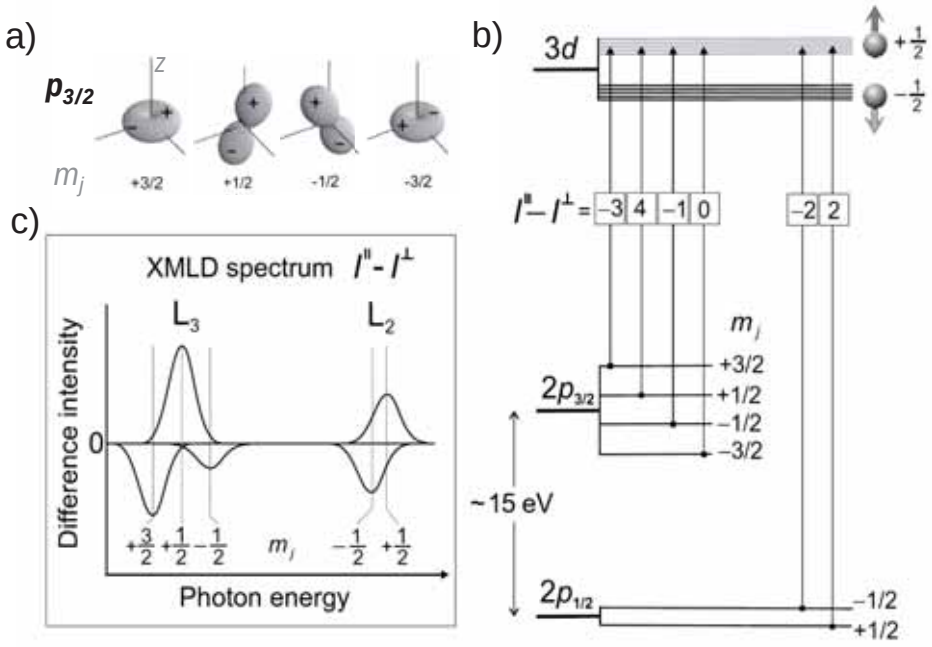

Figure 2.5: a) Charge distributions of $p_{3/2}$ substates considering spin quantization direction in the z axis; b) Possible $2p \rightarrow 3d$ transitions considering a single hole in the spin-up band. XMLD intensity is calculated as the difference in absorption for $\vec{E}$ vector parallel ($I_{\parallel}$) and perpendicular ($I_{\perp}$) to sample magnetization; c) Schematic representation of individual XMLD signals for the individual transitions from $2p$ sub-states. Figure adapted from [2]

We turn now to the magnetic effects on the linear dichroism. When a sample gets magnetically ordered, the spin-orbit coupling can lead to a deformation of the charge. This distortion is aligned with the atomic spins directions and therefore, XMLD is sensitive to ferromagnetic and antiferromagnetic orders.

The anisotropy of the charge density relative to the spin axis is shown in fig.2.5(a) for each of the $p_{3/2}$ substates. The sum of all substates leads to a spherical symmetry, thus, only if there is a splitting between m_j substates, a linear dichroism will appear. In the presence of exchange interaction a splitting between m_j states arises both in the valence and core shells. In fig.2.5(b), the transition probabilites for each of the p substates in the $p \rightarrow d$ transition are plotted. Here a single $spin - up$ hole is considered in a spherically symmetric d band (equal weight for all d_i substates) and x-rays incide with $\vec{E}$ vector parallel and perpendicular to the sample magnetization direction. The XMLD is then plotted as $XMLD = I_{\parallel} - I_{\perp}$ and will have independent contributions from all the anisotropic $2p$ substates, as depicted in 2.5(c).

While XMCD is odd in the magnetization (XMCD $\propto \langle M \rangle$), XMLD does not distinguish between antiparallel orientations of $\vec{m}$ (XMLD $\propto \langle M^2 \rangle$). Thus, XMLD can be applied to examine local magnetism of ferromagnetic as well as antiferromagnetic materials. XMLD can be applied to study the relative orientation of ferromagnetic and antiferromagnetic orders at interfaces [18], to explore element magnetic anisotropies [19] or extract local magnetocrystalline energies [20] in a wide range of magnetic materials.

The x-ray absorption experiments shown in this thesis have been performed in two beamlines: BACH beamline at Elettra synchrotron radiation source (Trieste, Italy), and BOREAS beamline at ALBA-CELLS synchrotron radiation source (Barcelona, Spain).

Part II

RESULTS

3

STRAIN AND INTERFACE INDUCED PHASE SEPARATION IN MANGANITE THIN FILMS

Charge localization promoted in manganite thin films by strain and interface related effects profoundly affect their magnetotransport properties, diminishing the performance of these materials in tunnel devices. In addition, structural distortions imposed by single crystal substrates and propagated through relevant distances in the films can also be determinant for the observed magnetic response. In this chapter we will study the origins of these phenomena and their relevance for the performance of manganite thin films as magnetic electrodes.

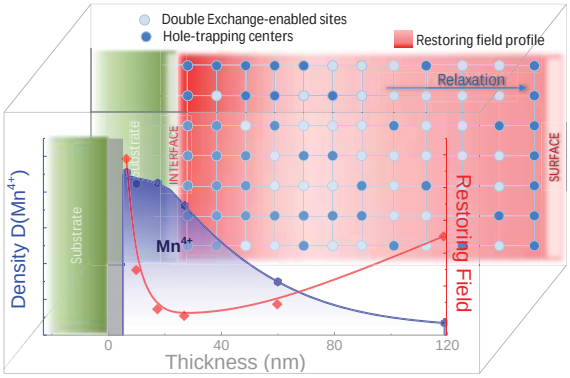

3.1 INTRODUCTION

Mixed valence manganese oxides with the formula $(R_{1-x}A_x)MnO_3$, where R= rare-earth cation ($La^{3+}, Nd^{3+}, ...$) and A=divalent alkali cation ($Sr^{2+}, Ca^{2+}, ...$) show a complex phase diagram in which the magnetic and transport behaviour finely depends on the doping of divalent cations (x). This doping modulates the number of holes that can move in the e_g orbital bands of the Mn ions. The electron transfer between Mn ions -which is mediated via oxygen ions- is spin and charge dependent: in order to have an effective transfer, a simultaneous jump of an electron from a Mn^{3+} ion to an adjacent oxygen and from the oxygen to the neighbouring Mn^{4+} ion occurs. The probability to have this electron jump is dependent on the spin state of the neighbouring Mn ions: if the spins of the two d shells are parallel, the transfer probability is the highest. This mechanism is known as double-exchange and was first proposed by Zener[21]. In this model, a degenerancy of the $Mn^{3+} - O - Mn^{4+}$ and $Mn^{4+} - O - Mn^{3+}$ states is considered; however, in an ordered lattice, this degenerancy can be lost, inhibiting the double-exchange mechanism [22]. It can be demonstrated that the doping for which the double-exchange interaction is optimized, leading to the highest Curie temperature and minimum electrical resistivity, occurs for $x \approx 1/3$ [23].

For this optimal composition, $La_{2/3}A_{1/3}MnO_3$ manganites are half-metallic ferromagnets displaying a full spin polarization, making them excellent candidates for electrodes in magnetic tunnel devices. However, despite of the high Curie temperature of these materials ($\approx 370K$), it is always observed that the tunnel magnetorresistance (TMR) in these devices decays rapidly and nearly vanishes at room temperature[24]. This unex-

pected large decay has been related to a different magnetism at the surface boundary of the films [25], resulting in a non-ferromagnetic and insulating "dead layer". Electronic phase separation (PS) -localization of regions with higher/lower carrier density- has been proposed as the origin of the detrimental magnetotransport properties. This PS can be promoted by orbital reconstructions associated to symmetry breaking at surfaces and interfaces[26, 27] (that will be discussed later in this thesis) as well as by spurious chemical gradients in the films [28].

In this chapter we will make use of $La_{2/3}Sr_{1/3}MnO_3$ (LSMO) films epitaxially grown on $SrTiO_3$ (STO) single crystal substrates as a prototypical system to explore the influence of structural distortions -either promoted by the substrate or by unavoidable structural relaxation- and the presence of interfaces strongly breaking the symmetry (either with the substrate or at the bare surfaces) in the magnetic properties of the films (magnetization, transition temperature, magnetic anisotropy and magnetic domain configuration) and we will study in detail the phase separation phenomena by means of nuclear magnetic resonance (NMR) technique, providing a new insight into the extension and origin of the magnetically depleted region, as well as on the thickness dependent magnetic anisotropy in the films, which are factors strongly degrading the magnetic and electronic homogeneity in the films.

3.2 STRUCTURAL AND MAGNETIC PROPERTIES OF $La_{2/3}Sr_{1/3}MnO_3$ FILMS

To study the thickness dependence of structural and magnetic properties, LSMO films were grown by pulsed laser deposition (PLD) on cubic STO single crystal substrates with (001) orientation, using the optimal conditions ($P = 0.2mbar$, $T = 725^oC$), that were obtained after proper optimization of the growing parameters (see appendix B), in order to achieve epitaxial films with flat surface and magnetic properties close to the bulk LSMO (saturation magnetization $M_S \approx 590emu/cm^3$, Curie temperature $T_C \approx 370K$). Substrates were thermally treated (1000^oC, $2h$ in air) previous to deposition, in order to get an atomically flat and single terminated surface. The number of pulses during deposition was varied in order to get thicknesses in the range between 3 and $370nm$. While for an intermediate range of $10 - 60nm$, x-ray reflectometry (XRR) was used to determine the thickness of the films, for lower and higher ranges, the value was estimated by proper calibration of the growth rate.

3.2.1 *Structure of LSMO thin films. Determination of pseudo-cubic lattice parameters*

The surface topography of the films was probed by atomic force microscopy (AFM). As shown in 3.1(a), LSMO films presents a flat surface with steps and terraces morphology, with ≈ 1 unit cell (uc) height. This kind of surface morphology was achieved for films with thicknesses lower than $30nm$, while for larger thicknesses, films develope into a more 3-dimensional growth.

The larger lattice parameter of STO (3.905Å) as compared to the LSMO pseudocubic lattice parameter in the bulk structure (3.873Å) [29] imposes a tensile strain in the film lattice, that causes a tetragonal distortion: the in-plane lattice distances (in the crystallographic $[100]$, $[010]$ directions) adapt to the STO planar distances and the out-of-plane parameter (in the direction $[001]$) gets reduced accordingly. Out-of-plane lattice parameters were measured by means of x-ray diffraction (XRD) $\vartheta - 2\vartheta$ scans for samples with thicknesses between 10 and $370nm$. In fig. 3.1(b) the film reflection appears at higher angles than STO substrate reflection and also higher than the reflec-

tion angle corresponding to bulk LSMO, indicating the contraction of the out-of-plane parameter as expected from the tensile strained tetragonal distortion of the cubic lattice. It can be observed how, for films with a thickness above $60nm$, the film reflection gradually moves towards the bulk LSMO value, indicating a progressive increase of the out-of-plane lattice parameter, signaling a structural relaxation in the LSMO structure, as discussed below. The film with $10nm$ thickness also shows a shift to lower angles, suggesting that for the films with reduced thickness, a gradual expansion of the unit cell occurs, which is at odds with the expected elastic deformation of the unit cell under tensile strain. This observation is in agreement with earlier results in LSMO [30] and $La_{2/3}Ca_{1/3}MnO_3$ (LCMO) [31], however, as shown in appendix C, this shift is attributed to an artifact of the measurement due to interference of diffracted waves from substrate and lattice, largely affecting the diffracion patterns in ultrathin films, and the correct lattice parameter cannot be calculated from the observed position of the diffraction pattern, but from simulation of the diffraction pattern considering the phase of the diffracted waves. Thus, for thicknesses above $27nm$, lattice parameters were obtained by fitting of LSMO diffraction peaks observed in fig. 3.1(b) [1] and, for films with thickness of $27nm$ and below, high-resolution diffraction experiments were made for more proper fittings to diffracted patterns (see appendix C). The resulting out-of-plane lattice parameters are represented in fig. 3.1(e) (solid squares), as a function of LSMO thickness.

The epitaxial relationship between substrate and film was furtherly checked by pole figure measurements, as shown in fig.3.1(c) for $27nm$ film. The (220) reflections of both substrate and film are observed for $2\theta \approx 68^\circ$ and $\chi \approx 45^\circ$. Exploring the full φ range, we find (202), (022), (-202) and $(0-22)$ poles of the LSMO film and of the STO substrate (bottom part of fig.3.1(c)), separated by $\Delta\varphi = 90deg$. These scans indicate single crystal in-plane orientation with $LSMO(001)[100]//STO(001)[100]$ epitaxial relationships.

For investigation of the lattice relaxation in LSMO films, we performed reciprocal space maps measurements around asymmetrical reflections for films between 27 and $370nm$, in order to get information on the in-plane lattice parameters. From the examination of the (103) reflection in (001)-oriented films (fig. 3.1(d)), coinciding in-plane reciprocal coordinates (q_x) -within the diffractometer resolution- for substrate and film demonstrates the fully strained state of the films until $370nm$. The calculated in-plane parameters for all measured films are plotted in fig. 3.1(e). From the plot, it is noticed that the structural relaxation in (001)LSMO films occurs via expansion of the out-of-plane parameter (keeping in-plane parameters unaltered due to clamping to the substrate), and consequent increase of unit cell volume, for films with thicknesses larger than $30nm$. This indicates that, in order to accommodate the epitaxial strain, the unit cell expands in volume either by elastic deformation of the lattice or by creation of extended or point defects. Indeed, the formation of twin domain arrays in LSMO films has been identified by means of high-resolution XRD measurements, pointing to a relaxation mechanism by tilts of the octahedral coordination polyhedra [32, 33] and nonhomogeneous cationic distributions have been observed by Electron Energy Loss Spectroscopy in strained films of LCMO and related compounds[34, 35, 36, 37].

1 To fit the diffraction peaks from LSMO layers, pseudo-voigt functions were used, considering the diffractions due to $k_{\alpha 1}$ and $k_{\alpha 2}$ lines, with the intensity of the later being half of the intensity of the former.

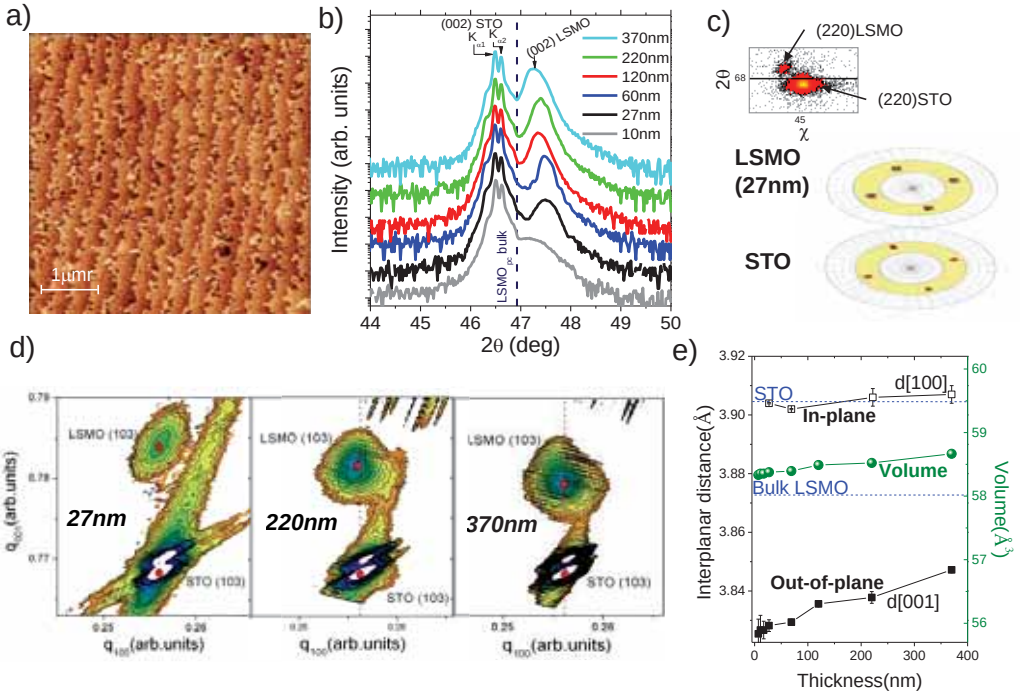

Figure 3.1: a) AFM image of $10nm$ thick LSMO film grown on STO. b)$\vartheta - 2\vartheta$ scans, showing the (002) symmetrical reflections STO substrate and LSMO films with different thicknesses, as indicated; dashed line indicates the expected reflection angle for bulk LSMO. c) Top: example of (220) reflections in $2\theta - \chi$ area scan; Bottom: pole figures showing the four equivalent (220) reflections corresponding to LSMO film ($27nm$) and STO substrate. d) Reciprocal space maps around the (103) reflection for 27, 220 and $370nm$ LSMO films deposited on STO substrates. e) Left: calculated interplanar in-plane (empty squares) and out-of-plane (full squares) distances as a function of films thickness; Right: Unit cell volume as a function of film thickness; Dashed line indicates the interplanar distance and unit cell volume in the (pseudo)cubic bulk structure of LSMO and STO.

3.2.2 *Magnetic properties. Determination of magnetization and Curie temperature*

LSMO films were measured by using a SQUID magnetometer. Sample magnetization was obtained by measuring hysteresis loops at low temperatures ($10K$) and Curie temperature was determined from the observed transition of field cooled curves taken at a field of $1kOe$, which was large enough to get a magnetic saturated state in all the samples. In fig.3.2(a,b), some examples of M(H) and M(T) curves - normalized by the LSMO film volume- are presented. It is evident from these curves that samples with lower thickness suffer a loss of magnetization and get magnetically ordered at lower temperatures than the thicker films,which is a common observation for manganite thin films [31, 38, 39]. In fig.3.2(c)(main panel), M_s and T_c calculated values are shown for all measured samples in the range of thicknesses $3 - 370nm$.

From the hysteresis loops, LSMO films can be considered as magnetically soft (saturation fields lower than $500Oe$ at low temperature). However, a thickness dependence is noticed from the magnetic loops, as shown in the inset of fig.3.2(a), which is a zoom from the main panel: while an initial drop of the coercive field H_c is observed for increasing thickness between 3 and $17nm$, an increase of H_c is observed for the $120nm$ film. The thickness tendency is more clearly presented in the inset of fig.3.2(c), where

the values obtained for all the measured films is plotted. From the dependence of $H_c(t)$, three contributions to the magnetic anisotropy of the films can be assumed: an intrinsic soft magnetocrystalline anisotropy, inherent to the structure of the films, a surface magnetic anisotropy, which contributes relevantly for the thinnest films, strongly enhancing their anisotropy, and a defect induced magnetic anisotropy, which also contribute to magnetically harden the films due to pinning effects at punctual or extended defects present in the films upon structural relaxation and thus contributes in films with larger thicknesses.

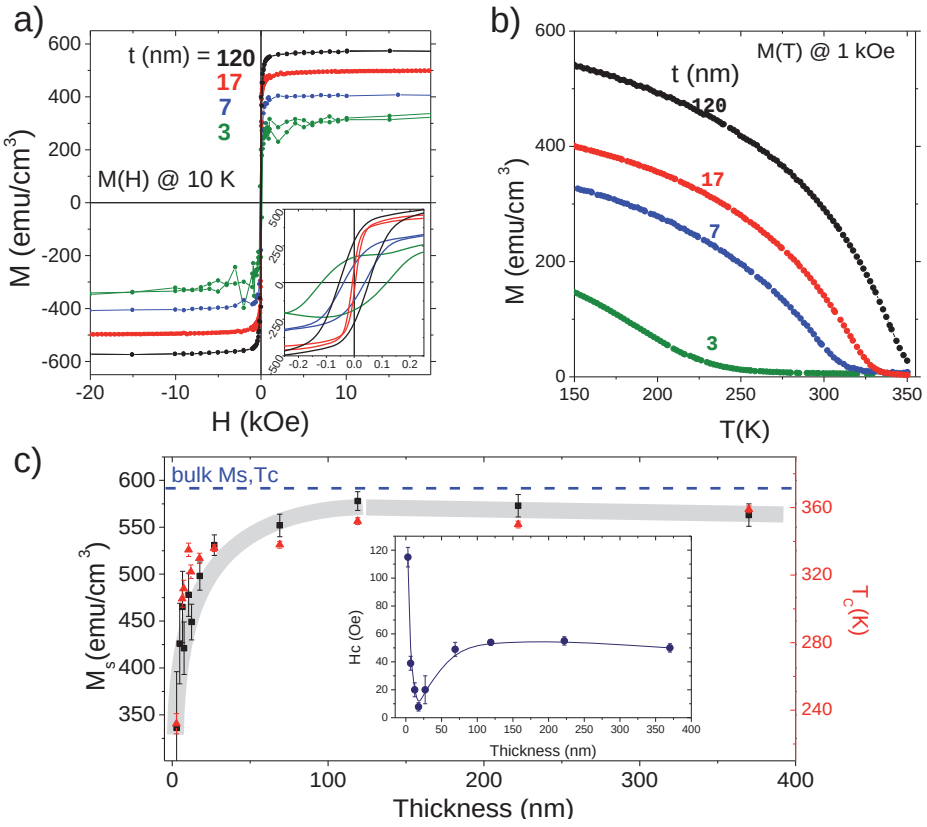

Figure 3.2: a) Magnetization versus magnetic field (applied in the plane of the samples) measured at $10K$, for LSMO samples with different thicknesses; inset: zoom in the low fields region of the magnetic loops. b) Magnetization versus temperature measured with an applied field of $1kOe$, for LSMO samples with different thicknesses. c) calculated saturation magnetization (left axis) and Curie temperature (right axis) as a function of LSMO thickness; inset: Coercive field as a function of sample thickness

3.2.3 *Magnetoelastic coupling between $La_{2/3}Sr_{1/3}MnO_3$ films and $SrTiO_3$ substrates*

The extreme sensitivity of manganites to structural modifications, that can alter the $Mn-O-Mn$ bond angles and distances -affecting the DE mechanism- can be effectively probed by means of the strong link between substrate and films structures demonstrated above. STO substrate, in this respect, provides an optimal system to test the influence of structural modifications in manganite thin films, due to the phase transition occurring at low temperatures affecting its crystal structure. More specifically: STO is a cubic perovskite at room temperature, however, at $105K$ it undergoes a tetragonal distortion induced by the rotation of TiO_6 octahedra, that displaces the oxygens

leading to an elongation of *c*-axis and contraction of *a*-axis [40]. This cubic to tetragonal transition produces the formation of domains with different orientations of the elongated *c*-axis, giving rise to a complex pattern of twins (changes of orientation of *a* and *c* axis) and antiphase (adjacent regions of opposite rotation patterns) structural domains. In addition, upon the occurrence of structural transition, soft phonon modes generate in the STO lattice, propagating the structural deformation with low energy cost. This transition involves small changes of lattice parameters, as oxygen displacements are less than $0.03\mathring{A}$.

In order to probe the magnetic response of LSMO films to the structural transition of STO substrate, we performed AC magnetic susceptibility measurements on some of the LSMO films characterized in the previous section, applying a small AC-magnetic field ($h_{ac} = 1Oe$) along different crystallographic directions, and measuring the components of the magnetic susceptibility response of the films (see appendix A for brief description of the technique).

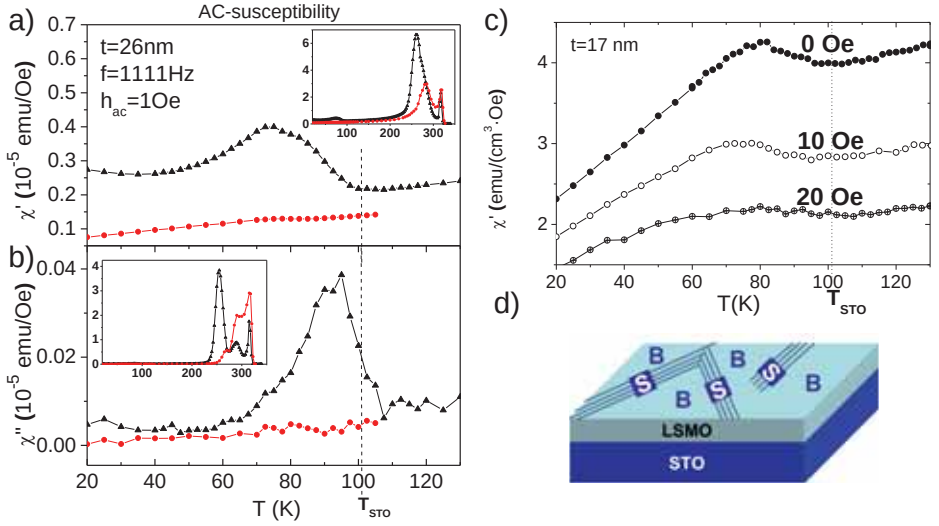

Figure 3.3: Temperature dependence of (a) the real and (b) imaginary components of ac susceptibility, measured at $1111Hz$, for the $26nm$ LSMO film. Black circles correspond to $h_{ac} \parallel [100]$, red triangles correspond to $h_{ac} \parallel [110]$. In the insets, the full temperature range for the measurements is shown.; c) Real component of ac susceptibility, χ', along [100] direction for $17nm$ LSMO film under superimposed dc-field in the same direction as the ac-field; d) Sketch illustrating the S and B magnetic domain patterns as described in text.

The temperature dependence of the in-phase (χ') and out-of-phase (χ'') components of the low-field AC-susceptibility for a $26nm$ film is shown in fig.3.3(a,b) (insets) for $h_{ac} \parallel [100]$ and $h_{ac} \parallel [110]$. The film orders magnetically below $320K$, as evidenced by appearance of non-zero χ'' below this temperature and a rapid increase of χ', which forms a peak just below the transition. At lower temperatures another peak develops in both components, reflecting the evolution of spontaneous magnetization and anisotropy; the enhanced susceptibility (χ') and losses (χ'') indicate the formation and freezing of the magnetic domain structure at a temperature slightly below the Curie temperature. It can be noticed that the susceptibility measured along [110] is substantially smaller than along [100] in agreement with the biaxial anisotropy of the LSMO film with $\langle 100 \rangle$ easy axes[41].

In the vicinity of the STO structural transition we observe that, while for $h_{ac} \parallel [110]$ the susceptibility changes smoothly on crossing the STO structural transition, there is a clear rise of both components on decreasing the temperature just below about $105K$ when $h_{ac} \parallel [100]$ and they go through a maximum at lower temperatures (fig.3.3(a,b)). The observation of χ' (T) and χ'' (T) susceptibility peaks developing close to T_{STO} strongly suggests signatures of changes in the magnetic structure related to the substrate structural changes. The fact that these peaks are only observed in the [100] main crystallographic directions suggests that this magnetic reconstruction takes place mainly along that directions. This anomaly in the ac-susceptibility was observed for several measured films (with thicknesses between 10 and $26nm$). As shown in fig. 3.3(c) the ac-susceptibility χ' (T) anomaly below T_{STO} is greatly suppressed upon superimposing a rather small dc-field ($\approx 20Oe$) parallel to $h_{ac} \parallel [100]$.

Twins and antiphase boundaries created in the STO substrate at T_{STO} can promote the occurrence of stripe regions (S) in the film, displaying a stripe pattern of magnetic domains with a small out-of-plane component of the magnetization alternatively pointing up or down, which in turn, form new magnetic domain boundaries [42, 43]. These S-regions are formed within the pre-existing large regions (B) with in-plane magnetization. Below T_{STO}, B-regions coexist and are bounded by magnetic stripes of S-regions (see sketch in fig.3.3(d)), as observed by magnetooptical microscopy [42, 43]. The particular magnetic domain pattern in these regions should not be identical to that existing above T_{STO}, since domain reconstruction must occur after changes in the domain boundary conditions and the magnetostatic energy triggered by S-regions.

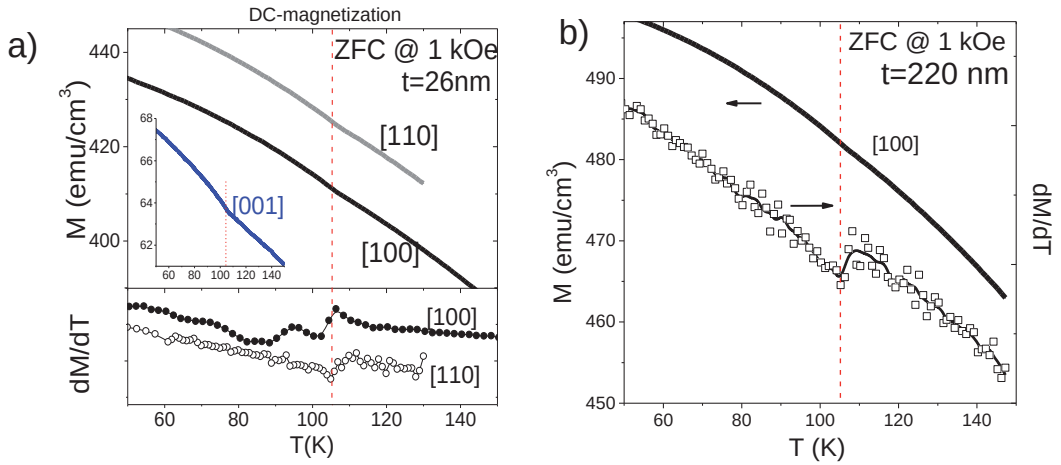

Figure 3.4: a) Top: Temperature dependence of magnetization for $26nm$ LSMO film with a $1kOe$ magnetic field, applied along [110], [100] and [001] (inset) directions; Bottom: Derivatives of the curves from top panel b) Temperature dependence of magnetization for $220nm$ film (left axis) and corresponding derivative dM/dT (right axis) under an applied field of $1kOe$ along [100] direction. Dashed line in all panels marks the STO structural transition temperature.

We turn now to the examine more carefully the DC-magnetization. Although the temperature dependence of the magnetization $M(T)$ appears to be smooth and featureless at all temperatures, a close inspection reveals a dip at $T \approx T_{STO}$ (fig. 3.4(a-top)). This feature in the magnetization is visible for different magnetic fields and for different orientations ([100], [110] and [001]) and is better appreciated in the derivatives dM/dT, shown in fig. 3.4(a-bottom). It is important to notice that the magnetization dip

($\sim 100K$) is still well visible even at $H = 1kOe$. and in films with the largest thickness ($220nm$, fig. 3.4(b)), signaling that the effect of strain propagates deep in the film.

The origin of this DC-magnetization dip, although also appearing at $\sim T_{STO}$, should be different to the domain reconstruction phenomena originating the peaks in the susceptibility. It can be argued that, across the closure domains formed at the new domain boundaries strongly antiferromagnetically coupled regions of antiparallel domains could appear. Such rigid non-collinear magnetic moment alignment would cause the reduction in magnetization at fields even higher than the technical saturation field.

Two limiting different scenarios have been proposed as responsibles for the magnetoelastic coupling in $La_{1-x}A_xMnO_3(A = Sr, Ca)$ thin films grown on STO: a dynamic one, in which the softening of the STO lattice couples to spin excitations of the manganite film [44], and a static response linked either to polyhedra deformation or rotation and twining [42, 43, 45, 46, 47]. Whereas the former points to a phenomenon limited to the immediate vicinity of the manganite/STO interface, the latter may, in principle, propagate much deeper in the films, which is in better accordance with our results.

3.3 INTERFACE AND BULK CHARGE LOCALIZATION IN MANGANITE THIN FILMS

3.3.1 *Nuclear magnetic resonance applied to the study of phase separation in manganites*

It has been shown that ^{55}Mn Nuclear Magnetic Resonance (NMR) is a powerful tool to disentangle phenomena contributing to the existence of magnetic and insulating dead-layers in manganite thin films [31, 38, 48, 49, 50]. Indeed, ^{55}Mn NMR spectra of ferromagnetic-double exchange interaction (DE) in manganites is dominated by a strong resonance line associated with $Mn^{3+/4+}$ ions participating in DE coupling and occurring at a frequency that, depending on the hole concentration, lies within the range $f_0 \approx 370 - 400MHz$ [31, 38, 48, 49, 50, 51, 52, 53]. It turned out that when recording NMR spectra of LSMO (and also of LCMO) as a function of film thickness (t), the intensity of this f_0 line was found to decrease linearly to zero at a finite thickness t_0 thus suggesting the presence of a non-ferromagnetic dead-layer in thin films[38]. Experiments conducted on granular LSMO and LCMO of different grain size led to similar conclusions[54, 55]. Of relevance here is that the thickness of the dead-layer (t_0) was found to be of about $2 - 5nm$. An interfacial dead-layer is also commonly invoked to explain the observed reduction of magnetization and conductance in thin films when reducing thickness[56]. Interestingly a similar thickness t_0 was found to separate the ferromagnetic/metallic and non-ferromagnetic/insulating regimes of thin films, somehow depending on the used substrates[57]. On the other hand, the suppression of the DE ferromagnetic contribution in the ^{55}Mn NMR spectra of LSMO and LCMO is accompanied by the gradually increasing importance of an additional resonant line occurring at lower frequency ($310 - 330MHz$). This line is attributed to localized ferromagnetic Mn^{4+} states [31, 38, 48, 49, 50, 51, 52, 53], which contribute to the total magnetization of the films but not to the conduction mechanism through electron hopping. Its presence is a fingerprint of the existence of PS in the material. To preserve charge neutrality, a third line corresponding to Mn^{3+} should be present at frequencies above $400MHz$, however, the strong anisotropy of Mn^{3+} hyperfine field causes a wide broadening of this line, preventing its observation [50]. We note that the relative intensity of the Mn^{4+} line is found to increase when reducing film thickness and accordingly, it is taken as a signature of charge localization associated to interface phenomena [31, 38, 48, 49, 50] which thus weakens the double-exchange coupling. However, detailed inspection of

reported data (References [38, 48, 50]), reveals intriguing features that cast some important questions on this interpretation. Indeed, in the reported data on LCMO films it can be observed [38, 48] that the intensity of the Mn^{4+} line keeps increasing well above the dead-layer thickness and only saturates for $t > 20 - 30nm$; in contrast, Sidorenko et al. [50] reported that in LSMO films the intensity of the Mn^{4+} line is independent on film thickness. These observations suggest that charge trapping is not restricted to interfaces, probably indicating a multiple origin for the charge trapping phenomena.

In order to shed a new light on this problem and to disentangle the distinct mechanisms of charge trapping and subsequent PS, we performed ^{55}Mn NMR measurements on our LSMO epitaxial thin films grown on STO substrates, previously characterized in section 3.2. It will be shown that phase separation (PS) is not restricted to an interface-related dead-layer, only few nm thick. Quite the contrary, and in contrast to early thoughts, it also occurs deep into the films. From detailed measurements of the dependence of the NMR intensity on the excitation r.f. field amplitude h_1, it is observed that the restoring fields sensed by spins of ^{55}Mn nuclei of ferromagnetic manganese display a distinctive magnetic hardness depending on film thickness. Specific analysis of the data allows to distinguish the contributions from both surfaces or interfaces and defects to the restoring field, thus unraveling the origins of the anomalous thickness depencence of the coercive field found in section 3.2 (recall fig.3.2(c)). These results evidence that surfaces and other defects promote distinguishable effects on the charge localization and magnetic anisotropy. These views have been confirmed by NMR analysis of LSMO films where engineered defects have been created after appropriate irradiation by energetic He^+ ions. While the results presented here provide a clear and new view of the extent and origin of the observed PS in manganite thin films, they also suggest hints on how to reduce it, allowing to obtain films with more homogenous electronic and magnetic properties as required for spintronic devices.

NMR experiments have been carried out at $4.2K$ with the use of a broadband spin echo spectrometer, in the absence of an external magnetic field. The Panissod protocol [58] has been applied to correct for the variation of the NMR enhancement factor within the studied sample, as explained in appendix A.

3.3.2 *Thickness dependence of hole localization*

In fig.3.5(a) we show the ^{55}Mn NMR spectra of LSMO films of various thicknesses ($6.5nm - 119nm$). The spin echo NMR intensity has been determined in such way as to ensure that the intensity is proportional to the fraction of resonating (^{55}Mn) nuclei [58] (section A.3.3). Therefore, the reduction of intensity when reducing film thickness is entirely due to a decreasing number of ^{55}Mn nuclei at the resonance. Careful inspection of spectra reveals the presence of two resonance lines: a main line appearing at a frequency $f_0 \approx 374MHz$, and a secondary line, at lower frequency $f_1 \approx 335MHz$ (fig.3.5(b)). The line at f_0 is associated with Mn ions having fast relaxing $Mn^{3+/4+}$configurations and participating in the DE coupling. Therefore Mn ions giving rise to this line are contributing to the magnetization and to electric conduction[31, 38, 48, 49, 50, 51, 52, 53]. The frequency of the f_0 line (indicated by arrows in fig.3.5(a-right panel)) shows a slight shift towards lower frequencies for low thicknesses. This frequency shift can be attributed to a depletion of the free carrier density in the conduction band, or a band narrowing resulting in the observed reduction of the Curie temperature (T_C) in these films[38, 48, 53]. Fig.3.5(b) shows also the NMR enhancement factor as a function of frequency, determined for this particular sample (thickness 27 nm). The NMR line occurring at lower

frequency is attributed in the literature to ferromagnetically coupled localized Mn^{4+} states[31, 38, 48, 49, 50, 51, 52, 53]. Accordingly, we assign the f_1 ($\approx 335MHz$) line to Mn^{4+} ions, which contribute to the total magnetization but do not participate in the conduction through electron hopping. In previous reports of NMR study on LSMO films [49, 50] and in LCMO [31, 38, 48] films, an additional resonance line due to Mn^{4+} was found at $f_2 = 312 - 322MHz$ and was attributed to charge trapping at interfaces. The different frequency values ($f_1 - f_2 \approx 15 - 20MHz$) suggest distinct charge localization mechanisms or magnetic coupling strength of Mn^{4+} species in these films, as discussed below. It should be noted, however, that similar high NMR frequency of Mn^{4+} line has been previously reported e.g. in $La_{0.85}Sr_{0.15}MnO_{3-\delta}$ for $\delta = 0$ [59].

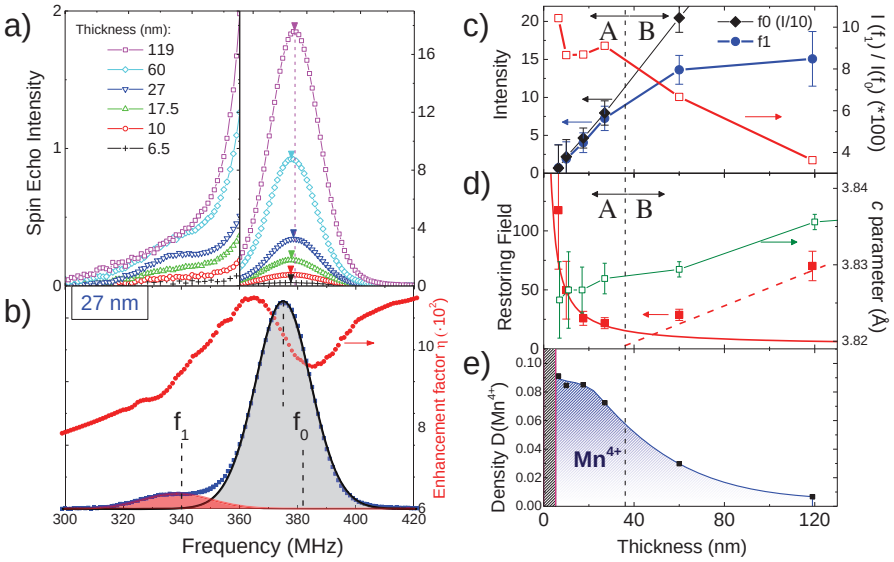

Figure 3.5: a) Right: spin-echo ^{55}Mn NMR spectra of LSMO films of various thicknesses with the spectrum intensity normalized to sample surface. Vertical line is an eye-guide. Left: zoom of the low frequency region; Spectra of 27 nm thick sample (blue points) and data fits to lines centred at f_0 and at f_1. The dotted line represents the intrinsic enhancement factor at each frequency point; c) Left axis: intensity of peak centred at f_0 (solid diamonds, intensity divided by a factor 10) and peak centred at f_1 (solid circles) as a function of thickness. Right axis (open symbols): Ratio between intensities of f_1 and f_0 peaks. d) Left axis: restoring field H_{rest} (see the text for the data fit description). Right axis: out-of-plane lattice parameter c of the films as a function of layer thickness. e) Depth-profile of the density $D(t)$ of localized Mn^{4+} ferromagnetic states (blue-shaded area). Black-dashed area indicates dead layer of non-ferromagnetic material.

As illustrated in fig.3.5(b), the intensity of the f_1 and f_0 lines can be extracted after a proper decomposition of the Mn^{4+} and $Mn^{3+/4+}$ contributions. As shown in fig.3.5(c-left axis, solid rhombi), the intensity of the DE peak at f_0 ($I(f_0)$) is linearly dependent on the layer thickness. Its intensity drops to zero for a thickness of about $4.6nm$ obtained from extrapolation, which is in agreement with previous reports [38, 48, 50] and interpreted as a signature of the presence of the non-(ferro)magnetic dead-layer located at interfaces. In fig.3.5 (c-left axis, solid circles) we also plot the intensity of the f_1 line ($I(f_1)$) for each film. It can be noticed that $I(f_1)$ initially increases almost linearly with the layer thickness but there is some sort of saturation for films above $40 - 50nm$. This is better illustrated by the intensity ratio $I(f_1)/I(f_0)$ (fig.3.5 (c, right axis, empty squares)), which displays two well defined regions (A and B). In region A, for film thicknesses

between 6 and 27nm, the intensity ratio $I(f_1)/I(f_0)$ remains roughly constant. Thus, in contrast with earlier reports [50], the contribution from localized Mn^{4+} ions does not remains constant, but it grows in parallel with the intensity of f_0 line when increasing film thickness in the range of a few tens of nanometers. This observation indicates that the f_1 line is not simply related to interface localization, as it grows with the volume of the samples. For larger thicknesses ($60-120nm$, region B), the relative intensity $I(f_1)/I(f_0)$ decays with increasing thickness, thus indicating that the Mn^{4+} contribution becomes less abundant in the spectra. At the same time, the Mn^{4+} line becomes broader and more extended to lower frequencies (see fig.3.5(a-left panel)), probably indicating that charge localization occurs in a wider variety of defective surroundings as film thickness increases. The distinct behaviour of $I(f_1)/I(f_0)$ in regions A and B as a function of thickness, also finds its correspondence in the restoring field (H_{rest}) as a function of the film thickness. The restoring field averaged over the NMR spectrum shows a non-monotonic behaviour as a function of thickness (fig.3.5(d-left axis, solid symbols). It is obvious that H_{rest} has a minimum value for the 27nm film, at the frontier between A/B regions, increases rapidly for thinner films and also shows some increase for thicker films. Increasing H_{rest} indicates that the spin precession giving rise to the NMR signal is harder to excite, i.e. require a stronger magnetic field. Therefore, the increase of H_{rest} for the thinner films can be interpreted in terms of an enhanced magnetic anisotropy, likely surface or dead layer-dominated, as it is well documented in metallic ferromagnets [60, 61]. In contrast, the H_{rest} increase observed for thicker films indicates a larger spin pinning that could be related to either an enhanced contribution of spins at magnetic domain walls when increasing film thickness or, alternatively, to other kind of defects producing a non-homogeneous magnetic texture. Indeed, in NMR experiments under zero-DC magnetic field, the NMR intensity is largely dominated by spins in non-homogeneously magnetized regions, such as domain walls [50, 62].

In correlation with coercive field explored in section 3.2.2, the behaviour of the restoring field can be attributed to the contribution of different sources to the mangetic anisotropy of the films, namely intrinsic "bulk" magnetocrystalline anisotropy, surface magnetic anisotropy (relevant in ultrathin samples) and defect induced magnetic anisotropy (observed for thicker films showing structural relaxation). In analogy to an expression for an effective anisotropy constant containing bulk and surface components [60, 61], the NMR restoring field $H_{rest}(t)$ can be written as: $H_{rest}(t) = H^S_{rest}(1/t) + H^V_{rest}(t)$, where H^S_{rest} and $H^V_{rest}(t)$ reflect the surface and bulk restoring fields which can be related to surface and bulk anisotropy fields, respectively, as probed by the resonating ^{55}Mn nuclei. The solid line through the data in fig. 3.5(d), corresponds to the fit using $H_{rest}(t) = H^S_{rest}(1/t) + H^V_{rest}$. It describes properly the experimental data for t smaller than the critical thickness $t_{cr} = 30nm$, providing values for the restoring fields $H^V_{rest} = 2.6(Oe)$ and $H^S_{rest} = 463(Oe \cdot nm)$. These values are consistent with a negligibly small magnetocrystalline anisotropy of cubic manganites [63, 41, 64] and confirms the prevailing role of the surface/dead layer in determining the magnetic stiffness of the layers, at least for the thicknesses smaller than the critical value t_{cr}. Above this thickness, however, the bulk contribution $H^V_{rest}(t > t_{cr})$ shows an increase proportional to the reduced thickness $t' = (t - t_{cr})$ with a slope of $0.77Oe$, as shown by a dashed line in fig.3.5(d), indicating the prevalence of a more inhomogeneous magnetic texture, likely associated to a gradually larger density of domain walls. Although available data does not allow quantifying the magnetic domain wall density, detailed observation of the X-ray diffraction data gives a hint. The evolution of the out-of-plane cell parameter of LSMO explored in section 3.2.1, and replotted in fig.3.5(d-right axis,

open symbols) shows an unambiguous expansion of the cell parameter, particularly evident for $t > 30nm$, indicating an elastic lattice deformation and signalling a relaxation mechanism leading to the creation of extended or point defects. These structural transformations, occurring for partially relaxed thicker films, could be at the origin of the anomalous increase of restoring field, caused by the increase of pinning centres at twin domains, dislocations or cationic defective regions.

For a better understanding of the origin of localized Mn^{4+} states, we need a function $D(z)$ describing their profile distribution along the depth z inside the film. Once we have $D(z)$, the intensity of the f_1 line for the film of thickness t should be given by $I(t) = \int_{t0}^{t} D(z)dz$, where, for simplicity, we write $I(t, f_1) \equiv I(t)$. To guess the distribution of the localized states, we assumed then that snapshots of the distribution $D(z)$ could be obtained from the intensities of the f_1 line at different thicknesses, so that we could extract the average profile distribution function as $D(z) = \frac{dI(t)}{dt}\Big|_{t=z}$, where $dI(t)/dt$ was evaluated from data in fig.3.5(c). Using this procedure, we finally obtained the average density profile $D(z)$ of localized Mn^{4+} states as a function of film thickness (fig.3.5(e), solid symbols and blue shaded area). In this figure a dead-layer of thickness t_0, as inferred from data of fig.3.5(c), has also been indicated (black dashed area). Data in fig.3.5(e) clearly evidences that charge localization extends much deeper in the film than the interface-related dead-layer and two regimes can be distinguished as a function of depth. In particular, whereas the density of Mn^{4+} remains roughly constant below a critical thickness t_{cr}, above this threshold it is strongly depressed and only a residual density extends to larger thicknesses.

3.3.3 *Charge localization in artificially created defects*

To further explore the charge localization phenomena and its NMR fingerprints (i.e. Mn^{4+}-related resonant lines), a set of LSMO films ($20nm$ thick), grown under nominally identical conditions, have been irradiated with different doses of light He^+ ions at different energies. For films irradiated with He^+ ions of $500keV$ at different doses, a small and controlled structural damage is caused in the samples. The He^+ beam is swept across the sample surface, producing collision cascades throughout all the film, displacing atoms from their original positions, before getting implanted deeply into the STO substrate. In fig.3.6(a), a simulation of the ions trajectory and the collision cascades are shown for the layer (left panel) and for the substrate (right panel) [2]. As shown in the simulations, the straight He^+ ion track produces a gradually expanding footprint of displaced ions within the film and finally stops at the substrate. According to simulations, at $500keV$ each He^+ ion produces about 0.4 atom vacancies, about 60% of them being oxygen vacancies. The irradiation dose was varied between 0 (reference sample) and $4.3 \cdot 10^{16} ion/cm^2$ resulting in a total number of vacancies in the LSMO layers between 0 and 10% with respect to total number of atoms in the film. On the other hand, the effects of the irradiation on the crystalline quality of the samples were monitored by Rutherford Backscattering Spectroscopy (RBS) and X-ray diffraction. RBS experiments were conducted by using highly energetic alpha particles ($1.57MeV$) as projectiles and probes measuring the backscattered signal. Both, random (sample not aligned with ion beam) and channeling (beam aligned with [001] crystallographic direction) spectra were acquired for all samples. A random spectrum for the non-irradiated reference sample ($A1$) is shown in fig. 3.6(b) (black points), where the observed peaks originate due to

2 Simulations were performed with TRIM software http://www.srim.org/

backscattered alpha particles by the different atoms in the LSMO film, while STO substrate produces backscattering of ions over wide energy regions, due to energy loss of ions when crossing the thick substrate.

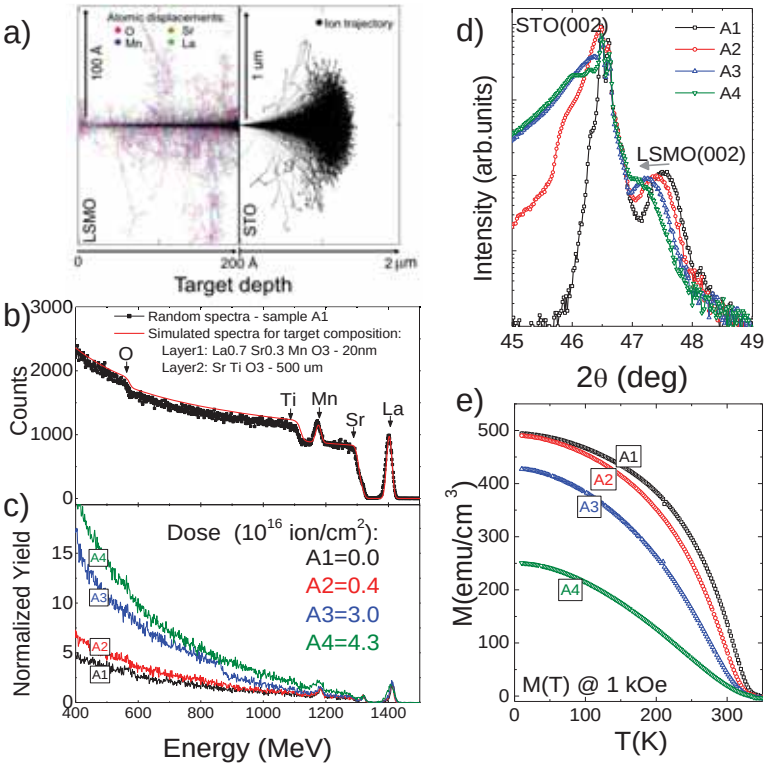

Figure 3.6: a) Simulated collision cascade for incident punctual He^+ beam in LSMO layer (left) and in STO substrate (right); black points show ions trajectories and coloured points show atoms displacements caused by beam; b) RBS spectrum in random sample-beam alignment for non-irradiated sample (black points); simulation of the spectrum with indicated composition and thicknesses values (red line); c) RBS-channelling spectra taken for samples irradiated with different doses; d) Diffraction pattern around (002) peak of STO/LSMO samples before (sample $A1$) and after ion irradiation (samples $A2 - A4$); e) Magnetization curves versus temperature for irradiated films.

Simulation of the spectrum (red line in fig. 3.6(b))[3] using as input parameters the nominal compositions and thicknesses for LSMO film and STO substrate results in good agreement with experimental data and enables the identification of independent atoms contribution to the spectra, as indicated in the figure. The effects of damage caused by irradiation are visible in fig.3.6(c), where channelling spectra are shown for samples irradiated at different doses ($A2$, $A3$ and $A4$), as compared to the reference non-irradiated sample ($A1$). The increased yield signal (normalized to charge of the impinging helium ions, the detector solid angle and the conversion factor of the multichannel analyser) with increasing dose is clearly visible for the energy regions corresponding to the lightest ions (Mn, Ti, O), signalling the increment of point defects due to irradiation-induced displacement of these atoms. Similarly, the reduced channelling observed over all energy range is also a signature of the enhanced formation of defects

3 Spectrum simulation performed using SIMNRA program http://home.rzg.mpg.de/~mam/

by irradiation. X-Ray diffraction $\theta - 2\theta$ scan measurements provide an additional view on the structural changes occurring in the substrates and in the LSMO layers (fig. 3.6(d)) produced by the implanted and colliding He-ions. It can be noticed in fig. 3.6(d) that after irradiation the substrate (002) peaks display a pronounced broadening towards lower angles indicating an expansion of the corresponding cell parameter. Of interest here is the evolution of the $LSMO(002)$ peak that also shifts towards smaller angles thus signalling an increment of the out-of-plane lattice parameter. It is interesting to note that the intensity of the $LSMO(002)$ peak remains rather constant, thus suggesting the absence of a significant amorphism of films due to irradiation. On the other hand, the irradiation effects have a clear impact on the magnetic properties of the films. In fig. 3.6(e) we show the temperature-dependent magnetization (measured using an in-plane magnetic field of $1kOe$) of the $A1 - A4$ samples. This data reveals that the magnetization is rapidly suppressed by He^+ irradiation, thus indicating the creation of non-ferromagnetic regions in the films. Interestingly, the Curie temperature remains barely unchanged for all films. This suggests that the regions unaffected by irradiation remain virtually unperturbed.

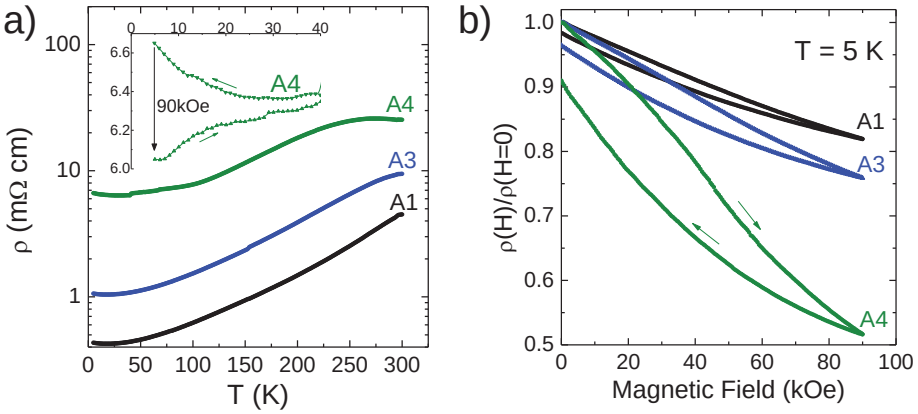

Figure 3.7: a) Temperature dependence of resistivity. Inset: zoom of the low-temperature region of the $\rho(T)$ data collected for sample A4 upon cooling down to $5K$ and the $\rho(T)$ measured upon heating, after a $\rho(H)$ measurement (from $H = 0$ to $90kOe$ and back to zero). Arrows indicate the sense of the temperature excursion. Axes and units are as in the main panel. b) Magnetic field dependence of resistivity measured at $5K$.

We have performed temperature-dependent resistivity measurements and magnetoresistance measurements on some of the irradiated films. In fig.3.7(a) we show some illustrative results. It can be appreciated that the resistivity ρ of the films gradually increases with irradiation dose. The low temperature magnetoresistance $MR(H) = \rho(H)/\rho(H = 0)$ has been measured after a zero-field cooling process down to $5K$, followed by the application of a magnetic field up to $90kOe$ and subsequent field retreat to zero. It can be appreciated in fig.3.7(b) that $MR(H)$ increases with irradiation dose and displays some hysteretic behaviour that becomes more apparent for larger doses. The increase of resistivity by irradiation simply reflects the irradiation-induced formation of non-conducting or spin-disordered regions in the film. The increase of magnetoresistance shown in fig. 3.7(b) is fully consistent with this view. More interesting is the hysteresis observed in fig.3.7(b). It reveals the coexistence of conducting and non-conducting regions of the film. Finally, the consequences of defects induced by irradiation and the subsequent charge localization on the transport properties of films are also reflected

in the low-temperature upturn of the resistivity observed in irradiated samples. As example, we show in fig. 3.7(a-inset) data of an illustrative sample (A4). It is clear that upon cooling, the resistivity displays a minimum which is related to charge localization effects. In the fig. 3.7(a-inset), we also include the data collected when heating up the sample after performing a $\rho(H)$ measurement ($0kOe$ to $90kOe$ and back to zero) at $5K$, as in fig 3.7(b). It is clear that the charge localization has been irreversibility erased by the magnetic field. The fraction of non-conducting regions is reduced by the magnetic field and they cannot convert back to insulating when retreating the magnetic field. This gives rise to the observed hysteretic behaviour. The increasing amplitude of the hysteresis upon irradiation indicates that irradiation is creating patches of non-conducting regions in the films. According to the magnetization data these regions are non-ferromagnetic. A similar hysteretic behaviour was previously suggested to be resultant of the presence of charge-ordered regions in the films[48]. The observed reduction of magnetization is in full agreement with this observation described above.

The ^{55}Mn NMR spectra of irradiated samples ($A1 - A4$) (fig.3.8(a)) reflect the reduction of magnetization throughout a dramatic reduction with increasing dose of the intensity in the main DE line at f_0 ($\approx 374MHz$). Nevertheless, in accordance with the observation of a robust T_C in all films, the frequency of the DE line remains unaltered (within a frequency margin of $0.5MHz$). Close inspection of NMR spectra reveals also the presence of additional lines (fig.3.8(a-inset)). Apart from the DE line at $f_0 = 374MHz$, a line situated at about $335MHz$ is also clearly visible. Its position coincides with the f_1 line observed in the non-irradiated, pristine samples discussed above. In addition, superimposed to the low frequency tail of f_1, we identify the contribution of a new resonant line, labelled f_3, at about $310MHz$ that, as discussed above, we assign –together with f_1, to localized Mn^{4+} states. A more accurate determination of the position of the weak f_3 line has been done by a Gaussian fit of the NMR spectra by fixing the position of the f_0 and f_1 lines to the values $374MHz$ and $335MHz$, respectively, obtained for the non-irradiated samples, which lead to $f_3 = 313MHz$. To extract the intensities of all f_0, f_1 and f_3 lines from all NMR spectra, we have subsequently fixed their positions to the values indicated above. The decomposition of the NMR signal into f_0, f_1 and f_3 components are presented and these fits are used to extract the corresponding intensities $I(f_0)$, $I(f_1)$ and $I(f_3)$ in all films ($A1 - A4$). In fig.3.8(b) (left axis, solid symbols), we show the dependence of $I(f_0)$, $I(f_1)$ and $I(f_3)$ on the He^+ radiation dose together with the corresponding loss of macroscopic magnetization of the samples with irradiation dose (fig.3.8(b), right axis, open symbols). It is clear that the DE contribution $I(f_0)$ and the localized-Mn^{4+} contribution $I(f_1)$, both decrease when increasing the irradiation dose. However, it is also clear that the decay of f_1 is slower than that of f_0. This can be better appreciated in fig.3.8(c), where the plot of the intensity ratio $I(f_1)/I(f_0)$ versus dose emphasizes the relative increase of $I(f_1)/I(f_0)$. The observed trend implies that irradiation damage promotes not only the suppression of ferromagnetic regions (DE $Mn^{3+/4+}$ and charge-localized ferromagnetic Mn^{4+}) by transforming them into non-magnetic regions (which account for the overall decay of f_0 and f_1) but it also indicates that additional charge-localization is induced. It thus follows that He^+ irradiated samples contain an increasing fraction of non-magnetic regions coexisting with magnetic regions which are composed of basically undisturbed areas giving rise to $I(f_0)$, $I(f_1)$ and $I(f_3)$ contributions and regions where the relative contribution of $I(f_1)$ is increased, as sketched in fig.3.8(c-inset).

As suggested by data in fig.3.8(b-c), in irradiated samples one may expect to find ferromagnetic regions where radiation-induced damage has created point defects rendering

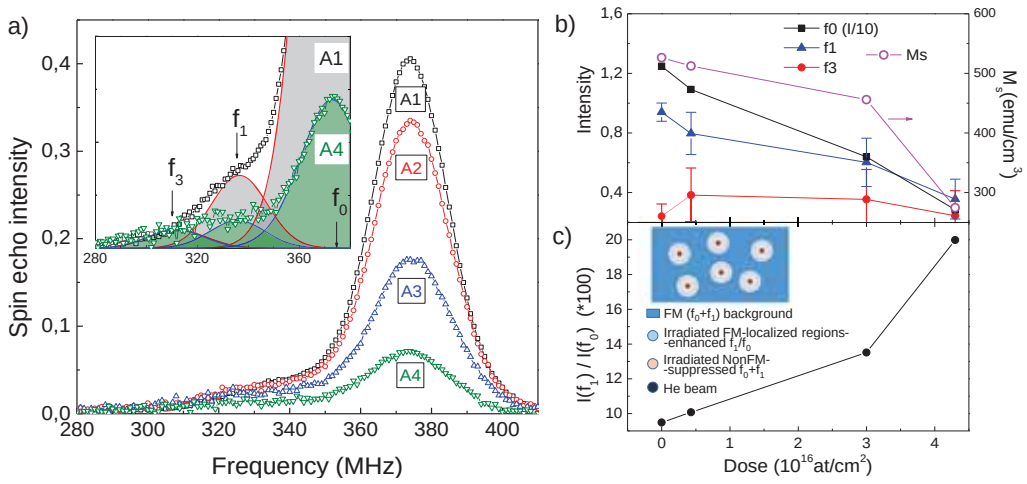

Figure 3.8: a)Normalized ^{55}Mn NMR spectra of irradiated LSMO samples; inset: comparison of reference sample $A1$ (not irradiated-black points) with sample $A4$ (irradiation dose=$4.3 \cdot 10^{16} ion/cm^2$-green points). Red and blue lines correspond to fittings to the lines centred at f_0, f_1 and f_3 frequencies; b) Left axis: Spin-echo intensity of lines centred at f_0 (black squares-intensity divided by a factor 10), lines centred at f_1 (blue triangles) and lines centred at f_3 (red circles), as a function of irradiation dose; Right axis: Saturation magnetization as a function of irradiation dose. c) Intensity ratio of the line centred at f_1 and the line centred at f_0. Inset: sketch of the distinct regions in the film after irradiation as inferred from the ^{55}Mn NMR data.

magnetization locally inhomogeneous. Like in the pristine films discussed above, under such circumstances the restoring field H_{rest} in defective and non-defective regions, should differ. Following the extensive description in Reference[58], we have inspected the spin echo NMR intensity as a function of h_1 for each frequency in the irradiated samples, thus enabling to separate the spectra corresponding to different soft and hard magnetic components. In fig.3.9(solid symbols) we plot the spin echo intensity as a function of the excitation field (in βh_1 units) for the f_0 frequency. It is clear that, upon irradiation, the optimum h_{1opt} field increases, thus illustrating that the ferromagnetic fraction remaining after the ion irradiation becomes magnetically harder. In fig.3.10 we plot the values of $H_{rest} = \beta h^{(2)}_{1opt}$ as a function of the dose (solid symbols). In this figure the coercivity field values extracted from the corresponding magnetization loops, measured at $10K$, are also included (open symbols). As expected, both set of data follow the same trend and illustrate the hardening of the manganite films by the enhanced PS induced by irradiation. A similar behaviour had been reported in phase separated magnetic oxide system [65]. A more detailed examination shows that for the non-irradiated sample ($A1$), the spin echo intensity as a function of the excitation r.f. field h_1 can be simply described by using a single log-normal distribution. In contrast, the intensity distribution of the irradiated samples ($A2$, $A3$ and $A4$) can be better described by a superposition of two different lognormal distributions centered on two different values of h_1, i.e. h^1_{1opt} and h^2_{1opt} corresponding to two different restoring fields $H^{(1)}_{rest} = \beta h^{(1)}_{1opt}$ and $H^{(2)}_{rest} = \beta h^{(2)}_{1opt}$, as it is illustrated in fig.3.9. It is interesting to note that a soft component exists in all irradiated films with a restoring field $H^{(1)}_{rest}$ similar to that of the non-irradiated sample. Probably, it reflects the response of pristine-like regions in the films, not affected by the ion irradiation. Therefore, this analysis clearly reveals that,

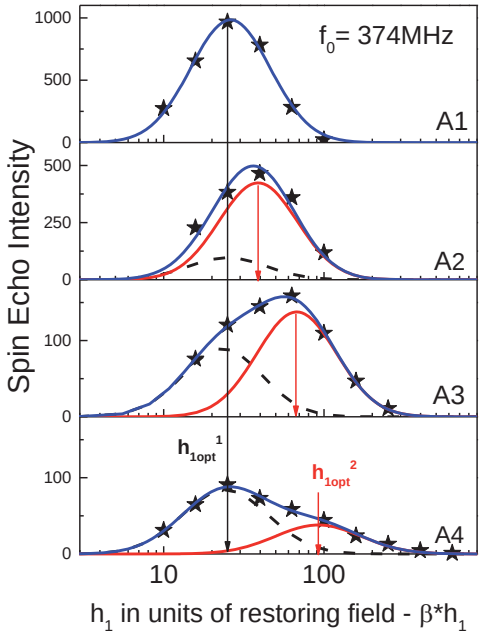

Figure 3.9: Spin echo intensity (solid symbols) of irradiated samples ($A1 - A4$) at the frequency of the main DE line ($f_0 = 374MHz$)) as a function of the rf field h_1 (in units of βh_1). Solid lines through experimental points are the results of the data fit using a single log-normal restoring field distribution of spin echo ^{55}Mn NMR intensity ($A1$ sample) or two log-normal distribution of NMR intensity as indicated by the corresponding dashed lines.

ferromagnetic regions with clearly higher restoring fields and of increasing abundance are produced by irradiation.

We finally note that the intensity of the minority contribution $I(f_3)$ ($f_3 = 313MHz$) remains almost insensitive to the He^+ irradiation dose thus indicating a different origin of the corresponding charge-localized Mn^{4+} states as discussed in the following. While this line could tentatively be attributed to charge trapping at interfaces (in the same way as Mn^{4+} line observed at similar frequency ($f_2 = 320 - 322MHz$ in References [31, 38, 48, 50]), it is more likely that its origin could be related to the damage caused by RBS measurements themselves which imply irradiating the samples with high energetic He particles. Experimental evidence pointing towards this interpretation can be found by comparing the spectral intensity of a non-irradiated He^+, but RBS-analysed, sample ($A1$) around $f_3 = 313MHz$), with the spectra of non RBS-analysed films of similar thickness (fig.3.11). It is evident that the f_3 line is absent in the films that have not been analysed by RBS (fig.3.11–inset). Although the channelling-RBS experiments were performed using highly energetic He ions, which should not have strong influence on the film microstructure, still some damage cannot be avoided. As the energy and dose for RBS experiments were unchanged, the damage caused in all the explored films should be similar, as observed.

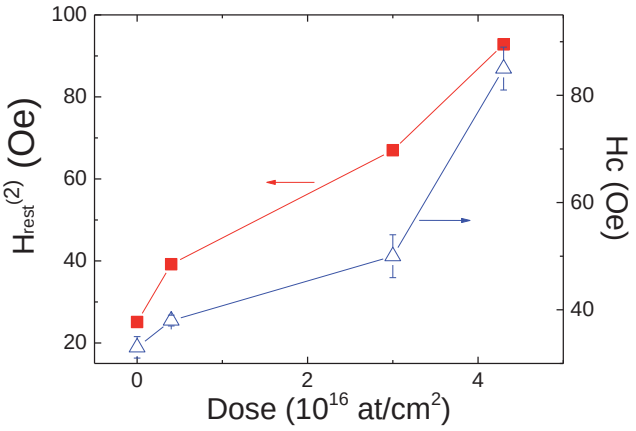

Figure 3.10: Restoring field $H_{rest}^{(2)} = \beta h_{1opt}^{(2)}$ (red squares - left axis) and coercive field (blue triangles - right axis) as a function of irradiation dose.

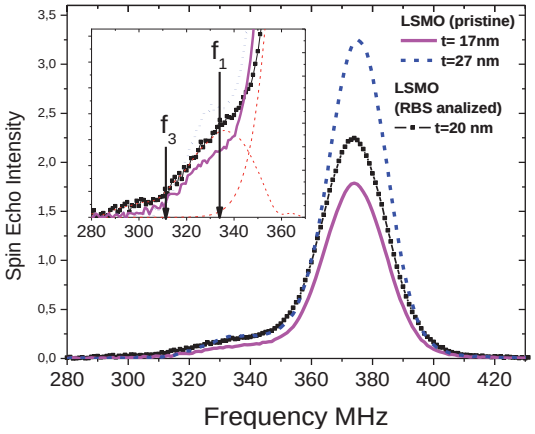

Figure 3.11: Comparison of the spin echo intensity of pristine (17.5nm and 27nm thick) and RBS-irradiated sample (20nm thick) (He$^+$ at 1.54MeV). Inset: Zoom of Mn^{4+} resonance lines. The positions of the f_1 and f_3 resonant lines are indicated.

3.3.4 *Concluding remarks*

In summary by using ^{55}Mn NMR, we have provided evidence of the existence of distinct localized Mn^{4+} states in LSMO films associated to hole trapping which is not restricted to the interface-dominated dead-layer but extends deep into the film. Although these different defective states display the resonance at a common frequency (around 335MHz, in our films), the distinct magnetic surrounding, either close to interface or to other defects, produce distinguishable local magnetic anisotropy and hardness. Interfaces and the associated breaking of symmetry in the coordination polyhedral of the metal ions ($Mn^{3+/4+}$) have been proposed to be the origin of the dead layer and phase separation in manganite thin films. The present results, although do not exclude this unavoidable effect as a source of charge localization, establish that PS occurs and extends several tens of nanometers deep into the films, away from the interface, thus pointing that extrinsic charge trapping centres are playing a prevalent role.

3.4 SUMMARY

In the present chapter we have studied the magnetic and structural properties of LSMO films grown on STO substrates. XRD characterization signals an epitaxial growth of the films, producing a coherent tensile strain that extends to thicknesses as large as 370nm, however films with a thickness above 30nm display a structural relaxation evidenced by the progressive growth of unit cell volume, that may be associated to the creation of punctual or extended defects. While films with thickness above 60nm display magnetic properties very close to the bulk LSMO, thinner samples show evident signs of magnetic depletion.

In addition, the magnetoelastic coupling between the magnetic domain structure of the LSMO and the STO structure was proved by ac and dc magnetic measurements at temperatures close to the cubic to tetragonal transition of STO, signaling a domain reconstruction in the films induced by the structural distortions of the substrate, accompanied by the creation of regions with enhanced anisotropy, that extend deep into the films, thus pointing to structural deformations in the LSMO induced by the substrate transition as the origin of the coupling mechanism.

By means of NMR spectroscopy, we have studied the charge localization phenomena and local magnetic anisotropy of LSMO films. The thickness dependence of NMR resonance peaks associated to itinerant charge and localized charge in Mn^{4+} sites reveals that charge trapping is not restricted to interfacial regions, as commonly accepted, but extends for several nm deep into the films. The restoring field related to the magnetic stiffness of Mn sites displays a thickness dependence equivalent to the observed macroscopic coercive fields, both pointing to the existence of three sources contributing to the magnetic anisotropy: a soft magnetocrystalline anisotropy inherent to the LSMO and two other contributions that enhance the anisotropy of ultrathin films (surface magnetic anisotropy) and of thicker films showing relaxation signatures (magnetic anisotropy due to pinning at defects). The enhancement of both charge localization and defect-induced magnetic anisotropy was furtherly proved by studying the NMR spectra of He^{+}-irradiated LSMO films, showing a clear increase of both effects with increasing damage produced by irradiation.

Thus, these results provide new information on the electronic phase separation phenomena and magnetic anisotropy in manganite thin films, and its relation with samples microstructure and provide guidelines for the growth of electric and magnetic homogeneous manganite films.

4

SURFACE SYMMETRY BREAKING EFFECTS ON THE ORBITAL OCCUPANCY OF MANGANITE THIN FILMS

Symmetry breaking produced by strain in thin films is known to affect the population of the d states in the valence or conduction band in transition metals. However, a larger rupture of the symmetry is present at the surfaces, that can profoundly alter the orbital hierarchy promoting electron localization in certain orbitals, as we will study in this chapter in optimally doped manganite thin films.

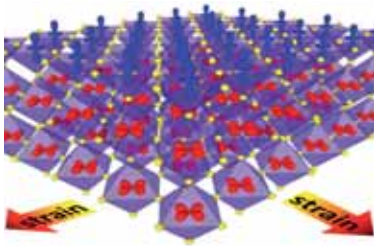

4.1 INTRODUCTION

Electron localization in manganites can be widely promoted by substrated-induced epitaxial strain in thin films. Mediated by Jahn-Teller (JT) interaction, strain tailors the occupancy of the d orbitals, that can lead to dramatic changes in the electron interactions which drive the functional properties of the *bulk* of the films. In $La_{1-x}Sr_xMnO_3$, the electron occupancy in the e_g ($x^2-y^2/3z^2-r^2$) orbitals strongly depends on the hole doping level (x) and the strength of the JT coupling [1]. In bulk $La_{2/3}Sr_{1/3}MnO_3$ (LSMO), the partially filled e_g orbitals are responsible for the metallic character and the carrier-mediated Mn^{m+}–O^{-2}–Mn^{n+} double exchange interaction is responsible for the ferromagnetic coupling. Epitaxial strain in LSMO thin films, similarly to the JT distortion, breaks the ($x^2-y^2/3z^2-r^2$) degeneracy and dramatically changes their transport and magnetic properties [66]. In agreement with simple electrostatic expectations, it has been shown [27, 39, 67, 68] that tensile strain favors x^2-y^2 occupancy whereas the compressive strain favors $3z^2-r^2$ occupancy, thus providing some understanding for the so-called magnetic and electric "dead" layers [38, 48, 57] observed in thin films. When two dissimilar oxides are brought together, charge transfer, electrostatic boundary conditions or/and elastic strain may also produce an additional modification of orbital filling which can produce charge, orbital and spin reconstructions [69, 70]. Similarly, interface-mediated bonding in heterostructures [71, 72] largely depend on the relative position of the ($x^2-y^2/3z^2-r^2$) orbitals at interfaces and thus their determination is of paramount importance.

Linear dichroism in the X-ray absorption (XLD) has been used to firmly demonstrate that, while tensile strain favors the x^2-y^2 occupancy, a compressive strain favors the $3z^2-r^2$ occupancy [27, 39, 68]. In section 4.2 of this chapter we will probe the strain tun-

ing on the orbital occupancy of LSMO epitaxial films, providing a method to calculate the orbital polarization.

A distinction of the surface and interface effects on the orbital occupancy requires of a more careful and detailed study and analysis of the XLD signal to separate the strain-induced "*bulk*" contribution from the surface or interface contribution. By studying the XLD signal dependence on the films thickness, and modeling this thickness dependence with a simple exponential decay, characteristic of the electron yield signal, we identify the XLD contribution from free surfaces in manganite films. In section 4.3, we will show that, although the $(x^2 - y^2/3z^2 - r^2)$ orbital configuration is primarily related to the strain-state, an additional well-defined contribution emerges at the free surface, favoring the occupancy of the out-of-plane oriented e_g orbitals. Moreover, we will show that this surface contribution can also be controlled by selecting the specific termination ($(La, Sr)O$ or MnO_2) of the film or the growth orientation.

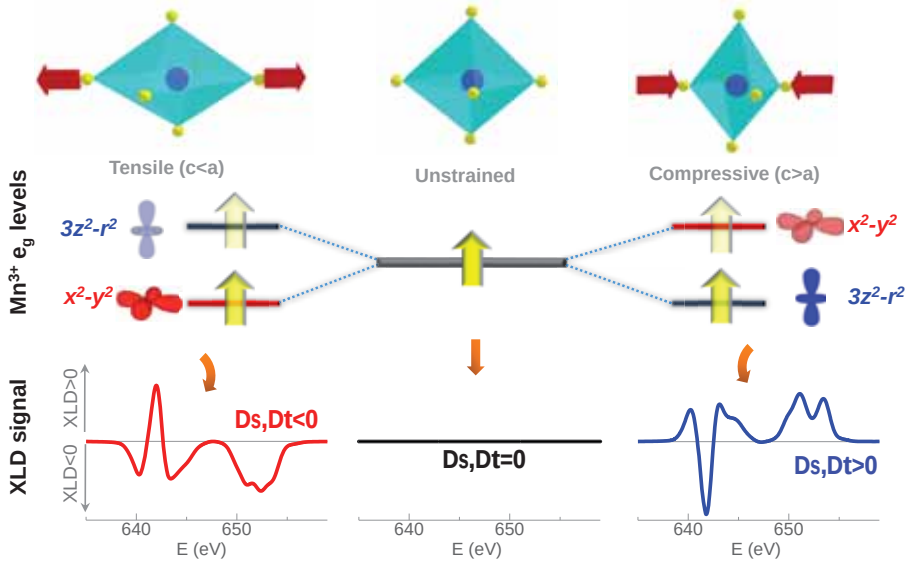

Figure 4.1: Top panel: Representation of the MnO_6 octahedral distortions as a function of strain; middle panel: subsequent effect of the Jahn-Teller distortion on the e_g levels of Mn^{3+} ions; bottom panel: X-ray linear dichroism simulated for the Mn L-edge of Mn^{3+} ion in a tetragonal crystal field with c<a (left), with c>a (right), and with octahedral field (center)

4.2 STRAIN TUNING OF ORBITAL OCCUPANCY

XLD derived from the absorption at the Mn-L edges gives information on the distribution of empty $Mn - 3d$ states: larger (smaller) absorption for in-plane polarization indicates more in-plane (out-of-plane) empty states in the e_g band and thus a higher occupancy of out-of-plane (in-plane) orbitals [27]. In (001)LSMO films the out-of-plane direction is $[001]$ (c-axis) and the in-plane $E_{||}$ is parallel to $[100]$ and therefore $I_{\perp}$ and $I_{||}$ are proportional to the hole occupancies of $3z^2 - r^2$ and $x^2 - y^2$ orbitals, respectively. Strain in epitaxial thin films is expected to create distortions in the MnO_6 octahedra, elongating (compressing) the c axis for compressive (tensile) strain (fig.4.1-top panel). This breaking of symmetry lifts the degeneracy of $3d$ orbitals, favoring the occupancy of the orbitals oriented along the elongated direction ($x^2 - y^2$ for tensile strain, and

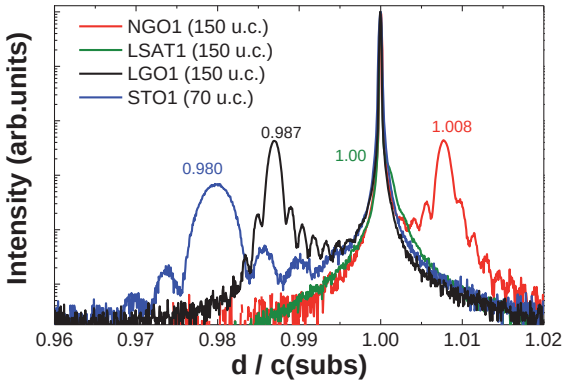

Figure 4.2: $\theta - 2\theta$ scans for films grown on the indicated substrates: $NdGaO_3$ (NGO)-150uc, $(LaAlO_3)_{0.3} - (Sr_2AlTaO_6)_{0.7}$ (LSAT)-150uc, $LaGaO_3$ (LGO)-150uc and $SrTiO_3$ (STO)-70uc

$3z^2 - r^2$ for compressive strain) (fig.4.1-middle panel). The XLD signals expected for the unstrained as well as the compressive and tensile states can be simulated [73][1] by introducing tetragonal distortion parameters to the crystal field (Ds, Dt) that cause a energy splitting in the e_g levels: $\Delta e_g = E(x^2 - y^2) - E(3z^2 - r^2) = 4Ds + 5Dt$. As it can be appreciated in the simulated spectra in fig. 4.2-bottom panel, the sign of the XLD spectra (defined as XLD=$I_{\parallel} - I_{\perp}$) around the L_2 edge ($648 - 660$eV) is a good indicative of the sign of this energy splitting (negative for $\Delta e_g < 0$ and positive for $\Delta e_g > 0$).

In order to study the strain-induced orbital tunability of manganite thin films, we grew LSMO samples with a thickness much larger than the typical TEY probing depth ($3nm$), grown on substrates having different mismatch ($\delta = \frac{a(subs) - a(film)}{a(film)}$) with the bulk LSMO pseudo-cubic lattice parameter: $SrTiO_3$ (STO) with $\delta = 0.8\%$, $LaGaO_3$ (LGO) with $\delta = 0.4\%$, $(LaAlO_3)_{0.3} - (Sr_2AlTaO_6)_{0.7}$ (LSAT) with $\delta = -0.1\%$ and $NdGaO_3$ (NGO) with $\delta = -0.5\%$, considering the pseudo-cubic in-plane lattice parameters. The thickness of the films was $60nm$ (corresponding to about 150uc of LSMO) for the films grown LGO, LSAT and NGO and $27nm$ (about 70uc) for film grown on STO.

The high resolution $\theta - 2\theta$ diffraction patterns around the (004) reflection of the LSMO films and substrates was recorded to explore the induced structural distortion. In figure 4.2, the reciprocal interplanar distances $d(004)$ (the interplanar (004) distance in LSMO) of all films have been normalized to that of the corresponding substrates $(1/c_{subs})$ for better comparison of the strain state of the films. The shift towards a lower $d(004)/c_{subs}$ ratio (< 1) for the film grown on STO illustrates the substrate-induced in-plane tensile state and the resulting shrinking of $d(004)$. The $d(004)/c_{subs}$ ratio is larger for the film grown on LGO as compared to STO and equals unity for sample grown on LSAT, as expected from the structural mismatch values. Similarly, the shift of $d(004)/c_{subs}$ to values > 1 as observed for film on NGO illustrates the corresponding compressive in-plane strain.

The c/a ratios calculated from the position of the (004) film reflection and the substrate in-plane parameter are listed in table 4.1. The comparison between the experimental values and the theoretical c/a ratios -calculated considering fully strained films with bulk LSMO unit cell volume- shows an accordance within a 0.6% maximum devi-

1 Atomic model calculations were performed using CTM4XAS software with a cubic crystal field 10 Dq = 1.6 eV and adding a tetragonal distortion inducing a splitting of the t_{2g} and e_g levels equal to $3Ds - 5Dt$ and $4Ds + 5Dt$, respectively. Here we used $Dt = 0.02$ and $Ds = 0.1$ (for c>a) and $Dt = -0.02$ and $Ds = -0.08$ (for c<a)

substrate	a(subs) (Å)	δ (%)	c/a(theor.) (Å)	c/a(ϑ-2ϑ) (Å)
STO	3.905	+0.8	0.976	**0.980**
LGO	3.887	+0.4	0.989	**0.987**
LSAT	3.87	-0.1	1.002	**1.00**
NGO	3.855	-0.5	1.014	**1.008**

a(LSMO bulk)=3.873Å [29]

Table 4.1: Cubic/pseudo-cubic lattice parameters, lattice mismatch with LSMO, theoretical c/a ratio (considering ideal volume conservation) and experimental c/a ratio (considering fully strained state) for the different substrates studied.

ation. This observation, together with the demonstration of nearly fully strain state of LSMO films grown on STO substrates for thickness as large as $370nm$ shown in section 3.2, denotes a fully strained state for all the studied films.

X-ray absorption spectroscopy (XAS) measurements were performed at the Mn $L_{2,3}$-edges with linear photon polarization parallel to the sample plane ($E_{\parallel}$) and almost perpendicular to it ($E_{\perp}$) in total electron yield mode. The spectra were recorded at temperatures well above the corresponding Curie temperatures (~400 K) to avoid any contribution from sample magnetic configuration to the XLD. The XLD spectra are calculated as the intensity difference ($I_{\parallel} - I_{\perp}$) between the spectra measured with in-plane ($E_{\parallel}$) and out-of-plane ($E_{\perp}$) polarizations. In (001)LSMO films, out-of-plane ($E_{\perp}$) corresponds to $E \parallel [001]$, thus mostly accessing transitions from $2p$ core levels to $3d(3z^2 - r^2)$ unoccupied levels; for in-plane ($E_{\parallel}$), the polarization was chosen such as $E \parallel [100]$, being mainly responsible for transitions $2p \rightarrow 3d(x^2 - y^2)$ (see inset of fig.4.3(a). The absorption spectra, obtained for each polarization and normalized to the incident incoming light, are shown in fig. 4.3(a-d) for all four samples. The data is normalized in the pre-edge region $(630 - 635eV)$[2]and divided by the maximum intensity of the averaged XAS, defined as $(I_{\parallel} + I_{\perp})/2$. The difference between the two spectra result in the XLD spectra shown in fig. 4.3(e-h). Here, a geometrical correction accounting for the grazing angle of incidence (60 deg respect to surface normal) has been applied, as explained in section 2.2 (eq.2.9).

Data in fig. 4.3(e-h) display a clear trend: a positive XLD signal is observed for the film on NGO, while a negative one is found for sample on STO. This indicates enhanced $3z^2 - r^2$ electron occupancy for the compressively strained film on NGO; conversely, the negative XLD signal for the tensile strained film on STO reflects a preferential $x^2 - y^2$ electron occupancy. These results are in agreement with previous findings [67]. However, a detailed inspection of the data for films on LGO and LSAT reveals an unexpected and remarkable $3z^2 - r^2$ contribution, especially dramatic in LSAT sample, where a clearly positive XLD is observed. We stress that the LSMO film on LSAT is barely unstrained and thus a mostly degenerated $(3z^2 - r^2/x^2 - y^2)$ occupancy should be expected and, accordingly, the XLD should vanish.

The tendency observed in 4.3(a-d) is better visualized in fig.4.4(a), where the integrated area under the XLD signal is plotted as a function of c/a ratio of the films. The tendency is shown to be robust and independent on the integration range, as both the

2 For this normalization, independent spectra $I_{\parallel}$ and $I_{\perp}$ are multiplied by an arbitrary factor in order to match intensities in the pre-edge region. Reliable XLD can be obained if both spectra result also coincident in the post-edge region at high energies ($E > E(L_2)$) where no dichroism is expected

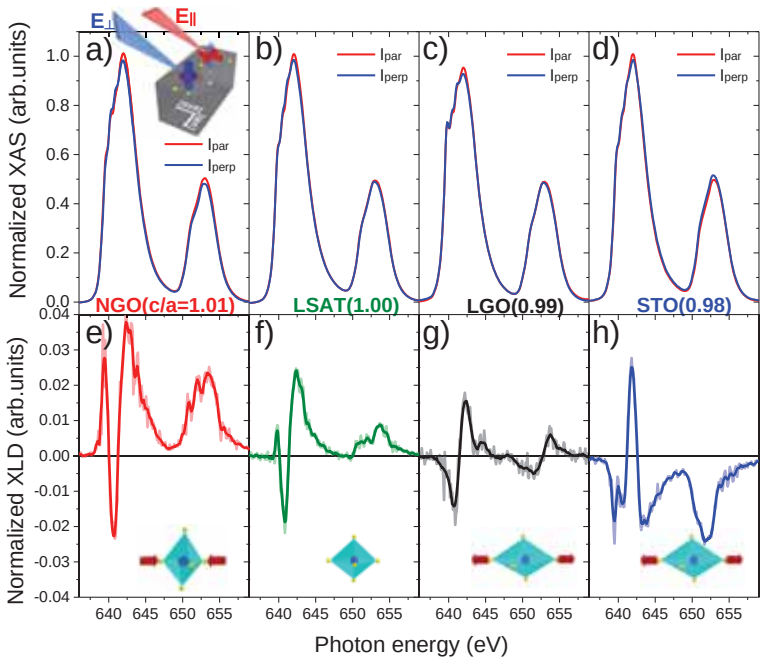

Figure 4.3: Polarized X-ray absorption measurements of samples grown on NGO (a), LSAT (b), LGO (c) and STO (d) substrates taken in grazing incidence with linear polarization mostly in-plane (red curves) and out-of-plane (blue curve); inset in (a): sketch of the orbitals explored for incident radiation polarized out of the plane of the samples ($E_\perp$) and in the plane of the samples ($E_\parallel$); XLD measurements for samples grown on NGO (e), LSAT (f), LGO (g) and STO (h) substrates; insets: corresponding MnO_6 octahedra distortion for each case.

total area under XLD (blue empty circles in the figure) and the area under L_2 edge region (red squares) show the same behaviour.

Following the procedure of refs.[15, 16], we can apply the sum rules for XLD [74] to quantify the orbital polarization of the films: from the total area under the XAS and XLD spectra we can calculate the ratio of holes in the e_g levels as:

$$X = \frac{h(3z^2 - r^2)}{h(x^2 - y^2)} = \frac{3\int_{L3,2} I_\perp(E)dE}{4\int_{L3,2} I_\parallel(E)dE - \int_{L3,2} I_\perp(E)dE} \tag{4.1}$$

, where $I_\perp = XAS - XLD/2$ and $I_\parallel = XAS + XLD/2$, after geometrical correction. The results of this calculation are shown in fig.4.4(b). Here, a ratio of holes $X > 1$ is obtained for film on NGO, while films on STO and LSAT show $X < 1$. For LGO sample we obtained a X value close to 1. The orbital polarization, is defined as [75]:

$$P = \frac{n_{x^2-y^2} - n_{3z^2-r^2}}{n_{x^2-y^2} + n_{3z^2-r^2}} \tag{4.2}$$

, considering $n_{x^2-y^2} = 1 - h_{x^2-y^2}$, $n_{3z^2-r^2} = 1 - h_{3z^2-r^2}$, $n_{e_g} = 2 - h_{e_g}$ [3] and eq. 4.1 we get:

$$P = \left(\frac{2}{n_{e_g}} - 1\right)\frac{X-1}{X+1} \tag{4.3}$$

3 For LSMO we consider that only spin-up states contributes to the absorption

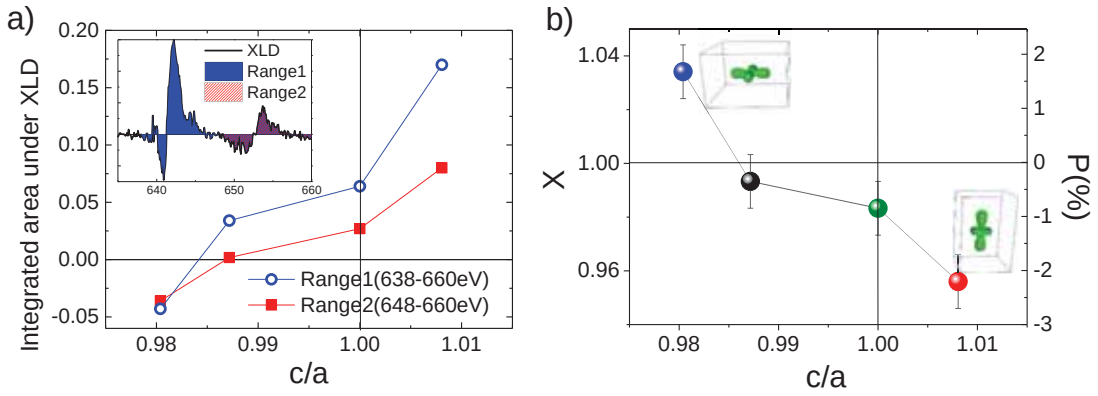

Figure 4.4: a) Integrated area under XLD for integration range 1 (blue circles) and range 2 (red squares) as a function of c/a ratio. The two integration ranges are indicated in the inset. b) Calculated holes ratio X (left axis) and orbital polarization P (right axis) as a function of c/a ratio. Negative values indicate preferential occupation of in-plane $3z^2 - r^2$ orbitals, while positive values indicate preferential occupation of $x^2 - y^2$ orbitals.

While the value of n_{e_g} will be discussed later in next chapter, for the moment we will consider $n_{e_g} = 1$, resulting in the polarization values depicted in fig.4.4(b-right axis), showing that for the studied range of strain, the orbital polarization can be tuned from $+1.7\%$ to -2%. For nearly unstrained films, as it is the case for LSAT sample, a significant negative polarization is observed ($P = -0.9\%$) and only for films with a tensile strain like that of LGO sample we obtain an orbital polarization close to zero ($n_{x^2-y^2} \approx n_{3z^2-r^2}$). These observations indicate that strain alone cannot be the only driving force for the orbital energetic ordering, and another source of dichroism slightly favours the occupancy of $3z^2 - r^2$ orbitals, pushing the polarization towards more negative values that those expected by strain-induced Jahn-Teller effect.

4.3 SURFACE SYMMETRY BREAKING EFFECTS ON ORBITAL OCCUPANCY

Jahn-Teller distortion, as induced by strain, is a way of reducing the symmetry, that promotes a preferential occupation in the anisotropic $3d$ orbitals. However, in thin films, a more drastic change of symmetry occurs at interfaces where the atomic environment is largely modified and this can have relevant consequences for the electron distribution in the $3d$ orbitals. Among all possible interfaces, the naturally occurring surface is the most dramatic one. As we will show in this chapter, the lack of oxygen neighbours strongly modifies the charge distribution around the surface Mn ions, promoting a large energy splitting in the e_g levels that can locally alter the orbital occupancy.

In the following we show how this surface contribution can be isolated from the bulk contribution, allowing for an identification of the surface orbital occupancy that superimposes to the strain induced occupancy in the ultrathin films, and how this surface effect depends on the manganite terminating layer and sample crystallographic orientation.

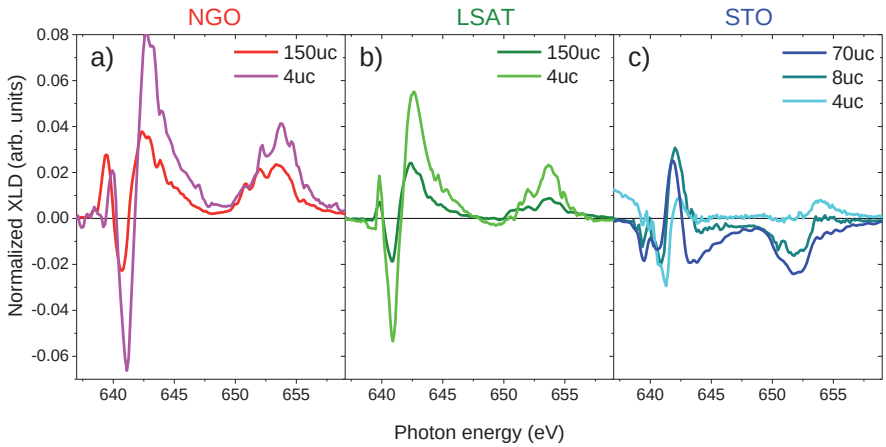

Figure 4.5: XLD spectra for thick ($t \geq 70uc$) and thin ($t \leq 8uc$) films, grown on NGO (a), LSAT (b) and STO (c) substrates

4.3.1 *Surface orbital polarization*

In order to enhance the surface contribution to XLD, we grew ultrathin film LSMO samples with a thickness of $4uc$ on NGO, LSAT and STO substrates. The thickness of these samples was controlled by RHEED system, monitoring the layer-by-layer growth during PLD deposition. In addition, 8 and $13uc$ samples were grown on STO, to study the evolution of XLD with thickness.

The observation of a fully strained state in the $150uc$ and $70uc$ LSMO films anticipates that the thinnest films used in this section ($\approx 4 - 13uc$) are also fully strained. The Curie temperature T_C and saturation magnetization M_S for these ultrathin films show a remarkable depression respect to bulk LSMO values ($T_C < 300K$, $M_S < 400emu/cm^3$), as it was shown in section 3.2, and as it is typically found in ultrathin manganite films [27, 31, 38, 39].

XLD spectra of the thinnest samples -measured in grazing incidence geometry and at $300K$ (in the paramagnetic state of the samples)- is shown in fig. 4.5, where the spectra of films with reduced thickness ($t < 10uc$) is compared with that of thickest films ($t \geq 70uc$). Due to the exponential decay of TEY signal, the dichroism originated in the first layers is always more relevant that the underlying layers. However, by reducing the sample thickness below the TEY probing depth ($\sim 3nm$), the "bulk" contribution (that of underlying layers) gets reduced and thus enhances the surface contribution to the total measured XLD signal. Therefore, the modifications in the XLD spectra for thinnest samples can be mostly attributed to surface effects.

It can be appreciated in fig.4.5 that the spectra of $4uc$ samples is substantially modified with respect to the thicker samples. In the case of samples grown on NGO and LSAT (fig.4.5(a,b)) the XLD signal is greatly enhanced, while for STO samples (fig.4.5(c)), a reduction of the dichroism is observed and eventually, for the thinnest sample ($4uc$) an inversion of the XLD sign is observed in the L_2 edge.

Computing the integrated area and applying the XLD sum rules we obtain the holes ratio $X = \frac{h(3z^2-r^2)}{h(x^2-y^2)}$ shown in fig. 4.6. While the strain tendency is conserved for the $4uc$ samples, we observe how the holes ratio X is displaced towards lower values for these samples. It is remarkable the case of STO ($c/a = 0.98$) where the X value changes sign in the thinnest samples.

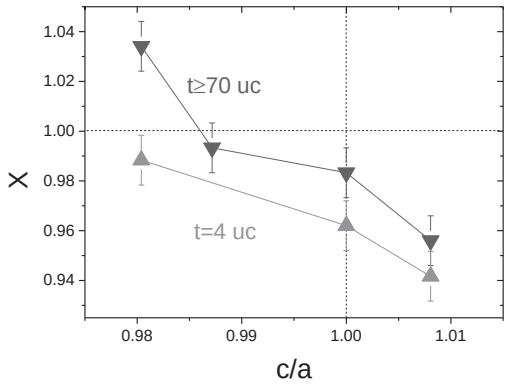

Figure 4.6: Holes ratio for thick ($t \geq 70uc$) and thin ($t = 4uc$) samples, as a function of c/a ratio

For LSMO films grown on STO we explored a larger thickness range, including $8uc$ (shown in fig.4.5(c)) and $13uc$ samples. The calculated X values are plotted in fig.4.7(a-blue circles). The thickness evolution of holes ratio X can be fitted by an exponential function of the form:

$$X = A + B\exp(-t/\delta) \tag{4.4}$$

where t is the thickness (in unit cells), δ is the decay factor, directly related to the TEY probing depth, $A = \lim_{t\to\infty} X$ is the bulk contribution to X (X_{bulk}), and the surface contribution can be extracted from $X(0) = X_{surf} = A + B$, therefore: $B = X_{surf} - X_{bulk}$. Eq. 4.4 can thus be written as:

$$X = X_{bulk} + (X_{surf} - X_{bulk})\exp(-t/\delta) \tag{4.5}$$

which allows us to separate bulk and surface contributions by fitting the experimental data. Fitting to X data on STO films (blue curve in fig.4.7(a)) leads to a δ value of $8.3uc$, which corresponds to $\sim 3nm$, in accordance to expectations [76, 77], and contrasting values for X_{bulk} (1.03) and X_{surf}(0.96). Fitting the data obtained for films on LSAT and NGO with eq.4.5 and using the same value for probing depth $\delta = 8.3$, leads to the curves plotted in fig.4.7(a). From the resultant X values we calculated the corresponding bulk and surface orbital polarizations (assuming $n_{eg} = 1$ in eq. 4.3), for each substrate series. The results, shown in fig.4.7(b), evidence a bulk strain-dependent orbital polarization that changes sign close to $c/a = 1$, and a surface orbital polarization which is less dependent on strain and always shows a negative sign, thus indicating that at the surface a preferential $3z^2 - r^2$ orbital occupancy is promoted.

A natural origin for the prominent orbital occupancy at the free surface could be a vacuum-interface induced contribution to the orbital configuration, favoring occupancy of the out-of-plane oriented $3z^2 - r^2$ states. This conclusion is supported by the theoretical work of Calderon et al. [69], who suggested that the free surface of (001)LSMO manganites should be prone to display a preferred occupancy of $3z^2 - r^2$ orbitals due to the absence of apical oxygen coordination and the resulting reduction of the repulsive Mn -$3d(3z^2 - r^2)$ to O-$2p(z)$ electron-electron interaction at the MnO_2 termination layer of the manganite. This surface-related $3z^2 - r^2$ contribution here disclosed should be, in fact, a lower limit, as electron occupancy at $3z^2 - r^2$ orbitals could have been partially

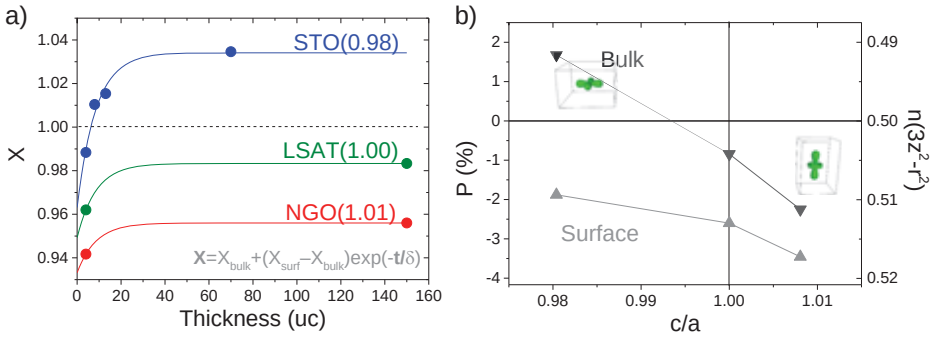

Figure 4.7: a) Holes ratio as a function of sample thickness; lines are resultant from the fitting to function indicated in the graph, for each series. b) surface and bulk orbital polarization as a function of c/a ratio.

reduced or screened by unavoidable surface contamination that would diminish the prominent surface contribution to the XLD.

4.3.2 *Tuning of orbital occupancy in single terminated films*

A stringent test of the above conclusions could be obtained by comparing the XLD spectra of LSMO films with either MnO_2 or $(La,Sr)O$ terminations at their free surface. In the MnO_2 terminated surfaces, the preferential $3z^2 - r^2$ occupancy of $Mn - e_g$ orbitals is expected to be larger than in the $(La,Sr)O$ terminated surfaces because of the square-pyramidal oxygen coordination of Mn^{m+} in the former and the octahedral oxygen coordination of the buried Mn^{m+} ions in the latter. This surface engineered terminations are achieved by the RHEED assisted layer-by-layer LSMO growth on (001)STO substrates having either TiO_2 or SrO terminations respectively, which promote either MnO- or $(La,Sr)O$- terminations, respectively.

Single terminated substrates were obtained by chemical etching and subsequent thermal annealing, according to common prescriptions [78, 79]. The RHEED pattern of STO-single terminated TiO_2 is shown in fig.4.8(a). As indicated by the monitored oscillations of the intensity of the specular spot during deposition, LSMO grows layer-by-layer on top of TiO_2-STO (fig.4.8(b)), and the Bragg spots on the $0th$ Laue circle in the pattern of the deposited film (fig.4.8(c)) attest for a flat surface. On the other hand, SrO-terminated STO RHEED pattern presents extra spots at intermediate positions on the 0^{th} Laue circle suggesting a surface reconstruction (fig.4.8(d)), and intensity oscillations of low amplitude are observed during deposition of LSMO (fig.4.8(e)). The RHEED intensity variation with deposition could be caused by mixed growth mode, with both layer-by-layer and step flow mechanisms occurring, with the pattern at the end of the deposition the pattern (fig.4.8(f)) signaling a flat surface.

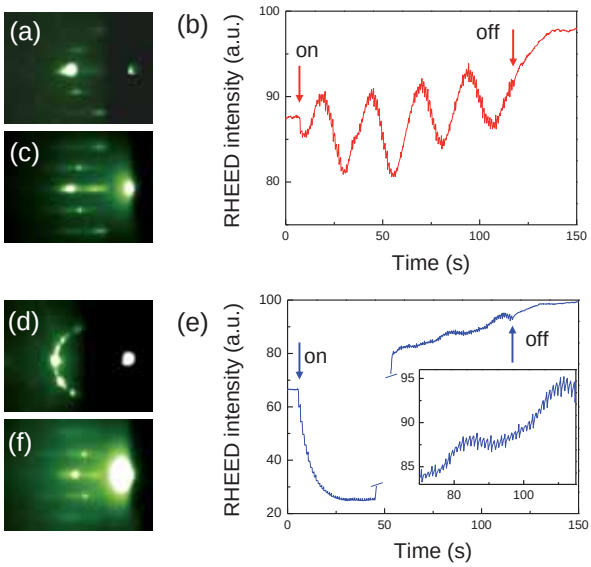

Figure 4.8: a) RHEED pattern of TiO_2-terminated STO substrate taken with the incident beam along STO[100]. b) Intensity oscillations of the specular spot. The arrows indicate the start and the end of the deposition. c) RHEED pattern of the deposited film TiO_2-terminated STO. (d) The RHEED pattern of the SrO-terminated STO taken along STO[100]. (e) The intensity of the specular spot (note that the intensity of the incident e-beam was manually increased); intensity oscillations are observed (see the zoom). f) RHEED pattern of the deposited film *SrO*-terminated STO.

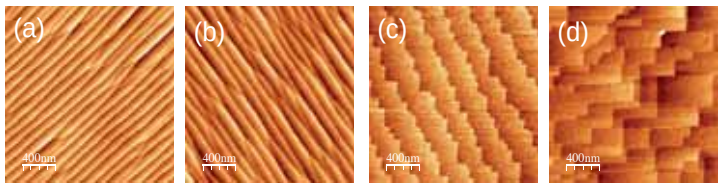

Figure 4.9: AFM images of TiO_2 (a) terminated (001)STO substrate and corresponding 4*uc* LSMO film grown on top (b). AFM images of *SrO* (c) terminated (001)STO substrate and corresponding 4*uc* LSMO film grown on top (d)

The atomic force microscopy images of TiO_2- and *SrO*-terminated (001)STO substrates are shown in fig.4.9(a) and fig.4.9(c), respectively; the corresponding images of the deposited 4*uc* thick LSMO films are shown in fig.4.9(b) and fig.4.9(d). The LSMO films on TiO_2-terminated STO present a terrace and step morphology mimicking the substrate, with 2*uc* high steps. The step bunching caused by the high temperature annealing done after chemical etching, is due to the relatively high miscut angle of the STO substrate (around 0.4^o). The *SrO*-terminated STO has a smaller miscut ($< 0.1^o$) and show steps of 1*uc* high, highly kinked along [100] and [010] directions, which is a distinctive hallmark of the *SrO* chemical termination. The LSMO film on *SrO*-terminated STO maintains the saw-like shape of the steps, but with a larger dispersion in the terrace width.

The XAS spectra of these films (fig.4.10), were taken in grazing incidence (30 degrees respect to surface plane) with linear polarization (both in-plane and out-of-plane ori-

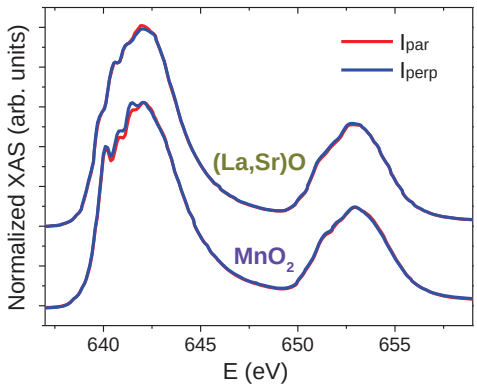

Figure 4.10: Polarized spectra of (La,Sr)O and MnO_2-terminated LSMO films

ented respect to the sample surface). In the XAS spectra of MnO_2 terminated film, some differential features in the low energy region of L_3 are exhibited. These features can be attributed to Mn^{2+}, which was observed to evolve during measurement (see appendix D). Although Mn^{2+}, not being a Jahn-Teller ion, should not contribute to XLD signal, its time-evolution during measurement can artificially affect the observed dichroism. In order to diminish this effect, beam flux in the sample was reduced and several spectra in alternate sequences ($E_\parallel - E_\perp - E_\perp - E_\parallel$) were acquired in order to reduce time-dependent effects.

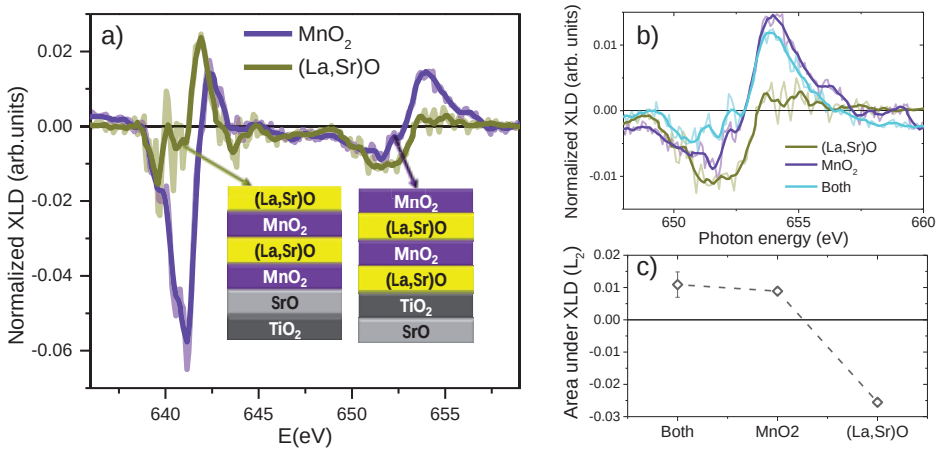

Figure 4.11: a) XLD spectra of (La,Sr)O and MnO_2-terminated LSMO films. b) Zoom of the XLD spectra in the L_2 region, including XLD on LSMO deposited on as-received substrate (cyan curve). c) Integrated area under XLD in the L_2 region for samples grown on as-received, TiO_2 and SrO terminated substrates.

In fig. 4.11(a) we show the XLD spectra of single terminated 4*uc* LSMO films. Although quality of data at L_3 edge does not allow for full range area integration to obtain the corresponding orbital polarization, a close look at L_2 edge (fig. 4.11(b)) shows that the LSMO-MnO_2 terminated film displays a somewhat more positive dichroism than its LSMO-$(La, Sr)O$ terminated counterpart, and comparable to that of 4*uc* LSMO with both terminations present. Integration of the XLD data in the L_2 energy region shows

that the corresponding XLD area value for $(La, Sr)O$ terminated LSMO sample is significantly more negative than MnO_2 and double-terminated LSMO, thus indicating a diminished $3z^2 - r^2$ occupancy, according to expectations.

4.3.3 *Orientational dependence of surface orbital localization*

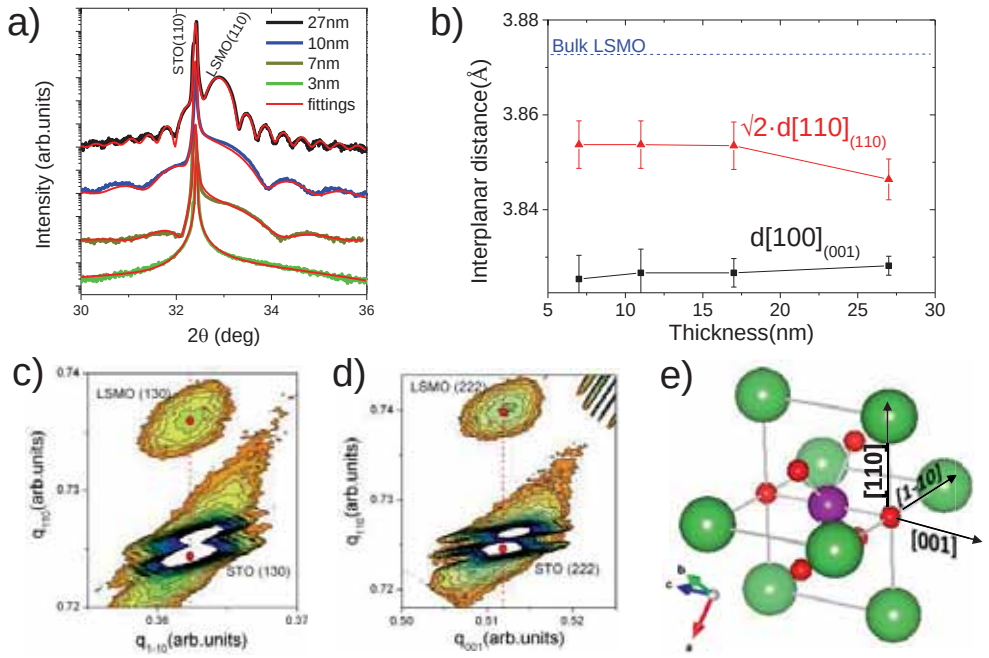

Figure 4.12: a) $\theta - 2\theta$ scans for the (110) reflection of LSMO films on (110) oriented STO substrates; red lines correspond to pattern fittings. b) Out-of-plane interplanar distances obtained from the XRD simulations for (110) films (red triangles) as compared to interplanar distances obtained for (001) films. c) Q-plot around the (130) reflection for 27nm film. d) Q-plot around the (222) reflection for 27nm film. e) Structure representation for (110) films, indicating in-plane ([001] and [1$\bar{1}$0]) and out-of-plane ([110]) crystallographic directions.

It follows from the arguments presented above, that the electron occupancy of out-of-plane orbitals should be favored irrespectively of the particular crystallographic plane of LSMO considered. This has been assessed by comparing the LSMO films of similar thickness grown simultaneously on (001) and (110)STO substrates. (110) films show slightly different structural characteristics to their (001) counterparts: in fig. 4.12(a), the $\theta - 2\theta$ patterns of several (110) LSMO films with thickness in the range $3 - 27nm$ is shown. Simulated patterns allowed for the extraction of out-of-plane parameters, as presented in fig. 4.12(b), resulting in slightly larger lattice parameters (after rescaling with factor $\sqrt{2}$) than (001) films. In plane parameters for the two orthogonal dissimilar in-plane directions were assessed by means of RSM exploring the (130) and (222) pseudocubic LSMO and STO reflections in order to have access to the [1$\bar{1}$0] and [001] in-plane directions, respectively. As evidenced in figs.4.12(c,d), both in-plane directions are coincident with those of the substrate, indicating a fully strained state of the samples, at least until the explored thickness of 27nm.

Thus, the strain response of the unit cell is different for samples with dissimilar orientations, being lower the out-of-plane contraction for (110) samples, resulting in a larger cell volume.

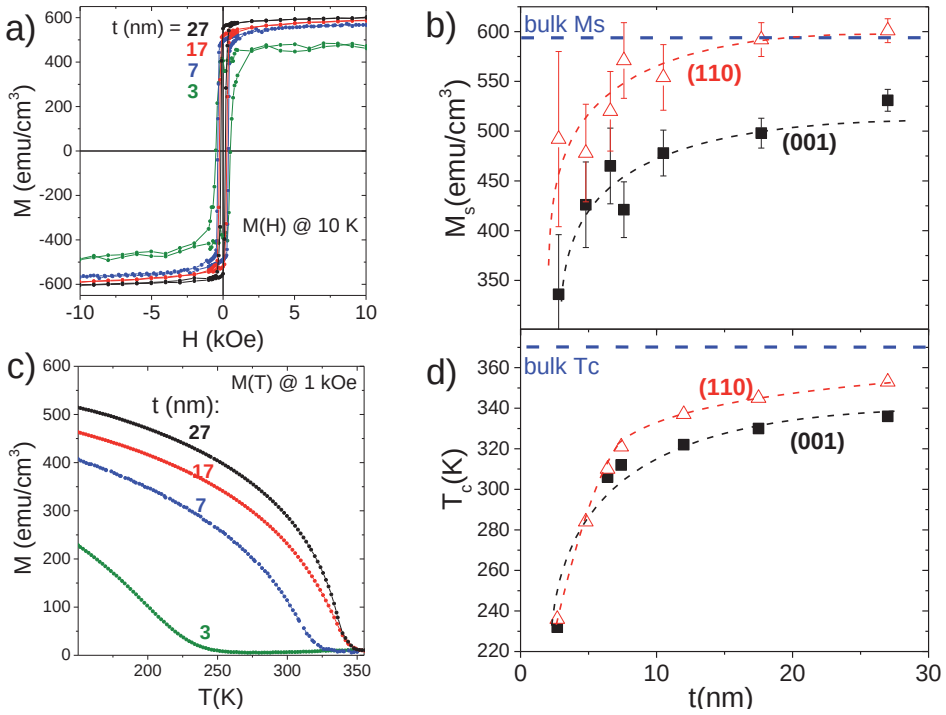

Figure 4.13: a) Magnetic field dependence of sample magnetization for LSMO(110) films. b) Saturation magnetization values as a function of thickness for (110) LSMO films (red triangles) as compared to (001) counterparts (black squares). c) Temperature dependence of LSMO(110) samples magnetization. d) Curie temperature as a function of thickness for (110) LSMO films (red triangles) as compared to (001) counterparts (black squares)

Notable differences are found in the magnetic response of both series of samples. In fig.4.13(a,c), some examples of M(H) and M(T) curves -volume normalized- are shown for (110) LSMO samples with different thicknesses. Although a depletion in both M_S and T_C is found analogously to (001) samples, when comparing M_S values obtained for both series of samples (fig.4.13(b)), as well as T_C values (fig.4.13(d)), we find that (110) samples show superior magnetic properties, reaching bulk LSMO values for lower sample thickness.

Before examining the XLD spectra of (110)LSMO samples, a point has to be clarified in the orbital geometry of (110) oriented samples: as pictured in fig.4.12(e), in (110) samples, *c*-axis ([001] direction) is along one of the in-plane directions, while [100] and [010] directions (in-plane *a* and *b* axis for (001) samples) are pointing 45 degrees out of the surface plane, defined by [001] and $[1\bar{1}0]$ crystallographic directions. In consequence, the disposition of e_g orbitals is different from that of (001) samples. In fact, for (110) orientation, $3z^2 - r^2$ orbital are oriented along one of the in-plane directions ([001]) and $x^2 - y^2$ orbitals are pointing out-of-plane, with their lobes at 45 degrees from the surface plane. A sketch of the orbitals orientation, and the corresponding interaction with linearly polarized light is shown in fig.4.14(a-inset).

In fig.4.14 we include data corresponding to films of 70*uc* and 8*uc* grown on (110)STO substrates. In the XLD signal (fig.4.14(b)), defined as $I_{\parallel} - I_{\perp}$, as conventionally, it can

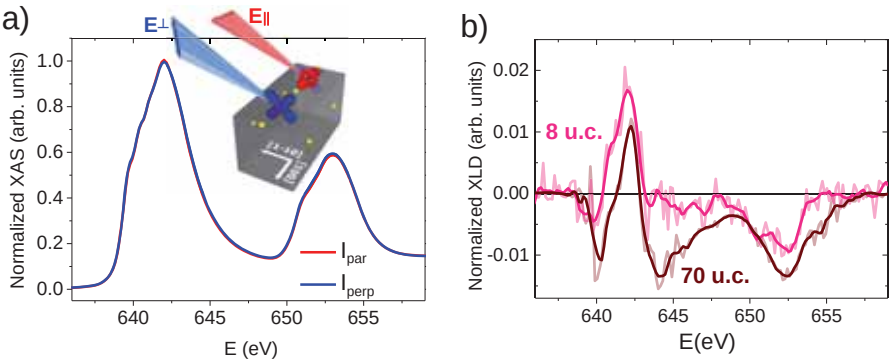

Figure 4.14: Polarized spectra of LSMO(110) (70*uc*) film with the measurement sketch indicating the orientation of e_g orbitals respect to linear polarizations of incident beam. b) XLD spectra of 8*uc* and 70*uc* (110) LSMO films.

be observed that the overall XLD is mostly negative, implying that the out-of-plane absorption $I_\perp$ is larger than the in-plane $I_\parallel$. Importantly, the amplitude of XLD signal is reduced when reducing film thickness thus indicating a gradual enhancement of the out-of-plane contribution when the surface contribution is larger. A comparable XLD signal was obtained when measured in normal incidence geometry, where the cross section for each of the light polarizations should be resembling.

Recalling that in this geometry, $E_\perp$ explores the $x^2 - y^2$ orbitals and $E_\parallel$ explores the $3z^2 - r^2$ orbitals, we now redefine the holes ratio X to be consistent with previous results, where it was defined as the ratio between out-of-plane oriented holes and in-plane oriented holes. In order to maintain this definition, we now calculate X for (110) films as:

$$X^{110} = \frac{h(x^2 - y^2)}{h(3z^2 - r^2)} = \frac{4\int_{L3,2} I_\perp(E)dE - \int_{L3,2} I_\parallel(E)dE}{3\int_{L3,2} I_\parallel(E)dE}$$

The calculated holes ratio values obtained from the integration of the area under the XLD/XAS spectra are shown in fig.4.15, together with the fitted curve to eq.4.5. A strain-induced preferential occupancy of $3z^2 - r^2$ orbitals is derived from these values, as well as a prominent surface-induced $x^2 - y^2$ occupancy more relevant in the thinnest films. These data thus confirm that also for (110) LSMO films, the out-of-plane orbitals determine the electron orbital occupation at the surface.

From the results of the fitting to eq.4.1, we derive the bulk and surface polarization values (assuming $n_{e_g} = 1$). The results are outlined in table 4.2 together with the (001) oriented films values. It is remarkable that (110) films on STO show lower orbital polarization values than the (001) analogues, both for surface and bulk. This lower prominence to show orbital polarization, both by strain effects or due to surface localization, could be at the origin of the enhanced magnetic properties observed in (110) oriented LSMO films.

4.4 SUMMARY

In this chapter we have provided experimental evidence that the symmetry breaking at the free surface of manganite thin films promotes a lifting of the degeneracy of the $3d - e_g$ electronic states of the transition metal and produces an enhanced electron occupancy of the out-of-plane oriented orbitals, irrespective of their symmetry ($3z^2 - r^2$ or $x^2 - y^2$). The resulting orbital filling can be modulated through strain, to the point that the e_g-

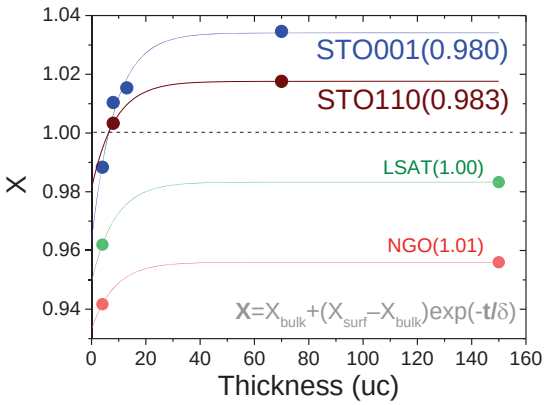

Figure 4.15: Holes ratio thickness dependence of LSMO films grown on STO(110), as compared to (001) films grown on STO, LSAT and NGO

substrate	c/a	Pbulk(%)	Psurf(%)
STO(001)	0.980	1.7	-1.9
STO(110)	0.983	0.87	-1.0
LSAT	1.00	-0.84	-2.6
NGO	1.008	-2.3	-4.5

Table 4.2: Summary of bulk and surface orbital polarizations obtained for the different studied substrates, as indicated.

band structure can be reversed for large enough tensile stress, populating preferentially the in-plane orbital states. The data depicted here show that the ultimate orbital filling at the free surface of $La_{2/3}Sr_{1/3}MnO_3$ depends significantly on the terminating atomic planes, i.e., $(La, Sr)O$ or MnO_2 and on the crystallographic orientation of the films.

5

CHARGE AND ORBITAL RECONSTRUCTIONS AT MANGANITE INTERFACES

At interfaces the electronic and chemical interactions of manganite layers with adjacent materials or with the atmosphere can locally alter the orbital hierarchy promoting reconstructions or charge deviations that will also profoundly affect the properties of the films at interfaces. Element selective spectroscopies provide a idoneous tool to explore the influence of the local environment in the electronic and magnetic configuration of transition metal ions.

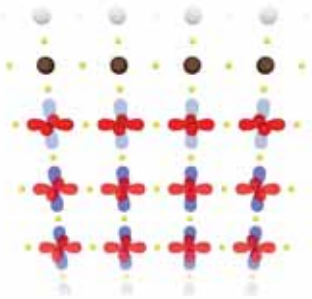

5.1 INTRODUCTION

Manganites, like most perovskite oxides, show a high surface reactivity, making them profitable as catalyst materials. However, this high reactivity can, in some cases lead to unexpected stoichiometric deviations or reduction/oxidation processes that can produce strong modifications in the functional properties. In order to study the effect of surface exposure to atmosphere, we compare in sec.5.2 the XAS spectra of "bare" LSMO films with that of "capped" films, where the manganite surface is protected and thus never exposed to atmosphere. We use different oxides structurally equivalent to LSMO as capping layer materials, showing that, not only atmosphere can produce a modification in the oxidation state of the surface Mn, but also the oxide cappings can promote redox reactions at the interface with the manganite, thus modifying the electronic distribution among the mixed-valence Mn ions, promoting or avoiding electron localization.

While at manganite free surfaces there exists an unavoidable breaking of symmetry that imposes a preferential orbital order, interfaces with other oxides are expected to remove or modify this orbital order, due to the different electron interactions between manganite orbitals at terminating layers and those of the capping layers. In section 5.3 we will study this orbital modifications at the interface between manganite thin films and different oxide capping layers, which will allow us to draw a simple picture for the orbital control phenomena at manganite interfaces, that could be extended to other transition metal oxides.

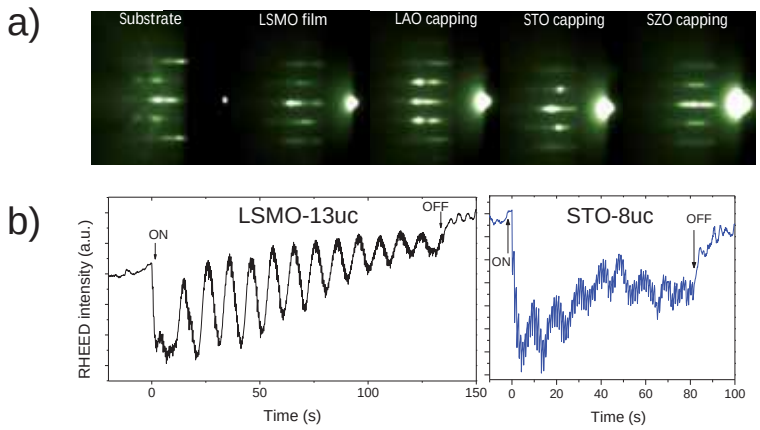

Figure 5.1: a) RHEED pattern of TiO_2-terminated STO substrate, LSMO film deposited on STO substrate and LAO, STO and SZO capping layers deposited ot top of LSMO films. b) Left panel: Intensity oscillations of the specular spot during growth of LSMO layer; Right: Intensity oscillations during growth of 8*uc* STO capping layer. The arrows indicate the start and the end of the deposition.

5.2 REDOX REACTIONS AT OXIDE SURFACES/INTERFACES

Whenever two oxides are grown together in a heterostructure, interfacial effects take an important role, locally modifying the properties of the materials. These interfacial effects manifest due to electrostatic phenomena, structural modifications or species diffusion between the two materials. In epitaxial oxide thin films, phenomena like the polar catastrophe or the movement of oxygen vacancies are determinant for the interfacial properties. Furthermore, at surfaces, the interaction of atmosphere atomic species can also produce large modifications in the oxide films. In this section we study the behaviour of interfacial layers in LSMO thin films, in contact with different environments (either with vacuum/atmosphere or with other oxides grown on top). Close examination of features in XAS spectra give us clues on the processes leading to redox reactions due to interaction of manganite surface with the adjacent environment.

5.2.1 *Samples preparation*

In order to examine interfacial effects in manganite films, three series of LSMO samples with controlled termination were grown by PLD-RHEED assisted deposition, on (001)STO-TiO_2 terminated substrates. RHEED system allowed to monitor the growth of the films and to ascertain a layer-by-layer growth and control the atomic termination of LSMO layer. On top of LSMO layer, an oxide capping layer was grown in the same deposition process, with similar conditions (725^oC and 0.1*mbar* oxygen pressure), which assures an epitaxial growth on top of LSMO.

All LSMO layers were grown with the same thickness (13 unit cells) – controlled by RHEED monitored growth –ensuring that atomic LSMO termination was MnO_2 in all cases. With this low thickness (around 5*nm*) we also guarantee that films grow epitaxially and with a tensile strain state as expected by the mismatch with STO substrate (+0.8%). To disentangle the influence of bare surface and oxide capping layer on the LSMO layer, we grew three set of samples with epitaxial capping layers on top of LSMO

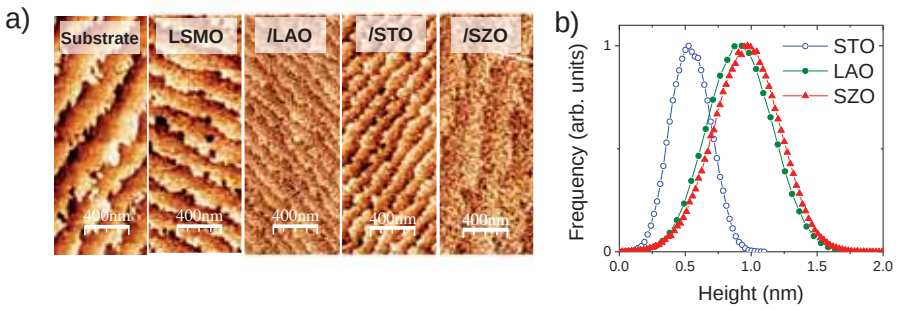

Figure 5.2: a) AFM images of STO substrate, bare LSMO sample and films capped with 8*uc* of LAO, STO and SZO. b) Height distribution for 8*uc* LAO, STO and SZO capped samples.

with varying thickness: 1, 4 and 8*uc*, each set with a different capping material (LAO, STO and SZO). In addition one LSMO bare film (with no capping material) was grown as a reference.

The RHEED pattern of TiO_2 terminated STO substrate is shown in fig.5.1(a). As indicated by the monitored oscillations of the intensity of the specular spot during deposition (fig.5.1(b-left panel)), LSMO grows layer-by-layer on STO substrate, and the Bragg spots observed in the RHEED pattern indicate a flat LSMO surface (fig.5.1(a)). Similar patterns are observed for capped films, however, the observed elongation of diffracted spots for LAO and SZO capped samples denotes an increased roughening at the surface (fig.5.1(a)). The layer-by-layer growth of the capping layers could only be observed for STO, which shows clear intensity oscillations during the growth process, as displayed in fig.5.1(b-right panel) for 8*uc* capping layer. In the case of SZO and LAO cappings, however, no clear oscillations were observed and the number of pulses needed to obtain the desired capping thickness was set according to preliminar growth rate calibration.

The AFM image of TiO_2 substrate is shown in fig.5.2(a). The steps and terrace morphology displayed by the substrate is reproduced in the LSMO film grown on top (also shown in the figure) and is maintained for the 8*uc*-LAO, STO and SZO capped samples. All films show a flat surface with low roughness values (RMS lower than 2.5$\AA$ in all cases). However, a full surface coverage may not occur for such ultrathin capping layers. In the graph of fig.5.2(b), the height distribution in the AFM images is shown for 8*uc* capped films. As it can be derived from these plots, the presence of holes larger than $1uc$ ($\sim 0.4nm$) is possible for all cappings and more probable for SZO and LAO cappings, where height distribution extends to depths as large as $1.5nm$ ($\sim 2.5uc$). Nevertheless, capping layers with 4 and 8*uc* thickness are expected to fully cover the LSMO film surface.

5.2.2 *Probing Mn valence state by XAS*

In order to explore the manganese valence state of the different samples, Mn-$L_{2,3}$ absorption edges were measured. The extreme surface sensitivity of the TEY measurements (probing depth lower than $5nm$) guarantees that we are mostly sensitive to LSMO top interface, in contact with either atmosphere or capping layer. Although the intensity of the raw signal measured profoundly depends on the capping material and thickness, it must be noted that by proper normalization, no variation in the probing depth of

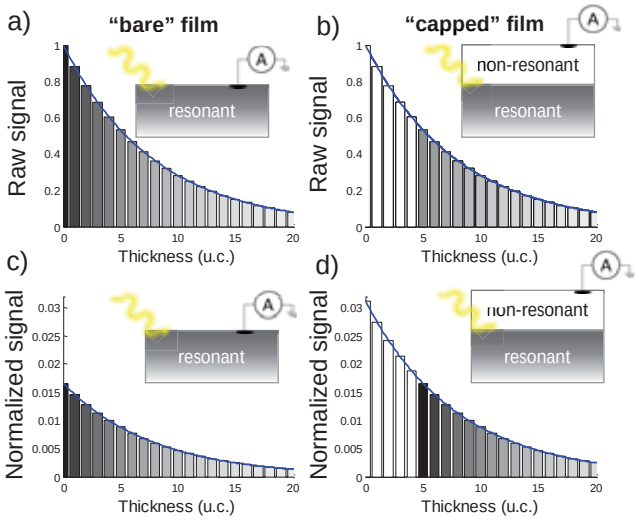

Figure 5.3: Representation of absorption intensity from stacking layers in a film: a) raw signal for a bare film; b) raw signal from capped film; c) signal normalized by the total intensity for a bare film; d) normalized signal for a capped film.

the signal is expected for the different capping thicknesses. To visualize this statement more clearly, we plotted in fig.5.3(a) the independent resonant absorption intensity of each layer in a bare film. The raw signal measured with TEY mode (which is normalized by the incident beam intensity) decays exponentially with the sample depth and the total signal measured will be the sum over all layers, having a more relevant contribution the superficial layers. When capping the film with another layer not contributing to the resonant absorption, the total measured raw signal will decay correspondingly due to the screening of measured current produced by the capping (fig.5.3(b)). This screening may depend on the capping thickness as well as on its conduction properties. Thus, a lower raw signal will be measured for capped films with a signal reduction not intrinsic to the film properties. However, when normalizing the spectra (figs. 5.3(c-d)) by the total measured intensity, both signals (from bare and from capped sample) can be compared, as their decay will be analogous, that is the absorption intensity for each layer shall be identical so that the depth information is equivalent in both cases (bare and capped sample).

In fig.5.4(a-c), the spectra for bare LSMO sample (no capping – LSMO film exposed to atmosphere) and films with 1, 4 and 8*uc* epitaxial capping are shown. For the normalization of the spectra, a background accounting for the two edge jumps was subtracted, and the resultant spectra were normalized to a constant area under the curves. Relevant changes in absorption spectra are observed when capping layers are grown on top of LSMO films. These changes are particularly evident in L_3 edge ($640 - 645eV$), zoomed in fig.5.4(d), where 8*uc* capped films spectra (colored curves) are compared with bare LSMO spectra (grey area). In this graph, we can clearly observe the modifications produced by the capping layers in the manganite interfacial layers. As the spectra are normalized by the area under the curves, which is proportional to the number of holes in the system, the local intensity variations are referred to the total number of accessible states. For the case of LAO and SZO capped sample (fig.5.4(d)), L_3 edge shows a clear shift towards higher energies respect to bare LSMO sample. At the same time, a clear reduction of the absorption intensity is observed at energies lower than the maximum absorption. However, while in the case of LAO capping (green curve), an increase of the

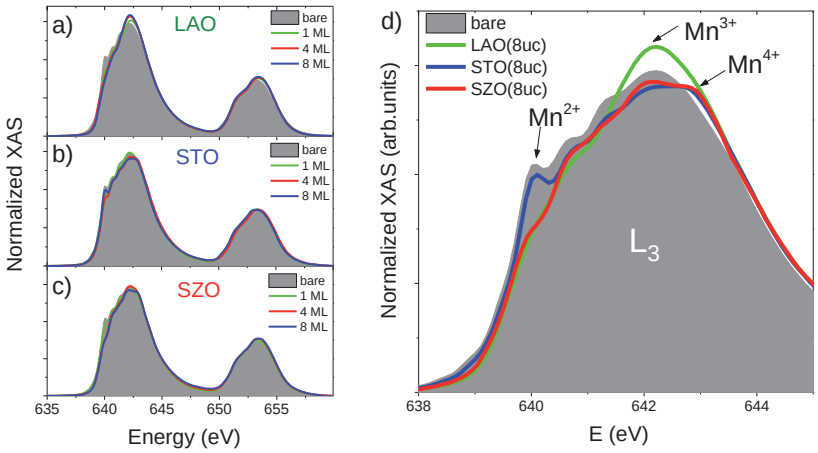

Figure 5.4: XAS spectra of bare LSMO sample (grey area) and LAO (a), STO (b) and SZO (c) capped samples with different capping thickness, as indicated. Zoom of L_3 region for bare and $8uc$ capped samples is shown in (d), where the main contributions of Mn^{n+} independent spectra are indicated

intensity at the maxima at $642eV$ is present, as well as slight increase in the high energy part, in the case of SZO capped layers (red curve), intensity at maximum is reduced and a shoulder at higher energies appears. For STO capping (blue curve), although not so manifest as for LAO and SZO cases, a reduction of absorption intensity is also observed at energies lower than the maximum, but no clear energy shift is present. Analogously to SZO, the intensity at the maximum of L_3 is reduced, and a shoulder appears at higher energies.

The spectral features of XAS can be interpreted in terms of different oxidation states contributing to the observed intensity or related to different crystal field atomic environments that modify the ground state configuration and therefore the transition probability at each energy. While the former consideration (different oxidation states) will be treated here, the later (crystal field modifications) will be studied in the next section.

In general, the high energy sensitivity of XAS technique allows to discern the contributions of Mn ions with different valences to the spectra: while main contribution at maxima of L_3 is due to Mn^{3+}, an increase of intensity at lower energies is often attributed to the presence of Mn^{2+} [80, 81, 82, 83, 84], and Mn^{4+} displays a maximum displaced to higher energies respect to Mn^{3+}[82, 85, 86, 87].

A better way to visualize the differences in XAS spectra for the different samples is shown in fig.5.5. The difference between spectra of capped samples and reference bare film has been represented for epitaxial LAO (fig.5.5(a-top)), STO (5.5(b-top)) and SZO (5.5(c-top)) -capped films. These difference spectra have been simulated with CTM4XAS program[1], considering the contributions from Mn^{2+}, Mn^{3+} and Mn^{4+} to the XAS spectra and summing their spectra weighted by a variable parameter, adjusted to obtain the best fit to experimental data.

The total spectra obtained by $I = W_1 \cdot I(Mn^{2+}) + W_2 \cdot I(Mn^{3+}) + W_3 \cdot I(Mn^{4+})$, where $-1 < W_n < 1$ is shown in the bottom of fig.5.5(a-c) for the simulation of $8uc$ capped films difference spectra, together with individual Mn^{n+} spectra. A considerable agree-

1 XAS spectra of Mn^{2+}, Mn^{3+} and Mn^{4+} in octahedral coordination were simulated for crystal fields $10Dq = 0.5, 1.6$ and $2.0eV$, respectively

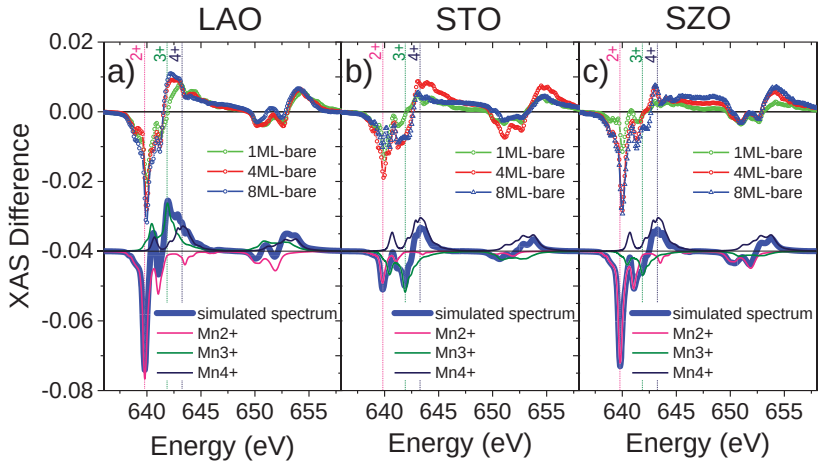

Figure 5.5: Spectra difference for LAO (a), STO (b) and SZO(c) capped films respect to bare film: experimental difference spectra are shown in the top part for 1, 4 and 8 uc capped samples and simulated difference spectra are shown in the bottom part for 8 uc sample, together with independent Mn^{n+} spectra multiplied by the corresponding weight parameters W_n

ment with experimental data was obtained[2], leading to the weight parameters represented in fig.5.6, as a function of capping layer thickness. Although a reliable quantitative information cannot be obtained from these values, they show the different tendency of Mn valence as a function of capping material. It can be appreciated in fig.5.6(a) that all three cappings produce a reduction of the Mn^{2+} content, being more relevant for LAO and SZO cappings, and increasing with capping thickness. Although not so evident from raw data, the simulations show that all cappings produce also an oxidation of Mn, leading to an increase of Mn^{4+} (fig.5.6(c)), which barely changes with capping thickness. Furthermore, a significant difference of the effect of the three capping materials is observed in fig.5.6(b), where an opposite trend of Mn^{3+} content is observed for LAO capped layers respect to STO and SZO: while LAO capping produces an increase of Mn^{3+}, STO and SZO tend to diminish the Mn^{3+} content. Both set of samples show a saturating behaviour in the Mn^{3+} contribution to XAS spectra as a function of capping thickness.

5.2.3 *Discussion on charge transfer effects*

The clear modifications of Mn valence state observed in our measurements show the large sensitivity of manganite surfaces to the atomic surrounding, either during growth process or a posteriori. The first consideration to be taken into account is the interaction between LSMO surface and the atmosphere. It has been reported that manganite surfaces, in contact with atmosphere, show a prominent Mn^{2+} peak in the XAS spectra. This observation has been interpreted as a reduction of $Mn^{3+/4+}$ ions due to interaction with atmospheric CO at the surface [88], that acts as a reducing agent contributing electrons to the system or removing oxygen. While the oxygen removal was shown to increase the Mn^{2+} content at the manganite surface [80], in LSMO films not exposed

2 Non-zero intensity in experimental difference spectra in the region between edges- 646-649 eV- can be attributed to non-perfect background subtraction for all samples, due to considerable overlapping between L_3 and L_2 edges.

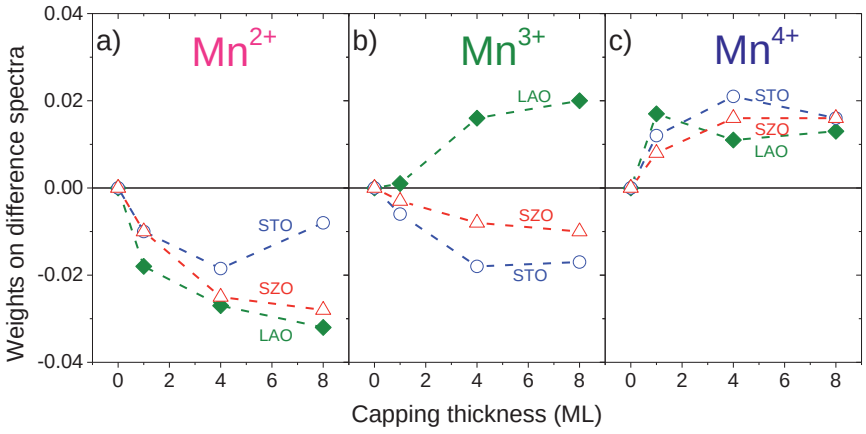

Figure 5.6: Weight parameters for Mn^{2+}, Mn^{3+} and Mn^{4+} independent spectra obtained from best fittings of difference spectra as a function of thickness for LAO, STO and SZO capped films.

to atmosphere, the creation of oxygen vacancies was not accompanied by the formation of Mn^{2+}[89]. A different mechanism for the formation of Mn^{2+} was proposed in ref.[90], where a charge disproportionation reaction $Mn^{3+} + Mn^{3+} \rightarrow Mn^{2+} + Mn^{4+}$ is suggested to take place in $La_{1-x}Ca_xMnO_{3-\delta}$ polycrystals. While the stabilization of $Mn^{2+} + Mn^{4+}$ complex may be limited in the bulk by the large cation size of Mn^{2+} (30% larger than Mn^{3+} [90]), oxygen displacements at the surface can favour this mechanism [91].

From our data analysis we can clearly sustain that bare LSMO films show the largest Mn^{2+} content, indicating a reduction caused by exposure of the films to atmosphere. Although we cannot discern the mechanism behind this Mn reduction, it seems clear that capping layers protect the sample surface from exposure to atmosphere, thus decreasing the Mn^{2+} content at the surface. The evolution of Mn^{2+} content with capping thickness can be associated to the increasing surface coverage with increasing amount of capping material, leading to better protection from atmosphere and thus avoiding the formation of Mn^{2+}.

It should not be rejected also the considerable beam damage produced during measurements under synchrotron radiation, that promotes the Mn reduction and consequent appearance of Mn^{2+} peaks in the spectra, during measurement. This effect was identified and diminished during our measurements, but a minor contribution can also occur due to unavoidable exposure to the beam. Further discussion on this phenomenon can be found in appendix D.

At this point it is important to notice the dissimilar behaviour between the different LSMO/capping interfaces. While the results for LAO capped samples can be explained as a result of surface protection from atmosphere, decreasing the Mn^{2+} content and, consequently, restoring the $Mn^{3+/4+}$ valence in the Mn cations, in the case of STO and SZO capped samples, further phenomena is involved, as an abnormal decrease of Mn^{3+}/Mn^{4+} ratio is observed, evidencing an oxidation process that leads to a hole-doping at the interface.

This oxidation process can be explained by different scenarios involving either charge transfer influenced by electrostatic phenomena at the interface (scenario 1), oxygen ex-

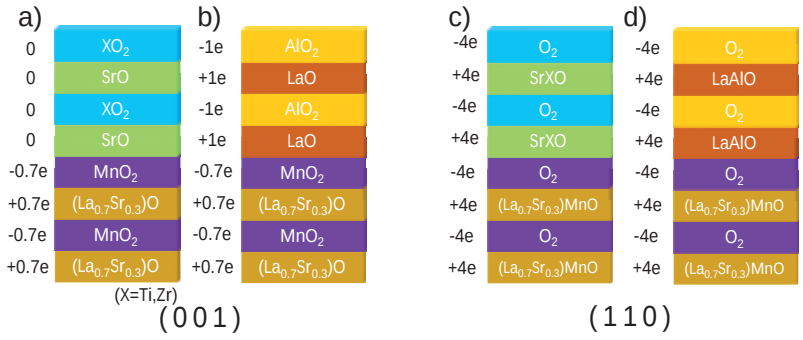

Figure 5.7: Representation of stacking planes and corresponding electrostatic charge for (001) LSMO/$SrXO_3(X = Ti, Zr)$ (a), (001) LSMO/LAO (b), (110) LSMO/$SrXO_3$ (c), and (110) LSMO/LAO (d) heterostructures.

change between manganite and capping layers (scenario 2) or considerations on the $Mn(3d) - O(2p)$ orbital hybridization in a not fully ionic picture(scenario 3):

1. In terms of electrostatic equilibrium at $LSMO/SrXO_3$ $(X = Ti, Zr)$ interface, LSMO is formed by stacking planes with alternate charge $(+\frac{2}{3}e/-\frac{2}{3}e)$, while in $SrXO_3$ all planes are neutral (see fig. 5.7(a)) , thus terminating the LSMO layer on an atomic plane exhibits a polar discontinuity, and a electronic reconstruction is expected at the interface, similarly to LAO/STO interfaces [92]. In our case, being $(La, Sr)O/MnO_2 \parallel SrO/XO_2$ the stacking sequence in the samples, it would be required injecting $1/3$ hole per unit cell at the interface, to compensate the interface charge. This hole doping is possible in the interfacial LSMO layers, thus promoting the oxidation of Mn [93, 94], and the consequent decrease of Mn^{3+}/Mn^{4+} ratio, which is consistent with our observations. Following this same reasoning for the $LSMO/LAO$ interface, LAO capping layer atomic planes are charged $(\pm 1e)$ (fig. 5.7(b)) and the electrostatic equilibrium would impose extra electrons at the MnO_2/LaO interface, so we would expect an electron doping at the interface, thus increasing the Mn^{3+}/Mn^{4+} ratio. However, for the case of LAO capping, data cannot confirm this scenario.

2. It is known that STO can act as an oxygen getter layer [95, 96] and also as an oxygen supplier. As shown in ref. [97], STO films/substrates can either give/take away oxygen during film growth due to large oxygen diffusion through STO. On the contrary, LAO was shown to have a larger tendency to retain oxygen. These results may indicate that STO capping layers, as well as SZO capping, can modify oxygen content in LSMO during growth process, while LAO capping does not interact with LSMO. Regarding our observation of decreasing Mn^{3+}/Mn^{4+} ratio in the LSMO/STO and LSMO/SZO interfaces, this would be in accordance with an increase of oxygen content in the LSMO layer.

3. The different atomic environment of Mn ions at the interface, respect to the bulk, and respect to the surface atoms, can lead to modified $Mn - O$ interactions at the interfacial layers. More specifically, the $Mn(3d) - O(2p)$ orbital hybridization at the LSMO terminating layer with the interfacial capping layer can depend on the local crystal field modifications introduced by the capping layer. A change in the hybridization strength or covalency can cause a change in the observed Mn

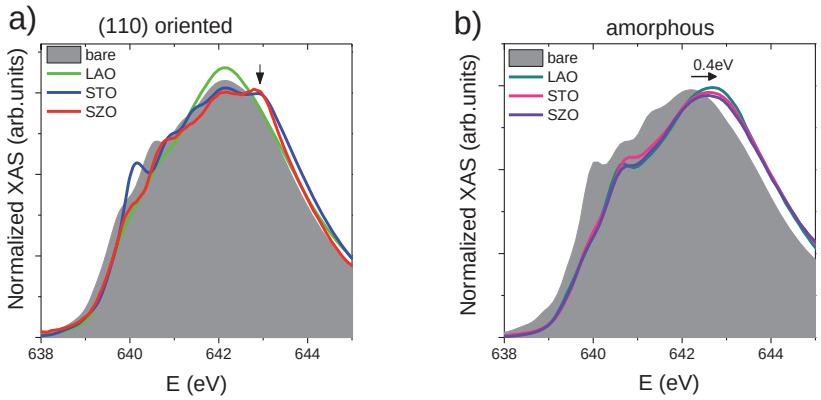

Figure 5.8: XAS spectra at the L_3 region obtained for bare and LAO, STO and SZO capped (110) LSMO samples (a) and for (001)LSMO samples capped with amorphous cappings (b).

valence due to the redistribution of electrons in the covalent $Mn-O$ bonds [98], that may depend on the capping layer.

In order to inspect the validity of scenario 1, we measured the XAS spectra of samples with same stacking and thickness (LSMO-13uc/capping-8uc), but grown on a STO(110) substrate[3]. For this orientation, the charge discontinuity at the interface disappears, as in all cases the atomic planes for LSMO and capping layers are charged equally ($\pm 4e$) (fig. 5.7(c,d)) and therefore, a polar catastrophe scenario can be excluded. Nevertheless, the features observed in the L_3 edge of the area-normalized XAS spectra for these samples show analogous features to that of (001) oriented samples (see fig.5.8(a)), that is, an increase of the intensity at the maximum for LAO-capped films, respect to the bare film, and increase of intensity at the high energy region of L_3 edge for STO and SZO capped films, showing that there exists a similar redox behaviour for Mn ions at LSMO/capping interfaces for both (001) and (110) oriented samples and thus declining the polar catastrophe scenario at these interfaces. On the other hand, no clear evidence of the tendency for Mn^{2+} content at the different samples could be derived from the XAS spectra of (110) films, probably due to the lower initial Mn^{2+} content at the surface of this bare film as compared to the (001) oriented film.

Although scenario 2 is more difficult to prove, a test experiment can be done: on top of LSMO (13uc thick) films grown at the standard conditions specified previously, we deposited capping layers of the same materials (LAO, STO, SZO) at close-to-room temperature. Capping layers were grown with the same number of pulses needed to obtain 8uc cappings at high temperature growth. By growing at low temperatures, the capping structure is expected to be amorphized. In the XAS spectra of amorphous capped films, shown in fig.5.8(b), a clear shift of L edge of about $400meV$ towards higher energies is evidenced in all samples, independently of capping material. This shift indicates an important oxidation process $Mn^{3+} \rightarrow Mn^{4+}$ at the LSMO interface with the capping, showing a spectral shape resembling to MnO_2 [87], thus indicating the formation of a new phase at the interface, probably promoted by the enhanced oxygen diffusion from capping amorphous layers.

Up to now we have considered a rigid ionic picture where the oxidation state is given by the local charge of Mn. However, for TMOs, a large degree of covalency can

3 To assure the same deposition conditions, these films were grown simultaneously to their (001) counterparts

exist, and therefore bonding electrons are shared between $O(2p)$ and $Mn(3d)$ electrons. Within this more complex picture, the observed Mn oxidation states can be altered by the charge regulation in the bonding states [98], that may redistribute the charge either localizing it in the oxygen or in the Mn ion or even transferring to the bonding states through the interface. A modification of the local crystal field in the Mn ion at the interface can readjust the $Mn-O$ hybridization scheme. This is the considered scenario 3, and in order to explore this phenomena, a more extensive study of the orbital configuration at interfaces is needed. We will dedicate the following section to study the electron distribution among $Mn-3d$ orbitals at LSMO/capping interfaces.

5.3 ORBITAL RECONSTRUCTION AT INTERFACES

It was shown in section 4.3 that the natural breaking of symmetry between the epitaxial film and the vacuum produces a special orbital occupancy at the d orbitals of the transition metal, due to the local modification of the crystal field produced by the absence of apical oxygen in the Mn at the terminating layers, resulting in a lowering of the energy of the orbitals oriented in that direction [69], that is, the $3z^2-r^2$ states in (001) films. This occupancy was shown to be partially modulated by controlling the manganite termination, thus either enhancing or removing the surface effect. One could think then, that capping the manganite films with a structurally similar oxide layer could lead to a complete removal of the surface effect, thus recovering the bulk orbital occupancy (or, due to the inherent structural distortion imposed by the substrate in thin films, the strain induced orbital occupancy). This is, however, a too simplistic view, as oxide capping layers can also affect the local crystal field by means of modified $Mn-O$ distances or second neighbour interactions ($Mn-O-X$), that can alter the local electric fields acting on the Mn-d orbitals, the Mn local charge, as described in previous section, or the $Mn-O$ hybridization, leading to a redistribution of the charge among the d orbitals.

In this section we will study the orbital polarization of the LSMO (001)-oriented films ($13uc$) capped with LAO, STO and SZO epitaxial layers ($1-8uc$), discussed in the previous section. Although the redox processes observed previously may indirectly affect the orbital occupation, the XLD signal is not expected to be directly influenced by the presence of Mn^{4+} or Mn^{2+} ions, as only Mn^{3+} ions have partially occupied e_g states and they will be the only ones contributing to XLD.

5.3.1 *Capping dependent-orbital configuration at interfaces*

The x-ray absorption intensity is represented in figs.5.9(a-c) for the LSMO films capped with $8uc$ of LAO, STO and SZO, measured at grazing incidence configuration with both linear polarizations ($E_{\parallel}$-red and $E_{\perp}$-blue). The XLD signal, calculated as $I_{\parallel}-I_{\perp}$ and normalized as explained in sec. 4.2, is shown in figs.5.9(d-f) for $0uc$ capping (bare sample), as well as 4 and $8uc$ capping thicknesses. Samples with $1uc$ capping were also measured but they did not show relevant differences in the XLD signal respect to the bare samples, indicating that one monolayer is not sufficient to produce significant changes in the dichroic signal of LSMO films. It can be thought that the deficient surface coverage by the capping layer with $1uc$ (see fig.5.2) is not enough to override the surface contribution to XLD.

Spectra of bare LSMO film ($13uc$) shows the same behaviour as those studied earlier in this chapter, with a predominant negative contribution, indicating an average preferential occupation of x^2-y^2 orbitals in the explored depth. This signal is less negative

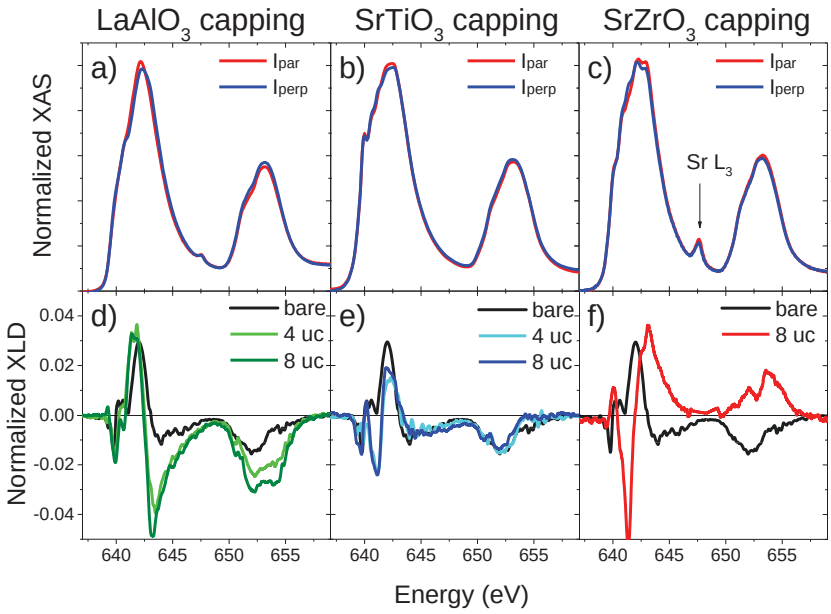

Figure 5.9: Polarized XAS spectra for LAO (a), STO (b) and SZO (c) $8uc$ capped samples. XLD spectra for bare and $4-8uc$ capped samples is shown in (d-f) for the different capping materials, as indicated.

than the XLD proved in thicker films (see section 4.3), accounting for the already well known surface $3z^2-r^2$ contribution to the XLD. For capped films, however, a rather different dichroic signal is observed, that is noted to be dependent on the capping material as well as on the capping thickness.

We firstly note that the XLD signal of LAO capped films show an increase towards a more negative signal (fig.5.9(d)), increasing with growing capping thickness. The increasing negative contribution on the spectra is related to a larger absorption of the out of plane orbitals, that is, larger number of unoccupied states in the $3z^2-r^2$ or, equivalently, larger occupancy of x^2-y^2 states. However, in the case of epitaxial STO capping, shown in fig.5.9(e), no relevant change is observed in the XLD spectra of capped samples, respect to the bare film, indicating that STO does not induce significative changes in the orbital reconfiguration at the surface/interface. Finally, for SZO capped films (fig.5.9(f)) an inversion of the XLD signal respect to bare LSMO is observed, indicating a larger occupancy of $3z^2-r^2$ states at the LSMO/SZO interface.

The holes ratio $X=\frac{h(3z^2-r^2)}{h(x^2-y^2)}$ can be calculated from expression 4.1, resulting in the values plotted in fig.5.10(a), as a function of capping thickness. This graph shows clearly the different behaviours for the three capping materials, however the X values here obtained are averaged over the signal probed depth. Following the conclusions of section 4.3, the XLD signal here measured is expected to have two contributions: a contribution coming from the "bulk" of the film, which is induced by the octahedra distortion due to strain effect, and a surface contribution due to the symmetry breaking described previously. In order to separate both contributions, we can assume that the X values here obtained are resultant of the sum of a surface (interface) contribution from the first manganite layer, and a bulk contribution, weighted by a exponential decay. This decay is determined by a constant δ (probing depth) which we will assume identical to the previous found value (nearly $3nm$), and bulk holes ratio value X_{bulk}, that can also

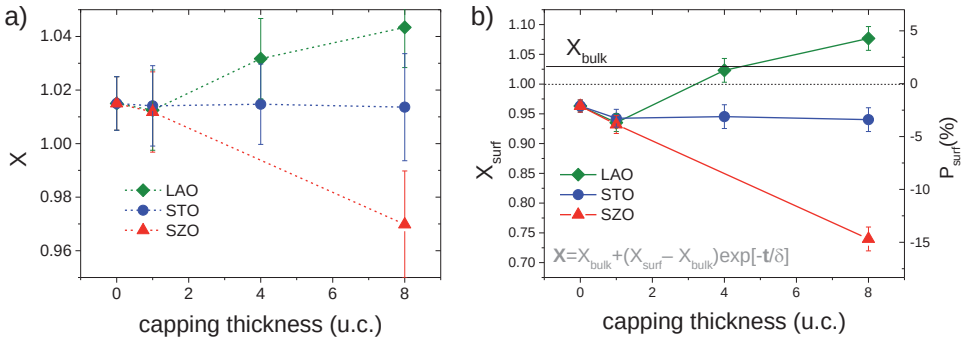

Figure 5.10: a) Holes ratio as a function of thickness for LAO, STO and SZO capped samples. b) Surface holes ratio (left axis) and surface orbital polarization (right axis) as a function of capping thickness.

be taken from the model described in sec.4.3 (for LSMO on STO substrate, $X_{bulk} = 1.03$). Thus, the surface holes ratio X_{surf} can be obtained from eq.4.5.

Using this simple model we obtain the surface hole ratios depicted in fig.5.10(b-left axis). From these values, the surface orbital polarization can be calculated using eq. 4.3. In fig.5.10(b-right axis), the orbital polarization $P = \frac{n_{(x2-y2)} - n_{(3z2-r2)}}{n_{(x2-y2)} + n_{(3z2-r2)}}$, considering $n_{eg} = 1$, is shown. Referring to bare manganite, which has a negative orbital polarization (-2.1%, meaning 0.51 electrons in $3z^2 - r^2$ orbitals at the surface), LAO capped samples tend to revert this surface orbital polarization. In fact, for $4uc$ capping, the polarization turns positive ($+1.3\%$), and even increases for $8uc$ ($+4.2\%$, or 0.48 electrons in $3z^2 - r^2$ orbitals), overriding the bulk strain-induced occupancy.

For STO capped samples, the tendency differs from LAO capping, maintaining or even increasing the $3z^2 - r^2$ occupancy observed at LSMO surface, and at least until $8uc$, no relevant modification of the orbital polarization is observed. A value of -3.5% is achieved for $8uc$ STO capping (0.52 electrons in $3z^2 - r^2$ orbitals). For SZO, on the other hand, a clear increase of the $3z^2 - r^2$ occupancy at the interface is derived from the values of X_{surf} obtained. With $8uc$ capping, a negative polarization of -14.7% is achieved (0.57 electrons in $3z^2 - r^2$).

Up to now, we have considered a single electron in the e_g orbitals of Mn^{3+} ions. However, from the observations of section 5.2, and the consideration of not fully ionic picture in the $Mn - O$ bonding, it is unavoidable to think that a fractional number of electrons may exist, which may depend on the capping layer. The observed modifications in the Mn-XAS for samples with a capping layer can invoke a partial increment or detriment of electrons in the Mn^{3+}-d orbitals, that should be considered for the calculation of the orbital polarization. In the fig.5.11(a), two cases (0.2 electron increment and 0.2 electron detriment) are considered, in comparison with the already treated case of $n_{eg} = 1$, showing the produced modification in the P_{surf} values for both cases (as calculated from expression 4.3), assuming a rigid band model (see fig.5.11(b)). The deviation of these values from the single electron picture can be larger than 10%, however, although orbital polarization can be increased (for $n_{eg} < 1$, lower Fermi level) or decreased (for $n_{eg} > 1$, higher Fermi level), the consideration of distinct number of electrons in the $Mn^{3+} - e_g$ states can never lead to a inversion of the observed orbital polarization, as sketched in fig. 5.11(b) where the displacement of Fermi level is shown to modify the occupation number in each band affecting the magnitude -but not the sign- of the orbital

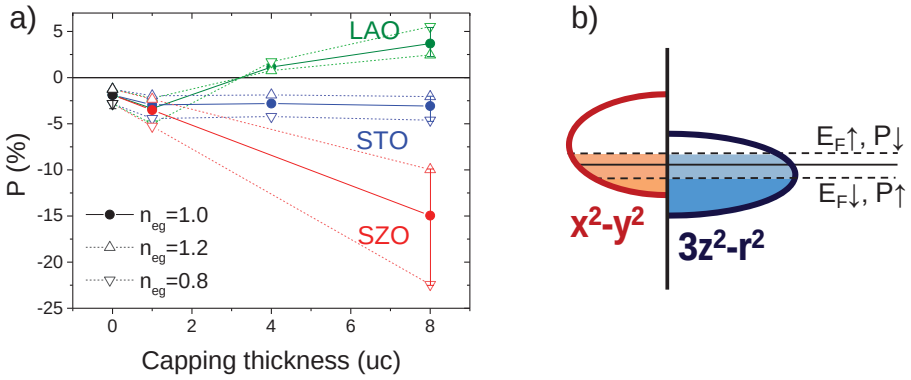

Figure 5.11: a) Surface orbital polarization obtained considering 1 (full circles), 1.2 (triangles pointing up) and 0.8 (triangles pointing down) electrons in e_g levels, as a function of thickness. b) Schematic representation of Fermi level displacement in a rigid band model, for the case of $P < 0$.

polarization P. In other words, although we cannot obtain precise values for surface orbital polarizations without precisely knowing the occupation number n_{eg}, the observed tendencies for the different capped samples are robust against any change of electron occupation.

Direct evidence of orbital reconstruction in LSMO/LAO interface

The surface orbital polarization inversion observed for LSMO/LAO samples suggests a profound orbital reconstruction at these interfaces, inverting the e_g occupation with respect to that of the free surface and, to some extent, recovering the $x^2 - y^2$ preferential occupancy corresponding to the strain-induced effect. The occurrence of this reconstruction was more deeply studied in samples with a reduced LSMO thickness in order to enhance the interface contribution to the XLD respect to the bulk contribution. LSMO samples with a thickness of $4uc$ were grown on STO substrates and capped with epitaxial LAO layers of 2 and $4uc$. A reference bare LSMO film was also grown. The substrates were treated to have a TiO_2 termination, as in the previous experiments, and PLD-RHEED system was used to obtain a controlled growth of $4uc$, with a terminating layer of MnO_2 at the surface/interface. The $Mn - L_{2,3}$ XAS spectra of these samples (fig.5.12(a)), here normalized by the maximum intensity, display analogous trends as the series of samples shown in previous section, with a reduced Mn^{2+} contribution in the capped samples, respect to bare film. More relevant here are the results shown in fig.5.12(b), where the XLD signal at the $Mn - L_{2,3}$ edges (normalized by XAS at $642eV$) is presented for the bare film and the LSMO films capped with 2 and $4uc$ of LAO. Due to the reduced thickness that enhances the contribution of surface effects, here bare LSMO film shows a predominant positive XLD signal (preferential $3z^2 - r^2$ occupancy), as expected from previous measurements. A drastic inversion of the XLD signal is observed in the case of LAO-capped films, turning the XLD signal from positive to negative with the growth of $2uc$ of LAO on top of LSMO. This negative signal is further increased for the film with $4uc$ of LAO capping, demonstrating the clear influence of the LAO capping in the electron distribution at the LSMO/LAO interface.

The values of surface holes ratio (X_{surf}) calculated from eq.4.5 are shown in fig.5.12(c-left axis), together with the corresponding surface orbital polarization calculated for $n_{eg} = 1$ (right axis). These values are consistent with those obtained for thicker LSMO

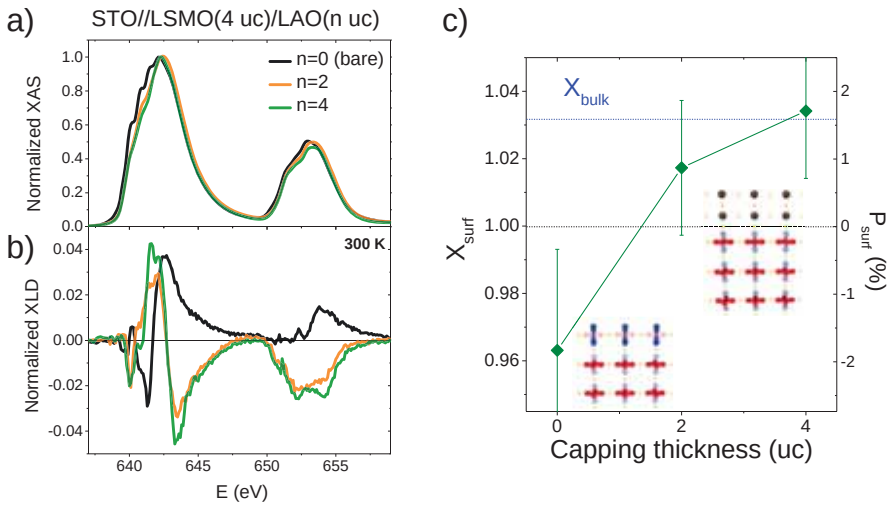

Figure 5.12: XAS (a) and XLD (b) spectra of bare LSMO(4*uc*) samples and capped with 2 and 4 uc of LAO. Surface holes ratio (left axis) and surface orbital polarization (right axis) of these films as a function of capping thickness.

capped films previously, confirming the orbital reconstruction scenario in LAO capped films.

Orbital reconstruction at LSMO/BTO interface

Up to now we have only considered "non-functional" materials as capping layers. While the use of insulating materials for magnetic tunnel junctions is compulsory, recent advances in the fabrication of all-oxide heterostructures have enabled the possibility to provide active functionality to the tunnel barriers, by implementing ferroelectric materials in the heterojunctions, giving rise to ferroelectric tunnel junctions (FTJs) [99]. The basic functioning of these devices would be the capability to change the magnetotransport properties at the electrode interfaces by tuning the polarization state of the ferroelectric tunnel barrier, thus obtaining a resistance switching effect by modulating the extension of the effective tunnel barrier.

Relevant works have been made in the exploration of FTJs properties combining manganite electrodes with $BaTiO_3$ (BTO) ferroelectric barriers [100, 101, 102], demonstrating the promising functionality of these heterostructures. However, in order to fully understand the effect of a ferroelectic tunnel barrier in the interfacial properties of the electrode, preliminar work is needed to explore the interfacial effects in the initial state of the ferroelectric material. Here we explore the effects of BTO capping layers on LSMO interfacial orbital polarization and (in the next section) in the magnetic interfacial properties, as compared to the bare LSMO films.

For that purpose a series of LSMO films was grown at the standard conditions, on $STO(001)$ substrates, with a thickness $\sim 13uc$ and in situ capped with BTO layers (2, 4 and $8uc$), grown at $700°C$ and $0.02mbar$ of oxygen pressure, in order to assure a coherent growth of BTO with preferentially *c*-oriented domains, which favors the out-of-plane orientation of ferroelectric domains [103, 104].

XAS spectra were measured at $Mn-L$ edges with linear polarization in grazing incidence configuration and calculated as $(I_{\parallel}+I_{\perp})/2$ (after proper geometric correction to the $I_{\perp}$ intensity). In fig. 5.13(a), the XAS normalized by the area under the spectra (after background subtraction) is shown at the L_3 region from bare LSMO as well as

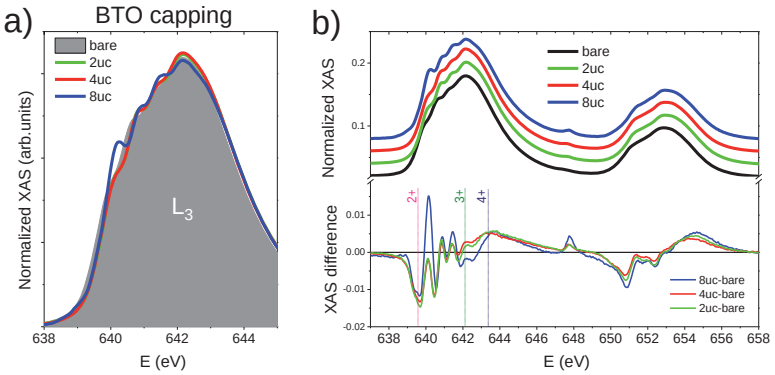

Figure 5.13: a) XAS spectra at the L_3 region for bare (grey area) and n uc BTO-capped LSMO films (color curves). b) Same XAS spectra at the complete energy region measured (top) and spectra difference between n uc BTO-capped and bare LSMO films (bottom). Dashed lines indicate the main Mn^{n+} contributions.

BTO-capped films. While the presence of different features at the low energy region may indicate slight variations in the Mn^{2+} contents, no relevant changes in intensity above $642eV$ are observed, thus ruling out significant modifications in the Mn^{3+}/Mn^{4+} ratio in capped films. An analysis considering spectra difference, as shown in fig. 5.13(b-bottom panel) reveals variations at least 50% lower than in the case of LAO, STO and SZO cappings, difficulting the difference spectra simulation.

Independent spectra do however show significant variations respect to bare sample. In fig. 5.14(a) the XAS spectra taken with both linear polarizations for $8uc$ BTO capped sample shows a notable dichroism, much larger than bare sample, that denotes relevant effects of crystal field distortion at the interface.

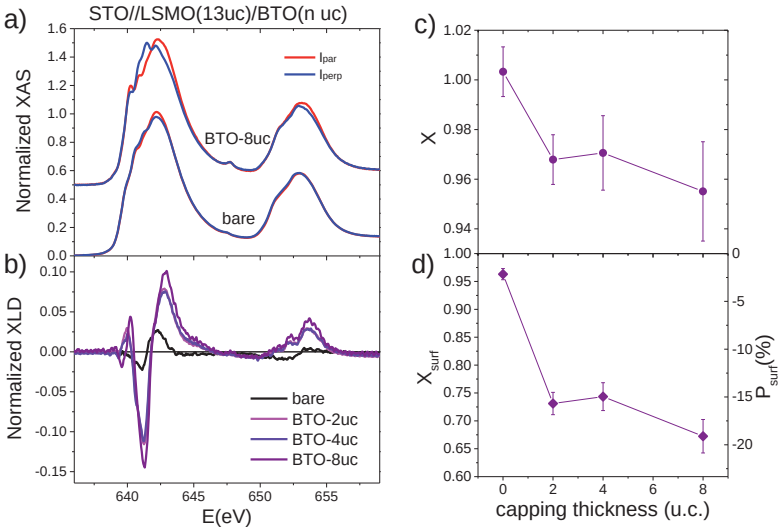

Figure 5.14: a) Linearly polarized spectra for bare (bottom) and $8uc$ BTO-capped (top) LSMO films, taken in grazing incidence configuration. b) XLD spectra of bare and BTO capped films. c) Holes ratio as a function of capping thickness. d) Surface holes ratio (left axis) and corresponding surface orbital polarization (right axis) as a function of capping thickness.

The XLD signal is resembling for all capping thicknesses (fig.5.14(b)) and shows an average positive sign, indicating a preferential occupation of $3z^2 - r^2$ orbitals, as demonstrated by the holes ratio $X = \frac{h_{3z2-r2}}{h_{x2-y2}}$, calculated by sum rules (fig.5.14(c)), which shows a decreasing tendency with increasing BTO capping thickness, thus signaling an increasing number of $x^2 - y^2$ holes, induced by BTO capping. By applying the model to obtain the surface holes ratio, outlined by eq.4.5, we find that -considering $n_{eg} = 1$- BTO capping can produce orbital polarizations as large as -19%, that is an orbital occupancy of 0.6 electrons in the $3z^2 - r^2$ states, which is the largest among all the studied cappings.

5.3.2 *Mechanisms for orbital reconstruction at interfaces*

The data shown here reveals an indisputable orbital reconstruction at the interface between epitaxial LSMO and capping layers, strongly dependent on the capping material and thickness (see fig.5.15). Indeed, capping thickness tends to reinforce the observed reconstruction for each capping material, increasing the magnitude of the orbital polarization with increasing thickness.

The obtained surface orbital polarizations -calculated according to our simple model (eq.4.5), that is, considering a reconstruction only in the interfacial layers- cannot be justified as resultant from a symmetry restoring at the interfaces: far from removing the surface preferential $3z^2 - r^2$ occupancy observed in bare films, capping layers largely distort the orbital anisotropy.

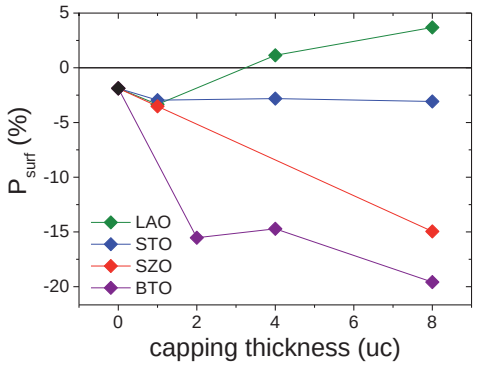

Figure 5.15: Surface orbital polarization of capped LSMO films as a function of capping thickness (a) and estimated $Mn - X$ distance at the interface (b) ($X = Al, Ti, Zr$)

The different behaviour observed for LAO capped films -where $x^2 - y^2$ is favoured at interface- and STO, SZO and BTO capped films, where $3z^2 - r^2$ occupancy is stabilized at the interface in different degrees, suggests a material dependent orbital reconstruction at the manganite interfaces. A first simple consideration can be to take into account local strain effects induced in the manganite by the capping layers, however, in the case of LAO, having a bulk cubic lattice parameter (3.79Å) smaller than LSMO (3.873Å), a compressive local strain would be expected thus favoring $3z^2 - r^2$ orbitals, opposed to what is observed. The cases of STO (3.905Å), SZO (4.1Å) and BTO (tetragonal with $a = 3.99$Å, $c \sim 4.04$Å) would also suggest reconstructions opposite to our findings.

Nevertheless, capping material structure can influence in the electronic structure of the underneath manganite layer, by modifying the Mn-O interatomic distances at the interface. Taking into account the strained out-of-plane lattice parameters of the LSMO film as well as the expected strained lattice parameters of LAO, STO, SZO and BTO

capping layers, one can draw conclusions based on the varying distances between Mn and the apical ion (Al, Ti or Zr). In figs.5.16(a-d) the interfacial layers of all the studied cases are sketched. In the first case (bare surface), the absence of apical oxygen in the Mn surface ion at the bare surface induces a lowering of the $3z^2 - r^2$ levels respect to $x^2 - y^2$, leading to a highly localized electron density of states at the $3z^2 - r^2$ levels. In reality, however, this picture would be a limiting case, as in ambient conditions, atmosphere molecules (OH, CO, ...) can be adsorbed to the MnO_2 surface, thus diminishing the electron localization.

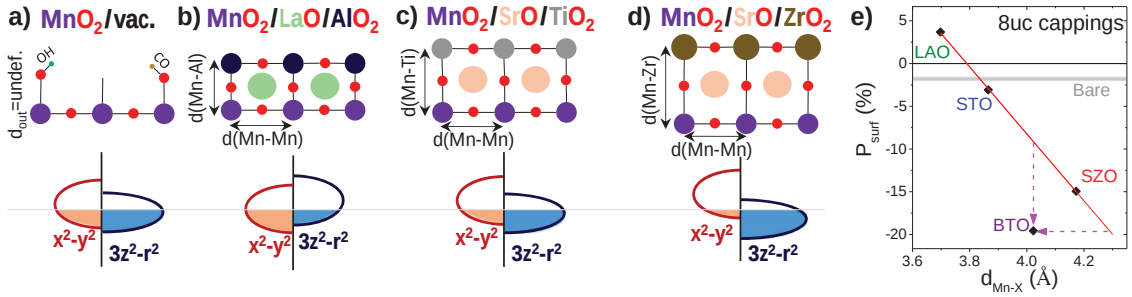

Figure 5.16: Representation of interface stacking planes for bare (a) and LAO (b), STO (c), SZO (d) capped samples indicating the idealized atomic distances (top part) and the resultant expected band diagrams of e_g levels at the interface. e) Surface orbital polarization as a function of expected $Mn - X$ atomic distances ($X = Al, Ti, Zr$) for LSMO films with $8uc$ capping layers.

This situation can be reverted if oxygen is restored to the apical position at the MnO_2 termination of the LSMO layer, as in fact it is observed in the case of LSMO/LAO interface (panel b). In principle a similar situation should be expected for the case of LSMO/STO interface (panel c), but due to the larger lattice parameter of STO, respect to LAO, an increased Mn-O distance is expected in the out-of-plane direction, probably avoiding the inversion of the e_g population at the interface. In SZO (as well as in BTO), even larger Mn-O distance in the out-of-plane direction is expected, thus leading to a lower electron repulsion in that direction and a major localization of electrons in $3z^2 - r^2$ levels. It is noticeable that this electron localization in $3z^2 - r^2$ states is significantly larger than in the case of bare samples.

Hence, according to this picture, $Mn - 3d$ orbital occupation at interfaces can be modulated by modifying interatomic distances at the interface, being this attainable by using capping materials with different lattice parameter. In fig.5.16(e), the orbital polarization observed at the manganite interface with each capping (with $8uc$ thickness) studied is represented versus the Mn-X distances (X=Al, Ti, Zr) expected considering fully strained capping layers with conserved volume respect to bulk values. One can see that P_{surf} follows a linear tendency as a function of d_{Mn-X} for the cases of LAO, STO and SZO cappings. However, BTO capping layers seem to escape this tendency, probably indicating the presence of polar displacements at the BTO interfacial layers increasing the $Mn - O$ distance. So far, due to the reduced thickness of the layers, we have not been able to check the ferroelectric state of the BTO films

This simple picture however, does not explain the capping thickness dependence of the orbital polarization, suggesting that more complex phenomena needs to be taken into account. In refs.[105, 106] it is considered that the structural asymmetry create internal electric fields that promote the displacement of the transition metal cations respect to the oxygen anions, thus either elongating or reducing the M-O bond distances

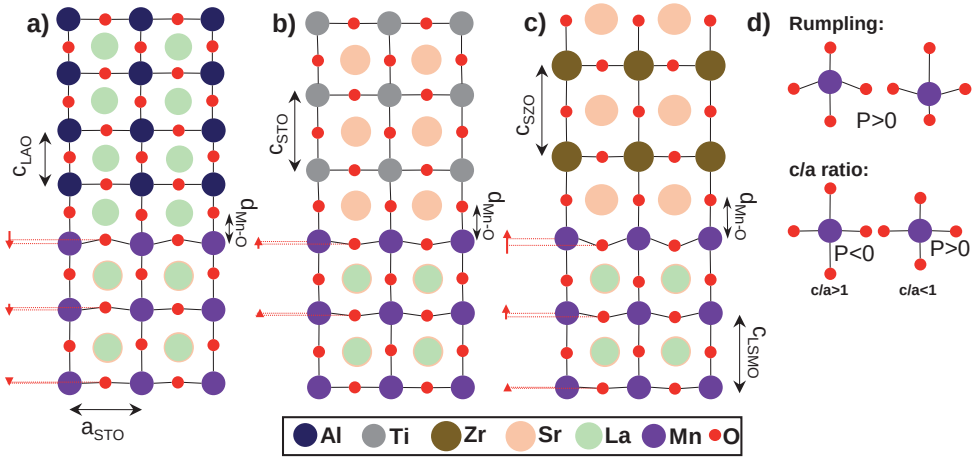

Figure 5.17: Representation of LSMO/capping stacking sequences considering the possible cation displacements at interfaces with LAO (a), STO (b) and SZO (c). Arrows indicate the magnitude of the rumpling distortion at each stacking plane. Rumpling and c/a ratio modifications are sketched in (d) with the corresponding orbital polarization P induced for each case.

responsibles for the orbital polarization and creating rumpling distortions. In fig.5.17 we envisage the possible distortions occurring at the different interfaces. Here, the vertical displacements between Mn and O have been indicated with red arrows. Following the conclusions from refs.[105, 106], these rumpling distortions and Mn-O separations can propagate for several unit cells in the manganite and the magnitude and extension of the distortion could depend on the capping material as well on its thickness. While anion-cation separations can either favor $x^2 - y^2$ (orbital polarization $P > 0$) or $3z^2 - r^2$ ($P < 0$), rumplings always favor the stabilization of $x^2 - y^2$ orbitals, as they always produce a diminished overlapping with in-plane oxygens (fig.5.17(d)). Thus, in our case, orbital occupation is mainly mediated by local modifications of c/a ratio.

Whereas these considerations are restricted to a local Jahn-Teller ionic picture, where the Mn orbital occupancy is regulated by the Mn-O electron repulsion, modulated only by Mn-O distances, a wider picture should be considered here, taking into account the $Mn(3d) - O(2p)$ hybridization. In ref.[75], the orbital polarization of $Ni - 3d$ levels at $LaNiO_3/LaXO_3$ interfaces was theoretically studied as a function of X cation. It was found by DFT calculations that orbital polarization was dependent on the energy of X orbitals as well as on X-O hybridization strength. Basically, it was found that a higher (lower) orbital polarization $P = \frac{n_{(x2-y2)} - n_{(3z2-r2)}}{n_{(x2-y2)} + n_{(3z2-r2)}}$ was resultant of a weak (strong) X-O hybridization or a strong (weak) mixing of Ni($3z^2 - r^2$) orbitals and apical O(p_z). Thus, X ions influence in the Ni orbital polarization by shifting the properties of p_z oxygen states, that is, regulating the X-O orbital admixture which influences in the Ni-O hybridization. These so called "chemical effects" were found to be determinant to the resultant orbital polarization, affecting P values more notably than Ni-O distances, which, in turn, enhance the chemical effects on P.

It should be mentioned, however, that in the case of ref. [75], all the studied X ions have (s) orbital symmetry. In our case, the lowest energy states in the X ions across the interface that can hybridize with oxygen bridge anions are $3s$ for Al^{3+}, $3d$ for Ti^{4+} and $4d$ for Zr^{4+}, all being initially empty in the nominal valence state of the capping materials.. Therefore, the states hybridizing with O(p) orbitals differ in symmetry (s vs d symmetry) and in radial extension ($3d$ vs $4d$) (sketches of the possible orbital

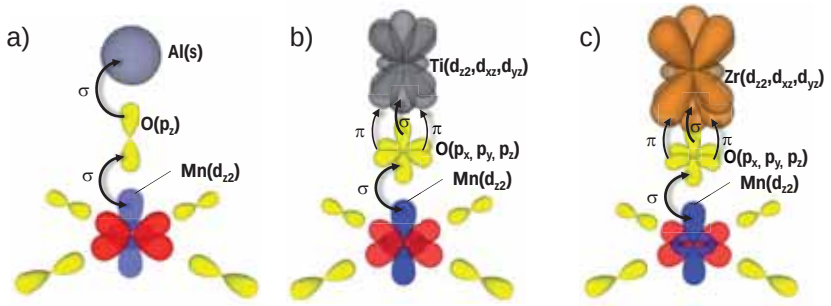

Figure 5.18: Considered orbital overlappings and possible charge transfer paths for $Mn-O-X$ interfacial bonds ($X = Al, Ti, Zr$).

hybridizations across interfaces are depicted in fig.5.18), being the experimental fact that cappings with *s* orbital symmetry stabilize a positive orbital polarization (thus in accordance with a weak X-O hybridization) and cappings with *d* orbital symmetry favor a negative *P* (in agreement with stronger X-O hybridization).

Unfortunately, in our samples we could not reliably evaluate the degree of $Mn-O$ covalency for each capping case. While this measurement is possible though the exploration of the pre-edge structure of $O-K$ edge, the overlapping between capping and LSMO film oxygen signals prevents from extracting quantitative information from the $Mn-O$ hybridization-related peaks.

In any case, it is found that both the reduced (increased) distance between Mn and apical oxygen through the interface and the reduced (increased) hybridization between interfacial oxygen and apical capping cations can influence in the negative (positive) orbital polarization observed in each case.

The consideration of these different hybridization schemes for the several capping layers should also be taken into account to explain the charge transfer phenomena discussed in section 5.2.3 as scenario 3, where the oxidation state observed was suggested to be resultant of the charge distribution through the oxygen bonding states across the interface. Charge transfer can therefore be regulated through the hybridization between Mn and capping cations, with oxygen acting as a bridge between them. For cappings favoring the O-X hybridization (as it could be the case of cappings with available *d* states in X cation) a more effective charge transfer from Mn to X could occur. Such phenomena was already proposed to take place in $LaMnO_3/SrTiO_3$ heterostructures[107], where the titanate was assumed to be doped by a charge transfer process mediated by the Mn-O-Ti hybridized bonds.

5.4 INTERFACE MAGNETISM

5.4.1 *Capping influence on macroscopic magnetic properties of LSMO films*

The effect of capping layers on the magnetic behaviour of the manganite layer was explored by means of SQUID measurements. In fig.5.19(a-d) field cooled curves measured for bare and capped films ($4-8uc$) are shown. All samples show a Curie temperature T_C lower than bulk LSMO value ($370K$), as commonly observed in thin films. Referring to bare LSMO samples, an increase of T_C is observed for LAO capped samples and, more significantly, for BTO capped samples, while STO and SZO cappings do not produce a clear relevant effect on the LSMO T_C.

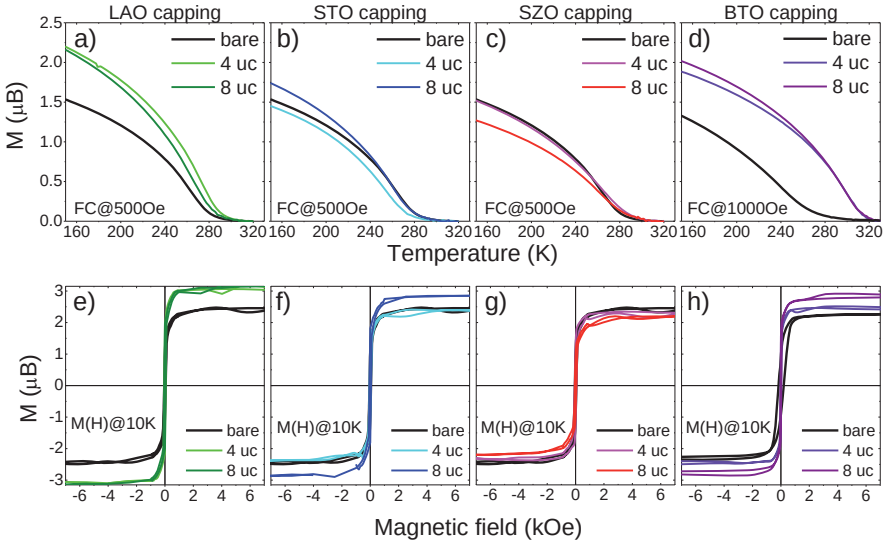

Figure 5.19: Field cooled curves (a-d) and magnetic loops (e-h) obtained for the bare films (black curves) and films capped with layers of the indicated materials and thicknesses. Magnetic field and temperatures used for the measurements are indicated in each panel

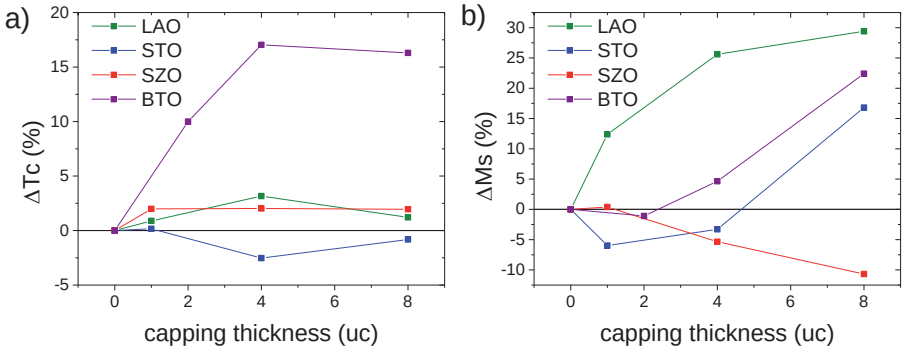

Figure 5.20: Variation of T_C (a) and M_S (b) respect to bare samples, as a function of capping thickness for the different capping materials

The magnetic hysteresis loops measured at $10K$ (fig.5.19(e-h)) show as well a reduced magnetization respect to bulk LSMO ($3.7\mu_B$) and an increased magnetization for LAO and BTO capped samples respect to the bare LSMO films, being less clear the effect on films capped with STO and SZO

The variations of T_C and M_S respect to bare LSMO sample are shown in figs.5.20(a,b) as a function of capping thickness for all the samples measured. From the plots it can be observed that BTO capped films show the largest T_C increment (reaching 17% for capping thickness $> 4uc$), and LAO capped films show the largest increment in magnetization (reaching 30% for $8uc$).

5.4.2 *XMCD at low temperatures - ferromagnetic phase at interfaces*

In order to investigate the origin of the observed modifications to the films magnetic properties induced by the capping layers, we studied the circular and linear dichroic

signals of several capped and bare samples at low temperatures. While x-ray magnetic circular dichroism (XMCD) provides information on the average magnetic moment of the more superficial layers of LSMO films, with x-ray magnetic linear dichroism (XMLD) we can reveal the presence of antiferromagnetic phases at the interfaces.

$Mn-L$ edge XAS spectra with circular (right(+) and left(-)) polarizations were measured at $2K$ in grazing incidence configuration. XMCD is mostly sensitive to the magnetic moments aligned in the direction of the x-rays propagation vector and the signal scales as $\cos\theta$, being θ the angle between the magnetic moment and the propagation vector. Thus, magnetic moments perpendicular to the light propagation vector will not contribute to the XMCD and the same will occur for antiferromagnetically coupled moments that will null their independent contributions to XMCD signal.

Therefore, in order to enhance the XMCD signal, a magnetic field was applied in the direction of the beam, thus aligning all the ferromagnetically coupled magnetic moments parallel to the light propagation vector. For that, a $2T$ magnetic field was applied in the direction of the beam (see inset in fig. 5.21(a)), large enough to saturate the magnetic moments of the sample (according to SQUID measurements). The XMCD signal was obtained as the difference between both polarizations, normalized to the maximum intensity of the averaged XAS ($I_{av} = \frac{XAS(+)+XAS(-)}{2}$). The normalized XMCD spectra for LSMO bare ($13uc$) and capped samples ($8uc$ capping thickness), shown in fig. 5.21(a-d), reveal the modifications in the Mn average magnetic moment induced by the capping layers. From the spectra of the capped samples, compared in each panel of the figure to the spectrum of the corresponding bare sample, it can be appreciated how there exists a considerable increment of the average magnetic moment in the LAO capped sample (panel a), while other cappings produce minor modifications.

Whether the uncertainty of XMCD rules applied to Mn-L edges [12] avoids to obtain a reliable value for the spin magnetic moment m_s, a comparison between different samples is possible. The spin magnetic moment m_s can be obtained from eq.2.3 as:

$$m_s = \frac{2\Delta L_2 - \Delta L_3}{I_{av}} \cdot h$$

, being ΔL_2 and ΔL_3 the XMCD areas under the L_2 and L_3 edges, I_{av} the area under the averaged XAS spectrum and h the number of holes in the Mn d levels (for the nominal composition of $La_{2/3}Sr_{1/3}MnO_3$, $h = 10 - (4 \cdot \frac{1}{3} + 3 \cdot \frac{2}{3}) \backsimeq 6.3$). The calculated modification of the average spin magnetic moment m_s^{av} in the capped films respect to the bare samples is shown in fig. 5.21(e) for the four cappings studied. While the tendency seems to confirm the results obtained in SQUID measurements, the values are in discrepancy. It needs to be reminded here that XMCD mainly explores the interfacial layers of LSMO with the capping, thus the signal is largely affected by the modifications in the magnetic moment produced at the interfaces. Moreover, SQUID measurements can be affected by random magnetic impurities present in the sample (usually in the substrates), while XMCD measures only the magnetic moment of Mn ions.

In any case, XMCD results confirm the dramatic increase of magnetization in the LSMO/LAO interface (60% increment), and reveals a detriment in the magnetic moment produced by STO and SZO cappings (9 and 20% detriment), and slight increment produced by BTO capping (9%).

For this calculation, the number of holes have been considered to remain constant in all samples. However, as we already know from the results exposed in section 5.2, bare films are prone to show a Mn^{2+} contribution at the surface (that is, extra electrons), that gets reduced in capped films. On the other hand for both STO and SZO capped

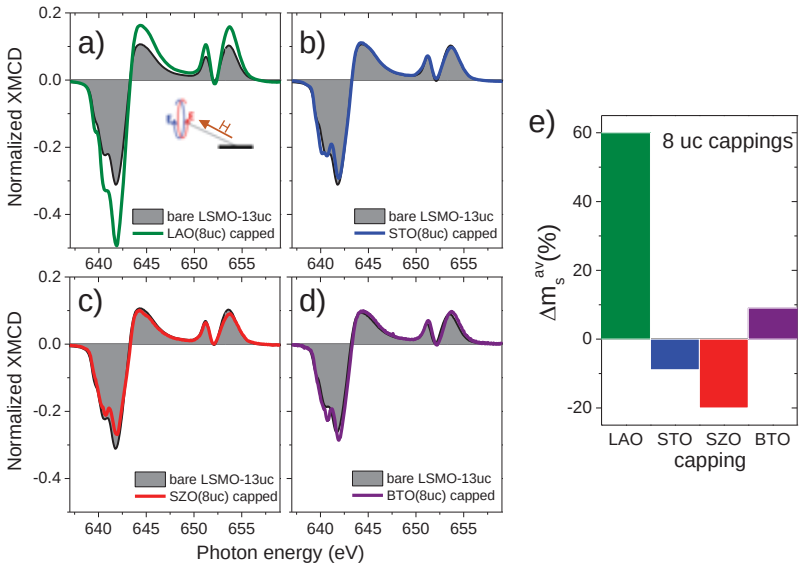

Figure 5.21: a) XMCD spectra taken at grazing incidence at $2K$ with $2T$ magnetic field applied in the direction of the beam for LSMO bare and $8uc$ capped samples; calculated m_s/n_h values are shown in the bottom part. b) SQUID M(T) curves measured at $500Oe$ in-plane magnetic field. c) SQUID M(H) curves measured at $10K$

films, increased Mn^{4+} contribution (extra holes) was detected at interfaces. These considerations would in fact decrease the calculated m_s value for bare samples and increase for STO and SZO capped samples, thus diminishing the difference Δm_s depicted in fig. 5.21(e). However, this difference would be increased for LAO and BTO cappings.

In order to enhance the surface and interface contributions to the XMCD, thinner bare and LAO-capped samples were measured. In the fig.5.22, the normalized XMCD signal of $4uc$ bare LSMO (black curve), measured at $5K$ in grazing incidence configuration and with a $2T$ field applied in the direction of the beam, is compared to the signal obtained for films capped with 2 and $4uc$ (orange and green curves, respectively). The observed increase in the magnetic moment is even more dramatic than for thicker films, exceeding 300% increase, and it is confirmed by macroscopic SQUID measurements, shown in the inset of the figure, where a notable increase of T_C is also observed ($\Delta T_C \sim 30K$), revealing a reinforced ferromagnetic interaction in the LSMO/LAO interface.

Moreover, from the shape of the XMCD signals for bare and capped samples, it can be disclosed a prominent contribution at $640eV$ in the XMCD signal of bare sample. By comparing the signal of bare sample (multiplied by a factor 4-red curve in fig.5.22) with that of capped samples, it can be appreciated how the intensity around $640eV$ is more relevant to the spectrum in the bare sample. This observation reveals a ferromagnetic contribution of Mn^{2+} at the bare surface of the samples.

5.4.3 *XMLD at low temperatures - antiferromagnetic phases at interfaces*

So far, we have explored the macroscopic magnetization (by SQUID) and microscopic average Mn magnetic moment (by XMCD) of bare and capped samples. The observed modifications in the magnetization at interfaces (revealed by changes in the M_S and T_C by SQUID and in the average spin magnetic moment by XMCD), indicate an effective influence of the different cappings in the magnetic interactions at the manganite inter-

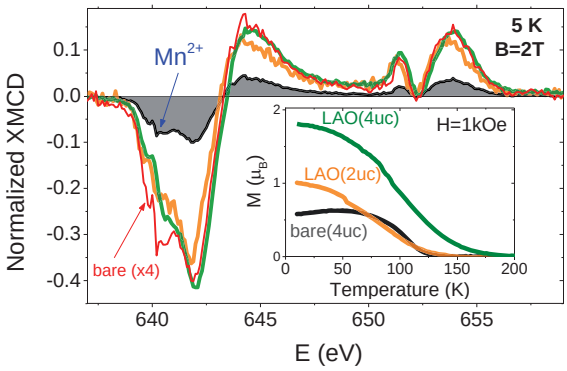

Figure 5.22: XMCD obtained for 4*uc* LSMO films, bare (black curve and grey area) and capped with LAO layers, 2 (orange) and 4 (green) uc. Red curve is a scaling of XMCD from bare sample; inset: Field-cooled curves of bare and LAO-capped samples taken with a 1*kOe* in-plane magnetic field

facial layers. From our observations, a clear increment of the ferromagnetic interaction is promoted by capping LSMO films with LAO and BTO capping layers.

To furtherly explore how this magnetic interactions are modified at interfaces, we performed XLD measurements at the $Mn - L$ edges at low temperatures, that allow to explore the presence of antiferromagnetic phases in the samples.

While in the paramagnetic phase (above sample T_C) XLD explores the orbital anisotropy, at low temperatures, when magnetic interactions come into play, XLD is also sensitive to the charge deformation produced by the spin-orbit coupling in the core and valence band levels, thus allowing to explore the anisotropy of the spin axis. Briefly, if spin axis is parallel to the beam direction, no difference in absorption due to magnetic moments will be present for both linear polarizations (with electric field components perpendicular to the beam) and therefore the "magnetic linear dichroism" (that we can name XMLD) will be zero (see sketch in fig.5.23(a)). On the other hand, if the spin axis is oriented perpendicular to the beam and mostly parallel to one of the electric field vectors of the incoming beam (and perpendicular to the other), the XMLD signal will be maximum. Furthermore, the shape of the XMLD signal will provide information on the orientation of the spin axis, relative to the beam incidence direction.

In order to separate the ferromagnetic and antiferromagnetic contributions, a magnetic field large enough to saturate the ferromagnetic component can be applied in the direction of the beam. In that way, the ferromagnetically coupled spins will align perpendicular to the photon polarization, thus canceling their contribution to XLD, and leaving only the antiferromagnetic contribution, that will not be affected by magnetic field, and the orbital contribution, that -assuming no temperature dependence- can be subtracted to the XLD considering the measurement taken at $T > T_C$.

Proceeding in this manner, by means of XLD measurement at low temperatures with applied magnetic field in grazing incidence configuration, a distinction of the predominant antiferromagnetic axis in the surface can be made. In the case of $Mn - L$ edges, the shape of the signal allows for distinction of an out-of-plane oriented axis, leading to a dichroic signal -after subtraction of orbital contribution- as depicted in fig. 5.23(b-bottom), corresponding to Mn showing $c - AF$ phase [108], or an in-plane oriented axis, leading to the curve depicted in fig. 5.23(c-bottom), similar to the signal found in other materials with in-plane antiferromagnetic alignment [18].

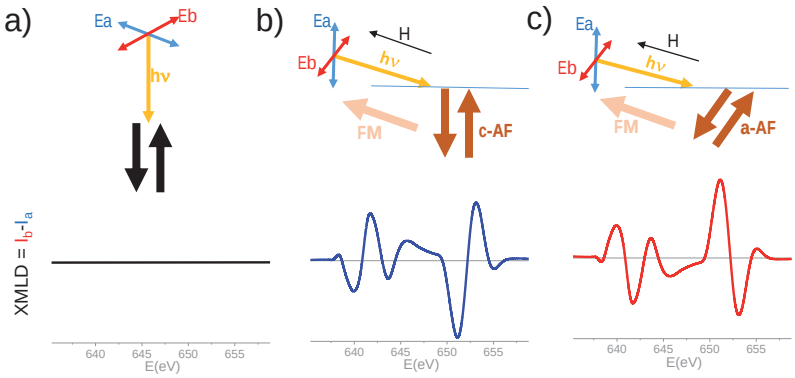

Figure 5.23: Sketches showing the relative orientation of incident beam (and E-field vectors) and ferromagnetic and antiferromagnetic moments in the different measurement configurations (top) and expected XMLD signals (bottom)

We applied this procedure to study the AF order at LSMO interfaces. Absorption spectra were acquired in grazing incidence configuration ($30deg$ incidence) with linear polarization both in-plane and almost out-of-plane, at low temperature ($2K$) and with a $2T$ magnetic field applied in the direction of the beam (see sketch in fig.5.24(a)). The dichroic signal, obtained as the difference in absorption obtained for both polarizations as $I_{\parallel} - I_{\perp}$, is shown in fig.5.24(a) for $13uc$ bare LSMO film and the corresponding $8uc$ LAO-capped sample, both at room temperature (in the paramagnetic phase) and at low temperature (in the magnetic phase), with an applied field to remove the ferromagnetic contribution. The subtraction of this two signals $(XMLD(2K, 2T) - XMLD(300K, 0T))$ is shown in fig.5.24(b) for bare and capped samples. Being the signal at L_3 more ill-defined, we can focused our analysis on the L_2 edge signal, that shows a characteristic shape with a positive (negative) sign in the lower energy region and negative (positive) sign in the higher energy region for in-plane (out-of-plane) preferential spin alignment (see 5.23(a,b)).

Paying attention to the signal at the L_2 edge (see fig.5.24(b)), XMLD of bare sample reveals an in-plane spin axis, which is at odds with previous findings in LSMO films [108, 109], where a $c - AF$ phase was detected for both bare and capped samples. Nevertheless, the XLD signal gets reverted for films capped with LAO and BTO, signaling a $c - AF$ phase at the LSMO interfacial layers. On the other hand, STO capped sample does not show signatures of signal reversal, and sample with SZO capping shows an intermediate signal that can be approximately reproduced by the average of the signals from bare and LAO-capped samples (orange curve in fig.5.24(b)), suggesting an intermediate spin axis orientation.

To furtherly explore the origins of the XMLD signals observed, we measured the temperature evolution of XLD in bare and LAO capped samples, that show opposite signs in the XMLD (XLD signal after subtraction of orbital contribution) at low temperatures. Interestingly, for bare LSMO films, a clear transition in the L_2 edge signal was observed. As depicted in fig. 5.25(a) for $13uc$ bare LSMO sample, when increasing T, the first peak of the L_2 edge XMLD signal changes sign, the transition being around $100K$. On the other hand, LAO capped sample, showed in fig.5.25(b) does not show any transition. This behaviour is more clear in panel (c), where the XMLD intensity at $651.4eV$ (first peak of L_2 edge, as indicated by dashed line in panels (a) and (b)) is plotted versus temperature. While LAO capped sample shows an out-of-plane axis related signal for the whole range of temperatures, vanishing for a T close to sample T_C, bare LSMO

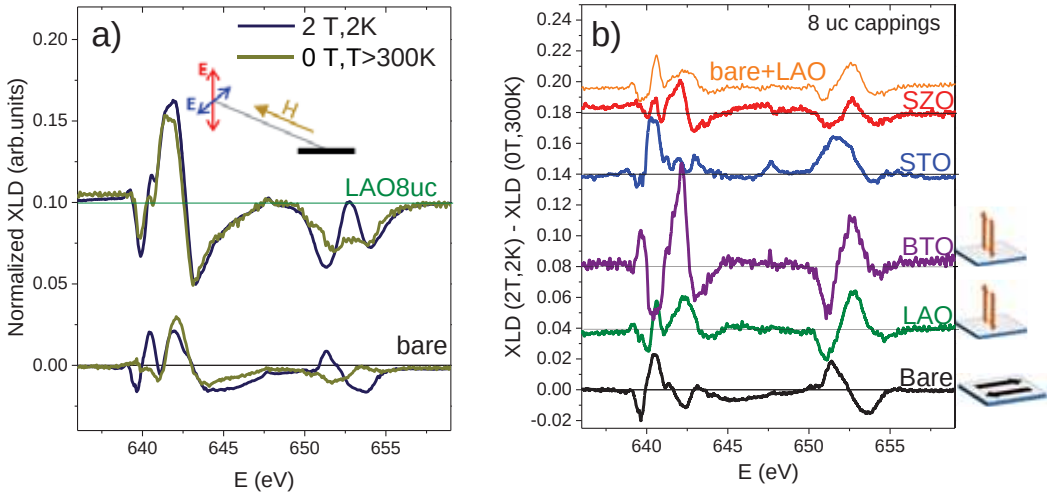

Figure 5.24: a) XMLD spectra measured in grazing incidence at $2K$ with $2T$ and at $300K$ with $0T$ for bare (bottom) and $8uc$ LAO capped (top) LSMO samples. b) Spectra obtained as a result of subtraction of XMLD spectra obtained at $300K, 0T$ from XMLD spectra at $2K, 2T$ in films capped with $8uc$ of the indicated cappings; upper curve (orange) shows the averaged signal between bare and LAO capped samples; sketches indicate preferential out-of-plane/in-plane AF spin alignment at the interfaces.

sample shows a in-plane axis signal at low temperatures, transiting to out-of-plane signal between 100 and $150K$, and finally vanishing at similar temperature as LAO capped sample. These measurements thus show that at the surface of LSMO samples two different magnetic contributions can be present and have a different temperature dependence, namely a in-plane oriented component that vanishes low temperatures ($100 - 200K$) and an out-of-plane component, that vanishes at higher temperatures (close to sample T_C). While the former is removed when capping LSMO samples with LAO (as well as BTO) capping layers, the later remains.

5.4.4 *Discussion on magnetic interactions at LSMO interfaces*

The magnetic behaviour at LSMO interfaces was studied in this section, showing important modifications strongly dependent on the interfaces considered (that is, on the capping materials in contact with the LSMO film). Firstly it was found that LAO and BTO capping layers promote an increased magnetization and Curie temperature in the LSMO films, whereas samples with STO and SZO cappings showed similar or depleted properties respect to bare LSMO films. In magnanites, the Curie temperature is associated to electron delocalization in the e_g levels and, for ultrathin films, a large in-plane delocalization is expected to increase the Curie temperature [110]. Therefore, electron localization in $3z^2 - r^2$ levels, as it is observed at the surface of bare LSMO films, is expected to deplete the T_C. LAO capping was shown to remove this surface effect and promote a stabilization of $x^2 - y^2$ orbitals, that could enhance the in-plane double exchange interaction leading to an increase of T_C in the films, as we observed in our films, confirming previous results on LSMO/LAO heterostructures increasing the ferromagnetism at interfaces[86, 94, 109]. BTO capped films, however, are shown to promote the occupancy of $3z^2 - r^2$ levels, largely than in bare surfaces and contrary to expectations,

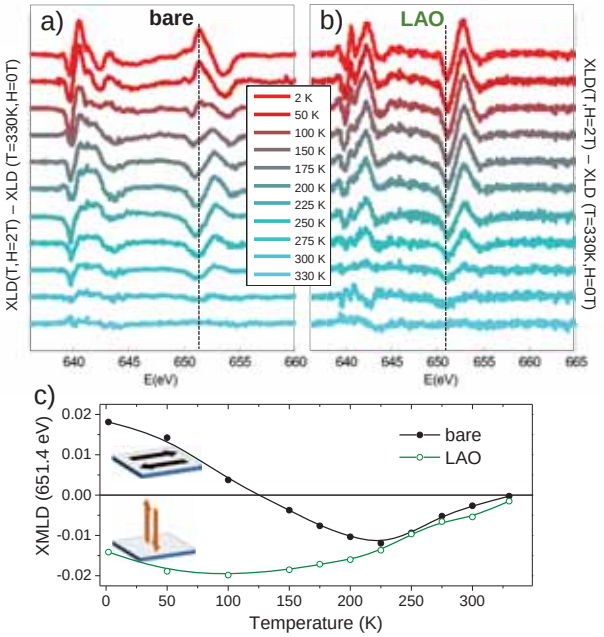

Figure 5.25: XMLD measured with $2T$ magnetic field in grazing incidence after subtraction of $330K$ signal measured without applied magnetic field, as a function of measurement temperature for bare (a) and $8uc$ LAO capped (b) LSMO samples. c) XMLD signal at $651.4eV$ (indicated by dashed lines in a and b) as a function of temperature; positive (negative) singal indicates preferential in-plane (out-of-plane) AF spin alignment.

a large increase of T_C is also found in these samples. Therefore, orbital ordering cannot be the only factor regulating the double exchange interaction at the interfaces.

In order to explore the presence of other magnetic phases, we measured the linear dichroism signal at low temperatures applying a magnetic field that is expected to supress the FM contribution. We found a prominent in-plane magnetic axis alignment -relevant for temperatures below $100K$- for bare LSMO films that could be interpreted as resultant of an a-type AF coupling, however it should not be discarded the existence of a hard ferromagnetic phase at the surface, not saturated with the applied magnetic field. Such enhancement of surface anisotropy was already studied in the previous chapter, where restoring field (associated with local magnetic anisotropy) was increased in the thinnest films, accounting for a large magnetic stiffness at the surface.

This magnetic behaviour at the surface could also be related to the presence of divalent manganese -Mn^{2+}- promoting a relevant exchange interaction at low temperatures. In fact, it has been proposed for $LaMnO_{3-\delta}$ films the occurrence of $Mn^{2+} - O - Mn^{3+}$ double exchange interaction, producing a robust ferromagnetism at the surface of the films [111]. This Mn^{2+} related contribution was observed to be relevant for temperatures below $100K$ and favor an in-plane orientation of the magnetization axis [84]. Further studies in this respect should be done to disentangle the Mn^{2+} contribution to the magnetic behaviour at the surfaces of the films.

On the other hand, a signal related to an out-of-plane spin axis was also identified at the interfaces with several capping layers (LAO, BTO and, to some extent, with SZO) that seems to be intrinsic to the LSMO layers and related to a c-AF phase present in the films, as pointed out in ref.[109], where identical XMLD signal was found irrespective of the capping layer used. Although in that case it was associated to preferential $3z^2 - r^2$ orbital ordering at the interfaces, here we can rule out this relationship, as in both

LAO and BTO-capped samples, having opposite orbital orderings at the interfaces, we identify an identical c-AF phase related XMLD signal. This phase was shown to be present even in bare films, where the previously mentioned signal associated to surface in-plane spin alignment overrides the c-AF related signal at low temperatures.

In summary, in bare films we observe an a-AF/in-plane FM phase relevant at low temperatures (below 100K) that is removed with different effectiveness by capping layers. The efficiency of the removal of this phase seems to be accompanied by increased magnetic properties (increased magnetization and transition temperature) and it is larger for LAO and BTO cappings. On the other hand, a c-AF phase is proposed to be present in all films, but only observed in the ones not showing the previously mentioned magnetic phase, and could be related to unavoidable phase separation phenomena occurring in LSMO films.

5.5 SUMMARY

In this chapter we have probed the influence of the atomic environment in the electronic structure of manganite films at bare surfaces and at the interface with dissimilar oxide capping layers. Absorption spectra reveals notable modifications in the Mn valence state, due to different redox processes occurring at LSMO terminating layers. We have shown that a relevant interaction with atmosphere in bare films due to reducing process takes place at the surface. Whereas oxide capping layers minimize this effect, other processes promote the observed charge deviations at the interfacial layers of LSMO films with the different capping materials. By exploring the influence of sample crystallographic orientation and capping crystallinity, eletrostatic-related phenomena could be disregarded as causative of the charge modifications.

Furthermore, it was shown that interfaces with other oxides can also induce strong modifications in the distribution of the electrons among the e_g orbitals in Mn^{3+} sites. This orbital reconstruction was shown to be determined by the capping material and thickness and could be correlated with the expected Mn-O distances: capping materials inducing an enlarged distance between interfacial Mn atoms and apical oxygens favour the occupancy of Mn orbitals oriented in the direction towards the apical oxygens ($3z^2 - r^2$ in the studied (001) oriented samples), while capping materials reducing this Mn-O distance lead to the inverse orbital population (preferential $x^2 - y^2$ in (001) samples).

Although most of these observations match with a simple ionic picture, the semicovalent behaviour of these materials needs to be taken into account. At the interfaces, the hybridization properties of Mn-O-X bonds (where X is a cation that depends on the capping material) can play a role in determining both the charge distribution and the valence state of Mn ions. In fact, our results could point to a dependence of the Mn orbital polarization on the symmetry of the available states in the capping X cations, where s (d) available orbitals in X cations favor the occupancy of $x^2 - y^2$ ($3z^2 - r^2$) Mn(3d) states. Thus, further experimental and theoretical work is necessary to elucidate the relevance of covalency effects in the electron distribution and in the charge transfer processes that lead to the observed Mn valence deviations at the interfaces.

Finally, the magnetic properties at the interfaces were studied. It was shown that the magnetic behaviour of LSMO films is widely dependent on the capping material and capping thickness, leading to large deviations in the measured magnetic moment and Curie temperature of capped films respect to bare films. It was shown that induced orbital order may not play a major role in the magnetic configuration, while the supression of hole/electron doping at interfacial layers can strongly enhance the ferromagnetism

at interfaces, in relation to magnetic depleted surfaces. Indeed, capping layers promoting increased magnetization and Curie temperature, were shown to be largely effective suppressing certain magnetic interactions present at the bare surfaces, and probably associated to the unavoidable Mn reduction observed in manganite surfaces.

6

ORBITAL MEDIATED CONTROL OF PHASE SEPARATION IN HALF-DOPED MANGANITE FILMS

Strain induced orbital order can be determinant for the phase selection in magnanite films. As it will be shown in this chapter, strain -via modulation of orbital occupancies- can trigger the magnetic state in half-doped manganite films, in a different manner depending on the electronic bandwith.

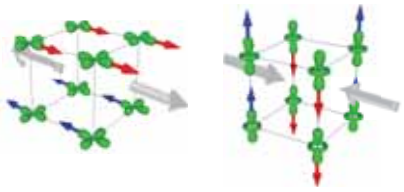

6.1 INTRODUCTION

In chapter 4 we demonstrated the effect of structural distortions on the orbital ordering in manganite thin films. The modification of orbital order can directly influence in the spin order, stabilizing different magnetic configurations depending on the preferentially occupied orbitals. The sensitivity of manganites (with the composition $Ln_{1-x}A_xMnO_3$ (Ln =lantanide, A =divalent ion)) to orbital order depends on the carrier density, that can be modified by composition (varying the hole doping factor x), as well as on the electronic bandwidth (W_0), related to the orbital overlapping (large overlapping leads to large electron delocalization and consequent wide bandwidth), that is dependent on the $Mn-O-Mn$ bond angles, that can be tuned by substituting the A cation (in general, cations with lower size promote lower bond angles and thus lower bandwidth).

Half-doped manganites (doping $x = 1/2$) represent a perfect playground to explore the effects of orbital occupancy in the spin order. Phase diagram of $La_{1-x}A_xMnO_3$ manganites situate $x = 1/2$ in the border of ferromagnetic metallic (for $x < 0.5$) and antiferromagnetic insulating ($x > 0.5$) phases in bulk compounds [112, 113]. Therefore, tuning the orbital occupancy by means of structural distortions (like the ones produced by strain in thin films) are expected to profoundly influence the magnetotransport properties of half-doped manganites. In fact, the strain dependent phase diagram in these compounds have been explored by first-principles band-structure calculations [66, 114], demonstrating that in tetragonally distorted films, the ground state can be tuned from antiferromagnetic C-type insulating (c-AF/I) to ferromagnetic-metallic state (FM/M) and antiferromagnetic A-type metallic (a-AF/M) by changing the strain from compressive (elongated c-axis) to tensile (compressed c-axis). This magnetic and electronic phase modulation has been experimentally demonstrated in $La_{1-x}Sr_xMnO_3$ films grown on different substrates by Konishi et al.[115]. More recently, Gutierrez et al. [116] showed by means of an exhaustive study of the transport and magnetic properties of $La_{1/2}Sr_{1/2}MnO_3$ (LSMO5) and $La_{1/2}Ca_{1/2}MnO_3$ (LCMO5) thin films with a controlled tetragonality, that the ground state of half doped manganite thin films can be effectively controlled via strain in LSMO5 films, largely modifying the magnetization and metallic behaviour with strain, while LCMO5 films, having a narrower bandwith, remain in an

antiferromagnetic insulating state independently of the applied strain. The lower tunability of LCMO5 has been explained in terms of larger electron localization, favouring the appearance of electronic phase separation and charge ordered phases.

In this chapter, following the work of Gutierrez et al. [116] we will fully address the orbital and magnetic orders induced by strain in thin films of LSMO5 (section 6.2) and LCMO5 (sec.6.3), grown on different single crystal substrates.

6.2 STRAIN INDUCED PHASE SEPARATION IN WIDE-BAND HALF-DOPED MANGANITES ($La_{1/2}Sr_{1/2}MnO_3$)

LSMO5 films with a thickness of $20nm$ were epitaxially grown by PLD on several (001)-oriented single-crystalline substrates, having different mismatch with LSMO5: $DyScO_3$ $(DSO : \delta = +2.13\%)$, $SrTiO_3$ $(STO : \delta = +1.22\%)$, $(LaAlO_3)_{0.3} - (Sr_2AlTaO_6)_{0.7}$ $(LSAT : \delta = +0.31\%)$, $LaAlO_3$ $(LAO : \delta = -1.71\%)$ and $YAlO_3$ $(YAO : \delta = -3.58\%)$. The films were deposited at $725°C$ in $0.2mbar$ oxygen atmosphere with subsequent free cooling in $100mbar$ oxygen pressure. The structural characterization of the films was performed by D.Gutierrez and G.Radaelli at ICMAB, and it is summarized in fig.6.1 and in ref. [116].

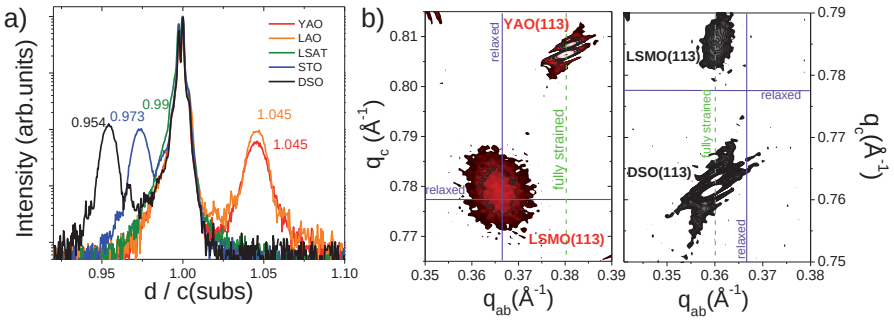

Figure 6.1: a)$\theta - 2\theta$ scans for the (002) reflection of LSMO5 films and substrates; c_{film}/a_{subs} are indicated in the corresponding film reflections. b) q-plots for the (113) pseudocubic reflections of LSMO5 films grown on YAO (left) and DSO (right) substrates; blue lines represent expected positions for completely relaxed film and dashed green line correspond to expected position for fully strained films.

The $\theta - 2\theta$ diffraction patterns around the (002) reflection of the LSMO5 films and substrates were recorded. In fig. 6.1(a) the reciprocal interplanar distances $d(002)$ of all films have been normalized to that of the corresponding substrates $(1/c_{subs})$ for better comparison of the strain state of the films. A shift of LSMO5 peak towards lower $d(002)/c_{subs}$ values is observed for films grown on DSO and STO, while the peak shiftes towards higher $d(002)/c_{subs}$ for films deposited on LAO and YAO, thus implying that films on DSO and STO are tensile strained $(d/c < 1)$ whereas those on LAO and YAO are under compressive strain $(d/c > 1)$. In order to ascertain the in-plane parameter of the films, reciprocal space maps (RSM) around the (113) reflections were collected. The RSM's for the films with largest strain are shown in fig.6.1(b). It can be appreciated how films on YAO substrate $(\delta = -3.58\%)$ show the (113) film reflection close to the reciprocal space coordinates for bulk LSMO5, indicating a structural relaxation of the films. On the other hand, films on DSO $(\delta = +2.13\%)$ show the in-plane coordinates of the film almost coinciding with that of the substrate, signalling a fully strained state of the films.

substrate	δ (%)	a(q-plot) (Å)	c(ϑ-2ϑ) (Å)	c/a
DSO	+2.13	3.925	3.761	**0.958**
STO	+1.22	3.907	3.803	**0.973**
LSAT	+0.31	3.87	3.833	**0.990**
LAO	-1.71	3.802	3.965	**1.043**
YAO	-3.58	3.864	3.891	**1.007**

a(LSMO5 bulk)=3.858Å

Table 6.1: Lattice mismatch, in-plane and out-of-plane calculated parameters and c/a ratio for all LSMO5 films ($20nm$ thick).

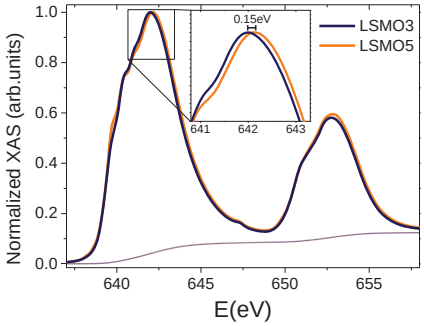

Figure 6.2: XAS spectra for $5nm$ $La_{2/3}Sr_{1/3}MnO_3$(LSMO) film (blue) and $10nm$ $La_{1/2}Sr_{1/2}MnO_3$(LSMO5) film (orange); inset: magnification of L_3 peak.

The in-plane lattice parameters (obtained by RSM's) and the out-of plane parameters (obtained by $\theta - 2\theta$) of all the LSMO5 samples are summarized in table 6.1, together with the resultant c/a ratio values, that denote the tetragonal distortion of the films.

The XAS spectra of LSMO5 films was obtained as the average over the absorption intensity for both linear polarizations ($(I_{\parallel} + I_{\perp})/2$), measured in TEY mode with the x-rays inciding at 60 degrees respect to surface normal. The XAS spectra of LSMO5 films is compared to that of LSMO films in fig.6.2, where the spectra of a $5nm$ LSMO sample grown on STO and that of a $10nm$ LSMO5 sample grown on STO are displayed. The energy calibrated spectra does not show any significative difference in the spectral shape, but a close look to the maximum of L_3 reveals an energy shift of $150meV$ for LSMO5 spectra respect to LSMO. This shift towards higher energies is a consequence of the larger Mn valence state of LSMO5 (3.5) as compared to LSMO (3.3) [85, 117].

X-ray natural linear dichroism at room temperature

XAS spectra of $20nm$ LSMO5 films grown on different substrates is shown in fig.6.3(a). A two peaks feature is clearly visible in the lower energy region of L_3 peak for all films except for DSO. The difference between a XAS spectrum presenting this double peak structure (LSAT) and a one not showing it (DSO) results in a spectrum (green curve at the bottom of fig.6.3(a)) that ressembles Mn^{2+} spectrum, as shown in the figure, where a Mn^{2+} simulated spectra is displayed for comparison (magenta curve). Although the origin of the presence of Mn^{2+} in these films has not been fully ellucidated, Mn reduction due to atmosphere exposure and aging effects may be involved (samples showing Mn^{2+} were one year older than the ones not showing it). A more detailed examina-

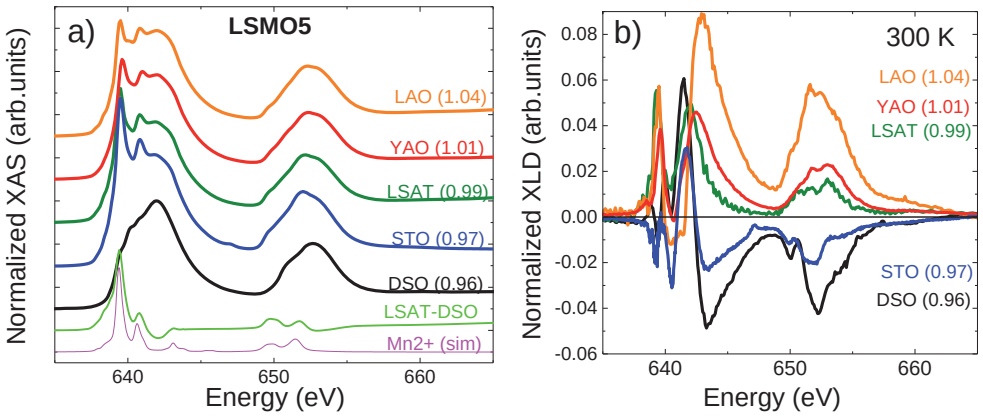

Figure 6.3: a) XAS spectra of LSMO5 films grown on the indicated substrates; green and magenta curves correspond to difference between LSAT and DSO sample XAS spectra and Mn^{2+}XAS simulation, respectively. b) XLD spectra of LSMO5 films measured at $300K$.

tion of the Mn reduction observed in manganite films and the effects on dichroism is presented in appendix D.

The XLD signal of LSMO5 films, measured at $300K$ in grazing incidence configuration (incidence angle $\theta = 30deg$), is displayed in fig.6.3(b). These spectra ressemble those reported previously in LSMO5 films grown both on LAO and STO substrates [118]. A clear evolution of XLD signal with tetragonal distortion of the films is evidenced from the figure, better visualized in fig. 6.4(a), where the integrated area under XLD spectra has been computed for all films, in the L_2 energy region (solid symbols) and in the whole energy range (empty symbols). The resembling tendency of both curves shows the robustness of data and indicates that Mn^{2+} (contributing mostly in the lower energy region of L_3) does not significantly contribute to the XLD signal, as expected. The negligible contribution of Mn^{2+} to XLD signal of LSMO5 samples is furtherly demonstrated in appendix D.

From the XAS and XLD area integration we can obtain the holes ratio $X = \frac{h(3z^2-r^2)}{h(x^2-y^2)}$ (eq. 4.1) and orbital polarization P (eq.4.3, assuming $n_{e_g} = 1$), as shown in fig.6.4(b). Analogously to LSMO films, also displayed in the plot, we observe a strain induced orbital polarization, mainly driven by Jahn-Teller distortion, favouring the occupancy of $x^2 - y^2$ orbitals for tensiled strained films (DSO, STO), reaching orbital polarizations as large as 6%, while compressively strained films (LAO,YAO) show a preferential occupancy of $3z^2 - r^2$ orbitals with orbital polarizations reaching -12%. Similarly to LSMO case, nearly unstrained films show an abnormal polarization (-5% for films on LSAT), revealing the surface symmetry breaking effect favouring a $3z^2 - r^2$ occupancy (see section 4.3).

X-ray magnetic circular and linear dichroism at low temperatures

At low temperatures, the films get magnetically ordered. With a view to disentangle the magnetic exchange interactions between Mn ions, we performed XAS measurements with circular and linear x-ray polarizations at low temperatures (below 5 K) and with applied magnetic fields (up to 2 T) in the direction of the x-ray beam.

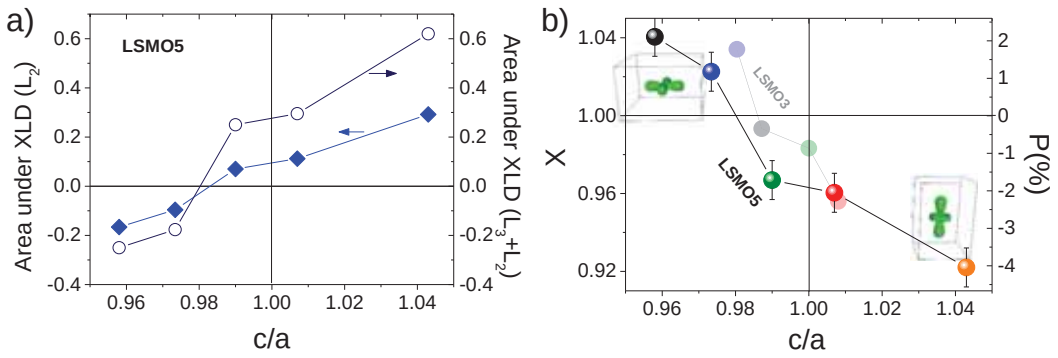

Figure 6.4: a) Integrated area under XLD spectra for L_2 edge region (left axis, rhombii), and $L_2 + L_3$ region (right axis, empty circles). b) Calculated holes ratio X (left axis) and orbital polarization P (right axis) of $LSMO_5$ films as a function of c/a ratio. Negative polarization values indicate preferential occupation of $3z^2 - r^2$ orbitals, while positive values indicate preferential occupation of $x^2 - y^2$ orbitals. $La_{2/3}Sr_{1/3}MnO_3$ (LSMO) films values are also indicated by semi-transparent symbols.

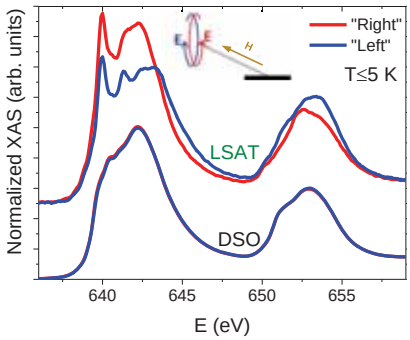

Figure 6.5: Polarized XAS spectra taken with right and left circular polarization at grazing incidence configuration and with a $2T$ applied field in the direction of the beam, as indicated in the sketch, for $LSMO_5$ sample on LSAT (upper curves) and $LSMO_5$ samples on DSO (bottom curves)

In fig. 6.5, we show two examples of XAS spectra taken with circular polarizations. As it can be appreciated, film on LSAT has an important dichroic signal in both edges, while the spectra of sample on DSO do not show any significative difference for both polarizations, indicating that films on LSAT are largely ferromagnetic whereas those on DSO are not.

The XMCD spectra (normalized by the maximum intensity in the averaged absorption spectra) for all measured samples is shown in fig. 6.6(a). It is noticed that samples with lower strain (LSAT, YAO) show the highest XMCD signal, which is reduced for strained films (both compressive and tensile) eventually reaching a null signal for sample on DSO. The application of XMCD sum rules [10, 11] -considering the nominal number of holes $n_h = 3.5$- results in the spin and orbital magnetic moments depicted in fig. 6.6(b-empty and full circles). While the orbital magnetic moment is negligible for all samples, the evolution of m_{spin} as a function of c/a ratio is clear. Although the tendency is reliable, it needs to be noted that the values obtained from applying sum rules to Mn $L_{2,3}$ edges can result in large errors for the absolute value of m_{spin}, due to the overlapping of L_3 and L_2 edges [12].

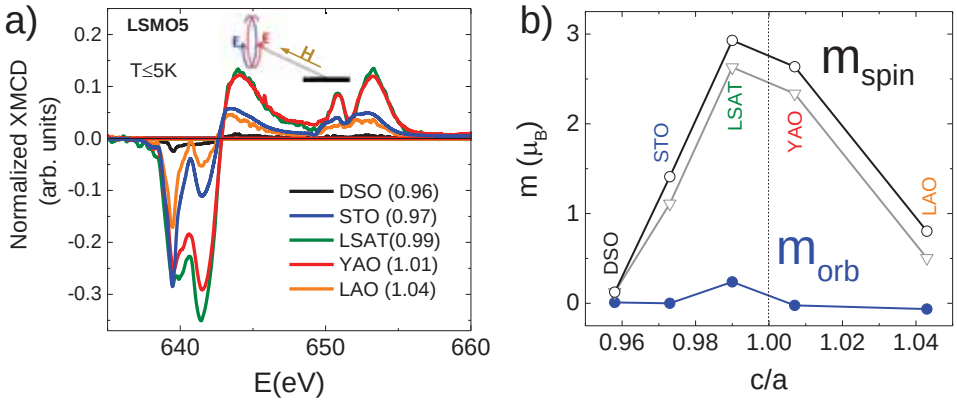

Figure 6.6: a) XMCD spectra of $LSMO_5$ samples grown on the indicated substrates. b) Calculated spin (black empty circles) and orbital (blue circles) magnetic moments as a function of c/a ratio. In grey empty triangles the corrected m_{spin} values substracting Mn^{2+}contribution are represented.

It is also important to remark that in the XMCD spectra of LSAT, STO, YAO and LAO samples, an important signal is visible at energies close to $640eV$, corresponding to the Mn^{2+} peak observed in XAS spectra for these samples, thus evidencing a ferromagnetic contribution of Mn^{2+}, parallel to the magnetic moments of $Mn^{3+/4+}$. The magnetic contribution of Mn^{2+} is furtherly studied in appendix D, where an excess magnetic moment of $0.3\mu_B$ due to Mn^{2+} is detected. The correction of this excess magnetic moment for all samples showing Mn^{2+} peaks in XAS leads to the values respresented in fig.6.6(b-empty triangles). This minor correction thus certifies that the Mn^{2+} contribution does not mask the strain tendency of the magnetic moment in these samples.

To study the existence of antiferromagnetically aligned spins in the samples measured the linear dichroism signal at low temperatures ($T \leq 5K$), proceeding in the same manner as in sec.5.4.3, that is, substracting the natural dichroism obtained at $300K$ and supressing the ferromagnetic contribution to XLD by means of a magnetic field ($2T$) aligned with the x-rays beam).

XLD measurements were performed in grazing and normal incidence geometries. We first discuss the results of grazing incidence XLD measurements. In this geometry, both XAS with linear photon polarization parallel to the sample plane ($E_{\parallel}$) and almost perpendicular to it ($E_{\perp}$) are registered. The magnetic linear dichroism (XMLD) curves -obtained after substraction of the XNLD measured at $300K$ (data in fig.6.3(b)) to the XLD measured at low temperature- of all measured samples are plotted in fig. 6.7(a).

Firstly, it can be noticed how the XMLD signal for the sample grown on LSAT ($c/a = 0.99$), after substraction of XNLD measured at $300K$, is barely zero. Thereby, no antiferromagnetic (AF) signal is detected in this configuration. All other samples, on the contrary, show a significative XMLD signal, accounting for an AF spin alignment. From the shape of the spectra, and comparing with previous works [18, 109], the orientation of the AF axis can be elucidated. A fine indicative for the AF axis orientation is the shape of the dichroic signal at L_2 edge ($648 - 655eV$), which corresponds to transitions from $2p_{1/2}$ to $3d$ levels. Exchange interactions split the $2p_{1/2}$ levels into two sublevels with magnetic quantum numbers $m_j = +1/2$ and $m_j = -1/2$; the charge distribution of these sublevels is anisotropic and this gives rise to a linear dichroism for each of the sublevels, whose sign depends on the relative orientation between the mag-

netization direction (that will affect the charge distribution) and the light polarization. It can be shown that for incident light parallel (perpendicular) to the AF-axis the shape of XMLD signal at the L_2 edge -defining the XMLD as $(I_{\parallel} - I_{\perp})$- is positive (negative) in the lower energy region and negative (positive) in the higher energy region [18, 109]. That being so, we can estimate the orientation of the AF-axis in the measured samples from the grazing incidence measurements: for samples on DSO ($c/a = 0.96$) and STO ($c/a = 0.97$), AF axis is mostly parallel to the beam incidence direction, and thus parallel to the sample surface, while for samples on YAO ($c/a = 1.01$) and LAO ($c/a = 1.04$), the AF axis is mostly perpendicular to the beam, and thus perpendicular to the sample surface. The evolution of the AF axis can be graphically visualized by monitoring the XMLD intensity at the first peak of L_2 dichroic signal ($650.8eV$), as plotted in fig. 6.7(c), as a function of c/a ratio. We observe how the signal at this peak changes from positive (mostly a-AF alignment) to negative (mostly c-AF alignment) when increasing the c/a ratio.

The spin alignment can be furtherly checked by measuring the XLD signal in normal incidence. In this geometry, no orbital contribution needs to be subtracted, as no orbital anisotropy is probed in normal incidence (same orbitals are explored for both linear polarizations), and spins with AF axis perpendicular to the sample surface do not give any dichroic signal. In fact, that is what we observe in 6.7(b) where samples on YAO and LAO have a negligible XMLD signal. On the other hand, a clear XMLD signal is observed for sample on DSO, signaling a preferential in-plane AF orientation that could be caused by the orthorhombic distortion existing in this substrate. Sample on STO however, does not show a clear shape of the XMLD, probably indicating a random in-plane direction of the AF domains.

Therefore, in this section it was shown that LSMO5 films under compressive strain ($c/a > 0$) show a preferential occupation of $3d(3z^2 - r^2)$ orbitals and an antiferromagnetic spin alignment perpendicular to the sample surface (c-AF). On the other hand, films under tensile strain ($c/a < 0$) show a preferential occupation of $3d(x^2 - y^2)$ orbitals and an antiferromagnetic spin alignment parallel to the sample surface (a-AF). Films having the lowest strain values ($c/a \sim 0$) show the smallest AF signal and the highest magnetic moment, thus indicating a preferentially ferromagnetic exchange interaction. However, still an orbital polarization is detected in unstrained films signaling a preferential occupation of $3d(3z^2 - r^2)$ orbitals, that can be attributed to surface symmetry breaking.

The results of the magnetic and orbital characterization shown here are in perfect agreement with the predicted phase diagram [66], shown in fig.6.8, demonstrating the intricate correlation between lattice, orbital and spin degrees of freedom in these systems. Our measurements here also reveal an important phase coexistence in some of the films, presenting both FM and AF orders simultaneously.

6.3 STRAIN INDUCED PHASE SEPARATION HALF-DOPED NARROW-BAND MANGANITES ($La_{1/2}Ca_{1/2}MnO_3$)

An analogous study of the orbital and magnetic order was performed in LCMO5 films, deposited by PLD under the same conditions as LSMO5 samples. The substrates used and sample thickness were also identical to LSMO5. The structural characterization resulted in analogous trend as LSMO5 samples, with nearly fully strained samples for all substrates except for samples on YAO and DSO, that showed partial relaxation. A summary of the in-plane and out-of-plane lattice parameters, obtained by means of q-

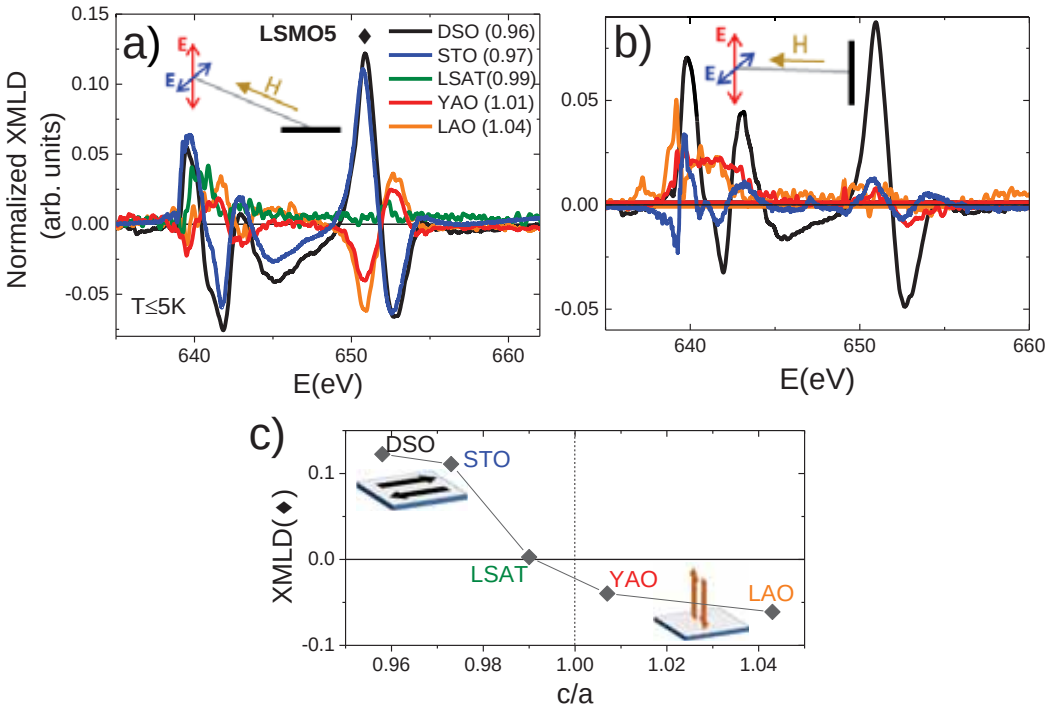

Figure 6.7: a) XMLD spectra of LSMO5 films grown on the indicated substrates, obtained as XLD($5K, 2T$)-XLD($300K, 0T$), in grazing incidence with magnetic field applied in the direction of the beam as sketched in the figure. b) XMLD spectra taken in normal incidence, as sketched. c) Intensity at the first peak of XMLD signal (indicated by rhombus in panel a) for grazing incidence measurements as a function of c/a ratio; positive (negative) signal indicates preferential in-plane (out-of-plane) AF spin alignment, as indicated by sketches.

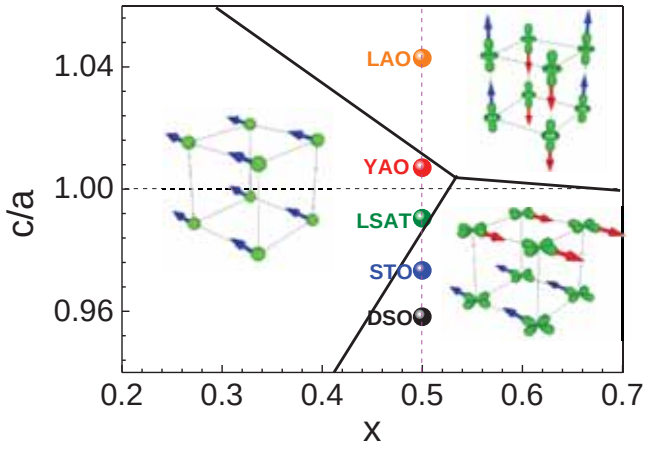

Figure 6.8: Phase diagram as calculated by Fang et al.[66] for tetragonally distorted $La_{1-x}Sr_xMnO_3$. Dots correspond to the c/a values obtained for our $La_{1/2}Sr_{1/2}MnO_3$ films. The pictures indicate the corresponding orbital and spin orders in each phase.

plots and $\theta - 2\theta$ scans (see ref. [116] for full structural characterization information) is shown in table 6.2.

substrate	δ (%)	a(q-plot) (Å)	c(ϑ-2ϑ) (Å)	c/a
DSO	+2.87	3.91	3.733	**0.955**
STO	+1.96	3.907	3.74	**0.957**
LSAT	+1.04	3.865	3.77	**0.975**
LAO	-0.99	3.793	3.88	**1.023**
YAO	-2.87	3.833	3.90	**1.017**

a(LCMO5 bulk)=3.830Å

Table 6.2: Lattice mismatch, in-plane and out-of-plane calculated parameters and c/a ratio for all LCMO5 films ($20nm$ thick).

XAS spectra, resulting from the average of intensities taken with in-plane and (almost) out-of-plane linear polarized light in grazing incidence configuration ($30deg$ incidence respect to sample surface) at $300K$ are shown in fig. 6.9(a). While no big differences are observed in the XAS for the different samples (and no relevant contributions from Mn^{2+}), XLD (fig.6.9(b)) reflects the differences in orbital occupancies for the different samples.

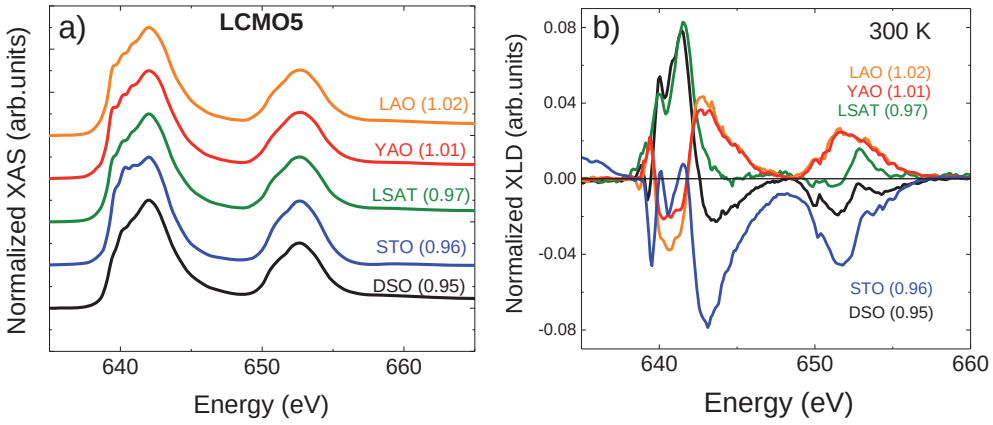

Figure 6.9: a) XAS spectra of LCMO5 films grown on the indicated substrates. b) XLD spectra of LCMO5 films measured at $300K$.

The area under the L_2 edge and under the total XLD spectra is plotted in fig.6.10(a) as a function of tetragonal distortion of the films (represented by c/a ratio). Although, within error, the tendency is similar, the strain modulation does not show as clear as in LSMO5 films. This is better visualized in the fig. 6.10(b), where the holes ratio X and orbital polarization for LCMO5 films is compared with LSMO5 series: while in LSMO5 the orbital polarization shows an almost linear dependence with the c/a ratio, the strain induced orbital tunability does not show as evident in LCMO5, where all samples show a negative orbital polarization (larger occupancy of $3z^2 - r^2$) except the sample on STO.

The magnetic moment of the samples was explored by means of XMCD measurements. Due to the largely insulating character of LCMO5 films leading to high resistance at low temperatures, XMCD measurements had to be acquired at $50K$. A magnetic field of $1T$ was applied in the direction of the beam to maximize the XMCD signal. The

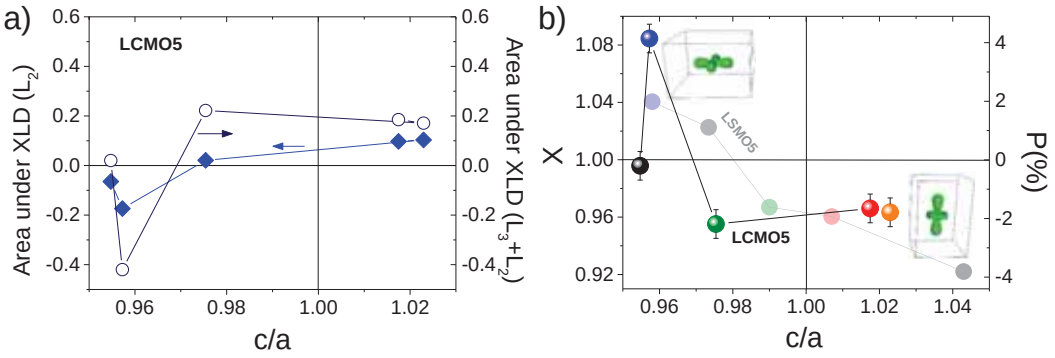

Figure 6.10: a) Integrated area under XLD spectra for L_2 edge region (left axis, rhombi), and $L_2 + L_3$ region (right axis, empty circles). b) Calculated holes ratio X (left axis) and orbital polarization P (right axis) of LCMO5 films as a function of c/a ratio. Negative polarization values indicate preferential occupation of $3z^2 - r^2$ orbitals, while positive values indicate preferential occupation of $x^2 - y^2$ orbitals. LSMO5 films values are also indicated by semi-transparent symbols.

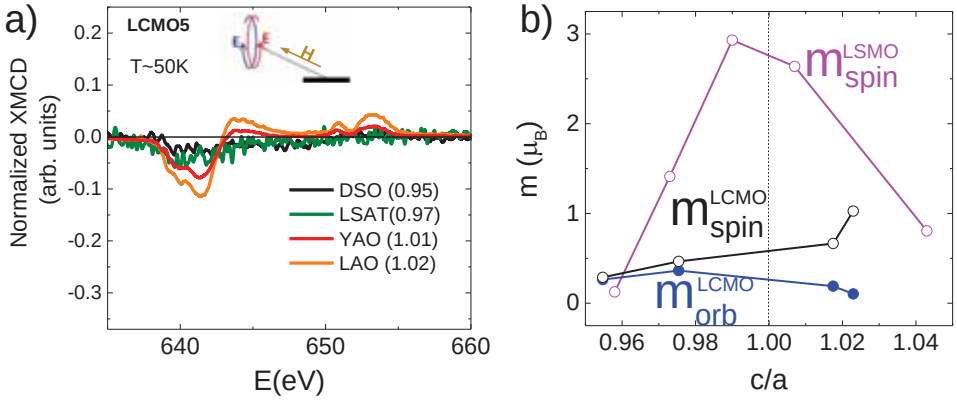

Figure 6.11: a) XMCD spectra of LCMO5 samples grown on the indicated substrates (vertical scale is the same as in fig.6.6). b) Calculated spin (black empty circles) and orbital (blue circles) magnetic moments as a function of c/a ratio for LCMO5 films. In magenta the m_{spin} values obtained for LSMO5 are shown for comparison.

spectra, normalized to the average absorption, are shown in fig. 6.11(a) for all samples measured. Only samples on YAO and LAO showed a visible XMCD signal, being quite reduced or almost zero for the rest of the samples in the series. The calculated spin and orbital magnetic moments are shown in fig. 6.11(b), where spin magnetic moment of LSMO5 samples is also shown for comparison. As observed here, the values for LCMO5 films lay far from the maximum expected magnetic moment of $3.5\mu_B$ for LCMO5, demonstrating that a ferromagnetic phase cannot be stabilized within the strain values explored here.

The antiferromagnetic spin alignment was explored by magnetic linear dichroism measurements in grazing incidence, also at $50K$. The XMLD spectra (obtained after subtraction of XNLD and suppression of ferromagnetic component by applying a $1T$ magnetic field) are shown in fig. 6.12(a) for the measured samples. Paying attention to the signal at the L_2 edge, it can be observed an inversion of the dichroic signal between tensile strained films (STO, DSO) and compressively strained films (LAO, YAO), as

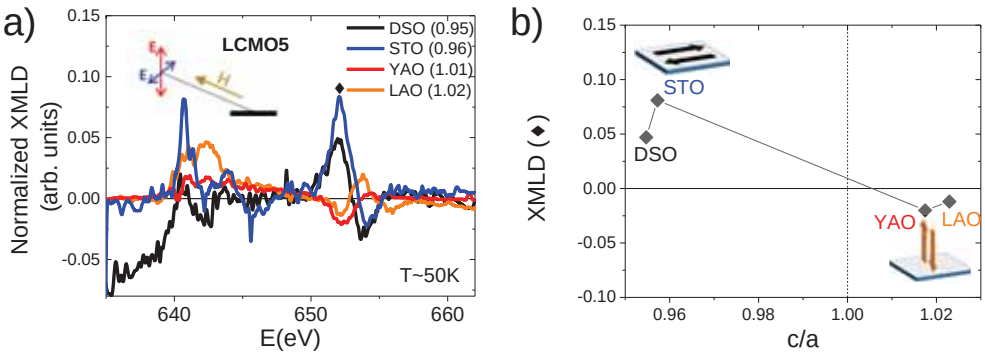

Figure 6.12: a) XMLD spectra of LCMO5 films grown on the indicated substrates, obtained as XLD(50K, 1T)-XLD(300K, 0T), in grazing incidence with magnetic field applied in the direction of the beam as sketched in the figure. b) Intensity at the first peak of XMLD signal (indicated by rhombus in panel a) for grazing incidence measurements as a function of c/a ratio; positive (negative) signal indicates preferential in-plane (out-of-plane) AF spin alignment.

evidenced by monitoring the intensity of the first peak in the L_2 edge signal, as a function of c/a ratio (fig. 6.12(b)), signaling a transition from a preferential in-plane AF spin alignment for tensile strained films to a preferential out-of-plane AF alignment for the compressive strained ones.

Thus, LCMO5 films show an orbital order less sensitive to tetragonal distortion in the films. Tensile strained films show an AF phase with in-plane oriented axis and compressive strained films show out-of-plane AF spin alignment in coexistence with a weak ferromagnetic signal, thus evidencing a notable phase separation in these films.

6.4 SUMMARY

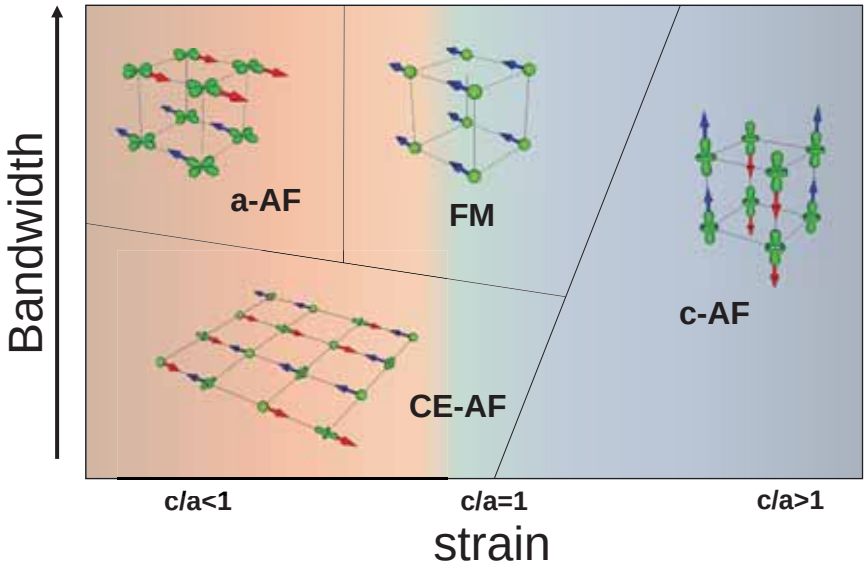

Figure 6.13: Tentative phase diagram for half-doped manganite films as a function of strain in the films

In this chapter we have explored the orbital and magnetic order in LSMO5 and LCMO5 thin films, epitaxially grown on substrates imposing a tetragonal distortion in the films. In LSMO5 a clear modulation of the orbital occupancy, promoted by the splitting of e_g levels due to the structural symmetry lowering, follows the expected tendency with strain in the films. This strain induced orbital occupancy matches perfectly with the expected magnetic phase diagram, where the stabilization of $x^2 - y^2$ levels (case of tensile strain) favors a $a - AF$ phase and the stabilization of $3z^2 - r^2$ levels (case of compressive strain) favors a $c - AF$ phase. While intermediate strain values show clear signatures of phase separation (coexistence of AF and FM phases), unstrained films show the largest magnetic moment values, signaling the stabilization of a FM phase.

On the other hand, LCMO5 films show a somewhat lower correlation between orbital polarization and structural distortion. Low temperature dichroism show a FM/$c - AF$ phase coexistence for compressively strained films, while tensile strained films show a barely null magnetic moment and an in-plane AF interaction, that may correspond to $a - AF$ phase or to the proposed CE-type ordering (consisting on FM zigzag chains coupled antiferromagnetically)[114].

These conclusions can thus be summarized in the tentative phase diagram pictured in fig.6.13

7

STRAIN TUNING OF ORBITAL STATES IN NICKELATE PEROVSKITE THIN FILMS

Nickelate perovskites constitute another prototypical system to explore the effects of strain induced structural distortions in the tuning of $3d$ orbital occupancy in thin films. In this chapter we will explore the influence of these structural distortions in the orbital polarization as well as on the degree of covalence, directly related to the conduction properties of the films, and the relevance of surface symmetry breaking effects

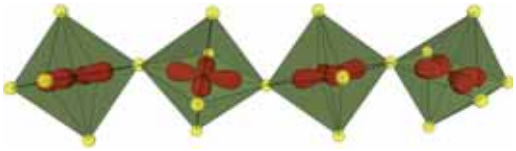

7.1 INTRODUCTION

As stated by M.L.Medarde in her review on $RNiO_3$ (R =rare earth) perovskites [119], these materials provide a remarkable opportunity to study the relationship between structural and physical properties. The main characteristic of these compounds is a sharp metal-to-insulator (M-I) transition occurring at a temperature T_{M-I} that can be correlated with the size of the R ion: the smaller the R ion, the larger T_{M-I} value is found. In addition, antiferromagnetic order appears at low temperatures.

In $RNiO_3$ compounds, the conduction bandwidth is determined by the degree of hybridization between oxygen p and nickel d orbitals: when the hybridization gets reduced a gap opens and the material becomes insulator. Thus, $Ni-O-Ni$ bond angles play a major role in the properties and, by reducing the R ion size, the perovskite structure gets distorted and the bond angles get reduced, thus reducing also the orbital overlapping [120].

In the same manner as R ions can control the bandwidth, strain in epitaxial films can be considered as a more suitable parameter to tune the properties of nickelate compounds via substrate-imposed structural distortions. This strategy has been proved to be effective in the control of M-I transition temperature in several compounds [121, 122], however the influence of strain on T_{M-I} was found to be strongly asymmetric, pointing to different kind of structural distortions for tensile and compressive strained films.

$LaNiO_3$ (LNO), contrary to the rest of compounds in the $RNiO_3$ series remains metallic and paramagnetic at all temperatures. Having a rhombohedral structure (while the rest of $RNiO_3$ compounds show orthorhombic symmetry), LNO displays the largest $Ni-O-Ni$ bond angle (165.2deg) [123], and the most stable stoichiometry, favouring its obtention in bulk and thin film form. The metallic character of LNO and its structural similarity with many oxide perovskite compounds makes of LNO highly profitable as electrode in oxide heterostructures. Recently, LNO has attracted the attention due to the theoretical possibility to obtain a 2D conduction confinement leading to orbital ordered superconducting phases in superlattices composed of thin LNO layers separated by insulator layers [124] and theoretical and experimental studies are focused on achieving

large orbital polarizations leading to electronic structure configurations resembling that of high-T_C cuprate superconductors [16, 75, 105].

Recent reports in LNO films have revealed asymmetric orbital response to substrate induced strain [125], thus suggesting a mechanism for strain control of the single e_g electron of Ni^{3+} (having a low spin configuration $3d^7 : (t_{2g}^6 e_g^1)$) different from the Jahn-Teller related distortion mechanism observed in Mn^{3+}[26, 27]. Indeed, strain-induced structural distortions have been shown to promote different octahedra rotation modes in the perovskite structure, modifying bonding angles and distances in a different way for tensile and compressive induced strains [126, 127], factors that can profoundly affect the orbital configuration and hybridization schemes in LNO thin films, requiring further investigation in this respect.

In this chapter we will explore the influence of structural distortions induced by biaxial strain in LNO thin films in the orbital ordering of $Ni-3d$ states and in the $Ni(3d)-O(2p)$ hybridization strength, probing as well the impact on the conduction properties of the films. Furthermore, the effects of symmetry lowering produced at the surfaces of the films or in structurally relaxed films will be examined.

7.2 STRAIN DEPENDENT TRANSPORT PROPERTIES OF $LaNiO_3$ EPITAXIAL THIN FILMS

7.2.1 *Structural characterization*

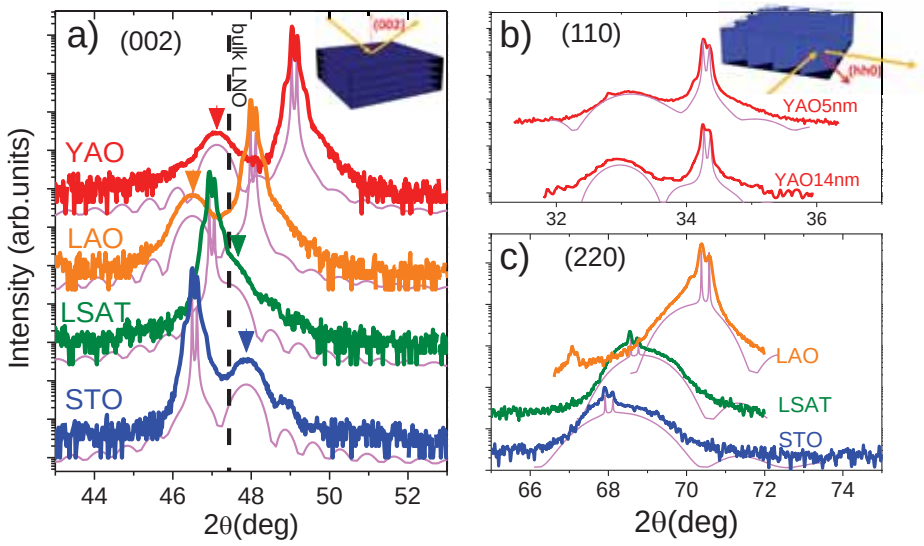

Figure 7.1: a)$\theta-2\theta$ scans around the symmetrical (002) reflection of 14nm *LNO* films and indicated substrates. Dashed line indicates the expected angular position for bulk *LNO* reflection. b) Grazing incidence $\theta-2\theta$ scans around (110) reflection for 5 and 14nm *LNO* films on *YAO*. c) Grazing incidence $\theta-2\theta$ scans around (220) reflection for 14nm *LNO* films on *LAO*, *LSAT* and *STO* substrates.

Epitaxial growth of $LaNiO_3$ (*LNO*) films on single crystal substrates was achieved by PLD deposition technique at an oxygen pressure $P = 0.15mbar$ and keeping the substrate at a temperature $T = 700°C$. The number of laser pulses was varied to obtain films with nominal thickness between 2 and 35nm, according to previous growth

Substrate (mismatch*)	Film thickness (nm)	a (Å)	c (Å)	strain** (%)
STO (+2%)	14	3.89	3.80	+1.6%
LSAT (+1.0%)	14	3.86	3.82	+0.8%
LAO (−1.0%)	14	3.80	3.91	−0.8%
YAO (−3.1%)	14	3.82	3.85	−0.3%
YAO (−3.1%)	5	3.81	-	−0.5%
* mismatch = $(a_{subs} - a_{LNO})/a_{LNO}$				
** strain = $(a_{film} - a_{LNO})/a_{LNO}$	see substrate pseudo-cubic parameters in fig.1.2			

Table 7.1: In-plane (a) and out-of-plane (c) lattice parameters and calculated strain values for LNO films with the indicated thickness grown on the indicated substrates.

rate calibrations. We used single crystal substrates with a (001) orientation having a (pseudo)cubic lattice parameter smaller (YAO, LAO) or larger ($LSAT$, STO) than the pseudocubic parameter of LNO (3.83Å).

In the $\theta - 2\theta$ patterns of fig. 7.1 (a), we can observe the symmetrical reflections corresponding to (002) diffraction planes of substrates and films (the latter ones indicated by arrows) with a thickness of $14nm$. Biaxial strain promoted by cubic substrates is expected to induce a tetragonal distortion in the pseudocubic LNO lattice, elongating the lattice in the in-plane directions and therefore compressing in the out-of-plane c axis for tensile strain (case of STO and $LSAT$), while the contrary is expected in the cases of substrates inducing compressive strain (LAO and YAO). These expectations are in accordance with the position of the observed film reflections respect to the substrate: films on STO and $LSAT$ show reflections at higher angles than substrate (and also at higher angles than the expected reflection for bulk LNO), indicating compression of c axis, and films on LAO and YAO show the reflection at lower angles. However, the film on YAO, having the largest mismatch along the series, displays the film reflection at higher angles than expected, and close to the bulk LNO position, thus evidencing a lower effect of the biaxial strain.

The strained state of the films structure was furtherly explored by means of grazing incidence x-ray diffraction, which enables the access to symmetrical in-plane reflections. We explored the $(hh0)$ reflections of our films, thus accessing the in-plane lattice parameters of the films. As we observed by exploring the (110) reflection for films grown on YAO (see fig.7.1 (b)), the in-plane lattice parameter is not coincident with that of substrate (reflections appear at different angular positions), even for film thicknesses as low as $5nm$, thus confirming the rapid lattice relaxation occurring in films grown on YAO substrate (which have the largest mismatch with LNO: -3.1%). Films on other substrates however, show a barely coincident angular position for film and substrate in-plane (220) reflections, attesting for an almost fully strained state of the films. A summary of the lattice parameters obtained by exploring symmetrical reflections is shown in table 7.1.

So far we have considered the substrates to induce a tetragonal distortion, modifying the c/a ratio in the LNO films respect to bulk pseudocubic lattice parameters. However, a more intricate picture may be considered in LNO thin films, where the distortion induced by the substrate does not only modify the c/a ratio but can also promote rotations of the NiO_6 octahedra, thus furtherly lowering the structural symmetry. The oxygen octahedral rotations have been measured in epitaxial LNO films grown on

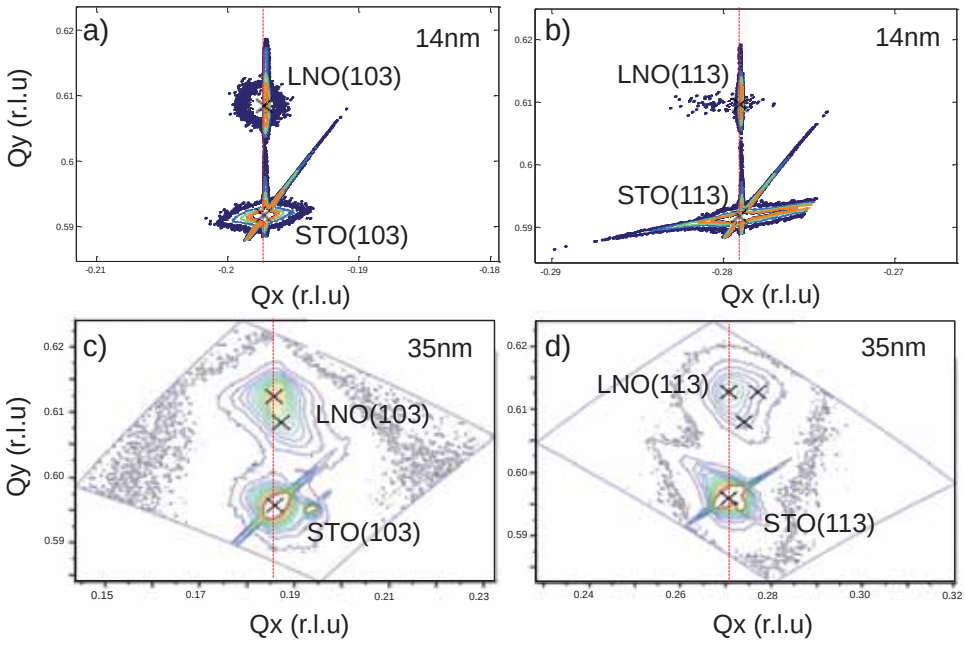

Figure 7.2: Reciprocal space maps around (103) (a) and (113) reflections in STO//LNO(14nm) , and around (103) (c) and (113) (d) reflections in STO//LNO(35nm)

LAO and STO substrates [127], showing different rotational patterns for both films, that force to describe the atomic structure by monoclinic space group. In order to explore to which extent this monoclinical distortion is relevant in our films, we measured different asymmetrical reflections by means of high resolution x-rays reciprocal space mapping in films deposited on STO substrates. In fig. 7.2(a) the RSMs around (103) and (113) reflections obtained for 14nm LNO film on STO are shown as example. Within the resolution of the diffractometer, a single LNO diffraction peak is observed[1] thus signaling a tetragonal structure in this film with no evident signatures of octahedra rotations that would induce the presence of extra peaks in the RSM.

The situation is however different in the case of thicker films. In fig 7.2(b), RSM around (103) and (113) reflections for 35nm LNO film on STO show a much broader structure where the contribution from different peaks can be evidenced: while still a predominant tetragonal fully strained phase is derived from the RSMs, the observed extra peaks signal a structural relaxation towards bulk LNO structure with the possible emergence of domains of lower symmetry phases that could be related to rhombohedral bulk *LNO* structural phase.

7.2.2 *Conduction properties*

The temperature dependent resistivity of LNO films was measured by four-contact Van der Pauw method, as described in appendix A. As expected, the films show a metallic behaviour in all range of temperatures. It is however noticeable (see fig. 7.3) an increasing resistivity when reducing films thickness and, for ultrathin films (2nm - fig.7.3(a)) a kink at low temperatures evidences a metal to insulator transition.

1 identical RSMs were obtained for the (-103), (013), $(0-13)$ and $(1-13)$ reflections

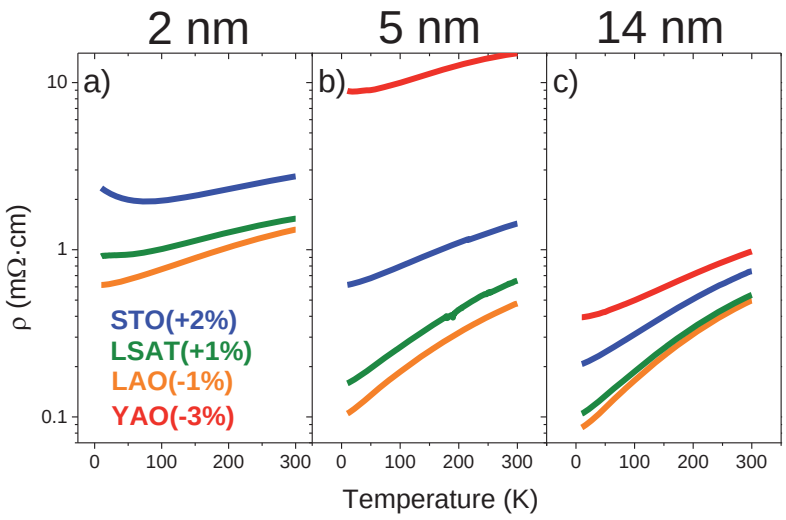

Figure 7.3: Temperature dependence of resistivity in $2nm$ (a), $5nm$ (b) and $14nm$ thick LNO films grown on the indicated substrates (in parenthesis the lattice mismatch between LNO and substrates)

For each thickness, a same sample sequence is observed: films grown on YAO display the largest resistivity, and the tendency of other samples is such that $\rho(STO) > \rho(LSAT) > \rho(LAO)$. While the increased resistivity of films grown on YAO can be attributed to the observed structural relaxation of these films, thus presenting more defects acting as scattering centers that disturb the metallic behaviour, in the rest of the films where similar sample quality and epitaxy is expected, the resistivity dependence can be related to strain effects. Indeed, the data suggest a favoured conduction for compressively strained films, while tensile strained films show reduced conductivity. This is even more evident for ultrathin samples (fig.7.3(a)), where film on LAO (mismatch -1%) show a clear metallic behaviour in all range of temperatures, while films on LSAT (mismatch $+1\%$) and -more markedly- on STO (mismatch $+2\%$) display a minima in the resistivity at low temperatures (below $50K$). The insulating behaviour at low temperatures was already reported for LNO films on STO [128, 129] and was associated to weak localization phenomena in ultrathin films, originated by quantum interference between the wavefunctions of scattered electrons, specially relevant at low temperatures, where the mean free path becomes comparable to the electron wavelength [130].

The temperature dependence of the resistivity could be fitted by using the following expression [130, 131, 132]:

$$\rho(T) = \frac{1}{\sigma_0 + a_1 T^p} + bT^\alpha \tag{7.1}$$

Here σ_0 is the classical Drude conductivity, while the term $a_1 T^p$ accounts for weak localization effects, where the exponent p reveals the relevance of electron-phonon (for $p = 3/2$) or electron-electron ($p = 1/2$) interactions in the localization effects. In our case, for thicker films ($t > 2nm$) a successful fitting at low temperatures was obtained for $p = 3/2$, while for the thinnest films ($t = 2nm$) a value of $p = 1/2$ resulted in better agreement with the experimental data, showing the relevance of electron-electron interactions in ultrathin films. The last term, bT^α, represents the temperature dependent scattering, where α varies depending on the scattering mechanism. At low temperatures electron-electron repulsion yields $\alpha = 2$, however in strongly correlated systems charge

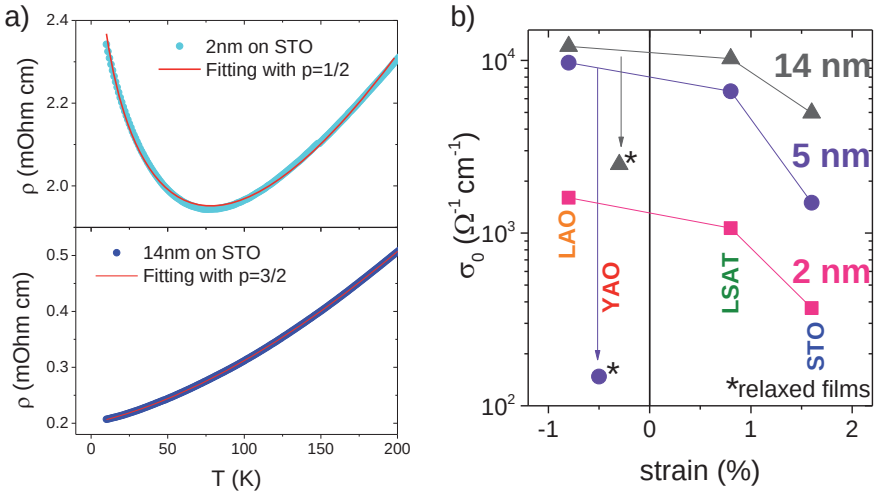

Figure 7.4: a) Fittings to experimental $\rho(T)$ curves using eq.7.1 for $2nm$ (top) and $14nm$ (bottom) LNO films on STO. b) Strain dependence of conductivity for LNO films with the indicated thicknesses

localization can reduce this value [133]. In our case, all fittings resulted in a value $\alpha \sim 1.3 - 1.4$, in accordance with previous reports [131, 133]. Some examples of the fittings obtained for LNO films on STO are shown in fig. 7.4(a).

The values of conductivity σ_0 obtained from the fittings (fig. 7.4 (b)) show the tendency of the conduction properties as a function of strain. As already observed in the resistivity curves, in fully strained films (those on LAO, LSAT and STO), larger conductivities are obtained for compressive strained films, while tensile strained films show reduced values. A large decrease is also found in partially relaxed films (those on YAO), not following the tendency observed for the other films in each thickness series.

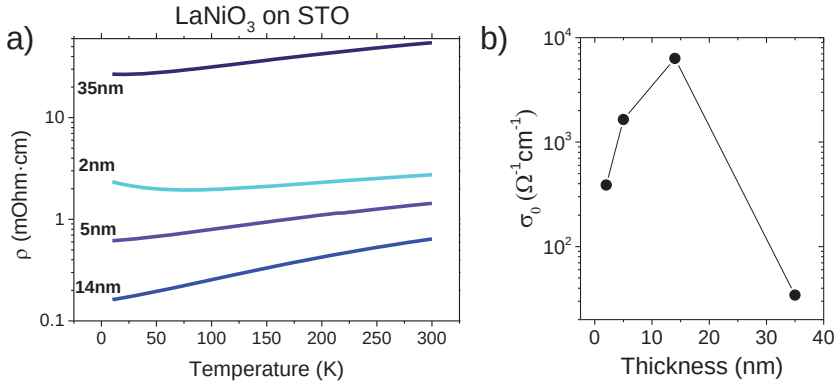

Figure 7.5: Temperature dependence of resistivity (a) and conductivity as a function of sample thickness (b) for LNO films on STO

The intimate link between structural and transport properties of the films is furtherly evidenced by studying the thickness dependence of resistivity curves. As shown in fig. 7.5 (a) for STO series, the conductivity increases with sample thickness in the range $2 - 14nm$, however, films with larger thickness ($35nm$) display a drop in the conductivity (fig. 7.5 (b)). This non-monotonic behaviour may be related to the observed structural transformations in the films, evolving with sample thickness. From the XRD studies

shown in previous section, it can be derived a tetragonal to (probably) rhombohedral structural transition with increasing film thickness, occurring between 14 and 35nm, presumably responsible of the conductivity drop. In fact, domain formation, associated to the rhombohedral distortion, can introduce twin boundaries or other extended defects affecting the conduction mechanisms in these samples.

7.3 STRAIN AND SURFACE INDUCED ORBITAL OCCUPANCY IN $LaNiO_3$ EPITAXIAL THIN FILMS

To explore in detail the origins of the strain and thickness dependent transport properties in LNO films, we examined the $Ni-L$ edge (in this section) and $O-K$ edge (in the next section) XAS in order to get insight into the distribution of $Ni-3d$ electrons and their hybridization with $O-2p$ states, respectively.

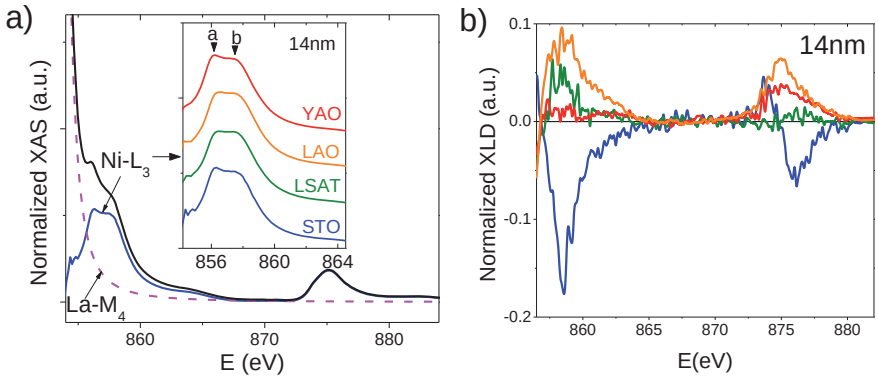

Figure 7.6: a) XAS spectrum for 14nm LNO film on STO (black) and resultant XAS curve (blue) after substraction of lorentzian fit to $La-M_4$ peak (dashed line); inset: zoom of La-peak subtracted XAS in the $Ni-L_3$ edge for 14nm LNO films grown on the indicated substrates. b) Normalized XLD spectra of 14nm LNO films.

$Ni-L$ edge absorption spectra were acquired at 300K in grazing incidence configuration (30 degrees incidence respect to sample surface) with linear polarization (both parallel and almost perpendicular to sample surface) measuring the total electron yield. The isotropic XAS spectra were obtained as the average of intensity obtained with both linear polarizations, $(I_{\parallel}+I_{\perp})/2$. In fig.7.6(a) the XAS spectrum of 14nm sample grown on STO is shown (black line, main panel). The $La-M_4$ edge absorption is unavoidably overlapping part of the $Ni-L_3$ edge, so a lorentzian fit to the La peak was subtracted from spectra, in order to leave alone the $Ni-L_3$ edge contribution. $Ni-L_2$, on the other hand, is not affected by any overlapping with La peaks.

The resultant $Ni-L_{2,3}$ spectrum resemble that of Ni^{3+} (see refs. [121, 122, 134, 135, 136]) and presents a double peak structure in the $Ni-L_3$ edge, as indicated in the inset of fig. 7.6(a) as peaks a and b. The splitting and relative intensity of these peaks have been associated to the $Ni-O$ hybridization strength [121, 122, 135, 136]. In our case, however, these two parameters (energy splitting and relative intensity) do not variate appreciably (within the error introduced by $La-M$ edge substraction) along the strain series. Therefore, as we will see in next section, other methods need to be employed to study the evolution of $Ni-O$ hybridization in these samples.

Nevertheless, the linear dichroic signal, $XLD = I_{\parallel}-I_{\perp}$ is not greatly affected by $La-M_4$ edge absorption signal and can provide reliable information on the orbital oc-

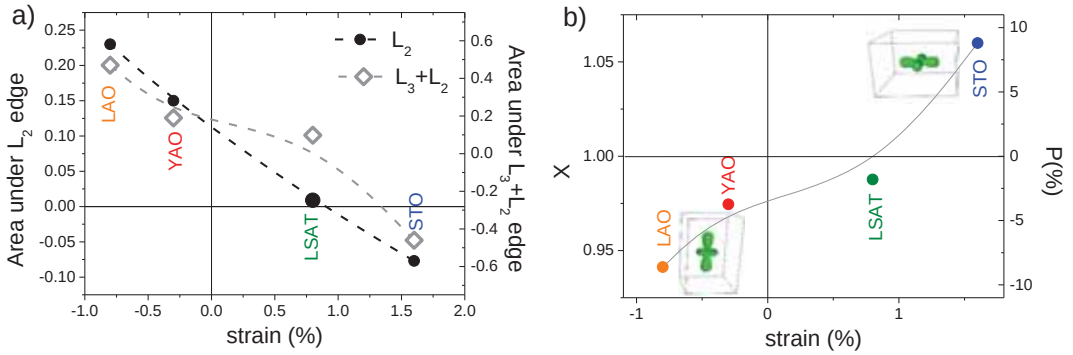

Figure 7.7: a) Area under XLD at L_2 edge (full circles) and under full spectra (empty rhombi). b) Holes ratio (left) and orbital polarization (right) obtained for $14nm$ thick LNO films as a function of strain in the films

cupancy of the single e_g electron in the $Ni^{3+} - 3d$ states (having a low spin configuration $3d^7 : (t_{2g}^6 e_g^1)$) . Indeed, the XLD spectra of $14nm$ LNO samples (fig.7.6(b)), normalized to $Ni - L_2$ absorption, reveal profound strain induced modifications in the electron occupancy of d orbitals. As observed in the figure, sample on LAO (compressively strained) shows a clear positive signal in both L edges, thus indicating larger absorption for in-plane oriented orbitals (more available states at in-plane orbitals), while sample on STO (tensile strained) displays a clearly negative signal (more available states in out-of-plane orbitals). Samples on LSAT (slight tensile strain) and on YAO (compressive - partially relaxed) show intermediate-barely positive signals.

The integrated area under XLD (in the region $858 - 882eV$) resulted in analogous tendency as the integration in the L_2 edge region - not affected by $La - M_4$ edge (fig. 7.7 (a)), thus proving the robustness of the data. In the same manner as in manganites (chap. 4), we can apply the sum rule to the XLD [15, 74], to obtain the ratio of holes in the $3d - e_g$ levels, $X = \frac{h(3z^2-r^2)}{h(x^2-y^2)}$. The results, depicted in fig. 7.7 (b) as a function of strain in the films, demonstrate the effective tunability of orbital occupancy induced by Jahn-Teller distortion in the films, favouring the occupancy of $x^2 - y^2$ ($3z^2 - r^2$) orbitals for tensile (compressive) strain. The orbital polarization can be calculated as:

$$P = \frac{n_{x^2-y^2} - n_{3z^2-r^2}}{n_{x^2-y^2} + n_{3z^2-r^2}} = \left(\frac{4}{n_{e_g}} - 1\right)\frac{X-1}{X+1} \tag{7.2}$$

, where the factor 4 accounts for all spin up and spin down e_g states (while for LSMO we only counted with spin up states in eq.4.3). Assuming a constant number of e_g electrons $n_{eg} = 1$ along the series, the orbital polarization is altered from -9% to 9% approximately (fig.7.7-right axis), within the explored strain regime (from -1% to $+1.6\%$). This result thus is at odds with previous report showing an asymmetric orbital response to strain in LNO films [125], but seems to be coherent with more recent results in LNO superlattices grown on different substrates imposing tensile strain [16].

Being revealed the strain induced orbital polarization, we studied the thickness dependence of absorption signal in order to ascertain the surface effects on the orbital configuration in ultrathin LNO films by measuring the $Ni - L$ edge XAS/XLD of STO samples series in the thickness range $2 - 35nm$. It is firstly noticed, in the XAS spectra (fig. 7.8(a)) an evolution of the absorption signal, specially evident in the $Ni - L_3$ edge, where a large modification in the double peak structure previously mentioned is

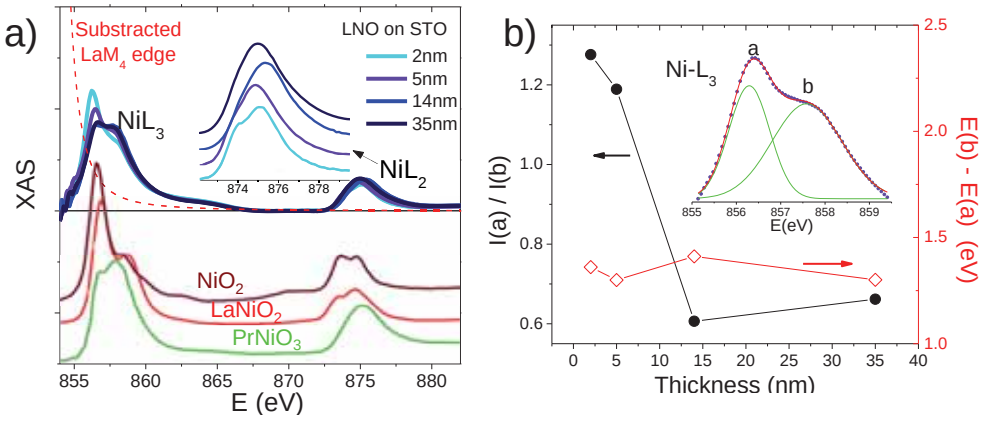

Figure 7.8: a) Top: $Ni-L$ edge XAS spectra of LNO films grown on STO, for different sample thicknesses; inset in top: zoom of $Ni-L_2$ edge; Bottom: Reference XAS spectra from ref.[134]. b) Intensity ratio between a and b peaks in $Ni-L_3$ edge, obtained from gaussian fitting as shown in the inset for $5nm$ LNO sample.

observed. Comparing our experimental spectra with others reported in literature (see bottom panel of fig.7.8(a)), we can identify a spectral shape resembling Ni^{3+} for thicker films ($\geq 14nm$), however, thinner films, displaying a prominent larger intensity in the low energy region of the $Ni-L_3$ edge, and an incipient double peak structure in the $Ni-L_2$ edge (see inset of fig. 7.8(a)) shows a closer similitude to the reported spectra associated to Ni^{2+}.

These spectral variations can also be interpreted in terms of modified orbital hybridization. Indeed, the origin of the double peak in Ni^{3+} edge is attributed to a multiplet structure due to the presence of ligand holes ($\underline{L}$) from $O(2p)$ hybridized states, leading to a Ni ground state configuration $3d^7 + 3d^8\underline{L} + 3d^9\underline{L}^2$, where the relevance of ligand terms depends on the degree of hybridization. Experiments and calculations show that in the insulating state a clear splitting of this double peak structure is observed [135]. While the splitting energy was directly correlated with the charge transfer energy (the energy necessary for one $O(2p)$ electron to jump to the $Ni(3d)$ state) [121] it was shown that similar values of energy splitting could be found for different $RNiO_3$ films, and splitting was only dependent on the measurement temperature, showing a larger value in the insulating regime than in the metallic one [136]. On the other hand, the intensity ratio between the peaks (named a and b as seen in fig.7.8(b-inset)) was shown to be strongly dependent on the R ion, increasing $I(a)/I(b)$ for decreasing R cation size [135], thus evidencing the influence of decreased hybridization on the XAS spectra. This increasing ratio was also observed in $SmNiO_3$ [122] and $EuNiO_3$[121] films by imposing a tensile strain.

In our case, although we cannot directly appreciate the strain evolution in our films, the peaks ratio -obtained by gaussian fitting of a and b peaks in the $Ni-L_3$ measured at $300K$ (see inset in the fig.7.8(b))- show a clear evolution with sample thickness (fig.7.8(b-left axis)), notably increasing for $t < 14nm$. According to previous observations, this thickness dependence points to a weaker hybridization at the surface layers in the films, that would explain the depleted conduction properties observed in thinner films. On the other hand, the energy splitting between both peaks remains at a constant value of $1.3 \pm 0.05eV$ (fig.7.8(b-right axis)).

The orbital occupancy of the $3d$ states also shows a pronounced evolution with thickness. As shown in fig. 7.9(a), the XLD signal, mainly negative for $14nm$ film, as cor-

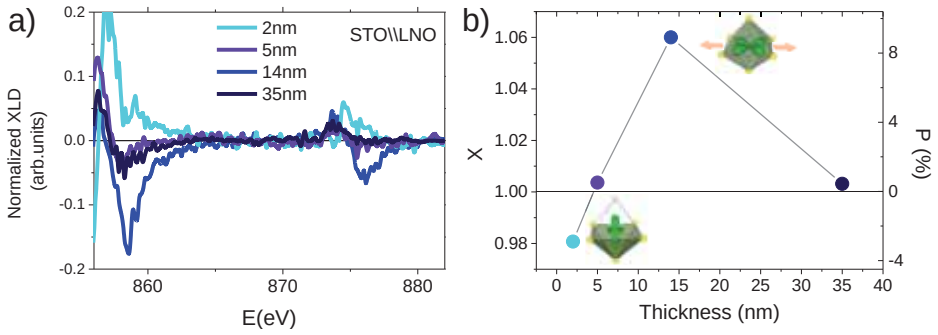

Figure 7.9: a) Normalized XLD spectra of LNO films grown on STO with different sample thicknesses. b) Holes ratio (left) and orbital polarization (right) obtained for STO//LNO films as a function of sample thickness

responding to tensile strain state in the films grown on STO, becomes positive when reducing the thickness, indicating a reversed orbital occupancy at the surface. Interestingly, thicker film ($35nm$) escapes from the observed tendency, showing a reduced XLD signal. The evolution of XLD signal with sample thickness, translated to holes ratio X and orbital polarization P, is represented in fig.7.9(b).

These data can be interpreted in the same way as the thickness dependent XLD found in manganite thin films (chap. 4): in thicker films, where the contribution of *bulk* orbital polarization -induced by strain effects- dominates the dichroic signal, the sign of the XLD is determined by this strain induced polarization; however, by reducing the sample thickness below the TEY probing depth ($\sim 3nm$), the signal originated at the surface layers becomes more relevant to the total XLD signal, and surface induced orbital polarization dominates the XLD. In this case, tensile strained films on STO show a positive orbital polarization in the *bulk* - as expected from strain effect, but a negative orbital polarization emerges at the surface, identically to LSMO films studied earlier in this thesis. The origin of this negative polarization can be attributed to surface symmetry breaking, favouring a $3z^2 - r^2$ occupancy, due to the reduced Ni coordination in NiO_2 terminating layers [137]. Furthermore, polar distortions observed at the surface of LNO films can also induce relative displacements between oxygen and cations in the out-of-plane z direction [138]. The elongated d_{Ni-O} distances in z also favours the occupancy of $3z^2 - r^2$ orbitals and polar distortions induce a decrease in the $Ni - O - Ni$ angles that could be responsibles of the weakened hybridization observed in the thinnest films.

From these conclusions we can therefore give an explanation to the observed asymmetric strain effects on the orbital polarization observed in previous reports [125]: while in the case of compressive strained films both strain and surface effects promote a $3z^2 - r^2$ occupancy in the e_g levels, for tensile strained films, surface layers show an opposite orbital occupancy to that of underneath layers and the resultant XLD signal will depend on the relative contribution of both effects to the total signal.

In thicker films, where structural relaxation takes place, strain is shown to be less effective at modulating the orbital occupancy, and in the most superficial layers -where structural relaxation is expected to be more pronounced- both significant octahedra rotations and reduced coordination can profoundly affect the orbital polarization, leading in this case to an almost negligible orbital polarization.

7.4 SPECTROSCOPIC EVIDENCE OF STRAIN-INDUCED MODIFICATION OF ORBITAL HYBRIDIZATION

Epitaxial strain, as discussed above, is known to promote modifications in the $Ni-O$ distances and $Ni-O-Ni$ bonding angles through octahedra distortions and rotations, modulating the $Ni(3d)-O(2p)$ orbital overlapping that regulates the hybridization strength responsible for the semicovalent character of nickelates.

This orbital overlapping is also responsible for the availability of excited states related to $O(2p)$ levels hybridized with $Ni(3d)$, that can be explored by $O(1s) \rightarrow O(2p)$ transitions originating the $O-K$ absorption edge. In fig. 7.10 (a) $O-K$ edge spectra of $14nm$ LNO films grown on LAO, LSAT and STO substrate are shown. The spectra have been normalized in the high energy region (above $550eV$). Each of the peaks observed in the spectra is related to hybridized states between oxygen and adjacent cations [139], as indicated in the figure. Of interest here is the prepeak showing up below $530eV$, associated to hybridization with $Ni(3d)$ states. The more available $O(2p)$ states (due to ligand holes introduced by hybridization with $Ni(3d)$), the larger absorption intensity will be observed in this prepeak. Thus, the $O-K$ prepeak intensity provides a measure of the orbital hybridization strength, that can be quantified by calculating the area under the prepeak [140].

Performing this integration in the spectra of the $14nm$ sample series leads to the values indicated in fig.7.10 (b-black points) as a function of strain, evidencing a strain modulation of the hybridization strength. In addition, the energy threshold of the prepeak shows a shift towards lower energies for increasing tensile strain (fig. 7.10 (b-red triangles), in accordance with previous reports [125]. This shift towards lower values can be explained as a result of larger occupancy of $O(2p)$ levels for tensile strained films, resulting in a better shielding of nuclear charge and consequent reduction of the binding energy of $O(1s)$ level [141].

Examination of the spectra for $5nm$ sample series (see fig. 7.10 (c)), resulted in analogous strain tendency of the prepeak intensity and energy threshold (fig. 7.10 (d)). It is however noticeable a double peak structure observed in the spectrum of the LNO film on STO, that could indicate the presence of divalent Ni^{2+} states for this sample, as shown in ref. [139]. Nevertheless, it cannot be ruled out the contribution from oxygen signal coming from STO substrate, which is known to have a contribution around $530eV$ [142].

Having into account the results depicted in section 7.2.2, we can correlate the macroscopic conduction properties of the films with the hybridization strength evidenced by spectroscopic measurements. This is represented in fig. 7.11, where the relationship between the $O-K$ edge prepeak area -affected by the strain in the films- and the conductivity of the samples is plotted. The induced distortions introduced by substrate-imposed strain in the films modulate the bandwidth via modifications of the $Ni-O$ hybridization. A larger hybridization (and thus larger bandwidth) is obtained in films subjected to a compressive strain, showing the largest conductivity values. Tensile strain reduces the hybridization and consequently -due to reduced bandwidth- the conductivity in the films gets depleted.

In $RNiO_3$ nickelates the transfer integral between $Ni(3d)$ and $O(2p)$ (proportional to the bandwidth) is given by [138]:

$$t_{pd} = K\frac{\sin(\theta/2)}{d_{Ni-O}^{3.5}} \tag{7.3}$$

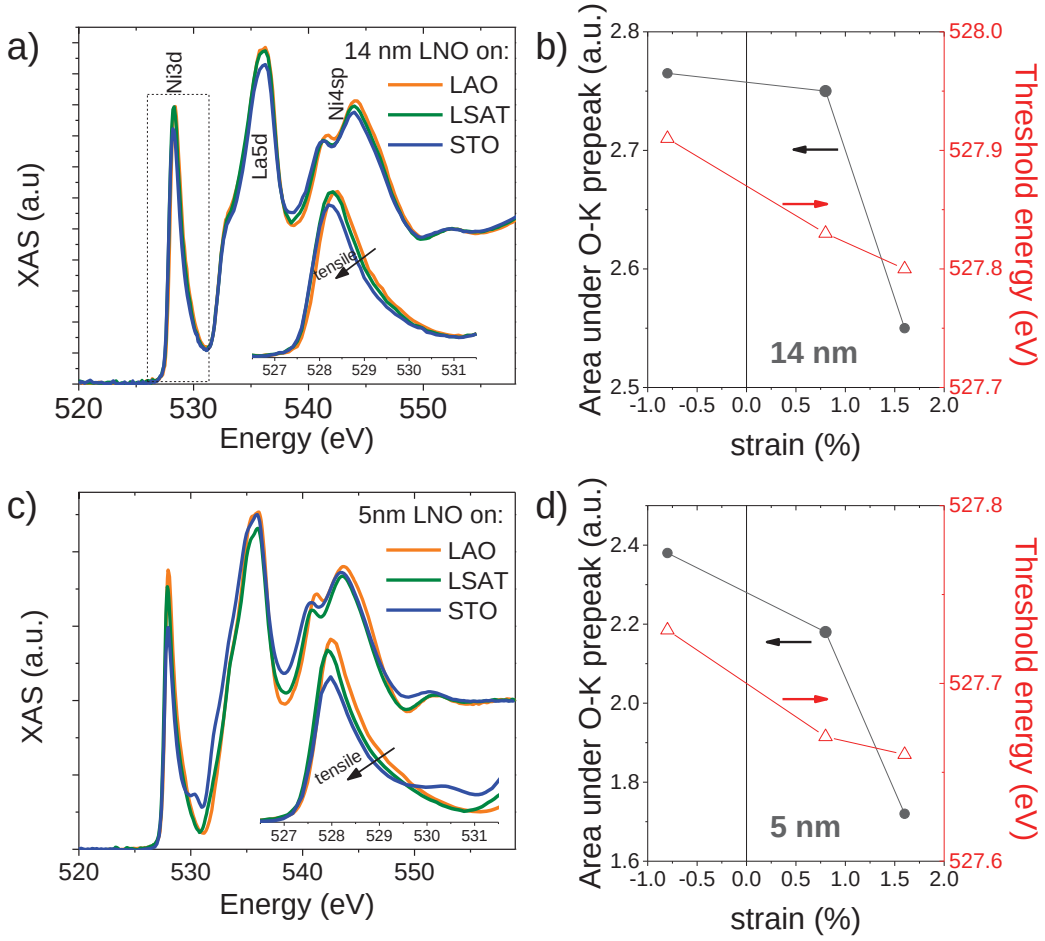

Figure 7.10: $O-K$ edge XAS spectra of 14nm (a) and 5nm (c) LNO films; in the insets, a zoom of the pre-peak region is displayed. Area under $O-K$ edge prepeak as a function of strain in the films for 14nm (b) and 5nm (d) thick films.

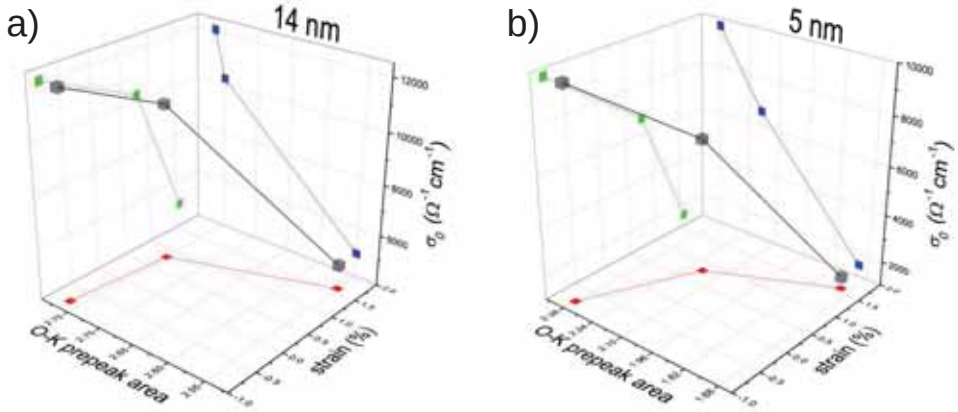

Figure 7.11: Plots showing the dependence of sample conductivity on the $O-K$ prepeak area and films strain for 14nm (a) and 5nm (b) thick LNO films.

, where θ and d_{Ni-O} are the $Ni-O-Ni$ in-plane bonding angle and $Ni-O$ in-plane bond distance, and K is determined from the $p-d$ orbital covalent hopping integral ($K = 13.7eV\mathring{A}^{3.5}$[138]). Values of θ and d_{Ni-O} have been reported for LNO films grown on STO and LAO ($\theta^{STO} = 165.8^{\circ}$, $\theta^{LAO} = 164^{\circ}$, $d^{STO}_{Ni-O} = 1.968\mathring{A}$, $d^{LAO}_{Ni-O} = 1.916\mathring{A}$)[127], leading to transfer integral values $t^{STO}_{pd} = 1.27eV$ and $t^{LAO}_{pd} = 1.39eV$. Thus, compressive strained films (LNO on LAO) are expected to display a larger transfer integral (larger bandwidth) than tensile strained films (LNO on STO), which is in accordance to our results showing larger hybridization (and larger conductivity) for compressive strained films. According to the structural data extracted by May et al. [127], the increased overlapping leading to enlarged hybridization would be mainly dictated by the reduced in-plane $Ni-O$ distances imposed by compressive strain.

7.5 SUMMARY

We have grown LNO films on different substrates, achieving fully strained epitaxial growth for films grown on substrates having a mismatch under 2% and for films having a thickness under $15nm$. Films grown on substrates with a lattice parameter 3% lower than bulk LNO (YAO) grow almost fully relaxed even for film thicknesses as low as $5nm$, while thicker films on other substrates (STO) start showing relaxation for film thicknesses larger than $14nm$.

It was shown that in fully strained films, the conductivity of the samples could be correlated with the strain state, showing larger conductivity values the films subjected to a substrate imposed compressive strain. The increased conductivity values in these samples could also be correlated to a larger degree of $Ni(3d) - O(2p)$ hybridization. However, ultrathin films show a large depletion of the metallic character as well as notable decrease in the hybridization strength.

The strain modulation of this hybridization could be correlated to the induced distortions in the $Ni-O$ in-plane distances: increased distances induced in tensile strained films reduce the orbital overlapping thus reducing the effective bandwidth. On the other hand, at the surface of the films, reduced coordination and polar distortions promote both charge localization and reduction of $Ni-O-Ni$ bond angles, also reducing the bandwidth at the surface layers.

The effect of these distortions is also noted in the orbital polarization: the orbital order of the films was shown to be strain-controlled, favouring the occupancy of x^2-y^2 ($3z^2-r^2$) orbitals in tensile (compressive) strained films. However, in ultrathin films, a relevant orbital polarization induced by surface symmetry breaking is evidenced, promoting the occupancy of $3z^2-r^2$ orbitals.

8

ORBITAL RECONSTRUCTION IN HIGHLY CONDUCTIVE OXIDE INTERFACES

At the interface between two band gap insulators, a highly conductive 2-dimensional electron gas emerges, in conjunction with a band reconstruction, induced by the quantum confinement at the interface. Here we show that the band symmetry of the interfacial states can be controlled with the crystallographic orientation.

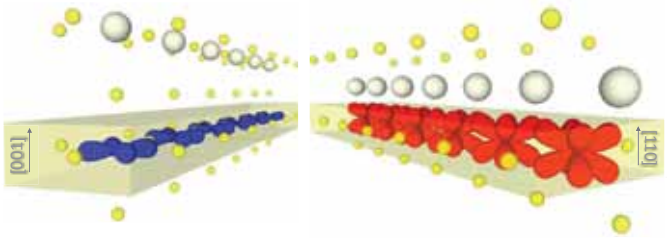

8.1 INTRODUCTION

Probably one of the most celebrated breakthroughs in the field of oxide materials (together with the discovery of high-T_C cuprate superconductors or the colossal magnetorresistance in manganites) has been the finding of metallic behaviour at interfaces between two band insulators: $LaAlO_3$ (LAO) and $SrTiO_3$ (STO) [143]. The conductance in these kind of heterostructures is highly confined (within few unit cells), forming a 2-dimensional electron gas (2DEG) with a sheet carrier density above one order of magnitude higher as compared to conventional semiconductors structures, where this kind of quantum well (QW) confinement can also be observed.

Interestingly, the 2DEG is only observed in STO/LAO heterostructures with STO-TiO_2 terminating planes [143] and for LAO thicknesses larger than a critical value [144], pointing to a microscopic origin related to a electrostatic reconstruction at the interface [143]. However, the dependence on oxygen content during growth[143, 145] and the recent observation of 2DEG at interfaces with crystal orientations not showing a polar discontinuity [146, 147, 148] or even in STO surfaces cleaved in ultra-high vacuum [149], suggest the influence of different mechanisms like the formation of oxygen vacancies generating free carriers at the interface [150, 151, 152].

Independently of the still unclear origin of the 2DEG in these systems, these TMO interfaces provide an ideal playground for the exploration of new physics at interfaces. Indeed, the much narrower bandwidth of d electronic levels of transition metals -as compared to the wide s or p bands- results into the emergence of complex electronically correlated states not present in the traditional semiconductors. Epitomizing this complexity, both magnetism and superconductivity have been reported to emerge at the LAO/STO interface [153, 154, 155, 156]. The microscopic nature of the interface magnetism has been related to the orbital energy hierarchy of $Ti(3d)$ crystal field splitted t_{2g} and e_g levels [157, 158] and even spectroscopic investigations emphasize the specific role of $t_{2g}(d_{xy})$-states regarding the emergence of magnetism [159]. While the vast majority of these studies have been carried out on (001)-oriented oxide quantum wells, the recent

discovery of 2DEGs generated along other crystal orientations [146, 147, 148], opens up novel perspectives in the physical understanding of low-dimensional complex phases. Given that these novel quantum wells are confined along different crystal orientations, the different spatial distributions of t_{2g} states with respect to the axis of confinement necessarily implies an different orbital configuration depending on the orientation of the quantum wells.

In this chapter we will explore the orbital hierarchies of the $Ti(3d)$ states on (001) and (110) oriented STO\\LAO interfaces. By comparing the results obtained for both orientations and for bare STO surfaces, we will determine the influence of the quantum well orientation and the emergence of 2DEG on the orbital symmetry of the lowest energy available states at interfaces.

8.2 ORBITAL SYMMETRY AND HIERARCHY AT (001) AND (110) LAO/STO INTERFACES

Samples were grown by PLD assisted with in-situ RHEED on (001) and (110)-oriented STO single crystals, following the growth procedure described in refs. [146, 160]. LAO films of different thicknesses t were deposited, with $t = 0$ and 8 monolayers (MLs) for (001) and $t = 0$, 2, 9 and 18 MLs for (110), respectively. Samples with $t = 0$ correspond to bare (001) and (110) STO substrates. Importantly, post-growth in-situ annealing was performed to promote the removal of residual oxygen vacancies [152].

The low temperature magnetotransport backs up the two-dimensional character of these quantum wells [148] and scanning transmission electron microscope (STEM) images certify that (001) and (110)-oriented interfaces are atomically flat and that any reconstructed surfaces with local $\{100\}$ microfacets can be ruled out for the (110)-interfaces [148], thus the different structural characteristics of both interfaces should lead to different electronic band character, as we will show in the following.

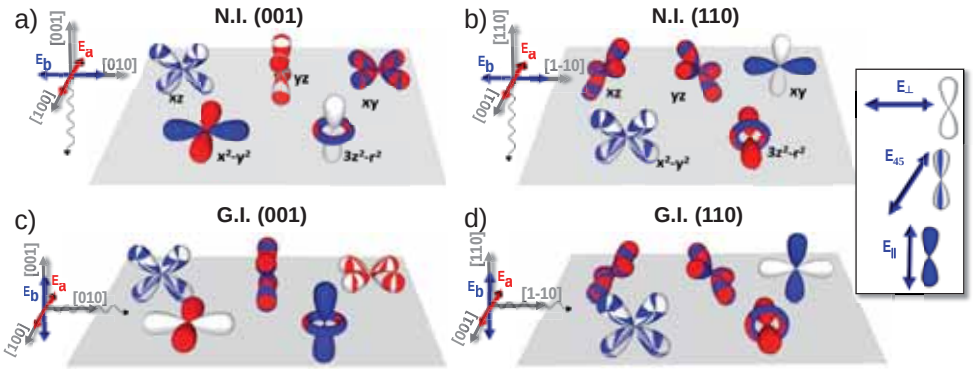

Figure 8.1: Schematics of the interaction of the linearly polarized light with the d-orbitals for normal incidence of x-rays on (001)-oriented samples (a) and (110)-oriented samples (b); same schematics for the case of grazing incidence on (001) samples (c) and (110) samples (d). Colour legend is shown in the box.

XAS spectra at the $Ti - L_{2,3}$ edges were acquired with linear x-rays polarization at room temperature in TEY mode, under different measurements geometry (normal and grazing -60deg respect to normal- incidence). Fig.8.1 shows a schematic description of the relationship between the photon beam linear polarization and the orbital symmetries in the different geometries for both sample orientations. In all cases, the linear

polarization vector E_a (red) was kept in-plane, i.e. $E_a||[100]$ for (001)- and $E_a||[001]$ for (110)-samples, respectively. Instead, polarization E_b (blue) was either in plane (normal incidence) or out-of-plane (grazing incidence). The orientation of E_b with respect to the crystal axes is given in figs.8.1(a-d) for each case. Photons interact with d-orbitals according to cross sections that depend on orbital symmetry. This interaction is the strongest when light polarization is along the direction of the orbital lobes, while it is null when they are normal with respect to each other [161]. The sketch in the insert of fig. 8.1 graphically depicts the different possibilities of electric field projection onto the orbital lobes (largest for coloured lobes, minimal for blank lobes). As a result, the TEY intensities I_a and I_b were recorded for the two orthogonal E_a and E_b polarizations, and the XLD signal was defined as the difference $XLD = (I_a - I_b)$, normalized to the maximum intensity of the averaged absorption $XAS = (I_a + I_b)/2$ at the L_3 edge.

The main peaks featured in the XAS spectra result from transitions from $Ti - 2p_{1/2}(L_2)$ and $Ti - 2p_{3/2}(L_3)$ core levels to unoccupied $Ti(3d)$-states and have a contribution from t_{2g} (d_{xz}, d_{yz}, and d_{xy}) and e_g (d_{3z2-r2} and d_{x2-y2}) levels (figs.8.2(a,b)). As in the case of Ti^{4+}, d states are empty, an XLD signal will only be detected if a energy splitting exists in the d states, thus yielding a polarization dependent energy position of the edges corresponding to each d state. As a result, Ti^{4+} XLD signal shows a significant derivative-like spectrum.

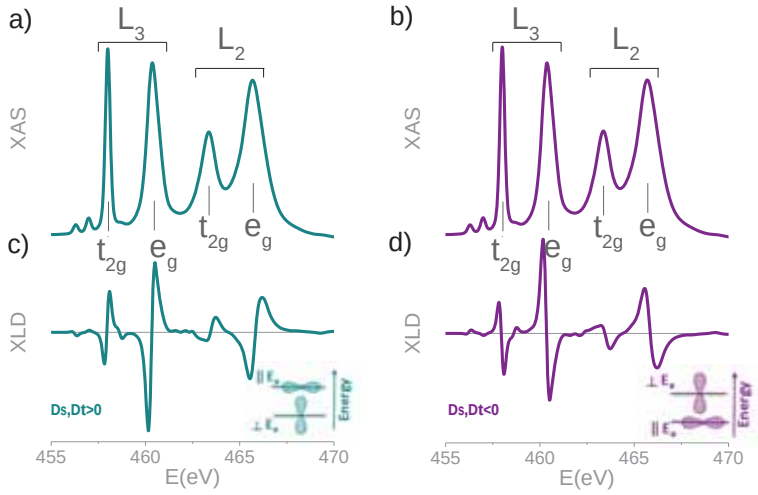

Figure 8.2: a) Scheme of relative energy position of d states under octahedral (left) and tetragonal (right) crystal fields. Simulations of XAS (b,c) and XLD signal (d,e) for Ti^{4+} in tetragonal crystal field with positive (b,d) and negative (c,e) distortion parameters. The corresponding orbital hierarchy is shown, as related to the relative orientation of light polarization and orbitals.

This XLD can be simulated by using the CTM4XAS software [73] in which tetragonal crystal field parameters Ds and Dt were defined.[1] From the shape of the XLD spectra, information on the orbital hierarchy can be inferred, and from the fitting to the simulated spectrum, estimated values of energy splittings for e_g ($\Delta e_g = 4Ds + 5Dt$) and t_{2g} ($\Delta t_{2g} = 3Ds - 5Dt$) levels can be obtained (see fig.8.2(a)).

While the averaged absorption spectra ($XAS = (I_a + I_b)/2$) for different tetragonal distortion parameters are indistinguishable (figs.8.2(b,c)), the XLD signal -corresponding

1 For the simulations, we used $10Dq = 2.0eV$, charge transfer parameters: $\Delta = 3eV$, $Udd = 4eV$ and $Upd = 6eV$, and Lorentzian broadenings: $0.06eV$ (for $L_3 - t_{2g}$), $0.22eV$ (for $L_3 - e_g$), $0.4eV$ (for $L_2 - t_{2g}$) and $0.5eV$ (for $L_2 - e_g$).

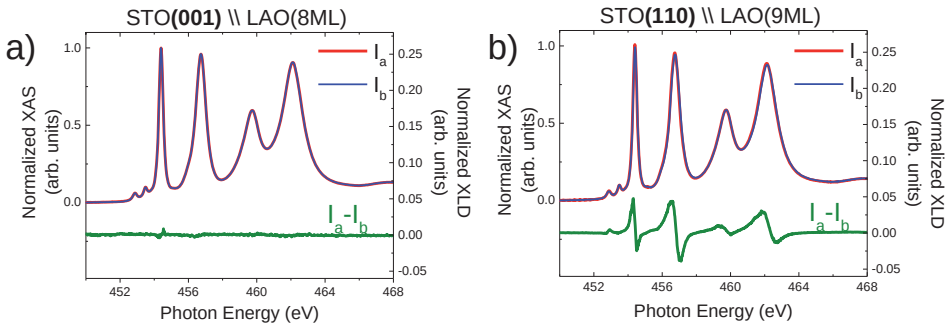

Figure 8.3: a) Normalized XAS spectra of sample LAO $(8ML)$/STO(001) measured at normal incidence. XAS curves are plotted for $E_a||[100]$ (I_a) and $E_b||[010]$ (I_b) polarizations. The XLD spectra $(I_a–I_b)$ is also shown. b) Normalized XAS and XLD spectra of sample LAO $(9ML)$/STO(110). Here the polarizations are $E_a||[001]$ (I_a) and $E_b||[1-10]$

to grazing incidence configuration- is strongly dependent on these parameters. In fig.8.2(d), the simulated XLD signal for positive tetragonal distortion parameters $(Ds, Dt > 0)$ is shown. Under this imposed distortion, the resultant orbital hierarchy is such that orbitals having lobes preferentially interacting with out-of-plane polarization (E_b) are lower in energy. While for (001) orientation these orbitals are xz, yz and $3z^2 - r^2$, for (110) case the corresponding out-of-plane oriented orbitals are xy and $x^2 - y^2$. The opposite case is presented in fig.8.2(e), where the XLD signal simulated for $Ds, Dt < 0$ is plotted. This signal, being inverted to the XLD depicted in fig.8.2(d), represents the reverse orbital hierarchy, in which orbitals preferentially interacting with in-plane polarization (E_a) are lower in energy. In this case for (001) orientation these orbitals are xy and $x^2 - y^2$, while for (110) orientation xz, yz and $3z^2 - r^2$ are the orbitals lowered in energy.

Consequently, the observation of XLD spectra of the same sign for both orientations necessarily implies that the degeneracy of t_{2g} and e_g bands is broken in opposite signs for (001)- and (110)-oriented samples.

We first discuss experiments done at normal incidence. Due to the inherent four-fold in-plane symmetry for (001)-samples, light should be absorbed equally for both photon polarizations. This is confirmed by the negligible XLD of the (001)-LAO/STO interface $(t = 8$ MLs) shown in fig.8.3(a). In contrast, the anisotropic character of (110)-interfaces imprints a distinctive nonzero XLD, as observed in the spectrum of the (110)-interface (t = 9 MLs), see fig.8.3(b).

In order to unveil the details of the reconstructed electronic structures, XAS spectra were measured also at grazing incidence (60 degrees away from the normal) that, in turn, allowed us quantifying the splitting between the t_{2g} and e_g sub-states. The XAS and XLD spectra recorded on bare STO substrates are shown in fig.8.4(a-d, black curves). The XLD spectra for both (001) and (110) orientations show a significant dichroic signal, revealing a removal of the orbital degeneracy at the STO surface. Both XLD spectra show the same spectral shape, signaling, as stated previously, an inverted orbital hierarchy for these two orientations. More specifically, the sign of the XLD implies that the lower energy states have xz/yz and $3z^2 - r^2$ character for (001)-surfaces, while they have xy and $x^2 - y^2$ character for (110)-surfaces. The observed degeneracy breaking at STO surfaces mimics the behaviour observed for (001)- and (110)-oriented manganites

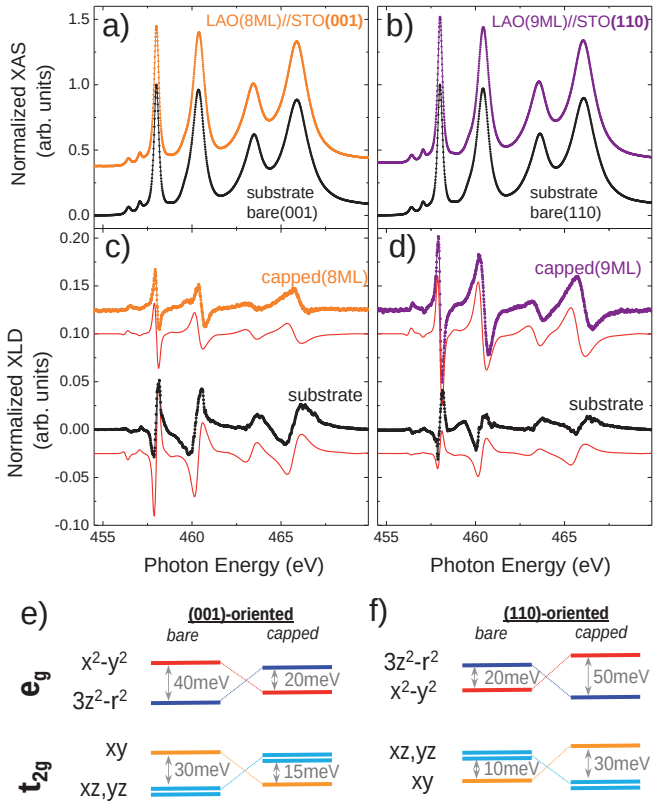

Figure 8.4: Normalized XAS spectra for bare STO surfaces as well as LAO/STO interfaces for orientation along [001] (a) and [110] (b). The LAO thickness is 8*ML* for (001)- and 9*ML* for (110)-interfaces. The corresponding XLD spectra are shown for (001)- and (110)-oriented samples in (c) and (d), respectively. Red lines correspond to XLD simulations by using CTM4XAS, shifted for clarity. The energy splittings for (001)- and (110)-oriented samples are sketched in (e).

presented in chap.4, in which the symmetry rupture at free surfaces is responsible for the orbital reconstruction, favouring the orbitals oriented in the out-of-plane direction.

The XLD spectra of STO capped by LAO layers was probed in samples with a number of LAO monolayers larger than the critical thickness required to obtain a 2DEG ($t_c = 4MLs$ for (001) [143], $t_c = 7MLs$ for (110) [146]). XAS/XLD on (001)STO capped with 8*ML* of LAO and (110) capped with 9*ML* are shown in fig.8.4(a-d). The XLD signal appears inverted with respect to bare STO surfaces, for both sample orientations, indicating that the electronic structure was reconstructed from that of bare surfaces, that is, for (001) LAO-capped substrates the lower energy states are xy and $x^2 - y^2$, while for (110) LAO-capped substrates they are xz/yz and $3z^2 - r^2$. In consequence, the degeneracy within the t_{2g} and e_g sub-bands is broken in opposite directions for bare and capped surfaces.

For a quantitative description of the reconstructed bands we performed atomic model calculations using the CTM4XAS software using typical crystal field and charge transfer parameters for Ti^{4+} in octahedral coordination [162, 163] and varying the tetragonal distortion parameters *Ds* and *Dt* to fit the experimental XLD curves. The simulated spectra, included in fig.8.4(c,d-red lines, shifted for clarity), show good agreement with experimental data.

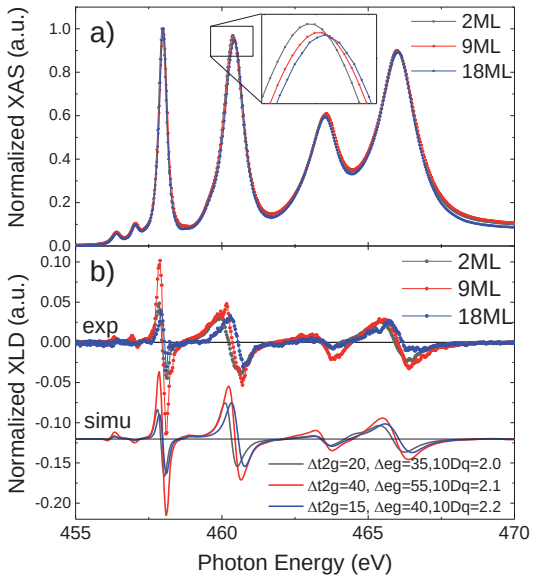

Figure 8.5: a) Normalized XAS spectra for (110)LAO/STO samples with LAO thickness $t = 2$, 9 and $18ML$; inset: zoom of $L_3 - e_g$ peak. b) Normalized XLD spectra from samples in panel a (top) and corresponding simulated XLD spectra with the indicated parameters.

Fig. 8.4(e) summarizes all the information extracted from CTM4XAS simulations: we observed that:

1. In (001)-oriented interfaces xy orbitals are lower than xz/yz levels by $15meV$, whereas $x^2 - y^2$ states are shifted down with respect to $3z^2 - r^2$ by about $20meV$. The same orbital hierarchy was reported by Salluzzo et al. [164];

2. Instead, the orbital energy hierarchy of (110)-oriented 2DEGs is reconstructed in an inverted way, i.e., xz/yz and $3z^2 - r^2$ states are lower than xy and $x^2 - y^2$ by $30meV$ and $50meV$, respectively.

We therefore conclude that the electronic structure of LAO/STO 2DEGs is completely refurbished when the quantum wells are confined along different crystal orientations, and that the hierarchy of states with different symmetry is reversed.

The spectra dependence with LAO capping thickness was monitored for (110)-oriented samples. XAS/XLD spectra of samples with different thickness of the LAO overlayer, $t = 2$, 9 and $18MLs$ is shown in fig.8.5. Careful inspection of the absorption spectra reveals important differences as a function of the capping layer thickness. For instance, a close-up of the e_g-peak of the $Ti - L_3$ edge (inset of fig.8.5(a)), shows that the peak is shifted to higher energies as the overlayer thickness is increased. As the XAS spectra of all samples were aligned to the $Ti - L_3(t_{2g})$ absorption edge, this shifting reveals a relative energy displacement between t_{2g} and e_g levels or, in other words, a shift in the crystal field. This shift is also noticeable -although less evident due to larger peaks broadening- in the L_2 edges. The corresponding XLD spectra show similar shape for all samples (fig.8.5(b-top curves)), with slight variations in energy positions and signal intensity that could be simulated with CTM4XAS (bottom curves). From the simulations, we derived the crystal field $(10Dq)$ as well as the t_{2g}- and e_g- energy splittings as a function of thickness and, in fig.8.5(c) we plotted the order of the energy levels, calculated as [165]:

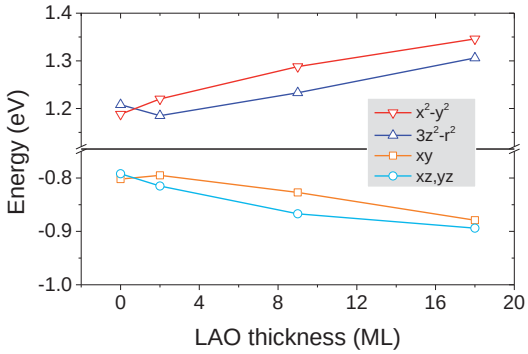

Figure 8.6: Energy levels order as calculated from expressions 8.1, as a function of LAO capping thickness for (110) STO/LAO samples

$$\begin{aligned} E(xz,yz) &= -4D_q - D_s + 4D_t \\ E(xy) &= -4D_q + 2D_s - D_t \\ E(3z^2 - r^2) &= 6D_q - 2D_s - 6D_t \\ E(x^2 - y^2) &= 6D_q + 2D_s - D_t \end{aligned} \tag{8.1}$$

The overall picture is that while the energy splitting at the t_{2g} and e_g states remains quite constant –within experimental error–, the crystal field splitting increases steadily with the LAO thickness, from $10Dq = 2eV$ at $t = 2ML$, to $10Dq = 2,2eV$ at $t = 18ML$, which could be related with an increased electron occupancy in the t_{2g} band [159].

Remarkably, it was found that an orbital hierarchy inversion with respect to bare surfaces is already observed at (110)-oriented sub-critical LAO thickness ($t = 2ML$, see XLD spectra in fig.8.5(b-blue points)), i.e. at interfaces that do not show any macroscopic conductance. Indeed, this inversion is also found in (001)-oriented interfaces [164], where even for $1ML$ LAO thickness a change in the XLD respect to that of bare surfaces was observed [166].

The orbital reconstruction mechanism in insulating (001) interfaces with under-critical LAO thickness ($t_c < 4ML$) was proposed to be related to structural distortions at the STO interfacial layers, where significant rumplings (displacements of oxygens towards the interface) were observed [166], and opposed to the rumplings detected in bare STO surfaces. It was shown, however, that these rumplings were strongly reduced in conducting interfaces, which, on the other hand, showed a larger dichroism than insulating ones.

At interfaces where 2DEG is present, quantum confinement along the z direction (normal to interface) is proposed to produce a splitting between the different d- bands, lowering the energy of the bands with lower effective mass (xy for (001) interfaces). This was proved in STO surfaces presenting a 2DEG, where the lowest energy bands were shown to have xy character [149], opposed to what is found in insulating STO surfaces, where surface symmetry breaking effects promote the lowering of xz, yz states.

While this phenomenology still needs to be proved for (110) interfaces, experimental results shown here point to similar qualitative explanation for both orientations.

8.3 SUMMARY

In this chapter we have shown the dissimilar hierarchy of the $Ti(3d)$ band electronic states at the LAO/STO interfaces with both (001) and (110) orientations. Our results show that, while in bare STO surfaces the degeneracy of t_{2g} and e_g levels is removed, lowering the energy of out-of-plane oriented orbitals, which is in accordance to surface symmetry breaking expectations, when capping STO with LAO overlayers, the orbitals lowered in energy turned to be the in-plane oriented orbitals, thus evidencing an orbital reconstruction for both (001) and (110) -oriented interfaces.

The dissimilar structure of both interfaces imposes a different orbital symmetry for in-plane and out-of-plane oriented orbitals in each case. While in the case of (001) interfaces, in-plane orbitals have xy and $x^2 - y^2$ symmetry, for (110) case, the in-plane orbitals have xz, yz and $3z^2 - r^2$ symmetry. These results open a way to explore the link between orbital symmetry and complex electronic phases at these interfaces [159, 167]. Indeed, orbital symmetry can profoundly affect the effective mass of the d bands, due to different overlapping between the highly anisotropic d orbitals [149], and can provide different intra- and interband pairing mechanisms leading to 2D superconductivity [168], along with other possibilities where selective orbital filling could control the conductivity and magnetism at interfaces.

Part III

SUMMARY AND OUTLOOK

SUMMARY

In this thesis we have addressed several topics. From them we select here the most important results obtained:

1. We have examined the electronic inhomogeneity present in manganite thin films, manifested by the presence of **localized hole trapping** promoting phase separation. Our results demonstrate that this phase separation is largely extended in the films, revealing the role of extrinsic charge trapping centers probably related to structural defects in the films. Indeed, artificially introduced punctual defects were shown to enhance this charge trapping. In addition, the magnetic anisotropy profile of the films could be extracted, revealing the contribution of interfaces and structural defects to the enhancement of magnetic anisotropy.

2. We have evidenced the **strain modulation of the electron occupancy** in the $3d(e_g)$ states of several transition metal oxide (TMO) thin films: $La_{2/3}Sr_{1/3}MnO_3$ (LSMO), $La_{1/2}Sr_{1/2}MnO_3$ (LSMO5) and $LaNiO_3$ (LNO), demonstrating that in all of them a Jahn-Teller picture correctly describes the phenomena inducing the preferential occupancy of the orbitals oriented in the direction of the elongated $TM-O$ distances. Moreover, the strain tuning of orbital occupancy was shown to be strongly effective in the magnetic phase selection of wide bandwidth half-doped manganites, LSMO5, while in $La_{1/2}Ca_{1/2}MnO_3$ (LCMO5) -having a arrower bandwith- strain was not so effective for the tuning of orbital/magnetic order, probably related to a larger tendency to show charge localization, as evidenced by the high insulating character of the films.

3. **Surface symmetry breaking** was shown to be a remarkable source of orbital polarization in TMO films, strongly favouring the occupancy of the orbitals having lobes oriented in the out-of-plane directions ($3z^2-r^2$ states in (001)-oriented epitaxial films and x^2-y^2 states in (110)-oriented films). This phenomena was explained as originated due to the reduced coordination at the surface of the films, where the abscence of apical oxygens in the out-of-plane direction strongly favours the occupancy of the orbitals directed normally to the surface, due to reduced Coulomb repulsion. In fact, partially restoring the coordination by proper terminating atomic layer selection was shown to be effective for the reduction of the surface symmetry breaking effect. Nevertheless, recent structural studies suggest that polar distortions present at the surface of the films may also have an influence in the observed orbital polarization at free surfaces.

4. The strain and surface induced distortions in the films were also shown to affect the **degree of covalency** in the ground state of the transition metal ions, promoted by the hybridization of the transition metal d states with oxygen p states. More specifically, it was shown that in LNO films compressive strain in the films promotes a larger hybridization strength, as expected from larger in-plane orbital overlapping due to reduced $Ni-O$ distances, than films under tensile strain. However, at the surfaces signatures of strongly reduced hybridization were evidenced, probably caused by the reduced coordination or the existence of polar

distortions largely diminishing $O - Ni - O$ bond angles. The strain and thickness correlation with hybridization strength could also be connected to the measured conductivity in the films.

5. The large reactivity of TMO is manifested at surfaces and at interfaces where different **redox** processes are susceptible to alter the nominal valence state of TM ions. In manganites a notable surface reduction was shown to be caused by exposure of manganite films to atmosphere. While capping layers protect from such reduction process, certain capping materials were shown to promote a Mn oxidation. As expected, both reduction and oxidation provoke a degradation of the magnetic properties of optimally doped manganite thin films. Although such oxidation processes have been proposed to be caused by charge transfer due to necessary electronic reconstructions occurring at certain interfaces, we could rule out this possibility by observing valence deviations at interfaces where no electronic reconstructions should be present. This was done by exploring different crystallographic orientations and amorphous capping layers. On the other hand, the influence of oxygen transfer between layers could not be discerned and requires further study.

6. The local modification of crystal field at interfaces between TMO epitaxial layers was evidenced by the observed **orbital reconstructions** at interfacial layers in the *d* states of the TM ions. Capping layers were shown to promote a reconfiguration of the orbital hierarchy, favouring different states depending on the capping layer and crystallographic orientation. In this respect, two systems where studied:

   a) At the interface between manganite films and dissimilar TMO layers, a dependence on the capping lattice parameter was derived, where cappings with smaller (larger) lattice parameter than the manganite film were proved to induce a preferential occupancy of in-plane (out-of-plane) oriented orbitals in Mn^{3+} ions at the interface. In addition, the induced orbital polarization was shown to be more prominent with increasing capping thickness. These two observations seem to point to a mechanism induced by structural distortions promoted by the capping layer and extending into the capped films. Nevertheless, it could not be disregarded the role of modified orbital hybridization in the interfacial states.

   b) At the highly conductive interface between two band gap insulating TMOs: $SrTiO_3$ (STO) and $LaAlO_3$ (LAO), the Ti^{4+} orbital hierarchy was shown to be reconstructed from that of bare surfaces. This orbital reconstruction is proposed to be induced by the presence of a quantum confinement that favours the bands with lower effective mass, and by the structural reconstruction occurring at STO and induced by the LAO overlayers. In our study, we showed that the orbital arrangement depends on the crystallographic orientation of the samples, favouring states with different symmetry depending on the orientation of the quantum well.

PERSPECTIVES

From the results and conclusions obtained in this thesis, and taking into account the trending topics in the investigation on transition metal oxides and their possible technological applicability, different research lines can be though to continue the work depicted here:

1. **Phase separation in manganites and Ferroelectric Tunnel Junctions (FTJ)**: We have evidenced here the large tendency of manganites to show phase segregation, specially relevant for compositions close to a phase transition, as it is the case for half-doped manganites. Although a large electroresistance has been obtained in FTJ where these materials are integrated, still more work needs to be done to prove the effectiveness of the metal-to-insulator transition at interfaces and their reproducibility. Thus, relevant experiments can be performed to address these points:
    a) X-ray absorption and dichroism experiments on half-doped manganite layers under operating conditions, i.e., integrated in switchable ferroelectric junctions.
    b) Magnetic sensitive x-ray photo-electron microscopy (XPEEM) that could provide a way to observe ferro- and antiferromagnetic domains simultaneously at the surface/interface in half-doped manganite samples, thus accessing the extension and arrangement of these phases.
2. **Charge and orbital reconstructions at interfaces**: We have demonstrated that the charge distribution and the orbital hierarchy at interfaces between TMO layers can be largely modified, however our results lead to open new questions of potential dramatic impact on our understanding of interface phenomena:
    a) How charge transfer across interfaces occur and affect the observed orbital hierarchies in heterostructures?
    b) How structural reconstruction at interfaces distort the local symmetry and how they correlate with the observed orbital reconstructions?
    c) Which is the role of oxygen affinity of component species and its influence in the electron distribution at interfaces?
    d) Can there be an influence of the polarity mismatch at interfaces in the electron distribution?
3. **Exploiting orbital engineering for green energy**: Our results suggest ways to tailor the orbital occupancy at surfaces, which can be profited for exploiding the capabilites of these materials in catalytic processes where the surface states are determinant. Groundbreaking experiments could be envisaged on this topic by:
    a) Studying *in-situ* oxide surface evolution during catalytic processes (e.g. water splitting) with XAS and XPS experiments.
    b) Dynamically tuning the surface electron states via electric fields and strain, with views to actively control the surface reactivity.
    c) Exploring ways to control the surface reactivity by orbital symmetry selection (as it can be modified e.g. with crystallographic orientation).

LIST OF PUBLICATIONS

Scientific publications derived from the work depicted in this thesis:

1. *2DEGs at $LaAlO_3/SrTiO_3$ interfaces: orbital symmetry and hierarchy engineered by crystal orientation,* D.Pesquera, M.Scigaj, P.Gargiani, A.Barla, J.Herrero-Martín, E.Pellegrin, S.M.Valvidares, J.Gázquez, M.Varela, N.Dix, J.Fontcuberta, F.Sánchez, G.Herranz (submitted to Phys Rev. Lett.)
2. *Interface and bulk charge localization in manganite thin films,* D.Pesquera, M.Wojcik, E.Jedryka, N.Dix, F.Sánchez, G.Herranz and J.Fontcuberta. Adv.Mater.Interfaces, doi: 10.1002/admi.201400079 (2014)
3. *Surface symmetry-breaking and strain effects on orbital occupancy in transition metal perovskite epitaxial films,* D.Pesquera, G.Herranz, A.Barla, E.Pellegrin, F.Bondino, E.Magnano, F.Sánchez, J.Fontcuberta. Nature Communications, 3, 1189 (2012)
4. *X-ray interference effects on the determination of structural data in ultrathin $La_{2/3}Sr_{1/3}MnO_3$ epitaxial thin films*, D.Pesquera, X.Marti, V.Holy, R.Bachelet, G.Herranz, and J.Fontcuberta, Appl. Phys. Lett., 99, 221901 (2011)
5. *Magnetoelastic coupling in $La_{2/3}Sr_{1/3}MnO_3$ thin films on $SrTiO_3$* , D.Pesquera, V.Skumryev, F.Sánchez, G.Herranz, and J.Fontcuberta, Phys. Rev. B, 84, 184412 (2011)
6. *Persistent two-dimensional growth of (110) manganite films,* R.Bachelet, D.Pesquera, G.Herranz, F.Sánchez and J.Fontcuberta, Appl. Phys. Lett., 97, 121904 (2010)

LIST OF COMMUNICATIONS

The work of this thesis has been presented by the author at several conferences/seminars :

1. *Spectroscopic determination of magnetic phase diagram of half-doped manganite thin films* - D. Pesquera, A. Barla, E. Pellegrin, F. Bondino, E. Magnano, G. Herranz, F. Sanchez, J. Fontcuberta. **Talk**. Annual meeting Nanoselect, Sant Feliu de Guíxols, Spain, June 2014.
2. *Orbital reconstructions in transition metal oxide heterostructures* – D. Pesquera, A. Barla, E. Pellegrin, F. Bondino, E. Magnano, P. Gargiani, J. Herrero, M. Valvidares, N.Dix, F. Sanchez, G. Herranz, J. Fontcuberta. **Poster**. Workshop on Oxide Electronics 20, Singapore, Sept. 2013.
3. *Strain tuning of $LaNiO_3$ thin films* – D. Pesquera, A. Barla, E. Pellegrin, F. Bondino, E. Magnano, J.M. Rebled, N.Dix, F. Sanchez, G. Herranz, J. Fontcuberta. **Talk**. European Materials Research Society Fall Meeting, Warsaw, Poland, Sept. 2013.
4. *Fine tuning of electron distributions in 3d and 4d transition metal oxides by strain and interface engineering* – D. Pesquera, A. Barla, E. Pellegrin, F. Bondino, E. Magnano, P. Gargiani, J. Herrero, M. Valvidares, N.Dix, F. Sanchez, G. Herranz, J. Fontcuberta. **Talk**. Joint European Magnetic Symposia, Rhodes, Greece, Aug. 2013.

5. *Exploring interfacial and strain effects in multifunctional oxide heterostructures* - **Talk**. First Scientific Meeting of ICMAB-ICN-CiN2 students, Bellaterra, Spain, May 2013.

6. Interface symmetry-breaking and strain effects on orbital occupancy in manganites - D. Pesquera, A. Barla, E. Pellegrin, F. Bondino, E. Magnano, G. Herranz, F. Sanchez, J. Fontcuberta. **Talk**. XXVIII trobades científiques de la mediterrània, Mahón, Spain, Oct.2012

7. *The role of chemistry and charge transfer at manganite interfaces* - D. Pesquera, A. Barla, E. Pellegrin, F. Bondino, E. Magnano, G. Herranz, F. Sanchez, J. Fontcuberta. **Poster**. Workshop on Oxide Electronics 19, Apeldoorn, Netherlands, Oct.2012.

8. *Orbital occupancy in manganite thin films* - D. Pesquera, A. Barla, E. Pellegrin, F. Bondino, E. Magnano, G. Herranz, F. Sanchez, J. Fontcuberta. **Poster**. International School of Oxide Electronics, Corsica, France, Oct. 2011.

9. *Interface symmetry-breaking and strain effects on orbital occupancy in manganites* - D. Pesquera, A. Barla, E. Pellegrin, F. Bondino, E. Magnano, G. Herranz, F. Sanchez, J. Fontcuberta. **Talk**. Workshop on Oxide Electronics 18, Napa Valley, USA, Sept. 2011.

10. *Magnetoelastic coupling in manganite thin films on $SrTiO_3$ crystals* - D. Pesquera, V. Skumryev, F. Sánchez, G. Herranz, J. Fontcuberta. **Poster**. Workshop on Oxide Electronics 18, Napa Valley, USA, Sept. 2011.

11. *Orbital occupancy in manganite films* - D. Pesquera, A. Barla, E. Pellegrin, F. Bondino, E. Magnano, G. Herranz, F. Sanchez, J. Fontcuberta. **Talk**. Annual meeting Nanoselect, Sant Feliu de Guíxols, Spain, June 2011.

12. *Interface phenomena and magnetic anisotropy in $La_{2/3}Sr_{1/3}MnO_3$ thin films* - D.Pesquera, R.Bachelet, G.Herranz , F.Sánchez and J. Fontcuberta. **Poster**. Annual meeting Nanoselect, Sant Feliu de Guíxols, Spain, July 2010.

Part IV

APPENDIX

A.1 GROWTH AND SURFACE CHARACTERIZATION

A.1.1 *Pulsed Laser Deposition (PLD)*

PLD is a powerful technique for the deposition of complex oxide thin films, heterostructures and superlattices, with well defined interfaces. In PLD, a pulsed ultraviolet laser is focused on a target material. If the energy provided by the laser is sufficiently high, each laser pulse ablates a small amount of material that creates a plasma plume -with the same composition as the target- directed towards a substrate, placed a few cm away from the target, where the film will be deposited. Usually the laser irradiates a small area of the target (few mm^2) during a short pulse time (in the order of ns). For oxides growth, flow of oxygen gas is introduced during the deposition, in order to get the desired stoichiometry of the films. Typical pressure ranges are in the order of 0.1-0.4 mbar. The particles from the plasma arrive to the substrate and get arranged according to the minimum energy. In order to increase the diffussivity of the atoms arriving at the substrate surface, this is heated to high temperatures (typically 600-800ºC). To prevent oxygen loss after the deposition of the film, an annealing in high oxygen pressure is sometimes required. A scheme of the PLD system is shown in fig A.1.

A.1.1.1 *Reflection High Energy Electron Diffraction (RHEED) system*

RHEED is used for in-situ monitoring the growth process during PLD deposition. RHEED allows for the growth rate control on monolayer level, determination of lattice parameters and substrate miscut angles, as well as for the study of the growth mechanisms and surface reconstructions in the substrates and deposited materials.

A highly energetic electron beam (E≈30keV) incides in the sample with a grazing angle (typically $<1-3$ degrees). The electrons scattered by the sample are registered by a phosphorous screen, showing the diffraction pattern of the sample surface. The

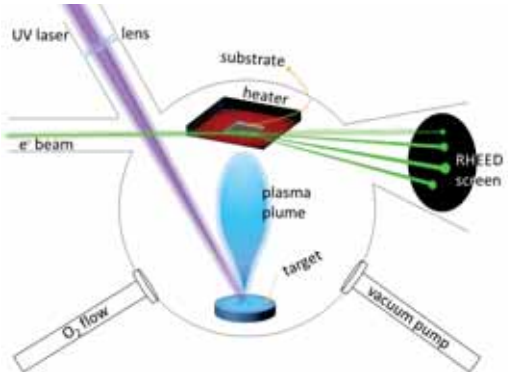

Figure A.1: PLD system representation with in-situ RHEED growth monitoring.

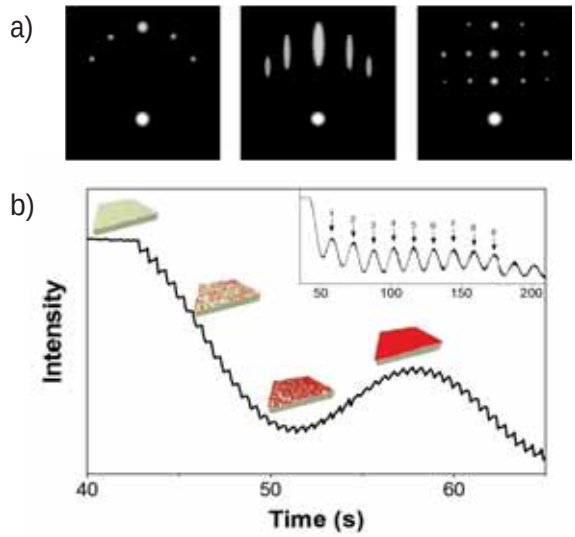

Figure A.2: a) Different RHEED patterns corresponding to perfect 2D surface (left), roughened 2D surface (center) and 3D surface (right); b) RHEED intensity oscillations, showing the corresponding substrate coverage for the first grown layer; larger time scan is shown in the inset (growth simulations extracted from [169]).

condition of diffraction is given by the Laue theorem: a diffraction spot is produced when the momenta of incident and diffracted beams differ by a reciprocal lattice vector. This condition is conventionally described by the Ewald sphere. For a 2D surface, the reciprocal lattice is described by infinite rods which intersect with the Ewald sphere forming diffraction spots, placed on concentric circles. Therefore, the RHEED pattern for a perfect 2D surface will appear like fig.A.2(a,left). For a non-perfect surface, the spots can get broadened or shifted. In the case of a 2D roughened surface, the most common observation is the appearance of streaks in the place of the diffracted spots (fig.A.2(a, center)). For a very roughened surface, or a film growing as 3D islands, the bulk reciprocal lattice will be observed, due to transmitted diffraction beam though these islands (fig.A.2(a, rigth)).

If the film grows layer by layer, the growth rate of the deposited film can be monitored. As the progressive roughening of a flat surface will produce a reduction of reflected intensity, the degree of surface coverage can be measured by registering the RHEED specular intensity, giving rise to a oscillation pattern as a function of time. From the period of this oscillations, the layer growth rate can be determined, as well as the concrete time (or number of pulses) for which a full layer is obtained.

For the films depositon, a KrF excimer laser was used in the two PLD deposition systems located at ICMAB. One of the chambers integrates a RHEED system. It uses a 30 kV electron gun and two-differential vacuum stages that allow monitoring the growth under high-pressure up to 0.5 mbar.

A.1.2 *Atomic Force Microscopy (AFM)*

AFM technique is used to probe the surface topography of solid (or even liquid) samples, with a nanometric resolution. A sharp tip with a diameter less than 10 nm is situated at the verge of a cantilever (100-200 μm long). The tip is approached to the sample until the interactions between the tip and the sample cause the bending of the

cantilever. This bending (also called deflection) is registered by detecting the reflection of a laser pointing onto the cantilever head. This way, as the tip is scanned though the sample, the cantilever deflection is measured. This is technique is known as *contact mode*.

The most common way to measure the sample's topography is the *dynamic mode*, in which the oscillation of the cantilever is produced near the sample's surface (typically 10-100 angstroms). This mode has the advantage of lowering the possible sample contamination and reducing the tip damage. On the other hand, the force registered will be some orders of magnitude lower than in contact mode. The cantilever is vibrated at a frequency close to its resonance (on the order of hundreds of kHz); when it is approached to the sample, changes in the oscillation frequency or in the amplitude are registered. At the same time, the phase lag between the input oscillation signal and the cantilever output can be recorded. This phase lag is used to monitor changes in the mechanical properties of the sample surface, detecting regions with different adhesion or friction. This information can, in some cases, be conected to chemical changes in the sample surface.

AFM images were taken with 5100 SPM system from Agilent Technologies located at the ICMAB. Images were analyzed using the software WSxM 3.0, from Nanotec Electronica S.L.

A.2 STRUCTURAL CHARACTERIZATION

A.2.1 *X-ray reflectometry (XRR)*

XRR allows to determine the thickness of thin films or heterostructures in a simple, non destructive way. The range of thicknesses that can be observed by means of XRR to determine samples thickness with enough accuracy is usually between 10 and 100 nm.

For the acquisition of the spectra, a x-ray beam (usually with the wavelength of Cu - Kα emission line) irradiates the sample, with a grazing angle incidence ϑ (typically between 0.5 and 5 degrees). The intensity reflected by the sample is detected and a spectra is obtained as a function of the incidence angle.

For low angles, below the so called critical angle ϑ_c , x-rays are totally reflected so no changes in the detected intesity are observed as a function of ϑ. The value of ϑ_c can be calculated from Snell's law

$$\vartheta_c = \arccos(n) = \arccos(1 - \delta - i\beta) \approx \arccos(1 - \delta) \approx \sqrt{2\delta} \tag{A.1}$$

,where δ and β are the dispersion and absorption components which determine the refraction index n. Commonly β is orders of magnitude lower than δ. As δ is directly proportional to the electronic density of the material ρ:

$$\delta = \frac{1}{2\pi} r_0 \lambda^2 \rho \tag{A.2}$$

,where $r_0 = 2.81 \cdot 10^{-5}$Å and ρ is the density in (el/cm^3); the critical angle is directly determined by the electronic density.

For $\vartheta > \vartheta_c$, photons can penetrate into the sample and the intensity registered at the detector decays as $sin(\vartheta)^{-4}$. However if there is more than one interface, a phenomena of interference can occur, modulating the intensity of the reflected beam due to the sum of the waves reflected at the different interfaces. In the simplest case of a single layer of finite thickness, the waves will be reflected at the top (air/layer surface) and bottom

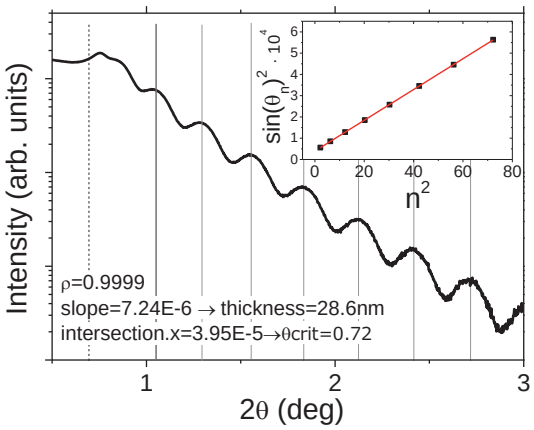

Figure A.3: Example of XRR measurement

(layer/substrate) interfaces. Due to the different optical path of these reflections, a pattern of maxima and minima will be observed (alternative constructive and destructive interferences).

From the position of the maxima and minima, the layer thickness can be determined, following the expresion:

$$\sin^2(\vartheta_i) = \sin^2(\vartheta_c) + i^2 \left(\frac{\lambda}{2d}\right)^2 \tag{A.3}$$

,where λ is the used wavelength and d is the sample thickness. i and ϑ_i are the order and angular position of the different maxima or minima. Typically i is an integer number, however, if the refraction index of the layer is lower than that of the substrate, there is a π shift in the reflection. In that case, i must be considered as semi-integer.

The procedure to find the value of d consists on finding the position of maxima and minima in the reflectity curve and assign them the correct i values. The criterion for a good selection of i values consists on minimizing the residual for the fitting to eq.A.3, considering also the resulting value of ϑ_c to be close to the expected value[1] (fig.A.3).

When the sample consists of more than one layer, the reflecivity spectra can become more complex, as it will consist on interferences between multiple reflections. In this cases, the previously descripted method is not useful and a proper fitting of the reflectivity curve must be done. The Parrat method, described in APPENDIX A is the most commonly used algorithm to simulate and fit reflectivity curves. This model takes into account the dispersion and absorption components for each layer, as well as the scattering factors due to the roughness at each interface, and evaluates the total reflected intensity by the whole stacking of the sample.

XRR measurements were performed in the Rigaku Rotaflex RU-200B diffractometer, located at the ICMAB.

A.2.2 *X-ray diffraction (XRD)*

XRD measurements are mainly used to determine crystal structure in bulk crystalline materials. The use of XRD in epitaxial thin films is focused on the study of texture,

1 Tipically $2\vartheta_c \sim 0.6 - 0.7deg$ for ABO_3 oxides

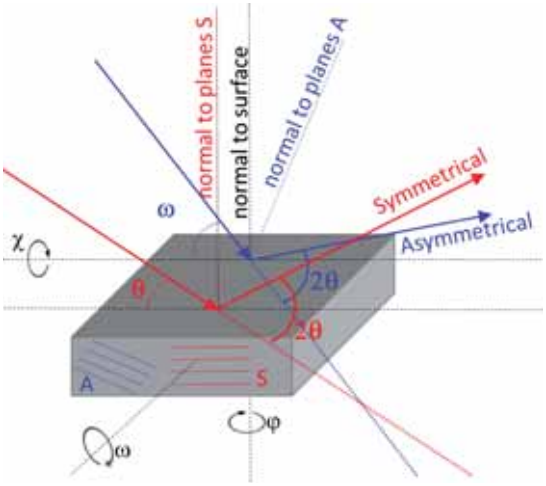

Figure A.4: Scheme for the measurement of symmetrical and asymmetrical reflections

epitaxial relationship between film and substrate and the determination of films lattice parameters.

A typical diffractometer apparatus is composed of a cathode ray tube that produce the x-ray radiation, a monochromator that selects the wavelength, divergence slits to shape the beam, filters to reduce the undesired characteristic lines coming out of the ray tube and passing the monochromator, sample holder, exit slits to control the instrumental resolution and detector. The final resolution of the spectra will depend not only on the monochromator but also in the settings of the rest of the components.

In thin films, XRD patterns allow to distinguish the type of growth achieved after the deposition. If the sample has grown amorphous, no pattern will be observed; if the film is polycrystalline, relatively narrow peaks corresponding to the different growth orientations can be identified; and if the sample grows crystalline, only one growth orientation will be observed. When growing thin films on single crystal substrates, a crystalline growth is expected. Furthermore, if the lattice mismatch between substrate and film is small enough, the epitaxial relationship between substrate and film can be achieved. XRD allows to examine the structural correlation between substrate and film.

For crystalline samples, two kinds of reflections can be observed (fig.A.4): those for which the incident beam is symmetric to the reflected one respect to the normal to the surface are called symmetric reflections; if they are not symmetric respect to the surface normal, they are referred to as asymmetrical reflections. The former ones explore the diffraction planes oriented parallel to the sample surface, while the later ones enable to explore other orientations.

Different configurations can be used to explore the texture of the films; here we described the techniques used in this thesis:

- **Pole figures:** Consists on a 2-dimensional map obtained by a 360 degrees rotation of the φ angle for a fixed ω and θ angles and for a specific range of χ (see angles notation in fig.A.4). By exploring the full rotation of φ, the observation of substrate and film reflections containing in-plane components and their symmetry can be explored. This way, in plane texture of the films can be deduced.

- **Theta-2theta:** Is the simplest way to explore symmetrical reflections. In a $\vartheta - 2\vartheta$ measurement, both sample and detector move together. The condition of diffraction is achieved when the incidence angle fulfills the Bragg's equation:

$$n\lambda = 2d \cdot \sin\vartheta \tag{A.4}$$

  ,where n is an integer and d is the interplanar distance in the out-of-plane direction of the sample. This way, the out of plane lattice parameter can be calculated.

In the same way, grazing incidence in-plane XRD (GIIXD) can be used to determine in-plane parameters. In a GIIXD measurement, the beam incides perpendicular to the sample normal. Thereby, the explored planes contain a in-plane lattice component that can be calculated in the same way as in a normal $\vartheta - 2\vartheta$ measurement.

- **Omega scans (Rocking curves):** Selecting an incidence angle ϑ that fulfills the Bragg's equation, it is possible to test the misorientation of the out-of-plane axis by keeping the detector fixed and changing the incidence angle around the condition of Bragg reflection. The full width at half maximum gives an indication of the degree of deviation of the explored planes. A perfect crystal will produce a sharp peak, while a sample with defects like mosaicity (existence of grains or domains with different orientations) or dislocations will give a broader peak.

- **Reciprocal Space Maps (RSM, Q-plots):** In RSM's several $\omega - 2\vartheta$ coupled scans are collected for different values of ω(that is, for different tiltings of the sample), around a reflection of the sample. RSM gives information of the in-plane and out-of-plane lattice parameters of the sample, of possible structural distortions, relaxation in the films or the presence of defects.

The positions in the reciprocal space for the chosen reflection are given by:

$$\begin{aligned} q_{\parallel} &= \tfrac{2}{\lambda}\sin(\vartheta)\sin(\vartheta-\omega) \\ q_{\perp} &= \tfrac{2}{\lambda}\sin(\vartheta)\cos(\vartheta-\omega) \end{aligned} \tag{A.5}$$

From the values of the wave vectors $q_{\parallel}$ and $q_{\perp}$obtained for the film reflections, one can calulate the distances in the real space, by knowing the relationship between the lattice in the real and reciprocal spaces. As an example, in a tetragonal system, with lattice parameters $a = b \neq c$, the reflection $[hkl]$, in-plane lattice parameter can be calculated as $a = \frac{\sqrt{h^2+k^2}}{q_{\parallel}}$,and out-of-plane parameter, $c = \frac{l}{q_{\perp}}$.

Further information can be obtained by examining the acquired maps. In figure A.5, some schems are shown regarding the position of the peaks and intensity gradients around them. In general, if a film grown fully strained on a single crystal substrate, the $q_{\parallel}$coordinates of film and substrate coincide for both symmetrical and asymmetrical reflections. Some indicators of relaxation can be found if a gradient of intensity towards the bulk expected position of the film material is observed. Also compositional gradients can be found along the relaxation line of the film (linking substrate and bulk position of the film).

Stardard resolution XRD measurements were taken using 2-circle diffractometer Siemens D500 and Bruker D8 Advance area detector at the ICMAB, while high-resolution measurements were adquired in PANalytical X'Pert Pro-MRD instruments located at CiN2 insitute in Barcelona, University of Barcelona and Charles University in Prague.

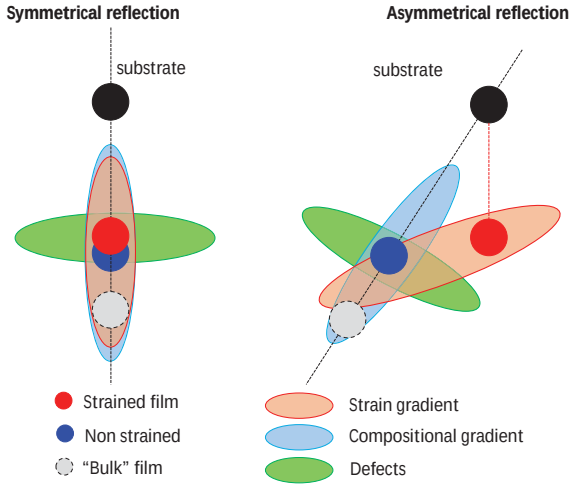

Figure A.5: Schematic representation of the possible reflections and gradients observed in a RSM. Adapted from [170]

A.2.3 *Rutherford Backscattering Spectrometry (RBS)*

RBS consists on the bombardement of a target sample with highly energetic light ions (in the order of few MeV). The energy lost by the backscattered ions depends on the masses of projectil and target atoms and the number of scattering events will depend on the atomic concentration of the target elements. The backscaterred ions are recordered with an energy sensitive detector, allowing for a quantitative determination of the compositon and thickness of the sample. RBS is specially sensitive to heavy elements and the probing depth is in the order of microns, depending on the energy and kind of ions used (usually ^4He).

In addition, RBS can be used to study the crystalline quality of the sample. This can be done by alligning the incident ion beam with a crystalline direction of the sample (that is, with a row of atoms). While surface atoms will be suffer from backscattering in the same way as a non-alligned sample, the atoms at higher depth are shielded from He ions, reducing the backscattering phenomena. This way, by measuring the reduction in the backscattering between a channeled and a random spectra, it is possible to measure the sample crystallinity.

A.2.3.1 *Ion implantation*

With the same equipement, but using ions in a lower energy range (hundreds of keV), ion implantation can be performed. While this technique is usually employed to change the physical properties of semiconductor materials, it can also be used to produce a controlled damage in thin film samples.

By proper selection of projectile ions and their energy, ions can cross the thin film layer, causing, by scattering phenomena, different atomic displacements, and get implanted in the substrate. This way, by regulating the irradiation dose, samples with different level of damage can be obtained.

Ion implantation, RBS and channeling measurements were performed at IKS institute in Leuven, using a 5SHD-2 linear Pelletron Accelerator.

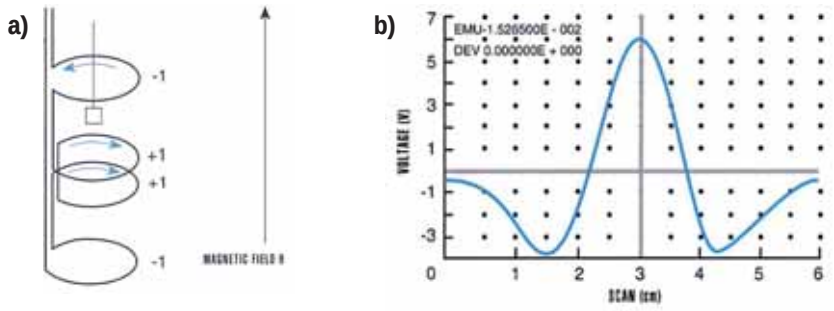

Figure A.6: **a)** Configuration of second-derivative coil ; **b)** SQUID response to magnetic dipole moving though detection coils. Extracted from [171]

A.3 MAGNETIC AND TRANSPORT MEASUREMENTS

A.3.1 *Superconducting Quantum Interference Device (SQUID)*

The Superconducting Quantum Interference Device is the most sensitive device for the measurement of magnetic fields. SQUID is actually a component of the Magnetic Properties Measurement System (MPMS), which consists of a superconducting magnet, a superconducting detection coil which detects the inductance generated by the sample, a SQUID connected to this detection coil and a magnetic shield surrounding the SQUID.

In the MPMS, the sample moves though the detection coils. The magnetic moment of the sample induces an electric current in the coils, which are connected to a SQUID input coil. Then, the SQUID produces an output voltage proportional to the induced current and, therefore, proportional to the change in the magnetic flux. SQUID devices are able to detect magnetic moments as small as $10^{-7} emu$.

A more detailed description of the detection coils configuration is presented in fig. A.6(a). This second-derivative coil configuration minimizes the possible current fluctuations produced by the magnetic field from the superconducting magnet. The top and bottom coils are set in clockwise turns while the two central coils are set in counterclockwise turn. Like this, the total magnetic flux created by the changes of the magnetic field are cancelled.

During a measurement, the sample goes though the detection coils, generating a position dependent signal as in figure A.6(b). The area under the curve is proportional to the magnetic moment. This measurement is ideal for point-like samples (samples with a size much smaller than the coils diameter. For large samples, shape corrections may be required .

Hysteresis loops and magnetization versus temperature curves were adquired with Quantum design MPMS XL-7T equipement at ICMAB, which enables a temperature range of 1.8 - 400 K and a magnetic field range of -7 to 7 T.

A.3.1.1

A.3.2 *AC Magnetic Susceptibility (ACMS)*

While DC magnetic measurements determine the equilibrium value of the magnetization, AC measurements can give information on the dynamics of the magnetization process in a sample. In ACMS measurements, a small AC field is applied to the sample,

producing a time-dependent moment that induces a current in the pickup coils. The induced moment is

$$M_{ac} = \chi \cdot h_{ac} \sin(\omega t) \tag{A.6}$$

, where h_{ac} is the ac excitation field, ω is the driving frequency and χ is the magnetic susceptibility, which -at low driving field frequencies- can be associated to the slope of the $M(H)$ curve that results form a DC measurement. By superimposing a DC magnetic field in the direction of excitation field, we can access different parts in the $M(H)$ curve.

However, if the frequency is high, the magnetization of the sample may suffer a delay respect to the driving field. In this case, the AC moment does not follow the DC curve and the magnetic susceptibility is described by a real and a imaginary component $\chi = \chi' + i\chi''$, or, alternatively, by amplitude $\chi = \sqrt{\chi'^2 + \chi''^2}$ and phase $\varphi = \arctan(\chi''/\chi')$ components. The imaginary component is related to dissipation or irreversible processes, like domain wall movement in ferromagnets.

ACMS is a powerful tool to explore magnetic transitions or to distinguish the sources for the magnetization processes in a magnetic material. In general, there are two distinct contributions to the ac-susceptibility [172] namely originating from domain magnetization rotation or from domain wall displacement – while for ac-field parallel to the domain magnetization the later is zero, the former contribution is maximum. By exploring the response of the sample under different excitation field magnitudes, frequencies or orientations respect to the sample, the relevance of both mechanisms can be revealed.

ACMS measurements were taken in a Quantum design Physical Property Measurement Systems (PPMS) at ICMAB, allowing for a field excitation range from $0.1Oe$ to $15Oe$, and a frequency range from $10Hz$ to $10kHz$.

A.3.3 *Nuclear Magnetic Resonance (NMR) spectroscopy*

The nuclei of many atoms possess magnetic and angular momenta. In the presence of a magnetic field H_0, the nuclei precess around the direction of the field, with a frequency ω_0, proportional to H_0. The constant of proportionality γ is the ratio between the magnetic and the angular momenta and therefore, it depends on the nucleus.

$$\omega_0 = \gamma H_0 = \frac{\mu}{\hbar I} H_0 \tag{A.7}$$

ω_0 is known as the Larmor frequency and usually is in the order of ten to hundreds MHz.

As the orientations of the magnetic moments respect to H_0 are quantized, the energy levels of the nuclei get splitted, separating the nuclei with the moments oriented parallel to the field from those oriented antiparallel. The energy required to flip a nuclear moment is $\hbar\omega$, with $\omega = \omega_0$, the Larmor frequency. If the correct energy is applied to the system, a transition occurs. This is the nuclear magnetic resonance.

From the macroscopic point of view, a rf field $H_1 \cos \omega t$ is applied perpendicular to the static H_0 field. If the frequency of the rf field couples to the precession frequency of the nuclei (if $\omega = \omega_0$), the nuclear spins will rotate about the direction of H_1 by $\gamma H_1 t$.

In a typical NMR experiment, an appropriate combination of intensity and duration of the rf field is applied to get a $\pi/2$ rotation of the spins ($\pi/2$ pulse). After the pulse, the precessing magnetization decays, inducing a rf current in a detection coil. This induced signal is called Free Induction Decay (FID), and the time constant T_2 for the decay of the nuclear spins in the $x - y$ plane is called spin-spin relaxation time, as the spin-spin

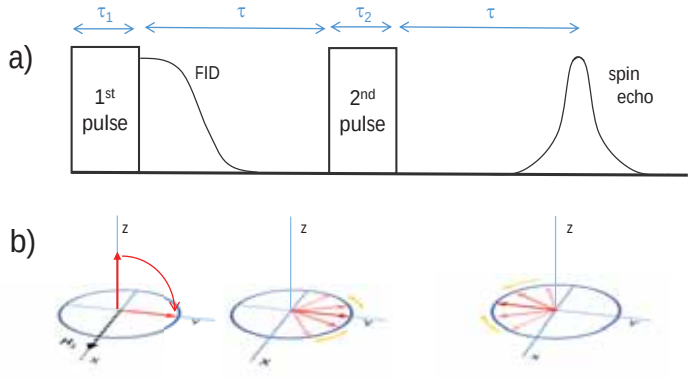

Figure A.7: 2-pulses NMR experiment: a) pulse excitation and system response sequence, b) schematic representation of the spin rearrangement in response to pulse excitations. Adapted from ref.[173]

interactions tend to disperse the spins and thus, to reduce the magnetization in the $x-y$ plane. In order to reduce effects of the magnetic field inhomogeneity, a π pulse is applied after a delay time which has to be $\tau \ll T_2$. After a time equal to the delay between the two pulses, the spins refocuse and induce a signal called *spin echo*. After some time, the spins will restablish the equilibrium in the direction of the applied field z. The time constant for the recovery of the magnetization along z is called T_1, spin-lattice relaxation time. In order to let the spins relax to the equilibrium position, the time delay between the sequence of pulses has to be $t_{rep} \gg T_1$. Usually, pulse duration and delay between pulses are in the order of few microseconds. The repetition time between pulse sequences is in the order of miliseconds.

A.3.3.1 *NMR applied to magnetic materials. Enhancement factor*

In magnetic materials, the spontaneous electronic magnetic moment creates a large internal field: the hyperfine field HF at the nuclei. Therefore, the nuclei are not directly excited by the external rf field h_1, but by the oscillation of HF due the the rotation of the local electronic moments surrounding the nuclei. The amplitude of this oscillation can be expressed as:

$$\xi = \frac{h_1}{H_{rest}} \tag{A.8}$$

,where H_{rest} is the restoring field, which is a measure of the magnetic stiffness of the material (or the restoring torque exerted on the moments upon small orientation changes). Thus the oscillation transverse component that is induced in the nuclei is given by:

$$H_{osc} = \xi \cdot HF = h_1 \frac{HF}{H_{rest}} = \eta \cdot h_1 \tag{A.9}$$

, where η is the enhancement factor. The electronic magnetization generates an oscillating component η times larger than the nuclear component and thus enhances the output signal of the spectra by this factor η.

In order to get the pure NMR spectra contribution from the nuclei, enhancement factor correction has to be taken into account.

The NMR response will be given by:

$$S(\omega, h_1) = \eta(\omega) R(\eta h_1) \frac{N(\omega)}{\omega} I(\omega) \tag{A.10}$$

, being R the spins response to ηh_1 excitation, I the instrument frequency response (usually independent of ω), and $N(\omega)$ the density of nuclei resonating at frequency ω (the real spectra).

Experimentally, NMR spectra is recorded for different intensities of rf field, in order to explore the restoring field distribution in the sample. For each frequency, the restoring field will be that for which the NMR intensity is maximum. A protocol [18] needs to be applied in order to correct for the variation of the NMR enhancement factor within the studied sample. The procedure consists in recording every NMR spectrum at several values of r.f. excitation field h_1 amplitude, varying over more than one order of magnitude. At each frequency point the intrinsic NMR enhancement factor η is computed and the signal intensity corrected accordingly, in addition to the standard correction for the f^2 dependence of NMR signal amplitude. The final NMR spectrum computed in this way, represents the intensity distribution which is proportional only to the number of nuclei resonating at a given NMR frequency f, and is not falsified by the frequency variation of the enhancement factor which may be different in different parts of the sample. The enhancement factor is determined by measuring h_{1opt}, i.e. the r.f. field amplitude that maximises the spin echo NMR signal. In addition, knowing h_{1opt} one can calculate the (frequency dependent) NMR restoring field $H_{rest} = (HF/\eta) = \beta \cdot h_{1opt}$ where β is the instrumental scaling factor.

All NMR spectra shown in this thesis were acquired at the Institute of Physics, Polish Academy of Sciences, Warszawa (Poland) by Dr. M. Wojcik.

A.3.4 *Resistivity measurements in Physical Properties Measurement System (PPMS)*

Figure A.8: Example of four point method for the measurement of sample resistivity

Transport properties of the samples were probed by means of resistivity measurements, carried out in a four-contacts configuration, in which the current is injected by two electrodes and the voltage drop is measured along the other two (see fig. A.8). Four-probes method allows to overcome the problem of voltage drop at the contacts or cables, specially when the sample to measure is expected to present low resistance ($< 1kOhm$). The electric contacts were done by silver paint. The relation between the resistance measured R and the resistivity is $\rho = CRd$, where d is the sample thickness and C is a geometrical factor that depends on the configuration of the contacts in the sample. Typically, a squared configuration is used, for which $C = 2ln(2)$ [174]. In order to obtain a precise value we average the resistance values obtained measuring along different pairs of electrodes (for example AB and AC in fig.A.8), and also averaging with the inversion of the current sense.

A physical properties measurement system (PPMS) located at the ICMAB allows the option of AC current for resistance measurements. Resistance vs temperature measurements can be performed in a range of temperatures from $2K$ to $400K$. The maximum

resistance that can be measured by the equipment is $20M\Omega$. In addition, resistance vs applied magnetic field can be done at a given temperature with a maximum magnetic eld of 9 Tesla.

Pulsed laser deposition growth of LSMO films on (001)STO substrates was optimized in order to obtain high quality films with functional properties close to that of the bulk LSMO. At the same time, we took a careful attention to the structural and morphological properties of the films, with the aim of reaching a coherent epitaxial growth on the substrate and getting an atomically flat surface, which is highly desiderable for the study of interfaces and for the application of these films as electrodes for tunnel magnetorresistance devices.

To explore the optimal conditions for the growth of LSMO films, several parameters in the PLD deposition procedure were varied. The main parameters that influence both in the films properties and in the structure and morphology are the oxygen pressure in the chamber and substrate temperature during growth. Other parameters like the laser repetition rate were shown to have minor effects on the films properties for frequencies larger than 1 Hz. Laser fluence and laser pulse energy were left unchanged. Also, the number of pulses was set to 2000 pulses, leading to an average films thickness of 28($\pm$3) nm, as measured by x-ray reflectometry.

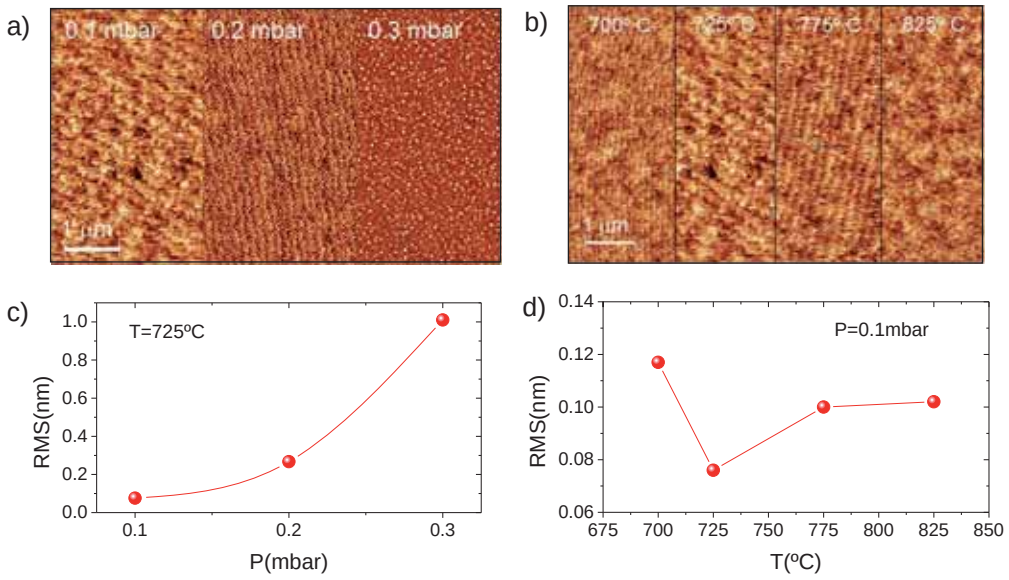

Figure B.1: a) AFM images for LSMO films grown at 725ºC and oxygen pressure of (from left to right) 0.1, 0.2 and 0.3 mbar; b)Films grown at 0.1 mbar pressure and substrate temperature (from left to right) 700, 725, 775 and 825 ºC; c and d) RMS values as a fucntion of oxygen pressure and substrate temperature respectively, obtained from the AFM images of a) and b)

Oxygen pressure is a crucial parameter in the growth of oxide thin films, as it can critically modify the properties of the material. In fig.B.1(a) we show how oxygen pressure can also influence in the surface morphology of the films. By setting a fixed substrate temperature (725ºC) we modified the oxygen pressure during deposition from 0.1 to 0.3 mbar. In the AFM images it can be clearly observed how for lower oxygen pressures a flat surface is obtained (root mean square (RMS) of the amplitudes lower

than 0.1nm) with a 2D growth morphology of steps and terraces, while by increasing the pressure, more 3D islands appear and the RMS increases until values close to 1nm for 0.3 mbar pressure (fig.B.1(c)).

The effect of temperature deposition on the surface roughness was also explored, by varying the substrate temperature from 700ºC to 825ºC, at a fixed oxygen pressure of 0.1mbar. It can be observed in the AFM images shown in fig.B.1(b) and the resulting RMS values (fig.B.1(d)) that the temperature factor does not strongly influence the surface morphology within the studied temperature range.

Although low oxygen pressures are more preferable to obtain a flat LSMO surface, the effect on magnetic properties is clearly detrimental. As shown in fig.B.2(a), SQUID measurements indicate that films grown at 0.1mbar have lower transition temperature and magnetization than the films grown at larger pressures. In fact, films grown at an oxygen pressure of 0.2mbar or larger shown M_S and T_C values close to that of the bulk LSMO. This observation can be understood as LSMO films grown at low pressure having a relevant amount of oxygen vacancies, thus diminishing the double exchange interaction between Mn ions. However, θ-2θ scans for LSMO films grown at 0.1 and 0.2 mbar do not show a significat difference in the position of the (002)LSMO peak (fig.B.2(b)). If oxygen vacancies were present, a displacement towards lower angles would be expected for LSMO diffraction peak (as a consequence of increased unit cell volume due to oxygen loss). A post-growth annealing process at high oxygen pressure (300mbar, 625ºC) was tested in one LSMO film grown at 0.1mbar pressure. The effect of annealing was contrary to the expected: an increased lattice parameter was found in this sample (fig.B.2(b)) and lower M_S and T_C values were obtained for this film (fig.B.2(a)). Thus, annealing is shown not to help to improve the functional properties of the films.

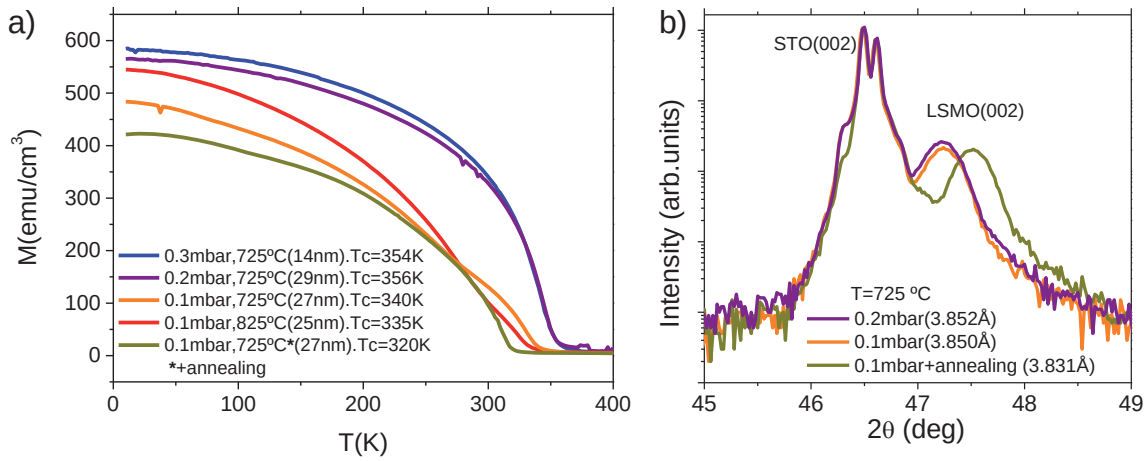

Figure B.2: a) Magnetization versus temperature curves for LSMO films grown at different oxygen pressures and substrate temperatures, as inidicated in the figure; b) θ-2θ scans for LSMO films grown at different conditions, as indicated.

The counter effect of oxygen pressure for obtaining, on one hand, films with flat surface and, on the other, films with optimal functional properties, leads to adquire a compromise between the tendencies observed for the two factors, so we chose our growth conditions as 0.2mbar oxygen pressure and 725ºC substrate temperature. Under these conditions, films show reasonable RMS values (lower than 0.2nm) and optimal magnetic properties.

X-RAY INTERFERENCE EFFECTS ON THE DETERMINATION OF STRUCTURAL DATA IN ULTRATHIN FILMS

In thin films, cell parameters are typically extracted from measured X-ray patterns by assuming incoherent superposition of diffracted waves by film and substrate. Whereas this standard approach is generally correct, this is not the case when the film is coherently grown on the substrate and the out-of-plane parameters of film and substrate are closely similar. In this case interference phenomena of diffracted waves can lead to an inaccurate description of the structural properties. Here we signal the importance of considering the superposition of the scattered waves by the substrate and film in the X-ray data analysis, which can, in some cases, lead to a radically distinct determination of lattice parameters from the conventional analysis of simple addition of intensities from substrate and film. We will exemplify this study with the analysis of high resolution X-ray diffraction data taken in our manganite $La_{2/3}Sr_{1/3}MnO_3$ thin films grown on $SrTiO_3(001)$ single crystals. XRD measurements have been done by using a X'Pert diffractometer (Cu-$K\alpha$ radiation).

In fig. C.1(a-c) we show $\theta - 2\theta$ diffraction scans around the (002) reflection for films of 10, 17 and $27nm$, respectively, showing the Bragg peaks (θ_B) for substrate and layer and the Laue oscillations. Data analysis can be attempted by fitting the film contribution to the diffraction pattern to the expected intensity dependence of Laue's oscillations:

$$I(Q) = \frac{\sin^2\left(\frac{1}{2}QNc\right)}{\sin^2\left(\frac{1}{2}Qc\right)} \tag{C.1}$$

, where N is the number of unit cells along the $[00l]$ direction, Q is the reciprocal lattice vector, given by $4\pi\sin(\omega)/\lambda$ where ω is the angle of the incident X-rays respect to the diffracting crystal planes and λ is the wavelength of the X-rays. From the fit, both the thickness (t) – related to N – and c-axis parameter of the film – related to maximum of intensity at the Bragg angle, i.e. for Q($\theta = \theta_B$) – can be extracted. Independently, the substrate peak could be adjusted to a pseudo-Voigt function centered in the reflection peak of the substrate. The results of these fits are shown (red solid lines) in figs. C.1(a-c). It is implicitly assumed here that the diffraction patterns of the LSMO layer and STO substrate can be simply added. One can observe that the shape of the Bragg peaks for substrate and film can be well adjusted but there is a clear shift of the fitted fringes when compared to the experimental ones. This shift is clearly asymmetric, being more pronounced for $\omega < \theta_B$ than for $\omega > \theta_B$. A similar discrepancy was observed in related materials and attributed to strain-gradients in the films [ ].

The thickness dependence of the c-axis values extracted using this approach are shown (solid circles) in fig.C.2. We first note that all c-values are smaller than the corresponding bulk value ($0.3873nm$ [15]) as expected from the tensile strain imposed by the STO substrate. However, data in fig.C.2 suggest that for the thinnest films, a gradual expansion of the unit cell occurs, which is at odds with the expected elastic deformation of the unit cell under tensile strain.

We will show in the following that these systematic discrepancies arise from the fact that the assumed incoherent superposition of diffracted waves for film and substrate is not adequate for epitaxial ultrathin films grown on closely matching substrates [16].

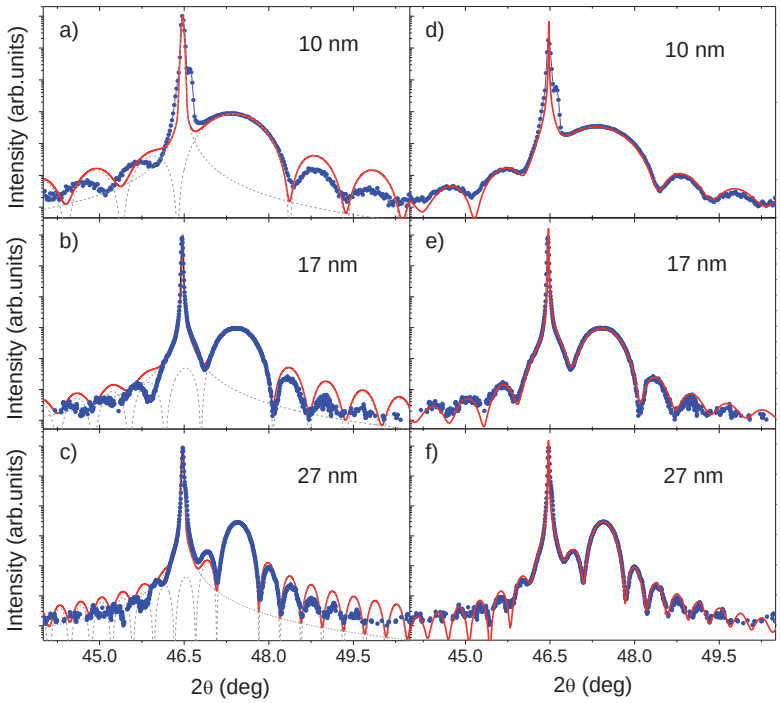

Figure C.1: $\theta - 2\theta$ X-ray diffraction patterns of selected LSMO/STO samples. Points are experimental data. In (a-c) solid lines correspond to results of fits by adding the film and substrate contributions (dashed lines); In (d-f) solid lines are fits using $|E_{SL}(\omega)|^2 = |E_S(\omega) + E_L(\omega)|^2$ as described in the text.

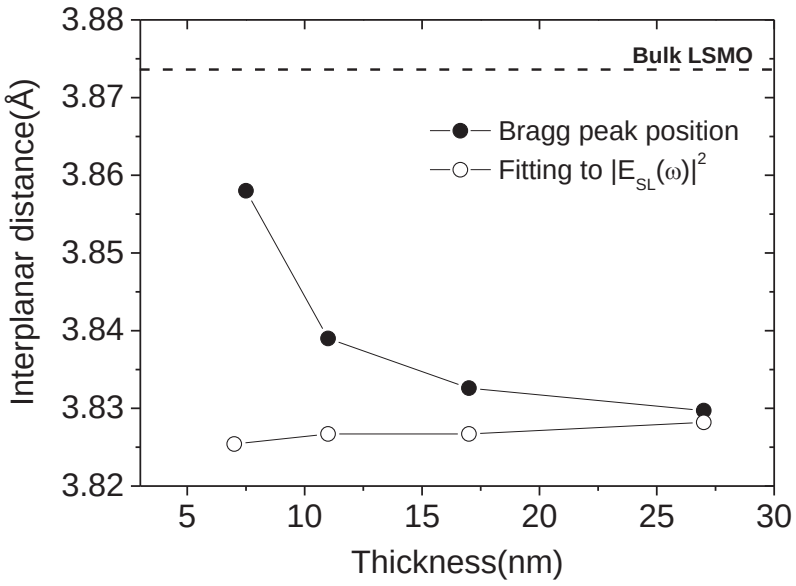

Figure C.2: Out-of-plane lattice parameters for LSMO films, calculated either by means of (black circles) Bragg's law from the position of the diffraction peak of the layer or (open circles) by fitting the data using $|E_{SL}(\omega)|^2 = |E_S(\omega) + E_L(\omega)|^2$ as explained in the text. Dashed line indicates the bulk value of c-axis of LSMO.

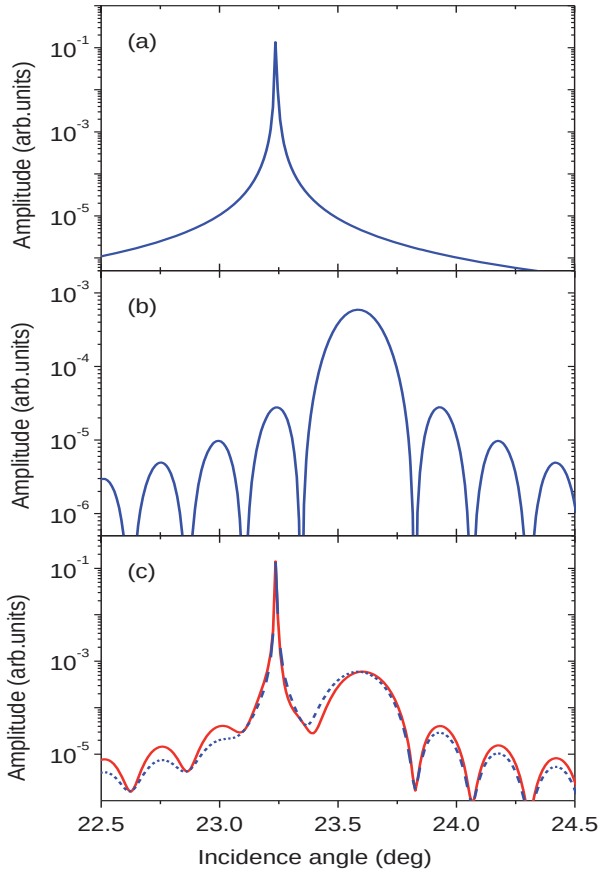

Figure C.3: (a, b) Amplitudes of the diffracted waves by the STO substrate (eq. C.2) and a LSMO layer (eq. C.4) respectively. c) Total diffracted intensity calculated as (blue) $|E^0_{SL}(\omega)|^2 = |E_S(\omega)|^2 + |E_L(\omega)|^2$ and (red) $|E_{SL}(\omega)|^2 = |E_S(\omega) + E_L(\omega)|^2$

The electric field of the substrate-diffracted beam E_S (relative to the incoming beam) must be obtained from the dynamical theory. For a symmetric reflection, the angular dependence of $E_S(\omega)$ can be written as [17]:

$$E_S(\omega) = -\left(\beta_S \pm \sqrt{\beta_S^2 - 1}\right) \tag{C.2}$$

, where β_S is,

$$\beta_S = \frac{1}{\sqrt{C_{lS} \cdot C_{-lS}}} \left(\sin(2\theta_B)(\omega - \theta_B) + C_{0S}\right) \tag{C.3}$$

and C_{lS} and C_{0S} are the $l-$ and $0-$term of the Fourier expansion of substrate's crystal polarizability [18]. C's are complex numbers and thus E_S is complex. θ_B is the Bragg angle of the $(00l)$ reflection. The sign in eq.C.2 should be chosen such as $|E_S| < 1$, which is the physically relevant solution. In fig.C.3(a) we show $|E_S(\omega)|^2$ calculated for the (002) reflection of the STO substrate which nicely reproduces the measured patterns (see figs.C.1(a-c)).

The electric field amplitude of the film-diffracted beam E_L can be obtained by either the kinematical or the dynamical approximation. In the simplest kinematical approximation, E_L is given by [17]:

$$E_L(\omega) = \frac{C_{lL}}{2\beta_L} \exp\left[\left(-i\frac{2\pi}{\lambda}\frac{\beta_L}{\sin(\theta_B)}t\right) - 1\right] \tag{C.4}$$

, where β_L is:

$$\beta_L = \frac{1}{\sqrt{C_{lL}C_{-lL}}}\left[\sin(2\theta_B)(\omega - \theta_B) + C_{0S} + 2\varepsilon\sin^2(\theta_B)\right] \tag{C.5}$$

, being t the thickness of the layer, λ the wavelength of the X-rays; C_{lL} and C_{0L} are the $l-$ and $0-$term of the Fourier expansion of film polarizability. $\varepsilon = (c_L - c_S)/c_S$ is the relative difference of out-of-plane cell parameters of substrate and film. In fig. C.3(b) we show $|E_L(\omega)|^2$, obtained using eq.C.4, for a LSMO layer of $t = 20nm$, and $\varepsilon = -2.4$ (appropriate for a fully strained LSMO on STO). It can be appreciated that $|E_L(\omega)|^2$ displays the characteristic Laue oscillations. Indeed, it can be shown that $|E_L(\omega)|^2$ is identical to $I(Q)$ given by eq.C.1.

In the case of interest here, i.e, a coherent film on a single crystalline substrate, the electric field amplitude of the diffracted beam by the substrate-film E_{SL} must be obtained by computing $|E_{SL}(\omega)|^2 = |E_S(\omega) + E_L(\omega)|^2$ with $E_S(\omega)$ and $E_L(\omega)$ as given by eqs.C.2 and C.4 [19]. The interference of the $E_S(\omega)$ and $E_L(\omega)$ diffracted beams strongly modifies the computed patterns and produces a shift of the measured maxima and an asymmetric intensity patterns at$\omega < \theta_B$ and $\omega > \theta_B$, as indicated by red-line in fig.C.3(c). $|E_{SL}(\omega)|^2$ differs significantly from the pattern calculated assuming no-interference of the diffracted beams ($|E^0_{SL}(\omega)|^2 = |E_S(\omega)|^2 + |E_L(\omega)|^2$) shown by blue-lines in fig.C.3(c).

In fig.C.1(d-f ,dashed lines), we show the results of the corresponding fits obtained using $|E_{SL}(\omega)|^2 = |E_S(\omega) + E_L(\omega)|^2$ as described above [20]. It can be appreciated that the fits are excellent and all asymmetries (maxima position and intensity) are well reproduced. The c-axes parameters extracted from these fits are included in fig. C.2 (open symbols). It is clear that when considering X-ray beam interference to fit the data, the extracted c-parameters display a monotonic increase when increasing thickness, as expected from a gradual tensile-strain relaxation, and in concordance with the data presented in section3.2.1, for larger LSMO thicknesses.

This illustrative example thus demonstrates that the interaction of diffracted beams by substrate and films should be considered to extract reliable structural information in ultrathin films.

In the following, a MATLAB code [1], exemplifying the ω scan simulation of a symmetric (002) reflection from a $STO/LSMO$ thin film:

```
lambda=1.5405980;
K=2*pi/lambda;
T=150;% layer thickness (amstrongs)
% SrTiO3:
hkl=2;
aS=3.905;
%http://sergey.gmca.aps.anl.gov/cgi/WWW_form.exe?template=x0h_form.htm
c0S=-0.29899E-04+1i*0.13516E-05; %xr0 , xi0  (n = 1 + xr0 /2 + i*xi0 /2)
chS=0.15430E-04+1i*0.12852E-05  ; %pol sigma
cmhS=chS;
% LSMO002:
azL=3.87;
c0L=-0.394E-04+1i*0.358E-05;
```

1 Dr.Xavi Marti is acknowledged for the elaboration of this code

```
chL=0.25E-04+1i*0.42325E-05; %pol sigma
cmhL=chL;
% components of the diffraction vectors:
hzS=2*pi/aS*hkl;
hzL=2*pi/azL*hkl;
% position of the substrate peak
theta=asin(hzS/2/K)*180/pi;
alphai=theta-2:0.01:theta+2;
[ES,ELdyn,ELkin,Idyn,Ikin,Pes1,Pes2]=XRDkindyn(lambda,c0S,chS,c0L,chL,hzS,hzL,T,
    alphai);
semilogy(alphai,abs(ELkin+ES).^2,'r','LineWidth',2);
ylabel('Amplitude'),xlabel('Incidence angle (deg)');



function [ES,ELdyn,ELkin,Idyn,Ikin,Pes1,Pes2]=XRDkindyn(lambda,c0S,chS,c0L,chL,hzS,
    hzL,T,alphai)
%
%  calculation of the waves diffracted from the substrate and the layer, as
%  well as the total diffraction curve %  Single pseudomorph layer o a semiinfinite
     substrate. Diffraction from
%  the substrate is calculated dynamically (disp. surface of the 2nd
%  order), diffraction from the layer is calculated dynamically or
%  kinematically
%  Coplanar case, S polarization
%
%  On input:
%  lambda..lambda
%  c0S .. chi_0 of the substrate
%  chS, cmhS .. chi_h, chi_{-h} of the substrate
%  c0L.. chi_0 of the layer
%  chL, cmhL .. chi_h, chi_{-h} of the layer
%  hx .. common lateral component of the rec. lattice vectors
%  hzS .. vertical component of the rec. lattice vector of the substrate
%  hzL .. vertical component of the rec. lattice vector of the layer
%  T .. layer thickness
%  alphai .. vector of the incidence angles in deg
%
%  On output:
%  ES .. vector of the complex amplitudes diffracted from the substrate
%  ELdyn .. vector of the complex amplitudes dynamically diffracted from
%  the layer
%  ELkin .. vector of the complex amplitudes kinematically diffracted from
%  the layer
%  Idyn .. vector of total diffracted intensities, the layer is calculated
%  dynamically
%  Ikin .. vector of total diffracted intensities, the layer is calculated
%  kinematically
%  The function is called by the command
%
%  [ES,ELdyn,ELkin,Idyn,Ikin]=XRDkindyn(lambda,c0S,chS,cmhS,c0L,chL,cmhL,hx,hzS,hzL
    ,T,alphai)
% K=2*pi/lambda; thetaB=asin(hzS/2/K); eta=alphai*pi/180-thetaB;
% deviation of the incident beam from the kinematical maximum:
% vertical strain in the layer: epsilon=(hzS-hzL)/hzL;
% dynamical diffraction in the substrate:
```

```
betaS=(eta*sin(2*thetaB)+c0S);
yS=betaS/sqrt(chS^2);
c1=-(yS+sqrt(yS.^2-1));
c2=-(yS-sqrt(yS.^2-1));
pp=abs(c1).^2;
jj=find(pp<1);
c3(jj)=c1(jj);
jj=find(pp>=1);
c3(jj)=c2(jj);
ES=c3;
% dynamical diffraction from the layer:
betaL=(eta*sin(2*thetaB)+c0L+2*epsilon*sin(thetaB)^2);
yL=betaL/sqrt(chL*chL);
c1=-(yL+sqrt(yL.^2-1));
c2=-(yL-sqrt(yL.^2-1));
        kz2mkz1=K*sqrt(chL^2)/sin(thetaB)*sqrt(yL.^2-1);
        cphi=exp(1i*kz2mkz1*T);
        ELdyn=c1.*c2.*(cphi-1)./(cphi.*c1-c2);
% kinematical diffraction from the layer:
        ELkin=chL/2./betaL.*(exp(-1i*(K/sin(thetaB)*betaL)*T)-1);
        Pes1 = (exp(-1i*(K/sin(thetaB)*betaL)*T)-1);
        Pes2 = chL/2./betaL;
%     Elkin = Pes1.*Pes2;

% total diffraction, dynamical layer:
        X=(c1.*c2.*(cphi-1)+ES.*(c1-cphi.*c2))./(cphi.*c1-c2+ES.*(1-cphi));
        Idyn=abs(X).^2;
% total diffraction, kinematical layer:
        Ikin=abs(ES+ELkin).^2;
end
```

EMERGENCE OF Mn^{2+} AT MANGANITE SURFACES

The functionality of manganite layers in magnetic tunnel junctions is limited due to interface phenomena [25]. As it has been studied in this thesis, phase segregation is promoted by the symmetry breaking at interfaces, that favors the electron localization, diminishing the magnetotransport performance of these materials in thin films. However, other extrinsic effects, also mentioned in the contents of this thesis, can promote chemical deviations at interfaces, manifested by modifications of the Mn valence state. By means of x-ray absorption measurements, these deviations of the Mn oxidation state can be identified at surfaces/interfaces. In particular, it is commonly observed the occurrence of a prominent peak in the $Mn - L$ pre-edge, associated to $p \rightarrow d$ transitions for Mn with a $2+$ valence state.

In this appendix we study the emergence of Mn^{2+} peaks in the absorption spectra of $La_{1-x}Sr_xMnO_3$ thin films, both by the effect of high flux synchrotron x-ray irradiation, or intrinsically present at films surfaces. We also study the influence of Mn^{2+} in the magnetic response of the films and explore possible pathways to diminish its contribution.

D.1 SYNCHROTRON X-RAY BEAM INDUCED MANGANESE REDUCTION

In synchrotron radiation experiments, x-rays produce changes in the studied materials via interaction of the photons with electrons in the solid. In some cases, the x-ray beam can produce undesired modifications in the samples, due to high brilliance of the source. This is the case of biological systems, where radiation damage is often observed [175, 176]. Catalytic systems containing multivalent elements can also suffer modifications due to radiation, altering the metal valence when exposed to the x-ray beam [177, 178, 179]. These effects are less studied in solid systems like complex oxides, where oxygen removal or modification of oxidation state can be promoted by x-ray beam.

During our X-ray Absorption Spectroscopy (XAS) studies of $La_{2/3}Sr_{1/3}MnO_3$ (LSMO) thin films we observed notable modifications of the spectra during data adquisition.The x-ray beam flux influence was identified and diminished, after proper study of the effects of radiation explored here.

D.1.1 *Time evolution of x-ray beam damage*

In figure D.1(a), a typical $Mn - L_3$ edge spectrum for LSMO sample ($5\,nm$ LSMO thin film on STO substrate) is shown (grey area under black curve), normalized by the area under the spectrum. As already pointed out in the main text of this thesis, the features in the XAS are influenced by the different electronic and structural environments of Mn ions present in the surface layers of the sample. Mn ions with dissimilar valence states have distinct independent contributions which are maximum at different energies. In that way, we can identify a maximum spectra intensity around $642\,eV$, corresponding to $Mn^{3+/4+}$ valence of LSMO samples. However, a prominent contribution at lower

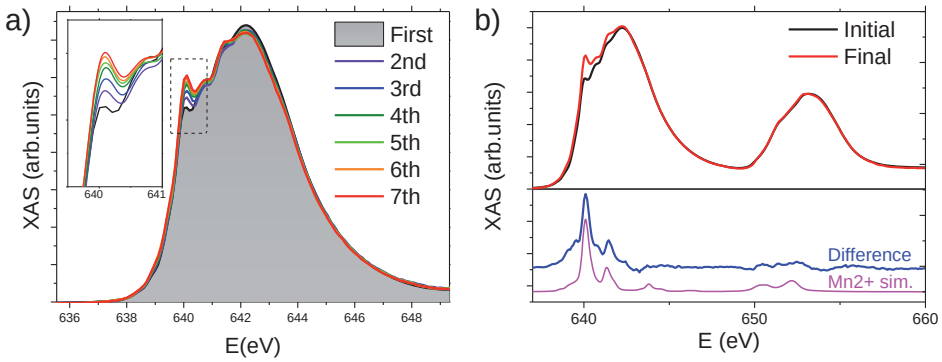

Figure D.1: a) $Mn - L_3$ XAS spectra of LSMO sample, registered during different consecutive runs. b) top panel: $Mn - L_{2,3}$ XAS spectra of LSMO sample before (black curve) and after (red curve) long exposition to x-ray beam; bottom panel: XAS difference between final and initial spectra (blue curve) and simulation of Mn^{2+} XAS spectra in octahedral coordination.

energies (see peak at $640eV$) can be attributed to the presence of Mn ions in a $2+$ oxidation state [80, 81, 82, 83, 84].

It was observed, during XAS measurements under synchrotron radiation a clear evolution of this peak at $640eV$, increasing with measurement time. In fig.D.1(a), area-normalized XAS spectra taken at a same point in the sample in several rounds is shown. The zoom in the inset clearly shows the intensity increment of this peak, evolving with the time under x-rays irradiation. In the area-normalized spectra it can be appreciated how the increase of intensity around $640eV$ occurs at the expense of intensity detriment at the maximum of the spectra, thus signaling a $Mn^{3+/4+} \rightarrow Mn^{2+}$ reduction process at the surface of the samples stimulated by x-ray beam irradiation. The difference between initial and final spectra (fig. D.1(b)) -here normalized by the intensity at the maximum- is shown in fig.D.1(b-bottom panel). The difference spectra ressembles that of simulated Mn^{2+} in octahedral coordination, thus confirming the identification of increasing Mn^{2+} contribution in XAS experiments under prolonged exposure to x-ray beam.

The influence on the x-ray linear dichroism (XLD) signal was also studied. XLD spectra (normalized to the maximum intensity of corresponding XAS) taken in grazing incidence ($XLD = I_{\parallel} - I_{\perp}$) were registered during beam exposure. In figure D.2, some examples of XLD spectra, taken with two XAS spectra ($I_{\parallel}, I_{\perp}$) are shown. Minor variations, that can be considered inside the noise levels of the measurement, are appreciated. In the inset of the figure, integrated area under XLD is shown as a function of measurement round, for integration regions around the L_2 edge and in the whole energy interval measured. It is observed how area deviations are larger in the whole energy integration range, probably caused by spurious intensity modifications in the $I_{\parallel}, I_{\perp}$ couples, due to progressive Mn^{2+} emergence, which is more notable in the L_3 edge region.

Once identified the problematic emergence of Mn^{2+} contribution and its possible influence in the analysis of XLD signal, we designed XAS/XLD experiments with perspectives to diminish both the effect of the beam induced reduction -by minimizing the radiation flux (using exit slits or meshes that notably reduce the beam intensity reaching the sample surface)- and the spurious influence in the XLD, by averaging over several polarization sequences $I_{\parallel} - I_{\perp} - I_{\perp} - I_{\parallel}$, that reduce the time-dependent effects in the dichroic signal.

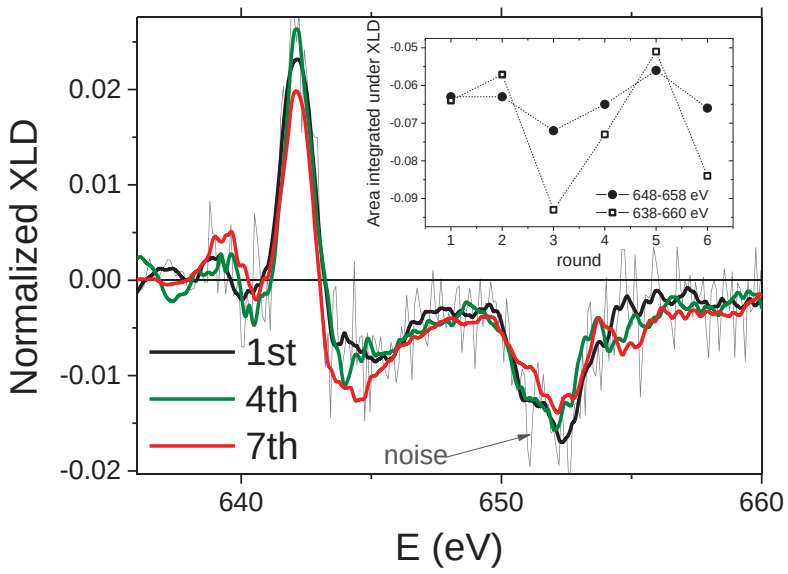

Figure D.2: XLD spectra of LSMO sample, registered during different consecutive runs; inset: evolution of integrated area under XLD signal as a function of time (represented by number of round)

D.1.2 *Depth extension of Mn^{2+} formation*

By means of partial electron yield (PEY) measurements, we could unveil the sample depth extension affected by x-ray irradiation. In PEY mode measurements, only electrons having a kinetic energy (KE) larger than some defined threshold are registered, contrary to TEY mode, in which all electrons generated at the surface layers in the de-excitation process contribute to the signal. The threshold for the KE is settled by a retarding voltage applied to a mesh placed between the sample and the channeltron analyzer that captures the electrons emitted by the sample exposed to x-rays. As the mean free path of electrons depends on their KE, probing depth is changed by modulating the KE of the emitted electrons (that is, varying the retarding voltage) [9].

We registered several $Mn - L_3$ edge XAS spectra in a $1.5nm$ LSMO sample, deliberately reduced by beam effects, in PEY mode under different retarding voltages. In fig. D.3 (a) some of these spectra are shown, as compared to spectra taken in TEY mode. It can be observed, by normalizing the intensity in the $642eV$ peak, that the intensity of the peak at around $640eV$, attributed to Mn^{2+}, largely depends on the KE of electrons. In fig. D.3 (b),we plotted the relative intensity between the two observed XAS peaks $I(640eV)/I(642eV)$, as a function of electrons KE. The resultant curve is essentially ressemblant to the characteristic KE dependence of electrons mean free path, indicating that electrons with low mean free path (coming from the most superficial layers in the sample) show the largest Mn^{2+} signal. Although we cannot calculate with accuracy the depth extension of the Mn^{2+} contribution, it is relevant to notice that we can observe this depth modulation in a $1.5nm$ ($\sim 4uc$) thick sample, thus indicating that Mn^{2+} appears mostly in a very localized region at the surface, of probably $1 - 2uc$.

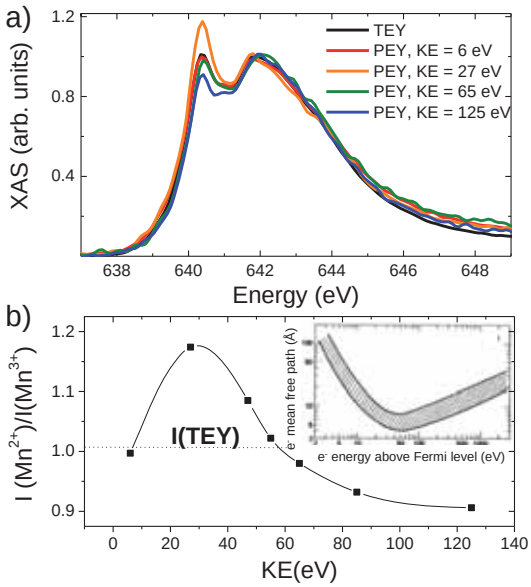

Figure D.3: a) $Mn - L_3$ edge XAS spectra registered in TEY (black curve) and PEY (coloured curves) mode under retarding voltages corresponding to the indicated electron kinetic energies. b) Intensity ratio between XAS peak at $640eV$ and peak at $642eV$, as a function of electrons kinetic energy; inset: typical distribution of electrons mean free path as a function of kinetic energy above the Fermi level [180].

D.2 INTRINSIC PRESENCE OF Mn^{2+} AT MANGANITE SURFACES

While extrinsic Mn^{2+} presence in thin films due to beam damage effects could be controlled and avoided to some extent, it was observed during synchrotron experiments in LSMO films that, at the surface of the films, there is a notable Mn^{2+} contribution, more difficult to exclude.

The presence of this Mn^{2+} component in XAS spectra was already studied in refs. [80, 91, 89, 81, 88] and, although a clear origin could not be attributed, the presence of oxygen vacancies and the effect of reducing agents in the atmosphere were proposed as responsibles of the observed Mn reduction at the surface of the films.

It was also studied, in the content of this thesis (see 5.2), the notable effect of capping layers, contributing to decrease or even completely eliminate the Mn^{2+} component. Thus, LSMO films never exposed to atmosphere (capping layers were in-situ deposited on LSMO during growth process), show a depleted Mn^{2+} content, reinforcing the effect of atmosphere reducing agents as probable cause of the appearance of Mn^{2+} at the surfaces.

D.2.1 *Strain dependence of Mn^{2+} formation*

While the factors contributing to enhance the presence of Mn^{2+} at the surface of the films could not be disclosed, we found significant variations within sample series (deposited at the same conditions, with same film thickness), signaling a relevant dependence of the Mn^{2+} content as a function of the strain imposed in the films by the different substrates. An example is shown in fig. D.4(a), where ultrathin LSMO films deposited on STO, LSAT and NGO substrates show clear dissimilar spectral features in the low energy region of the $Mn - L_3$ edge. While these features could not be attributed

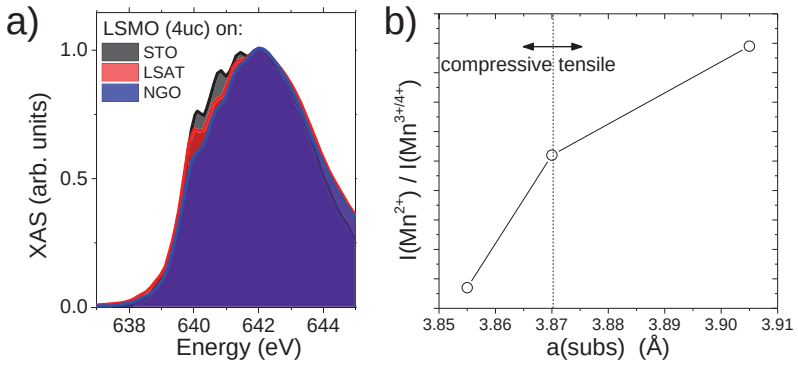

Figure D.4: a) XAS spectra (at the $Mn - L_3$ edge) of LSMO samples grown on STO, LSAT and NGO substrates. b) Intensity ratio between peaks at $640eV$ and $642eV$ as a function of in-plane lattice parameter of the films.

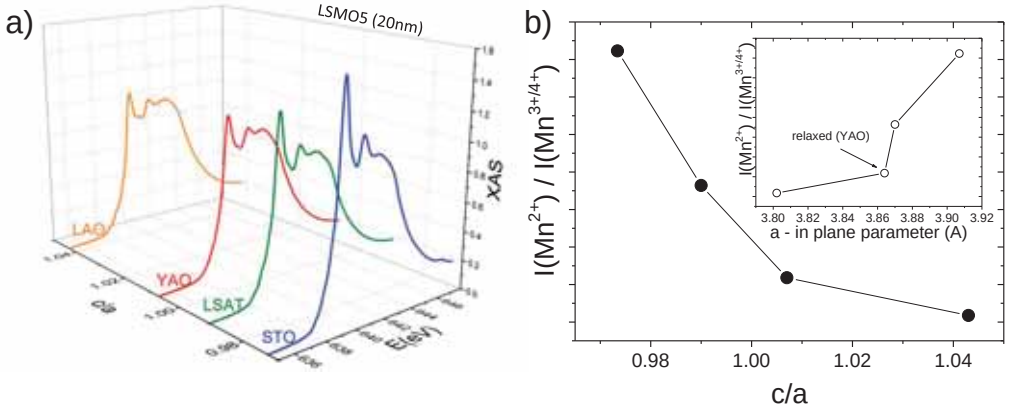

Figure D.5: a) XAS spectra (at the $Mn - L_3$ edge) of LSMO5 samples grown on LAO, YAO, LSAT and STO substrates. b) Intensity ratio between peaks at $640eV$ and $642eV$ as a function of c/a lattice parameters ratio; inset: same intensity ratio as a function of in-plane lattice parameter of the films.

to modifications in the crystal field due to substrate dependent distortions, they could in fact be accounted as variations in the Mn^{2+} content as a function of strain in the films. If we plot the relative intensity of peaks at $640eV$ (Mn^{2+}) and $642eV$ ($Mn^{3+/4+}$), as a function of in-plane lattice parameter of the films (coinciding with substrate in-plane parameter in these cases) a correlation is found (see fig.D.4(b)), showing an increased Mn^{2+} content for tensile strained films.

Similar tendency was observed in other series of samples. A remarkable example was found in $La_{1/2}Sr_{1/2}MnO_3$ (LSMO5) samples where, as shown in sec.**??**, a strong Mn^{2+} contribution was found in the XAS spectra, here replotted in fig. D.5(a) as a function of c/a ratio. While the origin of the high intensity of Mn^{2+} related peaks for these samples could not be discerned, although probably related to aging effects[81], the ratio of intensities $I(640eV)/I(642eV)$ was found to clearly decrease for increasing c/a ratio (fig.D.5(b)) and, comparable to LSMO samples, increases with increasing in-plane lattice parameter of the films (inset in fig.D.5(b)).

Therefore, although more experiments are required to clearly discern the factors governing the presence of Mn^{2+} at the surface of manganite thin films, our experiments show that films under a tensile lattice strain tend to show an increased Mn^{2+} content.

This observation could be explained by increased oxygen vacancy content at the surface of tensile strained films that would help to expand the manganite lattice and hence to minimize the elastic energy. It could also be proposed a different reducing mechanism in which the reduction of Mn is favoured by the increased lattice parameter, allowing for the formation of larger Mn^{n+} cations. In this respect, Mn^{2+} is 30% larger than Mn^{3+}, thus increased lattice parameter could favour the appearance of Mn^{2+}. As it was stated in ref.[91], the energy needed to displace surrounding oxygen atoms at the surface is much smaller than in the bulk, possibiliting the creation of Mn^{2+} at the surface of the films.

D.2.2 *Contribution of Mn^{2+} sites to linear and circular dichroic signals*

The presence of Mn^{2+} at surfaces can profoundly modify the atomic environment [84] and the magnetic interactions [111]. In order to study the influence of Mn^{2+} in these characteristics we measured two similar LSMO5 samples (grown with the same conditions, on the same substrates) with large difference in the Mn^{2+} content at the surface (probably motivated by different age of the samples). We denominated these samples: sample A (showing Mn^{2+}) and sample B (not showing Mn^{2+}).

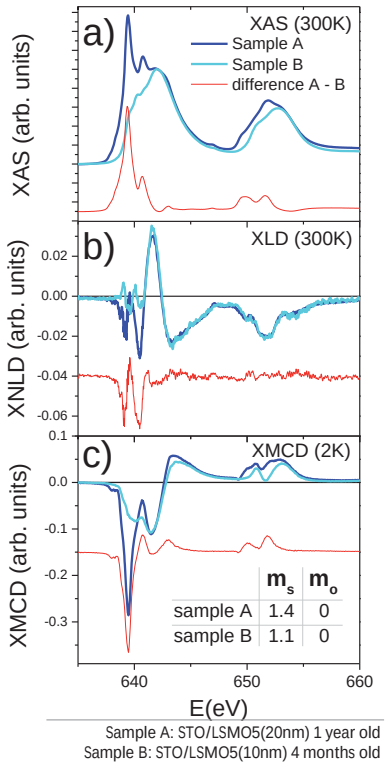

Figure D.6: Room temperature XAS (a) and XLD (b) and low temperature (2*K*) XMCD (c) spectra of LSMO5 samples grown on STO: blue curve corresponds to sample A (Mn-reduced sample), cyan curve corresponds to sample B (non-reduced sample) and red curve corresponds to spectra difference between them. Inset of panel c: calculated spin and orbital magnetic moments for both samples.

In panel (a) of fig. D.6 the clear difference between both samples in the XAS spectrum is shown. Red curve in the figure shows the difference between XAS spectra, clearly ressembling a Mn^{2+} spectrum, as shown previously (see f.e. fig.D.1(b)). The XLD signal

taken at $300K$ (above samples T_C) in grazing incidence is shown in panel (b). While the XLD signal is identical in L_2 edge, as expected (Mn^{2+} is not a Jahn-Teller ion), a visible difference is observed in the low energy region of L_3 edge. Although this residual signal could be attributed to minor differences between samples, an artifical contribution from Mn^{2+} could also be considered. The almost perfect matching of the rest of the spectrum, however, evidences a minor contribution of Mn^{2+} to the XLD.

The magnetic contribution to low temperature dichroism is studied in panel (c) of fig.D.6: A clear XMCD signal (here measured at $2K$ under $2T$ applied magnetic field) attributed to Mn^{2+} is observed. By applying sum rules to both samples (considering equal number of holes $n_h = 3.5$), a relatively minor difference in m_s values ($\sim 0.3\mu_B$) is obtained, thus showing a minor effect as compared to the bulk strain-related magnetic signal observed in these samples (see section **??**).

D.2.3 *Annealing treatment for Mn reoxidation*

Finally, it was proved in a test sample (LSMO($17nm$) on LAO), the effectiveness of an annealing process in reoxidating the surface of the samples. As observed in fig.D.7 (a-black curve), the sample showed an initial large content of Mn^{2+}, as evidenced by intense peak at $640eV$. After an annealing process with oxygen pressure $p(O_2) = 10^{-3}mbar$, at a temperature $T = 500°C$ during $1hour$, the sample spectra showed quite reduced intensity in the XAS spectra at the low energy region of L_3 (red curve), clearly signaling an oxidation process removing the initial Mn^{2+} content and restoring the initial $Mn^{3+/4+}$ valence state. The difference spectrum, also plotted in the figure shows the relevant decrease of the Mn^{2+} contribution to the final spectrum after annealing.

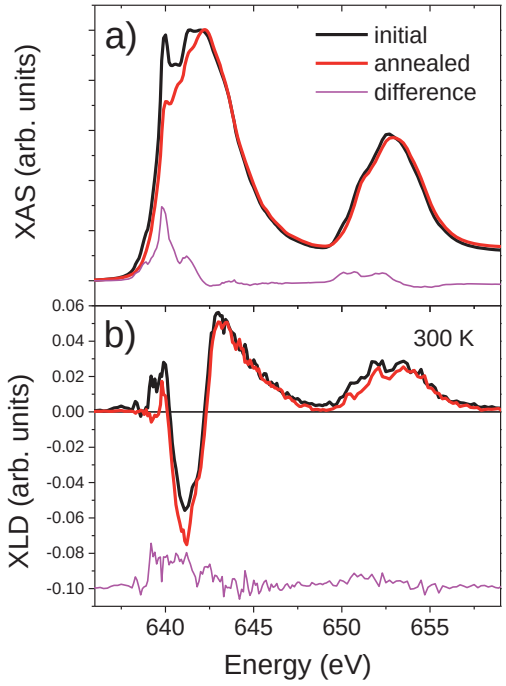

Figure D.7: XAS (a) and XLD (b) spectra of LAO//LSMO sample before (black) and after (red) annealing process; the difference between both spectra is also shown (magenta).

It is important to notice as well the insignificant influence of annealing process in the XLD spectra (fig. D.7(b)), proving the null contribution of Mn^{2+} to XLD, as expected.

The efficiency of this oxygenation process attests for a Mn reduction caused by oxygen vacancies at the surface of the films. As the oxygen content is restored, by means of the annealing process, Mn valence is also restored. Still, more study is necessary to explore the effects of annealing processes in thin film samples, as other phenomena like cation segregation can modify the stoichiometry and homogeneity of the samples.

Part V

ANNEX: LATTER RESULTS

LINEAR AND MAGNETIC DICHROISM IN $4d$ TRANSITION METAL OXIDES

E.1 INTRODUCTION

The methodology and results obtained for manganite and nickelate thin films presented in this thesis opens a way to explore orbital occupancies in other oxides. Of particular interest is $SrRuO_3$ (SRO) which is metallic and sits at the verge of a paramagnetic to ferromagnetic transition. Indeed, whereas SRO is ferromagnetic, this is not the case of $CaRuO_3$ [181]. Therefore, it may not be a surprise that the properties of SRO are very sensitive to fine tuning of its electronic properties. Indeed, by varying the strain and film thickness of SRO, different behavior are observed, leading to new transport properties [182] or even identifying new spin configurations [183], which could be explained by means of electron localization or modifications of the crystal field. In spite of these dramatic effects, little is known on the electronic occupancy of the $4d^4$ (t_{2g}^4 – low spin) electrons of SRO, and more precisely, on how the t_{2g} electrons occupy the available d_{xy}, d_{xz} and d_{yz} states and its impact on functional properties.

The first reason for this lack of experimental evidence is the limited accessibility of $Ru-L$ absorption edges in conventional synchrotron soft x-rays beamlines, due to their high energy ($> 2500eV$), being in the limit between soft and hard x-rays. The advances in the optics of new synchrotron beamlines have enabled the possibility to explore larger energy ranges. In particular, our study of $Ru-L$ edge XLD and XMCD performed at BOREAS beamline in ALBA synchrotron radiation source shows unprecedented data in this absorption edge, paving the way for new studies in these materials.

The second reason for the unreported data on Ru electron occupancy is the anticipated difficulty in obtaining large and clear dichroism signal in a $4d$ system where electron correlation effects are estimated to be lower, and having a t_{2g} configuration, where orbital hierarchy will be less affected by modifications of crystal field.

Nevertheless, we report here the results obtained for the XNLD at $Ru-L$ edge in SRO films grown under different strains, remarking the technical difficulties found for the adquisition of reliable dichroism signals due to possible artifacts masking the real sample dichroism of the samples. More clearly was found the XMCD signal at low temperatures in samples with different thicknesses, from which we show here some preliminar results.

E.2 ELECTRON OCCUPANCY OF $Ru-4d$ STATES IN $SrRuO_3$ THIN FILMS

SRO films with $16nm$ thickness (as probed by x-ray reflectometry) were grown by PLD deposition on single crystal substrates of STO, DSO, $GdScO_3$ (GSO) and $NdScO_3$ (NSO) with (001) orientation. The substrates temperature during growth was set to $675°C$ and the oxygen pressure was $0.2mbar$. With this conditions a step morphology was observed in films grown on STO, with low RMS values ($< 0.3nm$), while for samples grown on scandates, unavoidable appearance of holes during grown process superimpose to flat regions with low RMS (fig.E.1(a)).

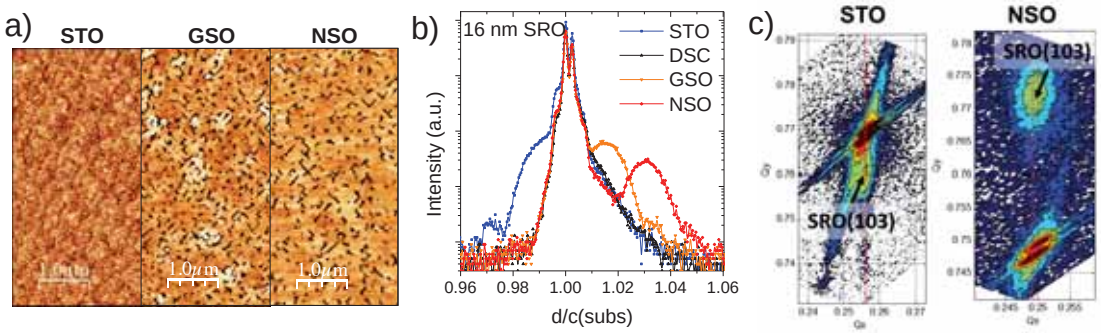

Figure E.1: a) AFM images of SRO films (16nm) grown on STO, GSO and NSO substrates. b) $\theta - 2\theta$ around (002) reflection for 16nm SRO films on the indicated substrates (angular position normalized to substrate reflection). c) RSMs around (103) reflection for SRO films grown on STO and NSO; film reflection is indicated.

substrate	mismatch (%)	a(q-plot) (Å)	c(ϑ-2ϑ) (Å)	c/a
STO	-1.1	3.91	3.922	1.003
DSO	-0.2	3.94*	3.914	0.993
GSO	0.6	3.97*	3.905	0.983
NSO	1.6	4.01	3.893	0.971

a(SRO bulk)=3.95Å

*not measured, fully strained expected

Table E.1: Measured lattice parameters of SRO films (16nm) and corresponding c/a ratio.

X-ray diffraction $\theta - 2\theta$ symmetrical scans around the (002) planes indicate a substrate induced modulation of the lattice tetragonality (fig. E.1(b)), and the RSMs around (103) reflection (shown in fig.E.1(c) for films grown on STO and NSO - largest compressive and tensile strains) indicate a fully strained state for all films. In table E.1 the measured lattice parameters for all films in the series are displayed, together with the corresponding c/a ratio that signals the tetragonal distortion in the films[1].

To explore the orbital occupancy of $Ru - 4d$ levels, XAS measurements at the $Ru - L$ edge ($2p \rightarrow 4d$ transitions) with linearly polarized x-ray were performed in grazing incidence (30deg incidence) at 300K, far above the SRO Curie temperature ($T_C = 160K$), acquiring the sample drain current. The averaged spectra $XAS = (I_{\parallel} + I_{\perp})/2$ (fig. E.2(a)) show featureless L_3 and L_2 edges, in close ressemblance with previously reported $Ru^{4+} - L$ edge spectra [185, 186], and an unidentified satellite structure in the high energy region of L_3. All samples show identical absorption spectra, revealing identical chemical state independently of strain. On the other hand, in the XLD signal (fig. E.2(b)) obtained as $XLD = (I_{\parallel} - I_{\perp})$ and normalized to the L_3 absorption peak, some modifications are observed for the different samples.

Although the shape of XLD signal reminds that of magnetic linear dichroic signals observed for Mn in chapters 5 and 6, no magnetic interactions are expected for Ru at such high temperatures (with respect to magnetic ordering temperature T_C). We can, therefore, in principle consider this XLD signal as natural dichroism originated due to orbital anisotropy.

1 Lattice parameters for scandate substrates were obtained from ref. [184]

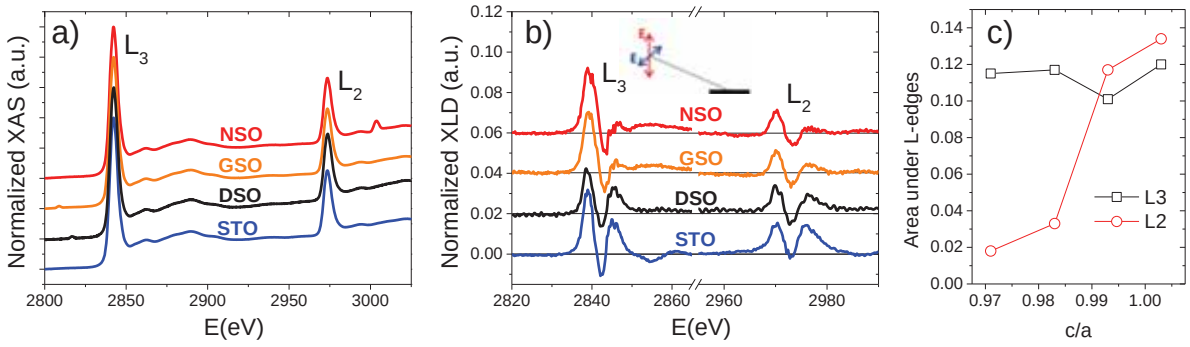

Figure E.2: a) $Ru-L$ edge XAS spectra of $16nm$ SRO films grown on the indicated substrates. b) Corresponding XLD measured in grazing incidence configuration. c) Area under XLD spectra around the L_2 (empty circles) and L_3(empty squares) edges.

Using the same methods as described in the main body of this thesis, we integrated the area under the L edges, as it should be proportional to the change in relative orbital occupancy between out-of-plane and in-plane oriented levels. We find (see fig. E.2(c)) that a correlation with structural distortion in the films can be found when integrating the L_2 edge area, indicating an increase of positive area (larger occupancy of out-of-plane oriented orbitals) when reducing the tensile strain in the films, as expected. The total area under L_3, however, does not show a clear dependence with strain.

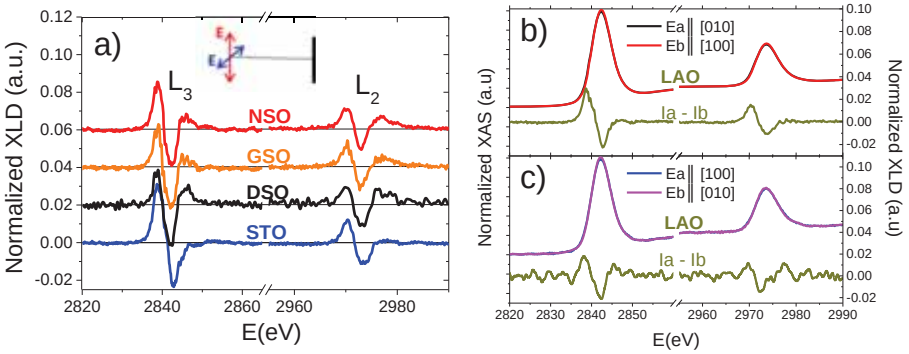

Figure E.3: a) Ru XLD signal measured in normal incidence configuration for SRO films on the indicated substrates. b) Ru XAS (left axis) and XLD (right axis) spectra measured in normal incidence for SRO film ($25nm$) grown on LAO substrate. c) Same as (b) with sample rotated by 90 degrees in plane.

To furtherly explore the linear dichroism in these samples we measured the XLD signal in normal incidence, thus probing the in-plane anisotropy of the charge distribution. Surprisingly, we find a relevant XLD signal, of similar magnitude and shape as in grazing incidence (fig. E.3(a)). This observation could indicate that samples have a lower-than-tetragonal symmetry, not observed in our x-ray diffraction measurements. In fact, scandate substrates have orthorhombic structure, that can induce a orthorhombic distortion with domains having preferential in-plane orientations in the SRO films. STO, on the other hand, is known to also influence in the in-plane anisotropy of SRO films, that can show a preferential in-plane orientation of orthorhombic domains induced by step morphology of the substrate [187].

In order to check the influence of substrate in the observed in-plane XLD, we measured at normal incidence the XLD of a SRO film ($25nm$) grown on LAO substrate,

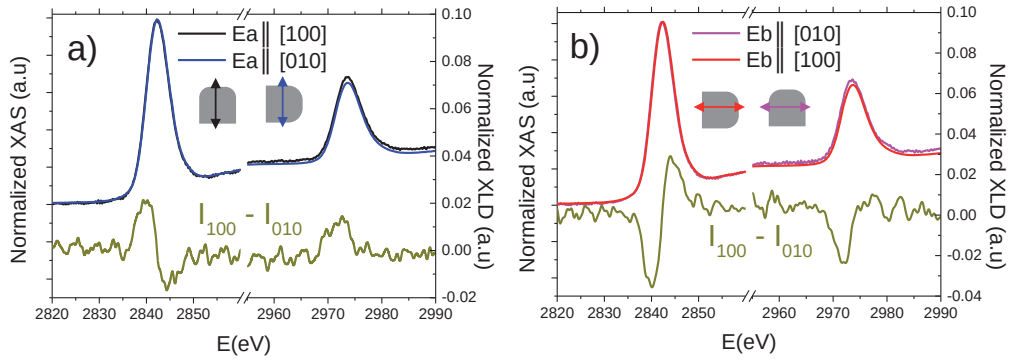

Figure E.4: a) XAS (left axis) and XLD (right axis) spectra of SRO sample grown on LAO, obtained by in-plane sample rotation with fixed photon polarization (vertical direction). b) same as (a), with fixed photon polarization in the horizontal direction. In both cases XLD is obtained as XAS($E \parallel [100]$)-XAS($E \parallel [010]$)

where no preferential domain formation is expected. We observed, however a similar XLD signal (fig. E.3(b)) as that of films grown on STO. Interestingly, when rotating the sample by 90 degrees, the sign of XLD was not inverted.

Indeed, by measuring the in-plane XLD with a fixed x-ray polarization and rotating the sample, as shown in fig.E.4(a,b), this dichroism is still well visible. The fact that for "vertical" (E_a) and "horizontal" (E_b) photon polarizations an inverted XLD is obtained points to an origin of the dichroism not intrinsic to the samples. Thus, further systematic work is required in this respect to exclude the possible influence of measurements artifacts.

E.3 MAGNETIC MOMENT OF Ru IONS IN $SrRuO_3$ THIN FILMS

The magnetic moment of Ru ions in SRO samples has been proposed to be tuneable by the crystallographic orientation of the films [183], allowing to obtain high-spin configurations that greatly enhance the measured sample magnetization. At interfaces, the local modification of crystal field can also strongly affect the spin configuration. Indeed, it has been theoretically proposed that orbital reconstructions can occur at the bare surfaces of (001) SRO films, lowering the energy of $e_g - 3z^2 - r^2$ (spin-up) states due to the symmetry breaking at the surface [188, 189]. This stabilization of $3z^2 - r^2$ states favors their occupancy on behalf of the occupancy of t_{2g} (spin down) states, thus promoting a high-spin configuration at the surface (see fig. E.5(a)-bottom) . In order to obtain this configuration, SRO films should present a RuO_2 layer termination to make this symmetry breaking effective.

In our films we did observe a relevant increase in the sample magnetization for thinnest samples. By comparing the magnetization -measured in SQUID at $10K$ and with the magnetic field applied in the out-of-plane direction- of $5nm$ SRO sample with that of $80nm$ sample (fig. E.5(b)), both grown on STO substrates, we observed an increase of magnetization of about 60% for the thinner sample, showing a value ($2.5\mu_B$) larger than the bulk SRO ($2\mu_B$)[2], that remains at larger temperatures (see measurement at $40K$ -red empty squares in the figure)

2 Experimentally, reduced saturated moment values are obtained, $M_S = 1.1 - 1.6\mu_B$ [183]

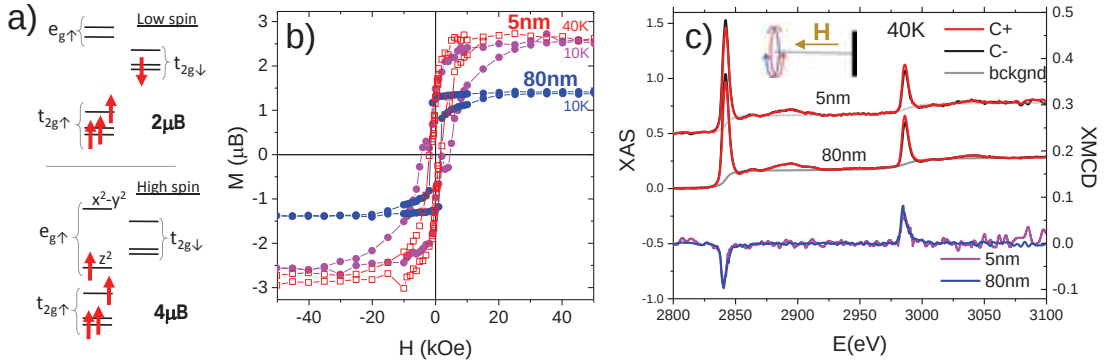

Figure E.5: a) Sketches for expected bulk low spin state in $Ru-3d$ states (top) and predicted high spin state at the RuO_2 termination (bottom). b) Magnetic loops for SRO samples 5 and 80nm thick grown on STO, measured at indicated temperatures with magnetic field oriented normal to the surface. c) XAS obtained with circular polarization (left axis) and resultant XMCD (right axis) of 5 and 80nm SRO samples, measured at $40K$ with magnetic field oriented normally to the surface.

To certify the existence of this high spin state at the surface of the films, we measured the Ru magnetic moment of these samples by XMCD. The high photon energies required for the $2p-4d$ excitations of the $Ru-L_{2,3}$ edges, force to work with a not fully circular photon polarization in order to have an appropiate beam flux. In our case, we worked with 70% circular polarization, with the beam inciding normally to the sample and a $6T$ magnetic field applied in the same direction (also corresponding to the easy axis of the samples). The XAS spectra obtained at $40K$ for both right and left circular photon polarizations are shown in fig. E.5(b-top) for both 5 and $80nm$ samples. The XMCD extracted from these measurements (fig. E.5(b-bottom)) and normalized to the XAS show similar magnitude of the dichroism for both samples, and the application of sum rules (eq.2.7) results in similar values for the spin ($m_s^{80nm} = 1.86\mu_B$ and $m_s^{5nm} = 1.83\mu_B$) and orbital ($m_o^{80nm} = 0.14\mu_B$ and $m_o^{5nm} = 0.18\mu_B$) magnetic moments, thus pointing to a low spin state at the surface of the films (fig. E.5(a)-top). Therefore, further measurements should be performed to understand the apparently contradictory SQUID and XMCD measurements.

E.4 SUMMARY

In summary we have, for the first time, reported the XLD and XMCD signal of SRO films, acquired at the $Ru-L_{2,3}$ edges. Although an incipient strain dependence of the magnitude of the XLD obtained in grazing incidence anticipates a modulation of orbital occupancy induced by the structural distortion in the films, the similar dichroism observed in normal incidence configuration reveals a more complex phenomena, either related to intrinsic structural in-plane anisotropy (and thus a lower-than-tetragonal symmetry should be considered) or due to extrinsic artifacts occurring during the measurements of XAS at such high energies. Further work is needed to clarify these points.

The XMCD signal, on the other hand shows up as a powerful tool to explore the spin state of ruthenate films as the large splitting between $L_2$and L_3 edges allows for a reliable application of sum rules. In our case, XMCD revealed the ressemblant magnetic moment of samples with different thicknesses, with a close to bulk value, excluding the possibility of high-spin states at the surface of the films.

BIBLIOGRAPHY

[1] Y. Tokura, "Orbital Physics in Transition-Metal Oxides," *Science*, vol. 288, no. 5465, pp. 462–468, Apr. 2000. [Online]. Available: http://www.sciencemag.org/cgi/doi/10.1126/science.288.5465.462 (Cited on pages 4 and 37.)

[2] J. Stöhr and H. C. Siegmann, *Magnetism: from fundamentals to nanoscale dynamics*. Springer, 2006. (Cited on pages 7, 9, 11, and 13.)

[3] H. Wende, "Recent advances in x-ray absorption spectroscopy," *Reports on Progress in Physics*, vol. 67, p. 2105, 2004. (Cited on pages 7 and 11.)

[4] C. Sorg, "Magnetic properties of 3d and 4f ferromagnets studied by X-Ray Absorption Spectroscopy," Ph.D. dissertation, Freie Universitat Berlin, 2005. (Cited on page 7.)

[5] M. W. Haverkort, "Spin and orbital degrees of freedom in transition metal oxides and oxide thin films studied by soft x-ray absorption spectroscopy," Ph.D. dissertation, Universität zu Köln, 2005. [Online]. Available: http://arxiv.org/abs/cond-mat/0505214 (Cited on pages 7 and 12.)

[6] M. de Broglie, "Sur une nouveau procede permettant d'obtenir la photographie des spectres de raies des rayons Rontgen," *Comptes Rendus*, vol. 157, p. 924, 1913. (Cited on page 7.)

[7] R. Nakajima, J. Stöhr, and Y. U. Idzerda, "Electron-yield saturation effects in L-edge x-ray magnetic circular dichroism spectra of Fe, Co, and Ni," *Phys. Rev. B*, vol. 59, pp. 6421–6429, Mar 1999. [Online]. Available: http://link.aps.org/doi/10.1103/PhysRevB.59.6421 (Cited on pages 7 and 11.)

[8] J. Stöhr, *NEXAFS Spectroscopy, Vol.25*. Springer, Berlin Heidelberg, 1992. (Cited on page 8.)

[9] K. Nakanishi and T. Ohta, "Improvement of the partial electron yield method in the higher-energy soft X-ray XAFS measurement," *Memoirs of the SR center Ritsumeikan University*, vol. 13, 2011. (Cited on pages 8 and 147.)

[10] B. T. Thole, P. Carra, F. Sette, and G. van der Laan, "X-ray circular dichroism as a probe of orbital magnetization," *Phys. Rev. Lett.*, vol. 68, pp. 1943–1946, Mar 1992. [Online]. Available: http://link.aps.org/doi/10.1103/PhysRevLett.68.1943 (Cited on pages 10 and 85.)

[11] P. Carra, B. T. Thole, M. Altarelli, and X. Wang, "X-ray circular dichroism and local magnetic fields," *Phys. Rev. Lett.*, vol. 70, pp. 694–697, Feb 1993. [Online]. Available: http://link.aps.org/doi/10.1103/PhysRevLett.70.694 (Cited on pages 10 and 85.)

[12] C. Piamonteze, P. Miedema, and F. M. F. de Groot, "Accuracy of the spin sum rule in XMCD for the transition-metal L edges from manganese to copper," *Phys. Rev. B*, vol. 80, p. 184410, Nov 2009. [Online]. Available:

http://link.aps.org/doi/10.1103/PhysRevB.80.184410 (Cited on pages 10, 73, and 85.)

[13] J. Stöhr and H. König, "Determination of Spin- and Orbital-Moment Anisotropies in Transition Metals by Angle-Dependent X-Ray Magnetic Circular Dichroism," *Phys. Rev. Lett.*, vol. 75, pp. 3748–3751, Nov 1995. [Online]. Available: http://link.aps.org/doi/10.1103/PhysRevLett.75.3748 (Cited on page 11.)

[14] C. T. Chen, L. H. Tjeng, J. Kwo, H. L. Kao, P. Rudolf, F. Sette, and R. M. Fleming, "Out-of-plane orbital characters of intrinsic and doped holes in $La_{2-x}SrxCuO_4$," *Phys. Rev. Lett.*, vol. 68, pp. 2543–2546, Apr 1992. [Online]. Available: http://link.aps.org/doi/10.1103/PhysRevLett.68.2543 (Cited on page 12.)

[15] E. Benckiser, M. W. Haverkort, S. Brueck, E. Goering, S. Macke, A. Frano, X. Yang, O. K. Andersen, G. Cristiani, H.-U. Habermeier, A. V. Boris, I. Zegkinoglou, P. Wochner, H.-J. Kim, V. Hinkov, and B. Keimer, "Orbital reflectometry of oxide heterostructures," *Nat. Mater.*, vol. 10, p. 189, 2011. [Online]. Available: http://dx.doi.org/10.1038/nmat2958 (Cited on pages 12, 41, and 100.)

[16] M. Wu, E. Benckiser, M. W. Haverkort, A. Frano, Y. Lu, U. Nwankwo, S. Brück, P. Audehm, E. Goering, S. Macke, V. Hinkov, P. Wochner, G. Christiani, S. Heinze, G. Logvenov, H.-U. Habermeier, and B. Keimer, "Strain and composition dependence of orbital polarization in nickel oxide superlattices," *Physical Review B*, vol. 88, no. 12, p. 125124, Sep. 2013. [Online]. Available: http://link.aps.org/doi/10.1103/PhysRevB.88.125124 (Cited on pages 12, 41, 94, and 100.)

[17] W. Wu, D. Huang, G. Guo, H.-J. Lin, T. Hou, C. Chang, C. Chen, a. Fujimori, T. Kimura, H. Huang, a. Tanaka, and T. Jo, "Orbital polarization of LaSrMnO4 studied by soft X-ray linear dichroism," *Journal of Electron Spectroscopy and Related Phenomena*, vol. 137-140, pp. 641–645, Jul. 2004. [Online]. Available: http://linkinghub.elsevier.com/retrieve/pii/S0368204804000908 (Cited on page 13.)

[18] Y. Takamura, F. Yang, N. Kemik, E. Arenholz, M. D. Biegalski, and H. M. Christen, "Competing interactions in ferromagnetic/antiferromagnetic perovskite superlattices," *Phys. Rev. B*, vol. 80, p. 180417(R), 2009. [Online]. Available: http://link.aps.org/doi/10.1103/PhysRevB.80.180417 (Cited on pages 14, 75, 86, and 87.)

[19] G. van der Laan, N. D. Telling, A. Potenza, S. S. Dhesi, and E. Arenholz, "Anisotropic x-ray magnetic linear dichroism and spectromicroscopy of interfacial Co/NiO(001)," *Physical Review B*, vol. 83, no. 6, p. 064409, Feb. 2011. [Online]. Available: http://link.aps.org/doi/10.1103/PhysRevB.83.064409 (Cited on page 14.)

[20] G. van der Laan, "Magnetic linear x-ray dichroism as a probe of the magnetocrystalline anisotropy," *Phys. Rev. Lett.*, vol. 82, p. 640, 1999. [Online]. Available: http://link.aps.org/doi/10.1103/PhysRevLett.82.640 (Cited on page 14.)

[21] C. Zener, "Interaction between the d shells in the transition metals," *Phys. Rev.*, vol. 81, pp. 440–444, Feb 1951. [Online]. Available: http://link.aps.org/doi/10.1103/PhysRev.81.440 (Cited on page 17.)

[22] J. B. Goodenough, "Theory of the Role of Covalence in the Perovskite-Type Manganites $[La, M(II)]MnO_3$," *Phys. Rev.*, vol. 100, pp. 564–573, Oct 1955. [Online]. Available: http://link.aps.org/doi/10.1103/PhysRev.100.564 (Cited on page 17.)

[23] G. Jonker and J. Van Santen, "Ferromagnetic compounds of manganese with perovskite structure," *Physica*, vol. 16, no. 3, pp. 337–349, Mar. 1950. [Online]. Available: http://www.sciencedirect.com/science/article/pii/0031891450900334 (Cited on page 17.)

[24] M. Viret, M. Drouet, J. Nassar, J. P. Contour, C. Fermon, and A. Fert, "Low-field colossal magnetoresistance in manganite tunnel spin valves," *EPL (Europhysics Letters)*, vol. 39, no. 5, p. 545, 1997. [Online]. Available: http://stacks.iop.org/0295-5075/39/i=5/a=545 (Cited on page 17.)

[25] J.-H. Park, E. Vescovo, H.-J. Kim, C. Kwon, R. Ramesh, and T. Venkatesan, "Magnetic Properties at Surface Boundary of a Half-Metallic Ferromagnet $La_{0.7}Sr_{0.3}MnO_3$," *Phys. Rev. Lett.*, vol. 81, pp. 1953–1956, Aug 1998. [Online]. Available: http://link.aps.org/doi/10.1103/PhysRevLett.81.1953 (Cited on pages 18 and 145.)

[26] D. Pesquera, G. Herranz, A. Barla, E. Pellegrin, F. Bondino, E. Magnano, F. Sánchez, and J. Fontcuberta, "Surface symmetry-breaking and strain effects on orbital occupancy in transition metal perovskite epitaxial films." *Nature communications*, vol. 3, p. 1189, Jan. 2012. [Online]. Available: http://www.ncbi.nlm.nih.gov/pubmed/23149734 (Cited on pages 18 and 94.)

[27] A. Tebano, C. Aruta, S. Sanna, P. G. Medaglia, G. Balestrino, A. A. Sidorenko, R. De Renzi, G. Ghiringhelli, L. Braicovich, V. Bisogni, and N. B. Brookes, "Evidence of Orbital Reconstruction at Interfaces in Ultrathin $La_{0.67}Sr_{0.33}MnO_3$ Films," *Phys. Rev. Lett.*, vol. 100, p. 137401, Apr 2008. [Online]. Available: http://link.aps.org/doi/10.1103/PhysRevLett.100.137401 (Cited on pages 18, 37, 38, 43, and 94.)

[28] S. Estradé, J. M. Rebled, J. Arbiol, F. Peiro, I. C. Infante, G. Herranz, F. Sanchez, J. Fontcuberta, R. Cordoba, B. G. Mendis, and A. L. Bleloch, "Effects of thickness on the cation segregation in epitaxial (001) and (110) $La_{2/3}Ca_{1/3}MnO_3$ thin films," *Applied Physics Letters*, vol. 95, no. 7, pp. –, 2009. [Online]. Available: http://scitation.aip.org/content/aip/journal/apl/95/7/10.1063/1.3211130 (Cited on page 18.)

[29] J. L. Maurice, F. Pailloux, A. Barthelemy, O. Durand, D. Imhoff, R. Lyonnet, A. Rocher, and J. P. Contour, "Strain relaxation in the epitaxy of $La_{2/3}Sr_{1/3}MnO_3$ grown by pulsed-laser deposition on $SrTiO_3$(001)," *Philosophical Magazine*, vol. 83, no. 28, pp. 3201–3224, Oct. 2003. [Online]. Available: http://dx.doi.org/10.1080/14786430310001603436 (Cited on pages 18 and 40.)

[30] R. Herger, P. Willmott, C. Schlepütz, M. Björck, S. Pauli, D. Martoccia, B. Patterson, D. Kumah, R. Clarke, Y. Yacoby, and M. Döbeli, "Structure determination of monolayer-by-monolayer grown $La_{1-x}Sr_xMnO_3$ thin films and the onset of magnetoresistance," *Physical Review B*, vol. 77, no. 8, pp. 1–10, Feb. 2008. [Online]. Available: http://link.aps.org/doi/10.1103/PhysRevB.77.085401 (Cited on page 19.)

[31] I. Infante, F. Sánchez, J. Fontcuberta, M. Wojcik, E. Jedryka, S. Estradé, F. Peiró, J. Arbiol, V. Laukhin, and J. Espinós, "Elastic and orbital effects on thickness-dependent properties of manganite thin films," *Physical Review B*, vol. 76, no. 22, pp. 1–12, Dec. 2007. [Online]. Available: http://link.aps.org/doi/10.1103/PhysRevB.76.224415 (Cited on pages 19, 20, 24, 25, 26, 33, and 43.)

[32] U. Gebhardt, N. V. Kasper, A. Vigliante, P. Wochner, H. Dosch, F. S. Razavi, and H.-U. Habermeier, "Formation and thickness evolution of periodic twin domains in manganite films grown on $SrTiO_3$ substrates," *Phys. Rev. Lett.*, vol. 98, p. 096101, Feb 2007. [Online]. Available: http://link.aps.org/doi/10.1103/PhysRevLett.98.096101 (Cited on page 19.)

[33] F. Sandiumenge, J. Santiso, L. Balcells, Z. Konstantinovic, J. Roqueta, A. Pomar, J. Espinós, and B. Martínez, "Competing Misfit Relaxation Mechanisms in Epitaxial Correlated Oxides," *Physical Review Letters*, vol. 110, no. 10, p. 107206, Mar. 2013. [Online]. Available: http://link.aps.org/doi/10.1103/PhysRevLett.110.107206 (Cited on page 19.)

[34] S. Estradé, J. Arbiol, F. Peiroó, I. C. Infante, F. Sánchez, J. Fontcuberta, F. de la Peña, M. Walls, and C. Colliex, "Cationic and charge segregation in $La_{2/3}Ca_{1/3}MnO_3$ thin films grown on (001) and (110) $SrTiO_3$," *Applied Physics Letters*, vol. 93, no. 11, p. 112505, 2008. [Online]. Available: http://scitation.aip.org/content/aip/journal/apl/93/11/10.1063/1.2981574 (Cited on page 19.)

[35] T. T. Fister, D. D. Fong, J. A. Eastman, P. M. Baldo, M. J. Highland, P. H. Fuoss, K. R. Balasubramaniam, J. C. Meador, and P. A. Salvador, "In situ characterization of strontium surface segregation in epitaxial $La_{0.7}Sr_{0.3}MnO_3$ thin films as a function of oxygen partial pressure," *Applied Physics Letters*, vol. 93, no. 15, p. 151904, 2008. [Online]. Available: http://scitation.aip.org/content/aip/journal/apl/93/15/10.1063/1.2987731 (Cited on page 19.)

[36] M. A. Torija, M. Sharma, J. Gàzquez, M. Varela, C. He, J. Schmitt, J. A. Borchers, M. Laver, S. El-Khatib, and C. Leighton, "Chemically Driven Nanoscopic Magnetic Phase Separation at the $SrTiO_3(001)/La_{1-x}Sr_xCoO_3$ Interface," *Advanced Materials*, vol. 23, no. 24, pp. 2711–2715, 2011. [Online]. Available: http://dx.doi.org/10.1002/adma.201100417 (Cited on page 19.)

[37] J. Gàzquez, S. Bose, M. Sharma, M. A. Torija, S. J. Pennycook, C. Leighton, and M. Varela, "Lattice mismatch accommodation via oxygen vacancy ordering in epitaxial $La_{0.5}Sr_{0.5}CoO_{3-\delta}$ thin films," *APL Materials*, vol. 1, no. 1, p. 012105, 2013. [Online]. Available: http://scitation.aip.org/content/aip/journal/aplmater/1/1/10.1063/1.4809547 (Cited on page 19.)

[38] M. Bibes, L. Balcells, S. Valencia, J. Fontcuberta, M. Wojcik, E. Jedryka, and S. Nadolski, "Nanoscale Multiphase Separation at $La_{2/3}Ca_{1/3}MnO_3/SrTiO_3$ Interfaces," *Physical Review Letters*, vol. 87, no. 6, p. 067210, Jul. 2001. [Online]. Available: http://link.aps.org/doi/10.1103/PhysRevLett.87.067210 (Cited on pages 20, 24, 25, 26, 33, 37, and 43.)

[39] M. Huijben, L. W. Martin, Y.-H. Chu, M. B. Holcomb, P. Yu, G. Rijnders, D. H. a. Blank, and R. Ramesh, "Critical thickness and orbital ordering in ultrathin

$La_{0.7}Sr_{0.3}MnO_3$ films," *Physical Review B*, vol. 78, no. 9, pp. 1–7, Sep. 2008. [Online]. Available: http://link.aps.org/doi/10.1103/PhysRevB.78.094413 (Cited on pages 20, 37, and 43.)

[40] J. F. Scott, "Soft-mode spectroscopy: Experimental studies of structural phase transitions," *Rev. Mod. Phys.*, vol. 46, pp. 83–128, Jan 1974. [Online]. Available: http://link.aps.org/doi/10.1103/RevModPhys.46.83 (Cited on page 22.)

[41] J. O´ Donnell, M. S. Rzchowski, J. N. Eckstein, and I. Bozovic, "Magnetoelastic coupling and magnetic anisotropy in $La_{0.67}Sr_{0.33}MnO_3$ films," *Applied Physics Letters*, vol. 72, no. 14, p. 1775, 1998. [Online]. Available: http://link.aip.org/link/APPLAB/v72/i14/p1775/s1&Agg=doi (Cited on pages 22 and 27.)

[42] V. K. Vlasko-Vlasov, Y. K. Lin, D. J. Miller, U. Welp, G. W. Crabtree, and V. I. Nikitenko, "Direct magneto-optical observation of a structural phase transition in thin films of manganites," *Phys. Rev. Lett.*, vol. 84, pp. 2239–2242, Mar 2000. [Online]. Available: http://link.aps.org/doi/10.1103/PhysRevLett.84.2239 (Cited on pages 23 and 24.)

[43] V. K. Vlasko-Vlasov, Y. Lin, U. Welp, G. W. Crabtree, D. J. Miller, and V. I. Nikitenko, "Observation of the structural phase transition in manganite films by magneto-optical imaging," *Journal of Applied Physics*, vol. 87, no. 9, pp. 5828–5830, 2000. [Online]. Available: http://scitation.aip.org/content/aip/journal/jap/87/9/10.1063/1.372536 (Cited on pages 23 and 24.)

[44] Y. Segal, K. F. Garrity, C. A. F. Vaz, J. D. Hoffman, F. J. Walker, S. Ismail-Beigi, and C. H. Ahn, "Dynamic Evanescent Phonon Coupling Across the $La_{1-x}Ca_xMnO_3/SrTiO_3$ Interface," *Phys. Rev. Lett.*, vol. 107, p. 105501, Aug 2011. [Online]. Available: http://link.aps.org/doi/10.1103/PhysRevLett.107.105501 (Cited on page 24.)

[45] M. Ziese, I. Vrejoiu, A. Setzer, A. Lotnyk, and D. Hesse, "Coupled magnetic and structural transitions in $La_{0.7}Sr_{0.3}MnO_3$ films on $SrTiO_3$," *New Journal of Physics*, vol. 10, no. 6, p. 063024, 2008. [Online]. Available: http://stacks.iop.org/1367-2630/10/i=6/a=063024 (Cited on page 24.)

[46] M. Egilmez, M. M. Saber, I. Fan, K. H. Chow, and J. Jung, "Correlation of structural phase transition and electrical transport properties of manganite films on $SrTiO_3$," *Phys. Rev. B*, vol. 78, p. 172405, Nov 2008. [Online]. Available: http://link.aps.org/doi/10.1103/PhysRevB.78.172405 (Cited on page 24.)

[47] A. G. Lehmann, C. Sanna, F. Congiu, G. Concas, and L. Maritato, "Pure ferromagnetism vs. re-entrant spin glass behaviour in epitaxial $La_{0.7}Sr_{0.3}MnO_3$ on $SrTiO_3(001)$ and $LaAlO_3(001)$: the role of the substrate structural transition," *physica status solidi (b)*, vol. 246, no. 8, pp. 1948–1955, 2009. [Online]. Available: http://dx.doi.org/10.1002/pssb.200844399 (Cited on page 24.)

[48] M. Bibes, S. Valencia, L. Balcells, B. Martínez, J. Fontcuberta, M. Wojcik, S. Nadolski, and E. Jedryka, "Charge trapping in optimally doped epitaxial manganite thin films," *Phys. Rev. B*, vol. 66, p. 134416, Oct 2002. [Online]. Available: http://link.aps.org/doi/10.1103/PhysRevB.66.134416 (Cited on pages 24, 25, 26, 31, 33, and 37.)

[49] S. Brivio, C. Magen, A. A. Sidorenko, D. Petti, M. Cantoni, M. Finazzi, F. Ciccacci, R. De Renzi, M. Varela, S. Picozzi, and R. Bertacco, "Effects of Au nanoparticles on the magnetic and transport properties of $La_{0.67}Sr_{0.33}MnO_3$ ultrathin layers," *Physical Review B*, vol. 81, no. 9, pp. 1–10, Mar. 2010. [Online]. Available: http://link.aps.org/doi/10.1103/PhysRevB.81.094410 (Cited on pages 24, 25, and 26.)

[50] A. Sidorenko, G. Allodi, R. De Renzi, G. Balestrino, and M. Angeloni, "Mn^{55} NMR and magnetization studies of $La_{0.67}Sr_{0.33}MnO_3$ thin films," *Physical Review B*, vol. 73, no. 5, p. 054406, Feb. 2006. [Online]. Available: http://link.aps.org/doi/10.1103/PhysRevB.73.054406 (Cited on pages 24, 25, 26, 27, and 33.)

[51] M. M. Savosta and P. Novák, "Two-phase character of metallic ferromagnetism in manganites," *Phys. Rev. Lett.*, vol. 87, p. 137204, Sep 2001. [Online]. Available: http://link.aps.org/doi/10.1103/PhysRevLett.87.137204 (Cited on pages 24, 25, and 26.)

[52] G. Matsumoto, "Study of $La_{1-x}Ca_xMnO_3$. I. Magnetic Structure of $LaMnO_3$," *Journal of the Physical Society of Japan*, vol. 29, no. 3, pp. 606–615, 1970. [Online]. Available: http://journals.jps.jp/doi/abs/10.1143/JPSJ.29.606 (Cited on pages 24, 25, and 26.)

[53] G. Allodi, R. De Renzi, G. Guidi, F. Licci, and M. Pieper, "Electronic phase separation in lanthanum manganites," *Physical Review B*, vol. 56, no. 10, pp. 6036–6046, Sep. 1997. [Online]. Available: http://link.aps.org/doi/10.1103/PhysRevB.56.6036 (Cited on pages 24, 25, and 26.)

[54] M. Bibes, L. Balcells, J. Fontcuberta, M. Wojcik, S. Nadolski, and E. Jedryka, "Surface-induced phase separation in manganites: A microscopic origin for powder magnetoresistance," *Applied Physics Letters*, vol. 82, no. 6, p. 928, 2003. [Online]. Available: http://scitation.aip.org/content/aip/journal/apl/82/6/10.1063/1.1543235 (Cited on page 24.)

[55] M. M. Savosta, V. N. Krivoruchko, I. A. Danilenko, V. Y. Tarenkov, T. E. Konstantinova, A. V. Borodin, and V. N. Varyukhin, "Nuclear spin dynamics and magnetic structure of nanosized particles of $La_{2/3}Sr_{1/3}MnO_3$," *Phys. Rev. B*, vol. 69, p. 024413, Jan 2004. [Online]. Available: http://link.aps.org/doi/10.1103/PhysRevB.69.024413 (Cited on page 24.)

[56] J. J. Kavich, M. P. Warusawithana, J. W. Freeland, P. Ryan, X. Zhai, R. H. Kodama, and J. N. Eckstein, "Nanoscale suppression of magnetization at atomically assembled manganite interfaces: Xmcd and xrms measurements," *Phys. Rev. B*, vol. 76, p. 014410, Jul 2007. [Online]. Available: http://link.aps.org/doi/10.1103/PhysRevB.76.014410 (Cited on page 24.)

[57] J. Z. Sun, D. W. Abraham, R. a. Rao, and C. B. Eom, "Thickness-dependent magnetotransport in ultrathin manganite films," *Applied Physics Letters*, vol. 74, no. 20, p. 3017, 1999. [Online]. Available: http://scitation.aip.org/content/aip/journal/apl/74/20/10.1063/1.124050 (Cited on pages 24 and 37.)

[58] P. Panissod, M. Malinowska, E. Jedryka, M. Wojcik, S. Nadolski, M. Knobel, and J. E. Schmidt, "Inhomogeneous structure and magnetic properties of

granular $Co_{10}Cu_{90}$ alloys," *Phys. Rev. B*, vol. 63, p. 014408, Dec 2000. [Online]. Available: http://link.aps.org/doi/10.1103/PhysRevB.63.014408 (Cited on pages 25 and 32.)

[59] A. M. De Léon-Guevara, P. Berthet, J. Berthon, F. Millot, A. Revcolevschi, A. Anane, C. Dupas, K. Le Dang, J. P. Renard, and P. Veillet, "Influence of controlled oxygen vacancies on the magnetotransport and magnetostructural phenomena in $La_{0.85}Sr_{0.15}MnO_{3-d}$ single crystals," *Phys. Rev. B*, vol. 56, pp. 6031–6035, Sep 1997. [Online]. Available: http://link.aps.org/doi/10.1103/PhysRevB.56.6031 (Cited on page 26.)

[60] P. Bruno and J.-P. Renard, "Magnetic surface anisotropy of transition metal ultrathin films," *Applied Physics A*, vol. 49, no. 5, pp. 499–506, 1989. [Online]. Available: http://dx.doi.org/10.1007/BF00617016 (Cited on page 27.)

[61] C. Chappert and P. Bruno, "Magnetic anisotropy in metallic ultrathin films and related experiments on cobalt films (invited)," *Journal of Applied Physics*, vol. 64, no. 10, p. 5736, 1988. [Online]. Available: http://scitation.aip.org/content/aip/journal/jap/64/10/10.1063/1.342243 (Cited on page 27.)

[62] A. M. Portis and A. C. Gossard, "Nuclear Resonance in Ferromagnetic Cobalt," *Journal of Applied Physics*, vol. 31, no. 5, p. S205, 1960. [Online]. Available: http://scitation.aip.org/content/aip/journal/jap/31/5/10.1063/1.1984666 (Cited on page 27.)

[63] L. M. Berndt, V. Balbarin, and Y. Suzuki, "Magnetic anisotropy and strain states of (001) and (110) colossal magnetoresistance thin films," *Applied Physics Letters*, vol. 77, no. 18, p. 2903, 2000. [Online]. Available: http://link.aip.org/link/APPLAB/v77/i18/p2903/s1&Agg=doi (Cited on page 27.)

[64] A. Shick, "First-principles calculation of uniaxial magnetic anisotropy and magnetostriction in strained colossal magnetoresistance films," *Physical Review B*, vol. 60, no. 9, pp. 6254–6257, Sep. 1999. [Online]. Available: http://link.aps.org/doi/10.1103/PhysRevB.60.6254 (Cited on page 27.)

[65] M. Sharma, J. Gazquez, M. Varela, J. Schmitt, and C. Leighton, "Coercivity enhancement driven by interfacial magnetic phase separation in $SrTiO_3(001)/Nd_{0.5}Sr_{0.5}CoO_3$," *Phys. Rev. B*, vol. 84, p. 024417, Jul 2011. [Online]. Available: http://link.aps.org/doi/10.1103/PhysRevB.84.024417 (Cited on page 32.)

[66] Z. Fang, I. Solovyev, and K. Terakura, "Phase diagram of tetragonal manganites," *Physical review letters*, vol. 84, no. 14, pp. 3169–72, Apr. 2000. [Online]. Available: http://www.ncbi.nlm.nih.gov/pubmed/11019039 (Cited on pages 37, 81, 87, and 88.)

[67] C. Aruta, G. Ghiringhelli, A. Tebano, N. Boggio, N. Brookes, P. Medaglia, and G. Balestrino, "Strain induced x-ray absorption linear dichroism in $La_{0.7}Sr_{0.3}MnO_3$ thin films," *Physical Review B*, vol. 73, no. 23, pp. 1–8, Jun. 2006. [Online]. Available: http://link.aps.org/doi/10.1103/PhysRevB.73.235121 (Cited on pages 37 and 40.)

[68] A. Tebano, A. Orsini, P. G. Medaglia, D. Di Castro, G. Balestrino, B. Freelon, A. Bostwick, Y. J. Chang, G. Gaines, E. Rotenberg, and N. L. Saini, "Preferential occupation of interface bands in $La_{2/3}Sr_{1/3}MnO_3$ films as seen via angle-resolved photoemission," *Phys. Rev. B*, vol. 82, p. 214407, Dec 2010. [Online]. Available: http://link.aps.org/doi/10.1103/PhysRevB.82.214407 (Cited on page 37.)

[69] M. J. Calderón, L. Brey, and F. Guinea, "Surface electronic structure and magnetic properties of doped manganites," *Phys. Rev. B*, vol. 60, pp. 6698–6704, Sep 1999. [Online]. Available: http://link.aps.org/doi/10.1103/PhysRevB.60.6698 (Cited on pages 37, 44, and 62.)

[70] H. Zenia, G. Gehring, G. Banach, and W. Temmerman, "Electronic and magnetic properties of the (001) surface of hole-doped manganites," *Physical Review B*, vol. 71, no. 2, p. 024416, Jan. 2005. [Online]. Available: http://link.aps.org/doi/10.1103/PhysRevB.71.024416 (Cited on page 37.)

[71] T. Maruyama, Y. Shiota, T. Nozaki, K. Ohta, N. Toda, M. Mizuguchi, A. A. Tulapurkar, T. Shinjo, M. Shiraishi, S. Mizukami, Y. Ando, and Y. Suzuki, "Large voltage-induced magnetic anisotropy change in a few atomic layers of iron," *Nature Nanotechnology*, vol. 4, no. March, pp. 158–161, 2009. [Online]. Available: http://dx.doi.org/10.1038/nnano.2008.406 (Cited on page 37.)

[72] J. D. Burton and E. Y. Tsymbal, "Giant Tunneling Electroresistance Effect Driven by an Electrically Controlled Spin Valve at a Complex Oxide Interface," *Physical Review Letters*, vol. 106, no. 15, p. 157203, Apr. 2011. [Online]. Available: http://link.aps.org/doi/10.1103/PhysRevLett.106.157203 (Cited on page 37.)

[73] E. Stavitski and F. De Groot, "The CTM4XAS program for EELS and XAS spectral shape analysis of transition metal L edges," *Micron Oxford England*, vol. 41, pp. 687–694, 2010. (Cited on pages 39 and 109.)

[74] G. van der Laan, "Sum rules and fundamental spectra of magnetic x-ray dichroism in crystal field symmetry," *J. Phys. Soc. Jpn.*, vol. 63, pp. 2393–2400, 1994. (Cited on pages 41 and 100.)

[75] M. J. Han, C. A. Marianetti, and A. J. Millis, "Chemical control of orbital polarization in artificially structured transition-metal oxides from first principles," *Phys. Rev. B*, vol. 82, p. 134408, Oct 2010. [Online]. Available: http://link.aps.org/doi/10.1103/PhysRevB.82.134408 (Cited on pages 41, 70, and 94.)

[76] B. H. Frazer, B. Gilbert, B. R. Sonderegger, and G. De Stasio, "The probing depth of total electron yield in the sub-keV range: TEY-XAS and X-PEEM," *Surface Science*, vol. 537, no. 1-3, pp. 161–167, Jul. 2003. [Online]. Available: http://linkinghub.elsevier.com/retrieve/pii/S0039602803006137 (Cited on page 44.)

[77] J.-S. Lee, D. Arena, P. Yu, C. Nelson, R. Fan, C. Kinane, S. Langridge, M. Rossell, R. Ramesh, and C.-C. Kao, "Hidden Magnetic Configuration in Epitaxial $La_{1-x}Sr_xMnO_3$ Films," *Physical Review Letters*, vol. 105, no. 25, pp. 1–4, Dec. 2010. [Online]. Available: http://link.aps.org/doi/10.1103/PhysRevLett.105.257204 (Cited on page 44.)

[78] G. Koster, B. L. Kropman, G. J. H. M. Rijnders, D. H. A. Blank, and H. Rogalla, "Quasi-ideal strontium titanate crystal surfaces through formation of strontium hydroxide," *Applied Physics Letters*, vol. 73, no. 20, p. 2920, 1998. [Online]. Available: http://link.aip.org/link/APPLAB/v73/i20/p2920/s1&Agg=doi (Cited on page 45.)

[79] R. Bachelet, F. Sánchez, F. J. Palomares, C. Ocal, and J. Fontcuberta, "Atomically flat SrO-terminated $SrTiO_3$ (001) substrate," *Applied Physics Letters*, vol. 95, no. 14, p. 141915, 2009. [Online]. Available: http://link.aip.org/link/APPLAB/v95/i14/p141915/s1&Agg=doi (Cited on page 45.)

[80] M. de Jong, I. Bergenti, V. Dediu, M. Fahlman, M. Marsi, and C. Taliani, "Evidence for Mn^{2+} ions at surfaces of $La_{0.7}Sr_{0.3}MnO_3$ thin films," *Physical Review B*, vol. 71, no. 1, p. 014434, Jan. 2005. [Online]. Available: http://link.aps.org/doi/10.1103/PhysRevB.71.014434 (Cited on pages 57, 58, 146, and 148.)

[81] S. Valencia, A. Gaupp, W. Gudat, L. Abad, L. Balcells, a. Cavallaro, B. Martínez, and F. Palomares, "Mn valence instability in $La_{2/3}Ca_{1/3}MnO_3$ thin films," *Physical Review B*, vol. 73, no. 10, p. 104402, Mar. 2006. [Online]. Available: http://link.aps.org/doi/10.1103/PhysRevB.73.104402 (Cited on pages 57, 146, 148, and 149.)

[82] B. Gilbert, B. H. Frazer, A. Belz, P. G. Conrad, K. H. Nealson, D. Haskel, J. C. Lang, G. Srajer, and G. De Stasio, "Multiple Scattering Calculations of Bonding and X-ray Absorption Spectroscopy of Manganese Oxides," *The Journal of Physical Chemistry A*, vol. 107, no. 16, pp. 2839–2847, Apr. 2003. [Online]. Available: http://pubs.acs.org/doi/abs/10.1021/jp021493s (Cited on pages 57 and 146.)

[83] S. Voss, M. Fonin, L. Burova, M. Burgert, Y. S. Dedkov, A. B. Preobrajenski, E. Goering, U. Groth, A. R. Kaul, and U. Ruediger, "Investigation of the stability of Mn_{12} single molecule magnets," *Applied Physics A*, vol. 94, no. 3, pp. 491–495, Oct. 2008. [Online]. Available: http://link.springer.com/10.1007/s00339-008-4911-6 (Cited on pages 57 and 146.)

[84] A. Galdi, C. Aruta, P. Orgiani, N. B. Brookes, G. Ghiringhelli, M. Moretti Sala, R. V. K. Mangalam, W. Prellier, U. Lüders, and L. Maritato, "Magnetic properties and orbital anisotropy driven by Mn^{2+} in nonstoichiometric $La_xMnO_{3-\delta}$ thin films," *Physical Review B*, vol. 83, no. 6, p. 064418, Feb. 2011. [Online]. Available: http://link.aps.org/doi/10.1103/PhysRevB.83.064418 (Cited on pages 57, 78, 146, and 150.)

[85] M. Abbate, F. M. F. de Groot, J. C. Fuggle, A. Fujimori, O. Strebel, F. Lopez, M. Domke, G. Kaindl, G. A. Sawatzky, M. Takano, Y. Takeda, H. Eisaki, and S. Uchida, "Controlled-valence properties of $La_{1-x}Sr_xFeO_3$ and $La_{1-x}Sr_xMnO_3$ studied by soft-x-ray absorption spectroscopy," *Phys. Rev. B*, vol. 46, pp. 4511–4519, Aug 1992. [Online]. Available: http://link.aps.org/doi/10.1103/PhysRevB.46.4511 (Cited on pages 57 and 83.)

[86] S. Valencia, Z. Konstantinovic, D. Schmitz, a. Gaupp, L. Balcells, and B. Martínez, "Interfacial effects in manganite thin films with different capping layers of interest for spintronic applications," *Physical Review B*, vol. 84, no. 2, p. 024413, Jul. 2011.

[Online]. Available: http://link.aps.org/doi/10.1103/PhysRevB.84.024413 (Cited on pages 57 and 77.)

[87] L. Zeng, A. Huegel, E. Helgren, F. Hellman, C. Piamonteze, and E. Arenholz, "X-ray absorption study of the electronic structure of Mn-doped amorphous Si," *Applied Physics Letters*, vol. 92, no. 14, p. 142503, 2008. [Online]. Available: http://scitation.aip.org/content/aip/journal/apl/92/14/10.1063/1.2908050 (Cited on pages 57 and 61.)

[88] S. Valencia, a. Gaupp, W. Gudat, L. Abad, L. Balcells, and B. Martínez, "Impact of microstructure on the Mn valence of $La_{2/3}Ca_{1/3}MnO_3$ thin films," *Physical Review B*, vol. 75, no. 18, p. 184431, May 2007. [Online]. Available: http://link.aps.org/doi/10.1103/PhysRevB.75.184431 (Cited on pages 58 and 148.)

[89] S. Picozzi, C. Ma, Z. Yang, R. Bertacco, M. Cantoni, a. Cattoni, D. Petti, S. Brivio, and F. Ciccacci, "Oxygen vacancies and induced changes in the electronic and magnetic structures of $La_{0.66}Sr_{0.33}MnO_3$: A combined ab initio and photoemission study," *Physical Review B*, vol. 75, no. 9, p. 094418, Mar. 2007. [Online]. Available: http://link.aps.org/doi/10.1103/PhysRevB.75.094418 (Cited on pages 59 and 148.)

[90] M. F. Hundley and J. J. Neumeier, "Thermoelectric power of inadequacy of the nominal valence approach," *Phys. Rev. B*, vol. 55, pp. 11 511–11 515, May 1997. [Online]. Available: http://link.aps.org/doi/10.1103/PhysRevB.55.11511 (Cited on page 59.)

[91] M. de Jong, I. Bergenti, W. Osikowicz, R. Friedlein, V. Dediu, C. Taliani, and W. Salaneck, "Valence electronic states related to Mn^{2+} at $La_{0.7}Sr_{0.3}MnO_3$ surfaces characterized by resonant photoemission," *Physical Review B*, vol. 73, no. 5, p. 052403, Feb. 2006. [Online]. Available: http://link.aps.org/doi/10.1103/PhysRevB.73.052403 (Cited on pages 59, 148, and 150.)

[92] N. Nakagawa, H. Y. Hwang, and D. A. Muller, "Why some interfaces cannot be sharp," *Nature Materials*, vol. 5, no. 3, pp. 204–209, Jan. 2006. [Online]. Available: http://www.nature.com/doifinder/10.1038/nmat1569 (Cited on page 60.)

[93] J.-L. Maurice, D. Imhoff, J.-P. Contour, and C. Colliex, "Interfaces in 100 epitaxial heterostructures of perovskite oxides," *Philosophical Magazine*, vol. 86, no. 15, pp. 2127–2146, May 2006. [Online]. Available: http://www.tandfonline.com/doi/abs/10.1080/14786430600640460 (Cited on page 60.)

[94] H. Yamada, Y. Ogawa, Y. Ishii, H. Sato, M. Kawasaki, H. Akoh, and Y. Tokura, "Engineered interface of magnetic oxides." *Science (New York, N.Y.)*, vol. 305, no. 5684, pp. 646–8, Jul. 2004. [Online]. Available: http://www.ncbi.nlm.nih.gov/pubmed/15286367 (Cited on pages 60 and 77.)

[95] J. D. Ferguson, Y. Kim, L. F. Kourkoutis, A. Vodnick, A. R. Woll, D. a. Muller, and J. D. Brock, "Epitaxial oxygen getter for a brownmillerite phase transformation in manganite films." *Advanced materials (Deerfield Beach, Fla.)*, vol. 23, no. 10, pp. 1226–30, Mar. 2011. [Online]. Available: http://www.ncbi.nlm.nih.gov/pubmed/21381119 (Cited on page 60.)

[96] G. Yuan, K. Nishio, M. Lippmaa, and A. Uedono, "Epitaxial $DyScO_3$ films as passivation layers suppress the diffusion of oxygen vacancies in $SrTiO_3$," *Journal of Physics D: Applied Physics*, vol. 43, no. 2, p. 025301, 2010. [Online]. Available: http://stacks.iop.org/0022-3727/43/i=2/a=025301 (Cited on page 60.)

[97] C. W. Schneider, M. Esposito, I. Marozau, K. Conder, M. Doebeli, Y. Hu, M. Mallepell, A. Wokaun, and T. Lippert, "The origin of oxygen in oxide thin films: Role of the substrate," *Applied Physics Letters*, vol. 97, no. 19, p. 192107, 2010. [Online]. Available: http://link.aip.org/link/APPLAB/v97/i19/p192107/s1&Agg=doi (Cited on page 60.)

[98] H. Raebiger, S. Lany, and A. Zunger, "Charge self-regulation upon changing the oxidation state of transition metals in insulators." *Nature*, vol. 453, no. 7196, pp. 763–6, Jun. 2008. [Online]. Available: http://www.ncbi.nlm.nih.gov/pubmed/18528391 (Cited on pages 61 and 62.)

[99] V. Garcia, M. Bibes, L. Bocher, S. Valencia, F. Kronast, A. Crassous, X. Moya, S. Enouz-Vedrenne, A. Gloter, D. Imhoff, C. Deranlot, N. D. Mathur, S. Fusil, K. Bouzehouane, and A. Barthélémy, "Ferroelectric control of spin polarization." *Science (New York, N.Y.)*, vol. 327, no. 5969, pp. 1106–10, Feb. 2010. [Online]. Available: http://www.ncbi.nlm.nih.gov/pubmed/20075211 (Cited on page 66.)

[100] J. Burton and E. Tsymbal, "Prediction of electrically induced magnetic reconstruction at the manganite/ferroelectric interface," *Physical Review B*, vol. 80, no. 17, pp. 1–6, Nov. 2009. [Online]. Available: http://link.aps.org/doi/10.1103/PhysRevB.80.174406 (Cited on page 66.)

[101] Y. W. Yin, J. D. Burton, Y.-M. Kim, A. Y. Borisevich, S. J. Pennycook, S. M. Yang, T. W. Noh, a. Gruverman, X. G. Li, E. Y. Tsymbal, and Q. Li, "Enhanced tunnelling electroresistance effect due to a ferroelectrically induced phase transition at a magnetic complex oxide interface." *Nature materials*, vol. 12, no. 5, pp. 397–402, May 2013. [Online]. Available: http://www.ncbi.nlm.nih.gov/pubmed/23416728 (Cited on page 66.)

[102] H. Lu, T. A. George, Y. Wang, I. Ketsman, J. D. Burton, C.-W. Bark, S. Ryu, D. J. Kim, J. Wang, C. Binek, P. a. Dowben, A. Sokolov, C.-B. Eom, E. Y. Tsymbal, and A. Gruverman, "Electric modulation of magnetization at the $BaTiO_3/La_{0.66}Sr_{0.33}MnO_3$ interfaces," *Applied Physics Letters*, vol. 100, no. 23, p. 232904, 2012. [Online]. Available: http://link.aip.org/link/APPLAB/v100/i23/p232904/s1&Agg=doi (Cited on page 66.)

[103] S. Mi, C. Jia, T. Heeg, O. Trithaveesak, J. Schubert, and K. Urban, "Heterostructures of $BaTiO_3$ bilayer films grown on $SrTiO_3$ (001) under different oxygen pressures," *Journal of Crystal Growth*, vol. 283, no. 3-4, pp. 425–430, Oct. 2005. [Online]. Available: http://www.sciencedirect.com/science/article/pii/S0022024805007797 (Cited on page 66.)

[104] A. P. Chen, F. Khatkhatay, W. Zhang, C. Jacob, L. Jiao, and H. Wang, "Strong oxygen pressure dependence of ferroelectricity in $BaTiO_3/SrRuO_3/SrTiO_3$ epitaxial heterostructures," *Journal of Applied Physics*, vol. 114, no. 12, p. 124101, 2013. [Online]. Available: http://scitation.aip.org/content/aip/journal/jap/114/12/10.1063/1.4821643 (Cited on page 66.)

[105] H. Chen, D. P. Kumah, A. S. Disa, F. J. Walker, C. H. Ahn, and S. Ismail-Beigi, "Modifying the Electronic Orbitals of Nickelate Heterostructures via Structural Distortions," *Physical Review Letters*, vol. 110, no. 18, p. 186402, May 2013. [Online]. Available: http://link.aps.org/doi/10.1103/PhysRevLett.110.186402 (Cited on pages 69, 70, and 94.)

[106] H. Chen, Q. Qiao, M. S. J. Marshall, A. B. Georgescu, A. Gulec, P. J. Phillips, R. F. Klie, F. J. Walker, C. H. Ahn, and S. Ismail-Beigi, "Dynamical control of orbital occupations via a ferroelectric-induced polar state in metallic manganites," p. 12, Sep. 2013. [Online]. Available: http://arxiv.org/abs/1309.2976 (Cited on pages 69 and 70.)

[107] J. Garcia-Barriocanal, J. C. Cezar, F. Y. Bruno, P. Thakur, N. B. Brookes, C. Utfeld, A. Rivera-Calzada, S. R. Giblin, J. W. Taylor, J. A. Duffy, S. B. Dugdale, T. Nakamura, K. Kodama, C. Leon, S. Okamoto, and J. Santamaria, "Spin and orbital Ti magnetism at $LaMnO_3/SrTiO_3$ interfaces." *Nature communications*, vol. 1, p. 82, Jan. 2010. [Online]. Available: http://www.ncbi.nlm.nih.gov/pubmed/20865798 (Cited on page 71.)

[108] C. Aruta, G. Ghiringhelli, V. Bisogni, L. Braicovich, N. B. Brookes, A. Tebano, and G. Balestrino, "Orbital occupation, atomic moments, and magnetic ordering at interfaces of manganite thin films," *Phys. Rev. B*, vol. 80, p. 014431, Jul 2009. [Online]. Available: http://link.aps.org/doi/10.1103/PhysRevB.80.014431 (Cited on pages 75 and 76.)

[109] S. Valencia, L. Peña, Z. Konstantinovic, L. Balcells, R. Galceran, D. Schmitz, F. Sandiumenge, M. Casanove, and B. Martínez, "Intrinsic antiferromagnetic/insulating phase at manganite surfaces and interfaces." *Journal of physics. Condensed matter : an Institute of Physics journal*, vol. 26, no. 16, p. 166001, Apr. 2014. [Online]. Available: http://www.ncbi.nlm.nih.gov/pubmed/24691398 (Cited on pages 76, 77, 78, 86, and 87.)

[110] A. Sadoc, B. Mercey, C. Simon, D. Grebille, W. Prellier, and M.-B. Lepetit, "Large Increase of the Curie Temperature by Orbital Ordering Control," *Physical Review Letters*, vol. 104, no. 4, p. 046804, Jan. 2010. [Online]. Available: http://link.aps.org/doi/10.1103/PhysRevLett.104.046804 (Cited on page 77.)

[111] J. J. Peng, C. Song, B. Cui, F. Li, H. J. Mao, Y. Y. Wang, G. Y. Wang, and F. Pan, "Exchange bias in a single $LaMnO_3$ film induced by vertical electronic phase separation," *Physical Review B*, vol. 89, no. 16, p. 165129, Apr. 2014. [Online]. Available: http://link.aps.org/doi/10.1103/PhysRevB.89.165129 (Cited on pages 78 and 150.)

[112] P. Schiffer, A. P. Ramirez, W. Bao, and S.-W. Cheong, "Low Temperature Magnetoresistance and the Magnetic Phase Diagram of $La_{1-x}Ca_xMnO_3$," *Phys. Rev. Lett.*, vol. 75, pp. 3336–3339, Oct 1995. [Online]. Available: http://link.aps.org/doi/10.1103/PhysRevLett.75.3336 (Cited on page 81.)

[113] A. J. Millis, "Lattice effects in magnetoresistive manganese perovskites," *Nature*, vol. 392, no. March, pp. 147–150, 1998. [Online]. Available: http://dx.doi.org/10.1038/32348 (Cited on page 81.)

[114] A. Baena, L. Brey, and M. J. Calderón, "Effect of strain on the orbital and magnetic ordering of manganite thin films and their interface with an insulator," *Physical Review B*, vol. 83, no. 6, p. 064424, Feb. 2011. [Online]. Available: http://link.aps.org/doi/10.1103/PhysRevB.83.064424 (Cited on pages 81 and 92.)

[115] Y. Konishi, Z. Fang, M. Izumi, T. Manako, M. Kasai, H. Kuwahara, M. Kawasaki, K. Terakura, and Y. Tokura, "Orbital-State-Mediated Phase-Control of Manganites," *Journal of the Physics Society Japan*, vol. 68, no. 12, pp. 3790–3793, Dec. 1999. [Online]. Available: http://jpsj.ipap.jp/link?JPSJ/68/3790/ (Cited on page 81.)

[116] D. Gutiérrez, G. Radaelli, F. Sánchez, R. Bertacco, and J. Fontcuberta, "Bandwidth-limited control of orbital and magnetic orders in half-doped manganites by epitaxial strain," *Physical Review B*, vol. 89, no. 7, p. 075107, Feb. 2014. [Online]. Available: http://link.aps.org/doi/10.1103/PhysRevB.89.075107 (Cited on pages 81, 82, and 89.)

[117] B. Cui, C. Song, F. Li, G. Y. Wang, H. J. Mao, J. J. Peng, F. Zeng, and F. Pan, "Tuning the entanglement between orbital reconstruction and charge transfer at a film surface." *Scientific reports*, vol. 4, no. 001, p. 4206, Jan. 2014. [Online]. Available: http://www.nature.com/srep/2014/140226/srep04206/full/srep04206.html (Cited on page 83.)

[118] W. Wu, D. Huang, C.-M. Huang, C.-H. Hsu, C. Chang, H.-J. Lin, and C. Chen, "Orbital polarization and Jahn-Teller distortion of strained thin films," *Journal of Magnetism and Magnetic Materials*, vol. 310, no. 2, pp. 813–815, Mar. 2007. [Online]. Available: http://linkinghub.elsevier.com/retrieve/pii/S0304885306019421 (Cited on page 84.)

[119] M. L. Medarde, "Structural, magnetic and electronic properties of $RNiO_3$ perovskites (R = rare earth)," *Journal of Physics: Condensed Matter*, vol. 9, no. 8, p. 1679, 1997. [Online]. Available: http://stacks.iop.org/0953-8984/9/i=8/a=003 (Cited on page 93.)

[120] G. Catalan, "Progress in perovskite nickelate research," *Phase Transitions*, vol. 81, no. 7-8, pp. 729–749, Jul. 2008. [Online]. Available: http://www.tandfonline.com/doi/abs/10.1080/01411590801992463 (Cited on page 93.)

[121] D. Meyers, S. Middey, M. Kareev, M. van Veenendaal, E. J. Moon, B. a. Gray, J. Liu, J. W. Freeland, and J. Chakhalian, "Strain-modulated Mott transition in $EuNiO_3$ ultrathin films," *Physical Review B*, vol. 88, no. 7, p. 075116, Aug. 2013. [Online]. Available: http://link.aps.org/doi/10.1103/PhysRevB.88.075116 (Cited on pages 93, 99, and 101.)

[122] F. Y. Bruno, K. Z. Rushchanskii, S. Valencia, Y. Dumont, C. Carrétéro, E. Jacquet, R. Abrudan, S. Blügel, M. Ležaić, M. Bibes, and A. Barthélémy, "Rationalizing strain engineering effects in rare-earth nickelates," *Physical Review B*, vol. 88, no. 19, p. 195108, Nov. 2013. [Online]. Available: http://link.aps.org/doi/10.1103/PhysRevB.88.195108 (Cited on pages 93, 99, and 101.)

[123] J. L. García-Muñoz, J. Rodríguez-Carvajal, P. Lacorre, and J. B. Torrance, "Neutron-diffraction study of $RNiO_3$ (R=La,Pr,Nd,Sm): Electronically induced structural changes across the metal-insulator transition," *Phys. Rev. B*, vol. 46, pp. 4414–4425, Aug 1992. [Online]. Available: http://link.aps.org/doi/10.1103/PhysRevB.46.4414 (Cited on page 93.)

[124] J. Chaloupka and G. Khaliullin, "Orbital Order and Possible Superconductivity in $LaNiO_3/LaMO_3$ Superlattices," *Physical Review Letters*, vol. 100, no. 1, p. 016404, Jan. 2008. [Online]. Available: http://link.aps.org/doi/10.1103/PhysRevLett.100.016404 (Cited on page 93.)

[125] J. Chakhalian, J. M. Rondinelli, J. Liu, B. a. Gray, M. Kareev, E. J. Moon, N. Prasai, J. L. Cohn, M. Varela, I. C. Tung, M. J. Bedzyk, S. G. Altendorf, F. Strigari, B. Dabrowski, L. H. Tjeng, P. J. Ryan, and J. W. Freeland, "Asymmetric Orbital-Lattice Interactions in Ultrathin Correlated Oxide Films," *Physical Review Letters*, vol. 107, no. 11, p. 116805, Sep. 2011. [Online]. Available: http://link.aps.org/doi/10.1103/PhysRevLett.107.116805 (Cited on pages 94, 100, 102, and 103.)

[126] G. Gou, I. Grinberg, A. M. Rappe, and J. M. Rondinelli, "Lattice normal modes and electronic properties of the correlated metal $LaNiO_3$," *Physical Review B*, vol. 84, no. 14, p. 144101, Oct. 2011. [Online]. Available: http://link.aps.org/doi/10.1103/PhysRevB.84.144101 (Cited on page 94.)

[127] S. J. May, J.-W. Kim, J. M. Rondinelli, E. Karapetrova, N. A. Spaldin, A. Bhattacharya, and P. J. Ryan, "Quantifying octahedral rotations in strained perovskite oxide films," *Phys. Rev. B*, vol. 82, p. 014110, Jul 2010. [Online]. Available: http://link.aps.org/doi/10.1103/PhysRevB.82.014110 (Cited on pages 94, 96, and 105.)

[128] R. Scherwitzl, P. Zubko, C. Lichtensteiger, and J.-M. Triscone, "Electric-field tuning of the metal-insulator transition in ultrathin films of $LaNiO_3$," *Applied Physics Letters*, vol. 95, no. 22, p. 222114, 2009. [Online]. Available: http://scitation.aip.org/content/aip/journal/apl/95/22/10.1063/1.3269591 (Cited on page 97.)

[129] R. Scherwitzl, S. Gariglio, M. Gabay, P. Zubko, M. Gibert, and J.-M. Triscone, "Metal-Insulator Transition in Ultrathin $LaNiO_3$ Films," *Physical Review Letters*, vol. 106, no. 24, p. 246403, Jun. 2011. [Online]. Available: http://link.aps.org/doi/10.1103/PhysRevLett.106.246403 (Cited on page 97.)

[130] G. Herranz, F. Sánchez, B. Martínez, J. Fontcuberta, M. V. García-Cuenca, C. Ferrater, M. Varela, and P. Levy, "Weak localization effects in some metallic perovskites," *The European Physical Journal B*, vol. 40, no. 4, pp. 439–444, Aug. 2004. [Online]. Available: http://www.springerlink.com/index/10.1140/epjb/e2004-00207-9 (Cited on page 97.)

[131] E. J. Moon, B. A. Gray, M. Kareev, J. Liu, S. G. Altendorf, F. Strigari, L. H. Tjeng, J. W. Freeland, and J. Chakhalian, "Strain-dependent transport properties of the ultra-thin correlated metal, $LaNiO_3$," *New Journal of Physics*, vol. 13, no. 7, p. 073037, Jul. 2011. [Online]. Available: http://iopscience.iop.org/1367-2630/13/7/073037 (Cited on pages 97 and 98.)

[132] G. Herranz, F. Sánchez, J. Fontcuberta, V. Laukhin, J. Galibert, M. García-Cuenca, C. Ferrater, and M. Varela, "Magnetic field effect on quantum corrections to the low-temperature conductivity in metallic perovskite oxides," *Physical Review B*, vol. 72, no. 1, p. 014457, Jul. 2005. [Online]. Available: http://link.aps.org/doi/10.1103/PhysRevB.72.014457 (Cited on page 97.)

[133] F. Rivadulla, J.-S. Zhou, and J. Goodenough, "Electron scattering near an itinerant to localized electronic transition," *Physical Review B*, vol. 67, no. 16, p. 165110, Apr. 2003. [Online]. Available: http://link.aps.org/doi/10.1103/PhysRevB.67.165110 (Cited on page 98.)

[134] J.-S. Kang, S. Lee, G. Kim, H. Lee, H. Song, Y. Shin, S. Han, C. Hwang, M. Jung, H. Shin, B. Kim, S. Kwon, and B. Min, "Valence and spin states in delafossite $AgNiO_2$ and the frustrated Jahn-Teller system $ANiO_2$ (A=Li,Na)," *Physical Review B*, vol. 76, no. 19, p. 195122, Nov. 2007. [Online]. Available: http://link.aps.org/doi/10.1103/PhysRevB.76.195122 (Cited on pages 99 and 101.)

[135] C. Piamonteze, F. de Groot, H. Tolentino, a. Ramos, N. Massa, J. Alonso, and M. Martínez-Lope, "Spin-orbit-induced mixed-spin ground state in $RNiO_3$ perovskites probed by x-ray absorption spectroscopy: Insight into the metal-to-insulator transition," *Physical Review B*, vol. 71, no. 2, p. 020406, Jan. 2005. [Online]. Available: http://link.aps.org/doi/10.1103/PhysRevB.71.020406 (Cited on pages 99 and 101.)

[136] F. Y. Bruno, S. Valencia, R. Abrudan, Y. Dumont, C. Carrétéro, M. Bibes, and A. Barthélémy, "Probing the metal-insulator transition in nickelates using soft x-ray absorption spectroscopy," *Applied Physics Letters*, vol. 104, no. 2, p. 021920, Jan. 2014. [Online]. Available: http://scitation.aip.org/content/aip/journal/apl/104/2/10.1063/1.4861132 (Cited on pages 99 and 101.)

[137] M. J. Han and M. van Veenendaal, "Electronic structure and orbital polarization of $LaNiO_3$ with a reduced coordination and under strain: A first-principles study," *Phys. Rev. B*, vol. 84, p. 125137, Sep 2011. [Online]. Available: http://link.aps.org/doi/10.1103/PhysRevB.84.125137 (Cited on page 102.)

[138] D. P. Kumah, A. S. Disa, J. H. Ngai, H. Chen, A. Malashevich, J. W. Reiner, S. Ismail-Beigi, F.-J. Walker, and C. H. Ahn, "Tuning the Structure of Nickelates to Achieve Two-Dimensional Electron Conduction," *Advanced Materials*, pp. n/a–n/a, Feb. 2014. [Online]. Available: http://doi.wiley.com/10.1002/adma.201304256 (Cited on pages 102, 103, and 105.)

[139] M. Abbate, G. Zampieri, F. Prado, A. Caneiro, J. Gonzalez-Calbet, and M. Vallet-Regi, "Electronic structure and metal-insulator transition in $LaNiO_{3-d}$," *Physical Review B*, vol. 65, no. 15, p. 155101, Mar. 2002. [Online]. Available: http://link.aps.org/doi/10.1103/PhysRevB.65.155101 (Cited on page 103.)

[140] J. Suntivich, H. a. Gasteiger, N. Yabuuchi, H. Nakanishi, J. B. Goodenough, and Y. Shao-Horn, "Design principles for oxygen-reduction activity on perovskite oxide catalysts for fuel cells and metal-air batteries." *Nature chemistry*, vol. 3, no. 7, pp. 546–50, Jul. 2011. [Online]. Available: http://www.ncbi.nlm.nih.gov/pubmed/21697876 (Cited on page 103.)

[141] M. Alexander, H. Romberg, N. Nücker, P. Adelmann, J. Fink, J. T. Markert, M. B. Maple, S. Uchida, H. Takagi, Y. Tokura, A. C. W. P. James, and D. W. Murphy, "Electronic structure studies on the n-type doped superconductors $R_{2-x}M_xCuO_{4-d}$ (R=Pr,Nd,Sm; M=Ce,Th) and $Nd_2CuO_{4-x}F_x$ by electron-energy-loss spectroscopy," *Phys. Rev. B*, vol. 43, pp. 333–343, Jan 1991. [Online]. Available: http://link.aps.org/doi/10.1103/PhysRevB.43.333 (Cited on page 103.)

[142] D. A. Muller, N. Nakagawa, and A. Ohtomo, "Atomic-scale imaging of nanoengineered oxygen vacancy profiles in $SrTiO_3$," vol. 430, no. August, pp. 657–661, 2004. [Online]. Available: http://dx.doi.org/10.1038/nature02756 (Cited on page 103.)

[143] A. Ohtomo and H. Y. Hwang, "A high-mobility electron gas at the $LaAlO_3/SrTiO_3$ heterointerface." *Nature*, vol. 427, no. 6973, pp. 423–6, Jan. 2004. [Online]. Available: http://www.ncbi.nlm.nih.gov/pubmed/14749825 (Cited on pages 107 and 111.)

[144] S. Thiel, G. Hammerl, A. Schmehl, C. W. Schneider, and J. Mannhart, "Tunable quasi-two-dimensional electron gases in oxide heterostructures," *Science*, vol. 313, no. 5795, pp. 1942–1945, 2006. [Online]. Available: http://www.sciencemag.org/content/313/5795/1942.abstract (Cited on page 107.)

[145] A. Brinkman, M. Huijben, M. van Zalk, J. Huijben, U. Zeitler, J. C. Maan, W. G. van der Wiel, G. Rijnders, D. H. A. Blank, and H. Hilgenkamp, "Magnetic effects at the interface between non-magnetic oxides." *Nature materials*, vol. 6, no. 7, pp. 493–6, Jul. 2007. [Online]. Available: http://www.ncbi.nlm.nih.gov/pubmed/17546035 (Cited on page 107.)

[146] G. Herranz, F. Sánchez, N. Dix, M. Scigaj, and J. Fontcuberta, "High mobility conduction at (110) and (111) $LaAlO_3/SrTiO_3$ interfaces." *Scientific reports*, vol. 2, no. 110, p. 758, Jan. 2012. [Online]. Available: http://www.nature.com/srep/2012/121022/srep00758/full/srep00758.html (Cited on pages 107, 108, and 111.)

[147] A. Annadi, Q. Zhang, X. Renshaw Wang, N. Tuzla, K. Gopinadhan, W. M. Lu, A. Roy Barman, Z. Q. Liu, A. Srivastava, S. Saha, Y. L. Zhao, S. W. Zeng, S. Dhar, E. Olsson, B. Gu, S. Yunoki, S. Maekawa, H. Hilgenkamp, T. Venkatesan, and Ariando, "Anisotropic two-dimensional electron gas at the $LaAlO_3/SrTiO_3$ (110) interface," *Nature communications*, vol. 4, p. 1838, 2013. [Online]. Available: http://www.nature.com/ncomms/journal/v4/n5/full/ncomms2804.html (Cited on pages 107 and 108.)

[148] G. Herranz, N. Bergeal, J. Lesueur, J. Gazquez, M. Scigaj, N. Dix, F. Sanchez, and J. Fontcuberta, "Orientational tuning of the 2D-superconductivity in $LaAlO_3/SrTiO_3$ interfaces," p. 5, May 2013. [Online]. Available: http://arxiv.org/abs/1305.2411 (Cited on pages 107 and 108.)

[149] A. F. Santander-Syro, O. Copie, T. Kondo, F. Fortuna, S. Pailhès, R. Weht, X. G. Qiu, F. Bertran, A. Nicolaou, A. Taleb-Ibrahimi, P. Le Fèvre, G. Herranz, M. Bibes, N. Reyren, Y. Apertet, P. Lecoeur, A. Barthélémy, and M. J. Rozenberg, "Two-dimensional electron gas with universal subbands at the surface of $SrTiO_3$," *Nature*, vol. 469, no. 7329, pp. 189–93, Jan. 2011.

[Online]. Available: http://www.ncbi.nlm.nih.gov/pubmed/21228872 (Cited on pages 107, 113, and 114.)

[150] A. Kalabukhov, R. Gunnarsson, J. Börjesson, E. Olsson, T. Claeson, and D. Winkler, "Effect of oxygen vacancies in the SrTiO3 substrate on the electrical properties of the $LaAlO_3/SrTiO_3$ interface," *Phys. Rev. B*, vol. 75, p. 121404, Mar 2007. [Online]. Available: http://link.aps.org/doi/10.1103/PhysRevB.75.121404 (Cited on page 107.)

[151] W. Siemons, G. Koster, H. Yamamoto, W. A. Harrison, G. Lucovsky, T. H. Geballe, D. H. A. Blank, and M. R. Beasley, "Origin of Charge Density at LaAlO3 on SrTiO3 Heterointerfaces: Possibility of Intrinsic Doping," *Phys. Rev. Lett.*, vol. 98, p. 196802, May 2007. [Online]. Available: http://link.aps.org/doi/10.1103/PhysRevLett.98.196802 (Cited on page 107.)

[152] G. Herranz, M. Basletić, M. Bibes, C. Carrétéro, E. Tafra, E. Jacquet, K. Bouzehouane, C. Deranlot, A. Hamzić, J.-M. Broto, A. Barthélémy, and A. Fert, "High Mobility in $LaAlO_3/SrTiO_3$ Heterostructures: Origin, Dimensionality, and Perspectives," *Phys. Rev. Lett.*, vol. 98, p. 216803, May 2007. [Online]. Available: http://link.aps.org/doi/10.1103/PhysRevLett.98.216803 (Cited on pages 107 and 108.)

[153] L. Li, C. Richter, J. Mannhart, and R. C. Ashoori, "Coexistence of magnetic order and two-dimensional superconductivity at $LaAlO_3/SrTiO_3$ interfaces," *Nature Physics*, vol. 7, no. 10, pp. 762–766, Sep. 2011. [Online]. Available: http://www.nature.com/doifinder/10.1038/nphys2080 (Cited on page 107.)

[154] Ariando, X. Wang, G. Baskaran, Z. Q. Liu, J. Huijben, J. B. Yi, A. Annadi, a. R. Barman, A. Rusydi, S. Dhar, Y. P. Feng, J. Ding, H. Hilgenkamp, and T. Venkatesan, "Electronic phase separation at the $LaAlO_3/SrTiO_3$ interface." *Nature communications*, vol. 2, p. 188, Jan. 2011. [Online]. Available: http://www.ncbi.nlm.nih.gov/pubmed/21304517 (Cited on page 107.)

[155] J. A. Bert, B. Kalisky, C. Bell, M. Kim, Y. Hikita, H. Y. Hwang, and K. A. Moler, "Direct imaging of the coexistence of ferromagnetism and superconductivity at the $LaAlO_3/SrTiO_3$ interface," *Nature Physics*, vol. 7, no. 10, pp. 767–771, Sep. 2011. [Online]. Available: http://www.nature.com/doifinder/10.1038/nphys2079 (Cited on page 107.)

[156] K. A. Kalisky, Beena Moler, B. B. Klopfer, C. Bell, H. K. Sato, M. Hosoda, Y. Hikita, H. Y. Hwang, and K. A. Moler, "Critical thickness for ferromagnetism in $LaAlO_3/SrTiO_3$ heterostructures." *Nature communications*, vol. 3, no. May, p. 922, Jan. 2012. [Online]. Available: http://www.ncbi.nlm.nih.gov/pubmed/22735450 (Cited on page 107.)

[157] N. Pavlenko, T. Kopp, E. Y. Tsymbal, G. A. Sawatzky, and J. Mannhart, "Magnetic and superconducting phases at the $LaAlO_3/SrTiO_3$ interface: The role of interfacial Ti 3d electrons," *Phys. Rev. B*, vol. 85, p. 020407, Jan 2012. [Online]. Available: http://link.aps.org/doi/10.1103/PhysRevB.85.020407 (Cited on page 107.)

[158] N. Pavlenko, T. Kopp, and J. Mannhart, "Emerging magnetism and electronic phase separation at titanate interfaces," *Phys. Rev. B*, vol. 88, p. 201104, Nov 2013.

[Online]. Available: http://link.aps.org/doi/10.1103/PhysRevB.88.201104 (Cited on page 107.)

[159] J.-S. Lee, Y. W. Xie, H. K. Sato, C. Bell, Y. Hikita, H. Y. Hwang, and C.-C. Kao, "Titanium dxy ferromagnetism at the $LaAlO_3/SrTiO_3$ interface." *Nature materials*, vol. 12, no. 8, pp. 703–6, Aug. 2013. [Online]. Available: http://www.ncbi.nlm.nih.gov/pubmed/23727948 (Cited on pages 107, 113, and 114.)

[160] R. Bachelet, F. Valle, I. C. Infante, F. Sánchez, and J. Fontcuberta, "Step formation, faceting, and bunching in atomically flat $SrTiO_3$ (110) surfaces," *Applied Physics Letters*, vol. 91, no. 25, p. 251904, 2007. [Online]. Available: http://scitation.aip.org/content/aip/journal/apl/91/25/10.1063/1.2825586 (Cited on page 108.)

[161] D. Koningsberger and R.Prins, *X-ray Absorption: Principles, Applications, Techniques of EXAFS, SEXAFS, and XANES*, C. A. vol. 92, Ed. John Wiley & Sons, 1988. (Cited on page 109.)

[162] F. M. F. de Groot, J. C. Fuggle, B. T. Thole, and G. A. Sawatzky, "$L_{2,3}$ x-ray-absorption edges of d^0 compounds: $K^+, Ca^{2+}, Sc^{3+}, and Ti^{4+}$ in Oh (octahedral) symmetry," *Phys. Rev. B*, vol. 41, pp. 928–937, Jan 1990. [Online]. Available: http://link.aps.org/doi/10.1103/PhysRevB.41.928 (Cited on page 111.)

[163] M. Matsubara, T. Uozumi, and A. Kotani, "Polarization dependence of resonant x-ray emission spectra in early transition metal compounds," *Journal of Synchrotron Radiation*, vol. 8, no. 2, pp. 393–395, 2001. [Online]. Available: http://dx.doi.org/10.1107/S0909049500016538 (Cited on page 111.)

[164] M. Salluzzo, J. Cezar, N. Brookes, V. Bisogni, G. De Luca, C. Richter, S. Thiel, J. Mannhart, M. Huijben, a. Brinkman, G. Rijnders, and G. Ghiringhelli, "Orbital Reconstruction and the Two-Dimensional Electron Gas at the $LaAlO_3/SrTiO_3$ Interface," *Physical Review Letters*, vol. 102, no. 16, p. 166804, Apr. 2009. [Online]. Available: http://link.aps.org/doi/10.1103/PhysRevLett.102.166804 (Cited on pages 112 and 113.)

[165] F. Hippert, *Neutron and X-ray Spectroscopy*. Springer, 2006. (Cited on page 112.)

[166] M. Salluzzo, S. Gariglio, X. Torrelles, Z. Ristic, R. Di Capua, J. Drnec, M. M. Sala, G. Ghiringhelli, R. Felici, and N. B. Brookes, "Structural and electronic reconstructions at the $LaAlO_3/SrTiO_3$ interface." *Advanced materials (Deerfield Beach, Fla.)*, vol. 25, no. 16, pp. 2333–8, 2332, Apr. 2013. [Online]. Available: http://www.ncbi.nlm.nih.gov/pubmed/23382034 (Cited on page 113.)

[167] A. Joshua, S. Pecker, J. Ruhman, E. Altman, and S. Ilani, "A universal critical density underlying the physics of electrons at the $LaAlO_3/SrTiO_3$ interface." *Nature communications*, vol. 3, p. 1129, Jan. 2012. [Online]. Available: http://www.ncbi.nlm.nih.gov/pubmed/23072799 (Cited on page 114.)

[168] R. M. Fernandes, J. T. Haraldsen, P. Wölfle, and A. V. Balatsky, "Two-band superconductivity in doped $SrTiO_3$ films and interfaces," *Phys. Rev. B*, vol. 87, p. 014510, Jan 2013. [Online]. Available: http://link.aps.org/doi/10.1103/PhysRevB.87.014510 (Cited on page 114.)

[169] Lippmaa laboratory web page: http://lippmaa.issp.u-tokyo.ac.jp/. (Cited on page 126.)

[170] M. C. for Materials Science and Engineering. X-ray diffraction shared experimental facility: http://prism.mit.edu/xray/. (Cited on page 131.)

[171] M. McElfresh, "Fundamentals of magnetism and magnetic measurements featuring quantum design's magnetic property measurement system," *Quantum Design*, vol. 11578, 1994. (Cited on page 132.)

[172] D.-X. Chen, V. Skumryev, and H. Kronmüller, "ac susceptibility of a spherical $Nd_2Fe_{14}B$ single crystal," *Phys. Rev. B*, vol. 46, pp. 3496–3505, Aug 1992. [Online]. Available: http://link.aps.org/doi/10.1103/PhysRevB.46.3496 (Cited on page 133.)

[173] J. Jay, "Etude par resonance magnetique nucleaire de l'ordre a courte distance danse le systeme cobalt/fer: de l'alliage massif a la multicouche," Ph.D. dissertation, Universite Louis Pasteur-Strasbourg I, 1995. (Cited on page 134.)

[174] H. Wieder, *Laboratory notes on electrical and galvanomagnetic measurements*. Elsevier Science, 1979. (Cited on page 135.)

[175] D. Slatkin, A. Hanson, K. Jones, H. Kraner, J. Warren, and G. Finkel, "Damage to air-dried human blood cells and tissue sections by synchrotron radiation," *Nuclear Instruments and Methods in Physics Research Section A: Accelerators, Spectrometers, Detectors and Associated Equipment*, vol. 227, no. 2, pp. 378–384, Nov. 1984. [Online]. Available: http://www.sciencedirect.com/science/article/pii/0168900284901505 (Cited on page 145.)

[176] K. Themner, P. Spanne, and K. W. Jones, "Mass loss during X-ray microanalysis," *Nuclear Instruments and Methods in Physics Research Section B: Beam Interactions with Materials and Atoms*, vol. 49, no. 1-4, pp. 52–59, Apr. 1990. [Online]. Available: http://www.sciencedirect.com/science/article/pii/0168583X9090215G (Cited on page 145.)

[177] J. Gerbrand Mesu, A. M. J. van der Eerden, F. M. F. de Groot, and B. M. Weckhuysen, "Synchrotron Radiation Effects on Catalytic Systems As Probed with a Combined In-Situ UVVis/XAFS Spectroscopic Setup," *The Journal of Physical Chemistry B*, vol. 109, no. 9, pp. 4042–4047, 2005, pMID: 16851461. [Online]. Available: http://pubs.acs.org/doi/abs/10.1021/jp045206r (Cited on page 145.)

[178] J. Yano, J. Kern, K.-D. Irrgang, M. J. Latimer, U. Bergmann, P. Glatzel, Y. Pushkar, J. Biesiadka, B. Loll, K. Sauer, J. Messinger, A. Zouni, and V. K. Yachandra, "X-ray damage to the Mn4Ca complex in single crystals of photosystem II: a case study for metalloprotein crystallography." *Proceedings of the National Academy of Sciences of the United States of America*, vol. 102, no. 34, pp. 12 047–52, Aug. 2005. [Online]. Available: http://www.ncbi.nlm.nih.gov/pmc/articles/PMC1186027/ (Cited on page 145.)

[179] F. Bondino, A. Barla, T. Schmitt, V. N. Strocov, J.-Y. Henry, and J.-P. Sanchez, "Revealing the insulating gap in $\alpha - NaV_2O_5$ with resonant inelastic x-ray scattering." *Journal of physics. Condensed matter : an Institute of Physics journal*, vol. 24, no. 32, pp. 325 402, 1–5, Aug. 2012. [Online]. Available: http://www.ncbi.nlm.nih.gov/pubmed/22809788 (Cited on page 145.)

[180] S. Hufner, *Photoelectron spectroscopy : Principles and Applications*. Springer, 2003. (Cited on page 148.)

[181] T. C. Gibb, R. Greatrex, N. N. Greenwood, and P. Kaspi, "Ruthenium-99 mossbauer studies of the magnetic properties of ternary and quaternary ruthenium(iv) oxides," *J. Chem. Soc., Dalton Trans.*, pp. 1253–1258, 1973. [Online]. Available: http://dx.doi.org/10.1039/DT9730001253 (Cited on page 155.)

[182] J. Xia, W. Siemons, G. Koster, M. R. Beasley, and A. Kapitulnik, "Critical thickness for itinerant ferromagnetism in ultrathin films of srruo$_3$," *Phys. Rev. B*, vol. 79, p. 140407, Apr 2009. [Online]. Available: http://link.aps.org/doi/10.1103/PhysRevB.79.140407 (Cited on page 155.)

[183] A. J. Grutter, F. J. Wong, E. Arenholz, A. Vailionis, and Y. Suzuki, "Evidence of high-spin Ru and universal magnetic anisotropy in $SrRuO_3$ thin films," *Phys. Rev. B*, vol. 85, p. 134429, Apr 2012. [Online]. Available: http://link.aps.org/doi/10.1103/PhysRevB.85.134429 (Cited on pages 155 and 158.)

[184] J. Schubert, O. Trithaveesak, A. Petraru, C. L. Jia, R. Uecker, P. Reiche, and D. G. Schlom, "Structural and optical properties of epitaxial $BaTiO_3$ thin films grown on $GdScO_3(110)$," *Applied Physics Letters*, vol. 82, no. 20, p. 3460, 2003. [Online]. Available: http://link.aip.org/link/APPLAB/v82/i20/p3460/s1&Agg=doi (Cited on page 156.)

[185] Z. Hu, H. von Lips, M. S. Golden, J. Fink, G. Kaindl, F. M. F. de Groot, S. Ebbinghaus, and A. Reller, "Multiplet effects in the Ru $L_{2,3}$ x-ray-absorption spectra of Ru(IV) and Ru(V) compounds," *Phys. Rev. B*, vol. 61, pp. 5262–5266, Feb 2000. [Online]. Available: http://link.aps.org/doi/10.1103/PhysRevB.61.5262 (Cited on page 156.)

[186] R. K. Sahu, Z. Hu, M. L. Rao, S. S. Manoharan, T. Schmidt, B. Richter, M. Knupfer, M. Golden, J. Fink, and C. M. Schneider, "X-ray absorption spectra at the Ru and Mn $L_{2,3}$ edges and long-range ferromagnetism in $SrRu_{1-x}Mn_xO_3$ solid solutions $(0 < x < 0.5)$," *Phys. Rev. B*, vol. 66, p. 144415, Oct 2002. [Online]. Available: http://link.aps.org/doi/10.1103/PhysRevB.66.144415 (Cited on page 156.)

[187] G. Herranz, F. Sánchez, N. Dix, D. Hrabovsky, I. C. Infante, J. Fontcuberta, M. V. García-Cuenca, C. Ferrater, and M. Varela, "Controlled magnetic anisotropy of $SrRuO_3$ thin films grown on nominally exact $SrTiO_3(001)$ substrates," *Applied Physics Letters*, vol. 89, no. 15, p. 152501, 2006. [Online]. Available: http://scitation.aip.org/content/aip/journal/apl/89/15/10.1063/1.2359296 (Cited on page 157.)

[188] P. Mahadevan, F. Aryasetiawan, A. Janotti, and T. Sasaki, "Evolution of the electronic structure of a ferromagnetic metal: Case of $srruo_3$," *Phys. Rev. B*, vol. 80, p. 035106, Jul 2009. [Online]. Available: http://link.aps.org/doi/10.1103/PhysRevB.80.035106 (Cited on page 158.)

[189] H.-T. Jeng, S.-H. Lin, and C.-S. Hsue, "Orbital Ordering and Jahn-Teller Distortion in Perovskite Ruthenate $SrRuO_3$," *Phys. Rev. Lett.*, vol. 97, p. 067002, Aug 2006. [Online]. Available: http://link.aps.org/doi/10.1103/PhysRevLett.97.067002 (Cited on page 158.)